

# Geological disasters in deep engineering: Mechanism, warning, and risk mitigation, volume II

**Edited by**

Guang-Liang Feng, Chi Zhang, Lijie Guo  
and Jun Zhao

**Coordinated by**

Zhi Zheng

**Published in**

Frontiers in Earth Science



## FRONTIERS EBOOK COPYRIGHT STATEMENT

The copyright in the text of individual articles in this ebook is the property of their respective authors or their respective institutions or funders. The copyright in graphics and images within each article may be subject to copyright of other parties. In both cases this is subject to a license granted to Frontiers.

The compilation of articles constituting this ebook is the property of Frontiers.

Each article within this ebook, and the ebook itself, are published under the most recent version of the Creative Commons CC-BY licence. The version current at the date of publication of this ebook is CC-BY 4.0. If the CC-BY licence is updated, the licence granted by Frontiers is automatically updated to the new version.

When exercising any right under the CC-BY licence, Frontiers must be attributed as the original publisher of the article or ebook, as applicable.

Authors have the responsibility of ensuring that any graphics or other materials which are the property of others may be included in the CC-BY licence, but this should be checked before relying on the CC-BY licence to reproduce those materials. Any copyright notices relating to those materials must be complied with.

Copyright and source acknowledgement notices may not be removed and must be displayed in any copy, derivative work or partial copy which includes the elements in question.

All copyright, and all rights therein, are protected by national and international copyright laws. The above represents a summary only. For further information please read Frontiers' Conditions for Website Use and Copyright Statement, and the applicable CC-BY licence.

ISSN 1664-8714  
ISBN 978-2-8325-3635-3  
DOI 10.3389/978-2-8325-3635-3

## About Frontiers

Frontiers is more than just an open access publisher of scholarly articles: it is a pioneering approach to the world of academia, radically improving the way scholarly research is managed. The grand vision of Frontiers is a world where all people have an equal opportunity to seek, share and generate knowledge. Frontiers provides immediate and permanent online open access to all its publications, but this alone is not enough to realize our grand goals.

## Frontiers journal series

The Frontiers journal series is a multi-tier and interdisciplinary set of open-access, online journals, promising a paradigm shift from the current review, selection and dissemination processes in academic publishing. All Frontiers journals are driven by researchers for researchers; therefore, they constitute a service to the scholarly community. At the same time, the *Frontiers journal series* operates on a revolutionary invention, the tiered publishing system, initially addressing specific communities of scholars, and gradually climbing up to broader public understanding, thus serving the interests of the lay society, too.

## Dedication to quality

Each Frontiers article is a landmark of the highest quality, thanks to genuinely collaborative interactions between authors and review editors, who include some of the world's best academicians. Research must be certified by peers before entering a stream of knowledge that may eventually reach the public - and shape society; therefore, Frontiers only applies the most rigorous and unbiased reviews. Frontiers revolutionizes research publishing by freely delivering the most outstanding research, evaluated with no bias from both the academic and social point of view. By applying the most advanced information technologies, Frontiers is catapulting scholarly publishing into a new generation.

## What are Frontiers Research Topics?

Frontiers Research Topics are very popular trademarks of the *Frontiers journals series*: they are collections of at least ten articles, all centered on a particular subject. With their unique mix of varied contributions from Original Research to Review Articles, Frontiers Research Topics unify the most influential researchers, the latest key findings and historical advances in a hot research area.

Find out more on how to host your own Frontiers Research Topic or contribute to one as an author by contacting the Frontiers editorial office: [frontiersin.org/about/contact](https://frontiersin.org/about/contact)

# Geological disasters in deep engineering: Mechanism, warning, and risk mitigation - volume II

## Topic editors

Guang-Liang Feng — State Key Laboratory of Geomechanics and Geotechnical Engineering, Institute of Rock and Soil Mechanics, Chinese Academy of Sciences (CAS), China

Chi Zhang — University of Vienna, Austria

Lijie Guo — Beijing Mining and Metallurgy Technology Group Co., Ltd., China

Jun Zhao — Anhui University of Science and Technology, China

## Topic coordinator

Zhi Zheng — Guangxi University, China

## Citation

Feng, G.-L., Zhang, C., Guo, L., Zhao, J., Zheng, Z., eds. (2023). *Geological disasters in deep engineering: Mechanism, warning, and risk mitigation - volume II*. Lausanne: Frontiers Media SA. doi: 10.3389/978-2-8325-3635-3

## Table of contents

04	<b>Editorial: Geological disasters in deep engineering: mechanism, warning, and risk mitigation—volume II</b> Guang-Liang Feng, Lijie Guo, Jun Zhao, Chi Zhang and Zhi Zheng
06	<b>Undrained strength of clay determined from simple shear test</b> Bin Huang, Shiqian Cai, Jingjing Li, Kunming Wu and Wenhui Yang
19	<b>Similar ratio experiment and characteristic analysis of quasi-sandstone</b> Lianghuan Yan, Jucai Chang, Longquan Qiao, Wenbao Shi, Tuo Wang, Dongdong Pang, Yuan Li and Yijun Guo
33	<b>Experimental and numerical research of crack propagation process and energy dissipation law of grouting specimens under radial impact load</b> Chang-Xing Zhu, Jia-Xin Sun, Jian Gong and Feng-E Wang
47	<b>A study on the shear strength characteristics and microscopic mechanism of coal-bearing soil under dry-wet cycles</b> Yakun Fan, Mingxin Zheng and Junhua Wu
62	<b>Numerical simulations of fatigue failure processes in intermittent jointed rock masses under the action of repeated stress waves</b> Shuyin Ma, Sheng Xue and Cheng Pan
73	<b>Failure mechanism and control of coal bursts triggered by mining induced seismicity in steeply inclined and extra thick coal seam</b> Jinrong Cao, Linming Dou, Jiang He, Guangan Zhu, Zhengyi Wang, Jinzheng Bai and Zepeng Han
91	<b>Modeling rules of regional flash flood susceptibility prediction using different machine learning models</b> Yuguo Chen, Xinyi Zhang, Kejun Yang, Shiyi Zeng and Anyu Hong
108	<b>Theoretical analysis of grouting reinforcement for surrounding rock of deep shaft based on stability and water inflow control</b> Peng Xiang, Hong Guang Ji, Guang Quan Zhang and Wen Guang Li
119	<b>DDA simulation study on fracturing failure reproducibility of heterogenous rock</b> Dayong Chen, Zheng Yang, Mingke Wang, Xufei Jiang and Youjun Ning
130	<b>Study on the time-varying fatigue reliability of the invert structure of subway tunnel under the action of train loads</b> Zhaofeng Chen, Linrong Xu, Changxi Huang, Lei Wu and Yonghui Shang





## OPEN ACCESS

EDITED AND REVIEWED BY  
Xingsen Guo,  
University College London,  
United Kingdom

\*CORRESPONDENCE  
Guang-Liang Feng,  
✉ glfeng@whrsm.ac.cn

RECEIVED 28 July 2023  
ACCEPTED 13 September 2023  
PUBLISHED 21 September 2023

CITATION  
Feng G-L, Guo L, Zhao J, Zhang C and  
Zheng Z (2023), Editorial: Geological  
disasters in deep engineering:  
mechanism, warning, and risk  
mitigation—volume II.  
*Front. Earth Sci.* 11:1268516.  
doi: 10.3389/feart.2023.1268516

COPYRIGHT  
© 2023 Feng, Guo, Zhao, Zhang and  
Zheng. This is an open-access article  
distributed under the terms of the  
[Creative Commons Attribution License  
\(CC BY\)](#). The use, distribution or  
reproduction in other forums is  
permitted, provided the original author(s)  
and the copyright owner(s) are credited  
and that the original publication in this  
journal is cited, in accordance with  
accepted academic practice. No use,  
distribution or reproduction is permitted  
which does not comply with these terms.

# Editorial: Geological disasters in deep engineering: mechanism, warning, and risk mitigation—volume II

Guang-Liang Feng<sup>1\*</sup>, Lijie Guo<sup>2,3</sup>, Jun Zhao<sup>4</sup>, Chi Zhang<sup>5</sup> and  
Zhi Zheng<sup>6</sup>

<sup>1</sup>State Key Laboratory of Geomechanics and Geotechnical Engineering, Institute of Rock and Soil Mechanics, Chinese Academy of Sciences, Wuhan, China, <sup>2</sup>BGRIMM Technology Group, Beijing, China, <sup>3</sup>National Centre for International Research on Green Metal Mining, Beijing, China, <sup>4</sup>Anhui University of Science and Technology, Huainan, China, <sup>5</sup>Department of Meteorology and Geophysics, University of Vienna, Vienna, Austria, <sup>6</sup>School of Civil Engineering and Architecture, Guangxi University, Nanning, China

## KEYWORDS

geological disasters, deep engineering, mechanism, warning, risk mitigation

## Editorial on the Research Topic

**Geological disasters in deep engineering: mechanism, warning, and risk mitigation—volume II**

## Introduction

In the pursuit of resources and space from the deep Earth, a multitude of deep underground projects have been completed, currently under construction, and have already been planned. These projects involve various fields, including water conservancy and hydropower, mining, transportation, deep laboratory research, national defense, and more. However, due to the complex geological environments and high ground stress, the construction of these projects frequently encounters various geological disasters, such as severe rockburst, significant deformation, substantial water inrush, and large-scale collapse. These geological disasters pose severe threats to construction safety and hinder the advancement of underground engineering practices. It is worth noting that the deformation behavior of surrounding rock and the development process of geological disasters differ significantly between deep and shallow engineering projects. Consequently, there is an urgent demand for the development of new geological disaster theories, monitoring techniques, warning systems, and risk mitigation methods tailored specifically to deep engineering conditions.

## Progress in the Research Topic

To draw the attention of scholars to geological disasters in deep engineering, the current Research Topic titled “*Geological disasters in deep engineering: mechanism, warning, and risk mitigation—volume II*” was organized. This volume showcases new theories, methods, and techniques developed to understand the mechanisms of geological disasters and provides insights

into warning systems and risk mitigation strategies. In total, 28 manuscripts were submitted, and out of these, 10 were selected for publication, resulting in a compilation of 10 papers authored by 49 researchers. These papers primarily focus on two main aspects. The first aspect explores the formation and evolution of geological disasters in deep engineering and their underlying mechanisms. The second aspect delves into warning methods and risk mitigation strategies.

## Formation and evolution of geological disasters in deep engineering and their mechanism

Zhu et al. investigated the crack propagation process and energy dissipation law of grouting specimens under radial impact loads. An impact test was conducted with varying air pressures using the split Hopkinson pressure bar test system. The failure mechanism of the samples was analyzed from the perspective of the dynamic failure process and energy dissipation. The research findings offer valuable insights for grouting-reinforced rock masses in deep roadways subjected to impact loads.

Chen et al. utilized the DDA method enhanced with the sub-block fracturing modeling algorithm and the Weibull distribution heterogeneity model to simulate pre-notched rock specimens. The study aimed to investigate the impact of heterogeneity on the reproducibility of macroscale strength and failure patterns of the specimens. This work highlights the significance of considering rock heterogeneity in practical rock engineering.

Fan et al. analyzed the relationship between shear strength and matric suction using direct shear tests on unsaturated coal-bearing soil, the filter paper method for matrix suction measurement, and scanning electron microscope tests. From a microscopic perspective, the internal reasons for the shear strength attenuation of unsaturated coal-bearing soil under dry-wet cycles were revealed. This study provides valuable supplementary information for understanding the engineering properties and stability of unsaturated coal-bearing soil.

Ma et al. studied the fatigue failure processes in intermittent jointed rock masses subjected to repeated stress waves. The failure processes of discontinuous jointed rock masses were numerically simulated using the Autodyn element software. This study holds practical significance for the long-term qualitative analysis of rock mass engineering.

Huang et al. present the results of a series of undrained strength tests using a Berkeley simple shear device, and an expression for the undrained shear strength of high plasticity clay was developed. The undrained shear strength of clay is a critical parameter for designing embankments and pile foundations.

Chen et al. investigated the time-varying fatigue reliability of the inverted structure of a subway tunnel under the influence of train loads. The findings from this study offer valuable insights into the health and reliability of subway tunnels and facilitate their condition monitoring.

## Warning methods and risk mitigation for geological disasters in deep engineering

Chen et al. conducted a study on regional flash flood susceptibility prediction, employing various machine learning models to develop modeling rules. This research holds practical

importance in the fields of flash flood and geological hazard prevention and control, road planning, and the development of suitable risk mitigation strategies in southwest and southern China.

The safe mining of steeply inclined and extra-thick coal seams presents significant challenges due to coal bursts. In light of mining-induced seismicity triggered coal burst in a typical steeply inclined and extra-thick coal seam, Cao et al. investigated the failure mechanism and control of such occurrences. This study sheds light on effectively managing coal bursts induced by mining-induced seismicity in steeply inclined and extra-thick coal seams.

Xiang et al. explored and established an elastic-plastic analytical formula for the grouted rock surrounding a shaft under the combined influence of thermal, hydraulic, and mechanical fields based on the Mohr–Coulomb yield criterion. This study provides a theoretical foundation for optimizing grouting reinforcement parameters in deep shafts.

The stability control of surrounding rock in deep roadways is increasingly challenging, with grouting reinforcement support emerging as the prevailing approach. Yan et al. conducted a study on a similar ratio experiment and characteristic analysis of quasi-sandstone, offering theoretical references for similar material simulation tests related to grouting in quasi-sandstone.

The construction of deep engineering projects demands a stronger focus on science and technology innovation. The papers featured in this Research Topic volume facilitate knowledge exchange within the deep geoengineering community, providing insights on enhancing the sustainability and disaster resistance of deep engineering projects.

## Author contributions

G-LF: Writing–original draft. LG: Writing–review and editing. JZ: Writing–review and editing. CZ: Writing–review and editing. ZZ: Writing–review and editing.

## Acknowledgments

We thank the various authors for submitting their work to this Research Topic and the reviewers who agreed to review individual contributions.

## Conflict of interest

LG was employed by BGRIMM Technology Group.

The remaining authors declare that the research was conducted in the absence of any commercial or financial relationships that could be construed as a potential conflict of interest.

## Publisher's note

All claims expressed in this article are solely those of the authors and do not necessarily represent those of their affiliated organizations, or those of the publisher, the editors and the reviewers. Any product that may be evaluated in this article, or claim that may be made by its manufacturer, is not guaranteed or endorsed by the publisher.



## OPEN ACCESS

## EDITED BY

Guang-Liang Feng,  
Institute of Rock and Soil Mechanics  
(CAS), China

## REVIEWED BY

Yong Wen,  
Zhongkai University of Agriculture and  
Engineering, China  
Fu-Quan Chen,  
Fuzhou University, China

## \*CORRESPONDENCE

Shiqian Cai,  
✉ cucumberhb@outlook.com

## SPECIALTY SECTION

This article was submitted to  
Geohazards and Georisks,  
a section of the journal  
Frontiers in Earth Science

RECEIVED 15 November 2022

ACCEPTED 12 December 2022

PUBLISHED 04 January 2023

## CITATION

Huang B, Cai S, Li J, Wu K and Yang W  
(2023), Undrained strength of clay  
determined from simple shear test.  
*Front. Earth Sci.* 10:1098846.  
doi: 10.3389/feart.2022.1098846

## COPYRIGHT

© 2023 Huang, Cai, Li, Wu and Yang.  
This is an open-access article  
distributed under the terms of the  
[Creative Commons Attribution License  
\(CC BY\)](https://creativecommons.org/licenses/by/4.0/). The use, distribution or  
reproduction in other forums is  
permitted, provided the original  
author(s) and the copyright owner(s) are  
credited and that the original  
publication in this journal is cited, in  
accordance with accepted academic  
practice. No use, distribution or  
reproduction is permitted which does  
not comply with these terms.

# Undrained strength of clay determined from simple shear test

Bin Huang<sup>1</sup>, Shiqian Cai<sup>1\*</sup>, Jingjing Li<sup>2</sup>, Kunming Wu<sup>1</sup> and Wenhui Yang<sup>1</sup>

<sup>1</sup>School of Architecture and Civil Engineering, Huizhou University, Huizhou, China, <sup>2</sup>Library, Huizhou University, Huizhou, China

The undrained shear strength of clay is an important parameter for the design of embankments, shallow foundations, and pile foundations. Among the various methods of testing undrained strength, the simple shear is essential when the shearing mode of the soil surrounding the pile is similar to that in a simple shear test. This study employs a series of undrained strength tests with a Berkeley simple shear apparatus. Three reconstituted natural clays and one artificial clay were tested with a range of coefficients of consolidation. The influence factors, including sample pre-consolidation pressure, saturation back pressure, shearing rate, height of specimen, consolidation stress, and lateral stress ratio, were investigated in undrained simple shear tests. The failure mode in simple shear and corresponding strength parameters are also examined. Based on the test data set, models for describing the undrained strength with simple shear for high plasticity clays are developed and compared to test data for normally consolidated reconstituted clay. Good agreement between models and intact Onsoy clay is also observed when allowance is made for the coefficient of consolidation and strength parameters of undisturbed clay and *in situ* stress state.

## KEYWORDS

undrained shear strength, simple shear, shearing rate, excess pore pressure, clay

## 1 Introduction

The undrained shear strength of soils is a key parameter in many applications. The standard methods to determine the shear strength of soils are broadly classified as laboratory (e.g., unconfined compression, unconsolidated/undrained (UU) triaxial compression, consolidated undrained (CU) triaxial compression, simple shear, fall cone, pocket penetrometer, torvane, and laboratory vane) and *in situ* procedures (e.g., cone penetration test (CPT)/T-bar/ball penetration test and vane test). The vane test is usually considered to give the best result. A penetration test would give crude correlation to strength unless there is a sufficient empirical or calibrated data set. All penetration tests need laboratory tests or *in situ* vane tests to calibrate the conversion factors. The pocket penetrometer, fall cone, and torvane are all used on the soil before it is extruded from the

tube section. Like penetration tests, these strength index tests cannot obtain strength directly and require conversion factors to calculate strength.

Unconfined compression is the best general-purpose test but underestimates strength because disturbance decreases effective stress. In order to reduce the sample disturbance effect, the recompression method (Bjerrum, 1973) or the SHANSEP method (Ladd & Foott, 1974) is applied in simple shear and triaxial tests. The CU test performed *in situ* confining pressure overestimates strength because disturbance leads to smaller water content upon reconsolidation. If the recompression method is used with the simple shear test, the specimen should be preloaded to approximately 75%–80% of the estimated preconsolidation stress of the specimen and then unloaded back to the estimated *in situ* vertical effective stress (ISO 19901-8, 2015).

Strengths measured in simple shear are generally lower than corresponding strengths measured in triaxial compression. Randolph & Wroth (1981) developed a theoretical expression between the two types of undrained shear strength. Based on 50 different clay data sets, Mayne (1985) suggested that the undrained shear strength from simple shear is on the order of  $0.7 \pm 0.2$  of the strength in triaxial compression.

The simple shear strength is sometimes more important because it represents the average mobilized strength for many cases (e.g., embankment stability on soft clays, soft ground beneath spread footings, and shaft resistance along pile foundations). The mode of shearing of the soil around the pile is very similar to that in a simple shear test (Randolph & Wroth, 1981). Furthermore, the intact specimens used in the simple shear test with a height of 20–30 mm are much smaller than those used in a triaxial test with a length of 150 mm or 200 mm for offshore clay (Randolph & Gourvenec, 2017). Therefore, simple shear is more popular than the triaxial test in the offshore industry due to cost-efficient sampling and rapid consolidation.

Two commonly used simple shear apparatuses based on cylindrical samples are the Berkeley simple shear device with normal rubber membrane (Rau, 1999) and the NGI simple shear device with a stacked ring or wire-reinforced membrane (Bjerrum & Landva, 1966; Dyvik et al., 1987). Some comparisons were made between the Berkeley and NGI simple shear devices (Acharya & Airey, 2017; Sharma et al., 2017). The Berkeley simple shear device has more clear stress state but also has the limitation of the non-uniformity of shear stress. A specimen with a large diameter:height ratio can minimize the uncertain effect. The stress states, boundary conditions, and failure modes in simple shear are discussed in many articles (Prevost & Høeg, 1976; Wood et al., 1979; Wroth, 1984; Budhu, 1984, 1985; Airey & Wood, 1987; Atkinson et al., 1991; Reyno et al., 2005; Joer et al., 2010; Verma & Wijewickreme, 2020).

This paper presents the results of a series of undrained strength tests using a Berkeley simple shear device. Three



FIGURE 1  
UWA simple shear apparatus.

reconstituted natural clays and one artificial clay were tested in this program. The influence factors, including sample pre-consolidation pressure, saturation back pressure, shearing rate, coefficient of consolidation, height of specimen, consolidation stress, and lateral stress ratio, were observed in undrained simple shear tests. Based on test results, an expression of undrained shear strength was developed for high plasticity clays, which was verified by tests on “old” UWA clay and intact Onsoy clay.

## 2 Simple shear test

### 2.1 Simple shear apparatus and test procedure

The simple shear apparatus used in this study, shown in Figure 1, was developed at the University of Western Australia. This apparatus is also called the Berkeley simple shear device. It follows a similar approach to a triaxial apparatus, with the specimen contained by a normal rubber membrane and subjected to cell pressure, but with the base of the specimen mounted on a platform that can slide horizontally. Simple shear tests are performed on cylindrical soil specimens, typically 50 mm or 72 mm in diameter and 20–30 mm tall. The specimen is consolidated in an identical way to a triaxial specimen, with cell pressure and back pressure applied under either isotropic or anisotropic stress conditions. Following consolidation, the undrained test is carried out by closing the back pressure valve while maintaining a constant specimen

TABLE 1 Summary of soil parameters.

Clay	Onsoy clay	Brunei clay	Bayswater clay	New Kaolin clay	Old Kaolin clay
LL (%)	63	60	57	70	61
PI (%)	28	30	26	34	34
Clay fraction (%)	66	49	33	70	79
Organic content (%)	3.7	3.1	9.5	0.2	0
$c_v$ (m <sup>2</sup> /yr)	1.4	1.8	0.48	7.0	2.0

Note: "New" Kaolin is relative to the UWA; Old Kaolin was used previously. Vertical coefficients of consolidation of clays are derived from consolidometer test under 50 kPa.

height achieved by stopping the motor. The cell pressure is adjusted during the undrained tests to maintain a constant total vertical stress.

## 2.2 Material and specimens preparation

Testing was conducted on four reconstituted clay specimens with high plasticity. Onsoy clay samples were retrieved from a depth of 3–4 m in a test pit in Onsoy, Norway. Brunei clay samples were provided in the form of tube samples recovered over depths between 5 m and 120 m from a single borehole at the site. Bayswater clay was obtained using an excavator from a depth of 4 m–4.5 m in Perth, Australia. New Kaolin clay is artificial clay currently used in UWA instead of the UWA Kaolin used previously (Lehane et al., 2009; Richardson et al., 2009; Chow et al., 2014; Mahmoodzadeh & Randolph, 2014). The characterizations of the four clays are listed in Table 1, and the properties of old Kaolin clay are also given.

When preparing the clay slurries, all debris, shells or other contaminants larger than 0.5 mm were first removed. The clay was then placed in a high-capacity mixer and mixed to a water content of approximately 1.75 to 2.0 times the liquid limit. After several hours of mixing to achieve a consistent slurry, the samples were transferred to large "Nally" bins, where they were repeatedly remixed with a hand mixer to maintain sample uniformity. The clay slurry was poured into 90 mm diameter tubes and consolidated in stages to a final vertical effective stress that was usually 3–5 kPa smaller than the test pressure. The samples were then extruded from the consolidation tubes and trimmed to test specimens using the thin-walled sample cutter. The specimens were 72 mm in diameter, and the heights after consolidation are shown in Table 2.

## 2.3 Testing program

The testing program is shown in Table 2. It consists of 17 tests for Onsoy clay, 3 tests for Brunei clay, 6 tests for Bayswater clay, and 4 tests for new Kaolin clay. Each clay shearing test was conducted in the undrained condition to

investigate the effect of shearing rate, consolidation stress, lateral stress ratio  $K$ , back pressure, and consolidation strain in the tube. According to Table 1, the four high-plasticity clays have a wide range of consolidation coefficients. Many tests are repeated.

## 3 Undrained shear test results

The height of specimens, excess pore pressure ratios, and lateral stress ratios, all at failure, and the undrained strength ratios obtained in simple shear tests are listed in Table 3.

### 3.1 Undrained strength

There was no apparent effect of lower back pressure (BP) and consolidation strain on undrained strength, so these tests were taken as repeat tests of the base case. The undrained strengths of all repeat tests are plotted in Figure 2 with respect to vertical consolidation stress. There is a certain range of undrained strength, which may be due to a lack of uniformity of samples and test operations or uncertainty during undrained shearing. However, there is a good response trend when plotting the relationship between undrained strength and excess pore pressure at failure (Figure 3). The increase in excess pore pressure at failure causes a decrease in undrained strength, which is in good agreement with the principle of effective stress. That is to say, the uncertainty of the strength during undrained shearing becomes certain in the effective stress analysis.

Figure 4 shows variation in the undrained strength ratio with vertical consolidation stress. The undrained strength ratio varies between 0.18 and 0.42, which is much larger than the actual value range (Jamiolkowski et al. (1985)). The undrained strength ratio decreases with the increase of vertical consolidation stress. From the Jurgenson–Rutledge hypothesis (Rutledge, 1947), the undrained strength ratio is constant for clay soils, assuming the curve of  $e_f \log \sigma_{vc}$  is parallel to the curve of  $e_f \log (\sigma_1 - \sigma_3)_f$ . Lehane et al. (2009) suggested that the undrained strength ratio may reduce slightly with an increase in effective stress level when the vertical effective stress is larger than 100 kPa. Boukpeti & White (2017) gave a non-linear failure envelope of the power law



TABLE 2 Testing program.

Test no.	$H_c$ : mm	$\sigma'_{vc}$ : kPa	$K=\sigma'_{hc}/\sigma'_{vc}$	Shearing rate, $v$ : mm/min	Description
Onsoy-SS1	26.3	50	0.5	0.1	Base case @ 50 kPa, $K=0.5$
Onsoy-SS2	26.0	50	0.5	2.5	Effect of shearing rate
Onsoy-SS3	24.7	150	0.5	0.1	Base case @ 150 kPa
Onsoy-SS4	26.4	50	0.5	0.1	Onsoy-SS1 repeat
Onsoy-B1	27.8	50	0.65	0.1	Effect of $K$ , Base case @ 50 kPa, $K=0.65$
Onsoy-B2	26.6	50	0.65	2.5	Effect of shearing rate
Onsoy-B3	27.6	50	0.5	0.1	Onsoy-SS1 repeat
Onsoy-B4	27.2	50	1	0.1	Effect of $K$
Onsoy-B5	28.5	50	2	0.1	Effect of $K$
Onsoy-B6	27.1	50	0.65	0.1	Effect of lower BP
Onsoy-B7	25.3	50	0.65	0.1	Onsoy-B1 repeat
Onsoy-B8	24.3	100	0.65	0.1	Effect of consolidation strain
Onsoy-B9	22.8	200	0.65	0.1	Base case @ 200 kPa
Onsoy-B10	27.6	100	0.65	0.1	Base case @ 100 kPa
Onsoy-B11	25.9	100	0.65	0.1	Effect of lower BP
Onsoy-B12	24.3	100	0.65	0.1	Onsoy-B10 repeat
Onsoy-B13	27.5	100	0.65	0.1	Onsoy-B10 repeat
Brunei-SS1	27.1	50	0.5	0.1	Base case @ 50 kPa
Brunei-SS2	27.1	50	0.5	2.5	Effect of shearing rate
Brunei-SS3	24.3	150	0.5	0.1	Base case @ 150 kPa
Bayswater-SS1	26.0	50	0.5	0.1	Base case @ 50 kPa
Bayswater-SS2	25.8	50	0.5	2.5	Effect of shearing rate
Bayswater-SS3	24.6	150	0.5	0.1	Base case @ 150 kPa
Bayswater-B1	26.2	50	0.5	0.1	Bayswater-SS1 repeat
Bayswater-B2	26.6	50	0.65	0.1	Effect of $K$
Bayswater-B3	24.0	100	0.65	0.1	Base case @ 100 kPa
New Kaolin-SS1	23.9	50	0.5	0.1	Base case @ 50 kPa
New Kaolin-SS2	23.8	50	0.5	2.5	Effect of shearing rate
New Kaolin-SS3	23.0	150	0.5	0.1	Base case @ 150 kPa
New Kaolin-SS4	23.8	150	0.5	0.1	New Kaolin-SS3 repeat

Note: To test the effect of consolidation strain, the preconsolidation pressure is 47 kPa, which is much smaller than the test pressure. To test the effect of lower BP, the back pressure is 200 kPa, while in other cases, it is 400 kPa.

relationship when effective normal stress is smaller than 10 kPa. Therefore, for a large range of stress, the failure envelope would be non-linear, which means there is a tiny cohesion of about 5 kPa for normally consolidated clay while applying the linear Mohr–Coulomb criterion. That is why the undrained strength ratio decreases with vertical consolidation stress in low stress and

only slightly reduces or is nearly constant in moderate or high stress.

The undrained strength ratio *versus* the lateral stress ratio  $K$  for Onsoy clay is shown in Figure 5. There is a clear increasing trend of  $\tau_f/\sigma'_{vc}$  vs.  $K$ . For a certain vertical consolidation stress, the larger the  $K$  value, the lower the void

TABLE 3 Summary of test results.

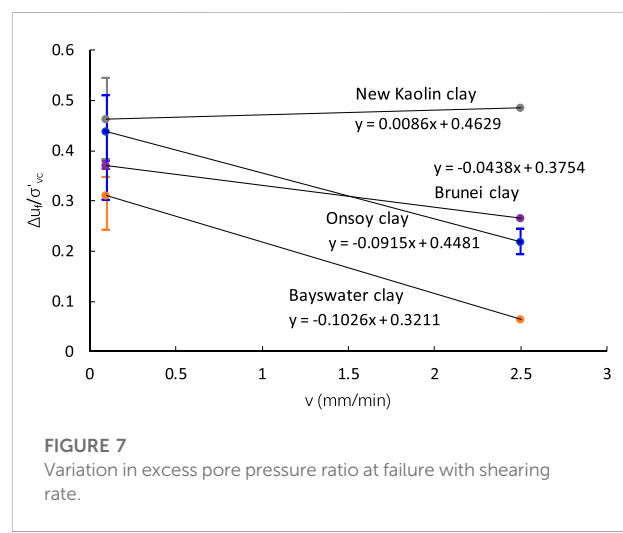
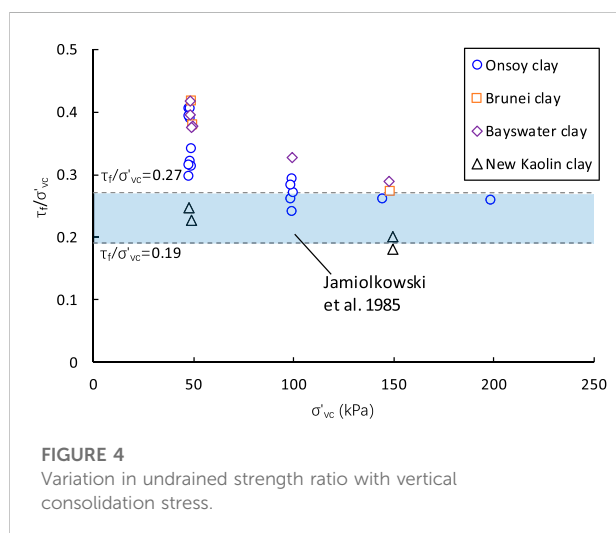
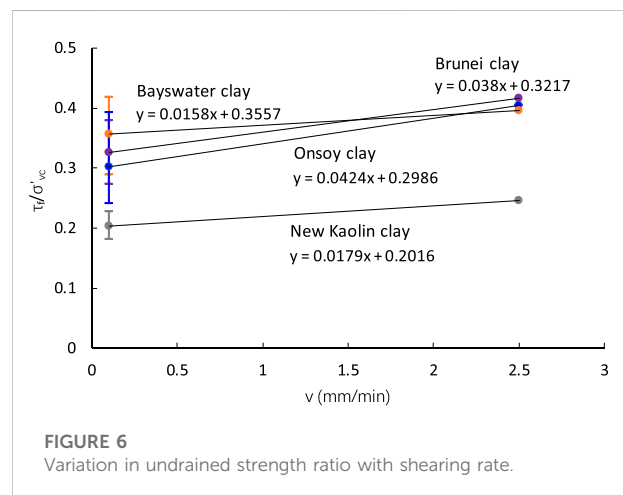
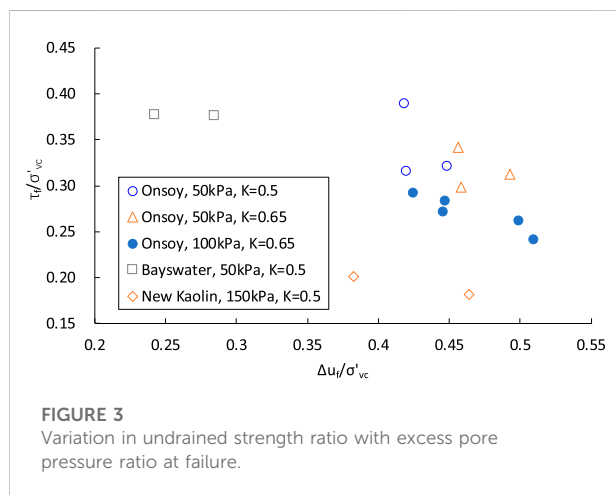
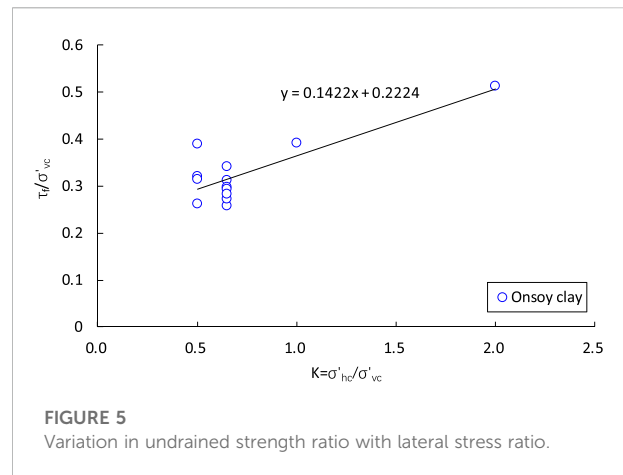
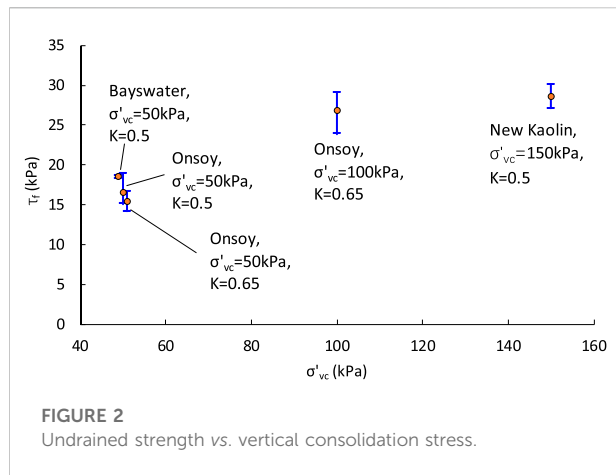
Test no.	$\sigma'_{vc}$ : kPa	$K$	$v$ : mm/min	$H_f$ : mm	$\Delta u_f/\sigma'_{vc}$	$\sigma_{hf}/\sigma_{vf}$	$\tau_f/\sigma'_{vc}$
Onsoy-SS1	50	0.5	0.1	26.3	0.42	0.95	0.39
Onsoy-SS2	50	0.5	2.5	26.0	0.19	0.96	0.40
Onsoy-SS3	150	0.5	0.1	24.7	0.41	0.90	0.26
Onsoy-SS4	50	0.5	0.1	26.4	0.45	0.93	0.32
Onsoy-B1	50	0.65	0.1	27.8	0.49	0.97	0.31
Onsoy-B2	50	0.65	2.5	26.6	0.24	1.03	0.40
Onsoy-B3	50	0.5	0.1	27.6	0.42	0.89	0.32
Onsoy-B4	50	1	0.1	27.2	0.40	1.01	0.39
Onsoy-B5	50	2	0.1	28.5	0.30	1.15	0.51
Onsoy-B6	50	0.65	0.1	27.1	0.46	0.95	0.30
Onsoy-B7	50	0.65	0.1	25.3	0.46	0.98	0.34
Onsoy-B8	100	0.65	0.1	24.3	0.50	0.95	0.26
Onsoy-B9	200	0.65	0.1	22.8	0.45	0.90	0.26
Onsoy-B10	100	0.65	0.1	27.6	0.45	0.91	0.27
Onsoy-B11	100	0.65	0.1	25.9	0.42	0.96	0.29
Onsoy-B12	100	0.65	0.1	24.3	0.51	0.97	0.24
Onsoy-B13	100	0.65	0.1	27.5	0.45	0.91	0.28
Brunei-SS1	50	0.5	0.1	27.1	0.38	1.23	0.38
Brunei-SS2	50	0.5	2.5	27.1	0.27	1.20	0.42
Brunei-SS3	150	0.5	0.1	24.3	0.36	0.92	0.27
Bayswater-SS1	50	0.5	0.1	26.0	0.24	0.80	0.38
Bayswater-SS2	50	0.5	2.5	25.8	0.06	0.89	0.40
Bayswater-SS3	150	0.5	0.1	24.6	0.34	0.88	0.29
Bayswater-B1	50	0.5	0.1	26.2	0.28	0.85	0.38
Bayswater-B2	50	0.65	0.1	26.6	0.33	0.97	0.42
Bayswater-B3	100	0.65	0.1	24.0	0.35	0.91	0.33
New Kaolin-SS1	50	0.5	0.1	23.9	0.54	1.04	0.23
New Kaolin-SS2	50	0.5	2.5	23.8	0.48	1.14	0.25
New Kaolin-SS3	150	0.5	0.1	23.0	0.46	0.96	0.18
New Kaolin-SS4	150	0.5	0.1	23.8	0.38	0.92	0.20

Note: In simple shear tests,  $H_f=H_c$  and  $\sigma_{vf}=\sigma'_{vc}$ .

ratio or water content. According to the shear strength theory developed by Hvorslev (1960), the strength at failure was a function of the effective normal stress and the void ratio at failure. Therefore, the increase in  $K$  leads to a decrease in the void ratio, resulting in an increase in undrained strength. The effect of  $K$  on effective stress will be discussed below.

Lehane and Jardine (1992) ascribed a moderate positive rate effect to viscous phenomena combined with variable degrees of particle sorting within the shear zone. Lehane *et al.* (2009) suggested that viscous effects dominate under the fully undrained condition, which is beneficial to resistance and strength. An overall increase in undrained strength with shearing rate was observed for the four clays (Figure 6).





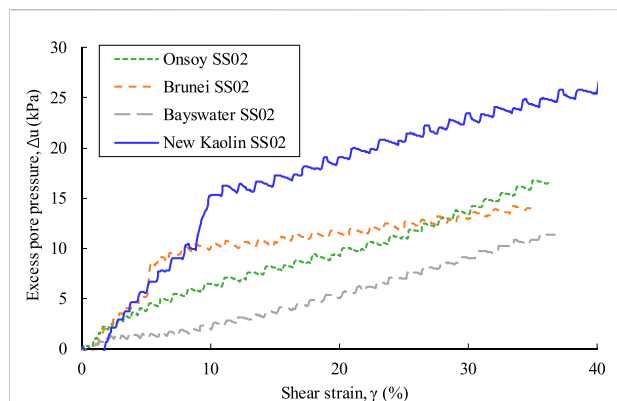


FIGURE 8

Excess pore pressure ratio plotted against shear strain at a shearing rate of 2.5 mm/min.

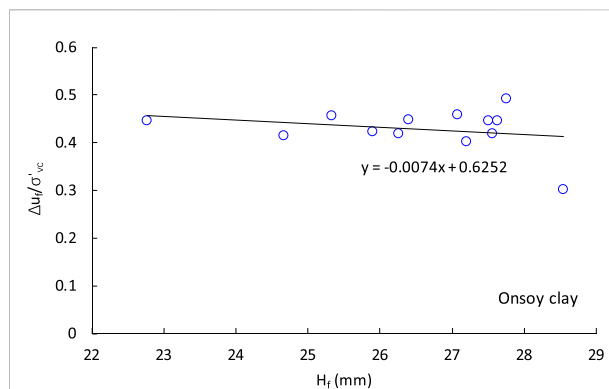


FIGURE 9

Variation in excess pore pressure ratio with specimen height, both at failure.

Although the undrained strength ratio at 0.1 mm/min for each material varies to some degree, the average values of each specimen do not change the overall trend of increasing. The effect of shearing rate on excess pore pressure is much more significant than undrained strength and will be discussed below. It appears that the gain of undrained strength for low permeability clay is mainly caused by smaller excess pore pressure than viscous effects due to a faster shearing rate.

### 3.2 Excess pore pressure

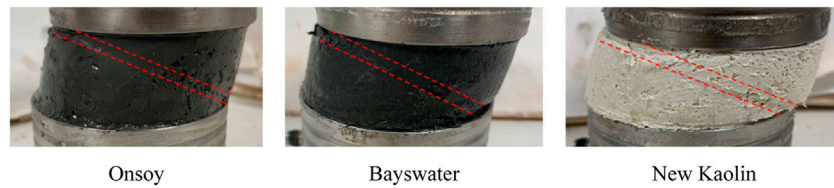
Variation in excess pore pressure ratio at failure with shearing rate is shown in Figure 7. Excess pore pressure decreases with strain rate after the strain is larger than 5% (Richardson & Whitman, 1963). At the fast shearing rate of 2.5 mm/min, the shear strain reaches 30% in only 3 min, and the specimen has already failed. Compared to the slow shearing of 0.1 mm/min, there is not enough time for the pore pressure to increase fully. However, there is no noticeable change between the slow and fast rates for new Kaolin clay. This is because the new Kaolin's coefficient of consolidation ( $7.0 \text{ m}^2/\text{yr}$ ) is much larger than the coefficients of the three other clays ( $0.48\text{--}1.8 \text{ m}^2/\text{yr}$ ), and the excess pore pressure is not only related to the shearing rate but also to the coefficient of consolidation.

To find the effect of the consolidation coefficient, the curves of excess pore pressure *versus* shear strain for the four clays are plotted together, as shown in Figure 8. They are all at an identical shearing rate of 2.5 mm/min, and the order of the coefficient of consolidation is new Kaolin > Brunei ≈ Onsoy > Bayswater (Table 1). After the shear strain becomes greater than 10%, the excess pore pressure of the new Kaolin is greater than that of other clays, Brunei's is close to Onsoy's, and Bayswater's is the smallest. There is a good agreement between excess pore pressure and the coefficient of consolidation. In other words, the clay with

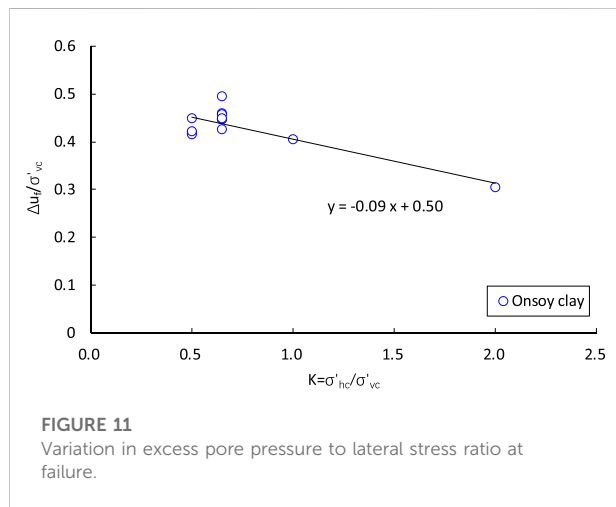
the larger coefficient of consolidation is more likely to generate excess pore pressure under undrained shearing.

The excess pore pressure ratio at failure decreases with the increase in specimen height, as displayed in Figure 9. In the triaxial test, excess pore pressure was measured with different height-to-diameter ratios, showing that the larger the specimen height, the smaller the pore pressure (Muraro & Jommi, 2021). The specimens in this investigation, contained by a flexible membrane and subjected to cell pressure, are subject to conditions similar to those of the triaxial test, and the corresponding excess pore pressure changes with the height of the specimen while shearing is also consistent.

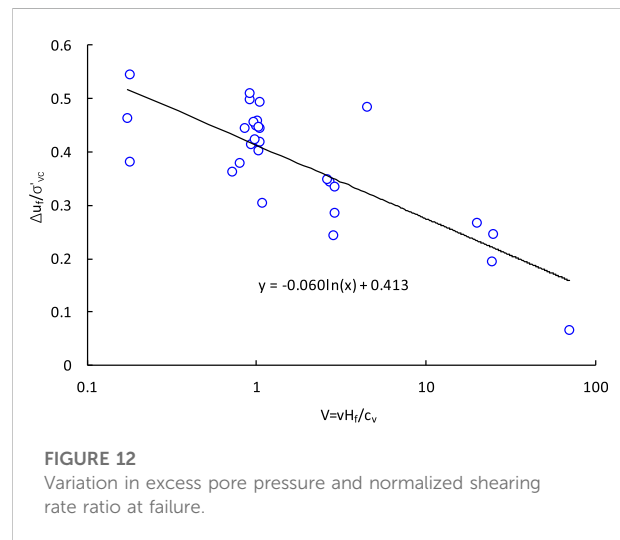
A soft clay sample may possibly contain a combination of both a discrete diagonal shear plane and the conventional type of simple shear deformation (Joer et al., 2010). In the flexible boundary, diagonal shear planes are formed through the specimen in the Berkeley simple shear device, generally from the back of the top platen to the top of the front of the bottom platen, and a visible shear plane forms at large strain greater than about 15% (Sharma et al., 2017). Figure 10 shows photographs of typical failure planes in a Berkeley simple shear device for each clay, with the same shear failure mode suggested by Budhu (1984) and Reyno et al. (2005). Shearing occurred in a shear band of thickness that resulted in the generation of excess pore pressure while neglecting possible pore pressure generation outside the shear band in the direct shear test (Boukpeti & White, 2017). For the simple shear test, the regions outside the shear plane still undergo shear deformation, and the excess pore pressure cannot be ignored, but due to stress concentration, the excess pore pressure of the shear plane is much larger than other regions, especially when the specimen is close to failure. The shear band thickness of clayey soil was 2–8 mm after shearing was completed, which is independent of the height and diameter of the specimen (Hicher et al., 1994; Gylland et al., 2014), while the shear band thickness decreases

**FIGURE 10**

Photographs of typical failure planes in a Berkeley simple shear device.

**FIGURE 11**

Variation in excess pore pressure to lateral stress ratio at failure.

**FIGURE 12**

Variation in excess pore pressure and normalized shearing rate ratio at failure.

with the shearing rate (Jostad et al., 2006; Gylland et al., 2014). Therefore, the diameter of the specimen has little effect on the excess pore pressure, and the larger the height of the specimen, the smaller the excess pore pressure due to diffusion and the averaging effect.

There is a definite decreasing trend in the ratio of excess pore pressure *versus* lateral stress shown in Figure 11. The decrease in excess pore pressure causes the effective stress to increase, which will contribute to the undrained strength. In addition to the smaller void ratio at failure induced by the increase of lateral stress ratio discussed above, the gain in effective stress is another factor to improve undrained strength, according to the shear strength theory developed by Hvorslev (1960). For Onsoy clay, the relationship between excess pore pressure and lateral stress ratio can be approximated by the following equation:

$$\frac{\Delta u_f}{\sigma'_{vc}} = 0.5 - 0.09K, \quad (1)$$

where  $K$  is the lateral stress ratio, and  $K = \sigma'_{hc}/\sigma'_{vc}$  and  $\sigma'_{hc}$  and  $\sigma'_{vc}$  are the horizontal and vertical consolidation stress of the specimen, respectively.

## 4 Formula for undrained shear strength

The above analysis shows that the lower the shearing rate, the larger the coefficient of consolidation, and the smaller the specimen height, the larger the excess pore pressure. Therefore, similar to the normalization of penetrometer velocity proposed by Finnie & Randolph (1994), the normalized shearing rate in the simple shear test can be established as follows:

$$V = \frac{v \cdot H_f}{c_v}, \quad (2)$$

where  $v$  is the shearing rate, expressed in mm/min,  $H_f$  is the height of the specimen at failure or after consolidation, and  $c_v$  is the vertical coefficient of consolidation.

Figure 11 shows little difference in excess pore pressure ratio between  $K=0.5$  and  $0.65$ , so these data can be plotted together as  $K=0.575$ . The relationship between excess pore pressure and normalized shearing rate for four clays tested with a  $K$  value of  $0.5$  and  $0.65$  is plotted in Figure 12. The excess pore pressure ratio

TABLE 4 Summary of strength parameters based on effective stresses.

Clay	Failure plane		Horizontal plane	
	$c'_f$ : kPa	$\phi'_f$ : °	$c'_h$ : kPa	$\phi'_h$ : °
Onsoy	4.7	27.6	5.8	21.8
Brunei	4.8	24.3	8.2	18.8
Bayswater	5.0	26.4	4.8	21.4
New Kaolin	4.0	17.9	5.1	15.3
Old Kaolin	8.3	21.1	5.8	19.5

and the normalized shearing rate have a good linear decreasing relationship in the semi-logarithmic coordinate.

The excess pore pressure ratio is given by

$$\frac{\Delta u_f}{\sigma'_{vc}} = 0.413 - 0.06 \cdot \ln V. \quad (3)$$

Combining Eq. 1 and Eq. 3, where the  $K$  value of Eq. 3 is 0.575, the lateral stress ratio can be taken into account in the equation, and the excess pore pressure ratio may be written as

$$\frac{\Delta u_f}{\sigma'_{vc}} = [0.413 - 0.06 \cdot \ln V] \times \frac{0.5 - 0.09K}{0.448}. \quad (4)$$

For an undrained simple shear test, taking  $H_f=25$  mm and  $v=0.1$  mm/min, Eq. 4 becomes

$$\frac{\Delta u_f}{\sigma'_{vc}} = \left[ 0.413 - 0.06 \cdot \ln \left( \frac{1.31}{c_v} \right) \right] \times \frac{0.5 - 0.09K}{0.448}, \quad (5)$$

where  $c_v$  is expressed in  $m^2/yr$ .

For soil in the field, the lateral stress ratio  $K$  can be calculated by Eq. 6, proposed by Mayne and Kulhawy (1982).

$$K = (1 - \sin \phi'_f) \cdot OCR^{\sin \phi'_f}, \quad (6)$$

where  $\phi'_f$  is the friction angle of soil based on effective stresses on the failure plane, and OCR denotes the over-consolidation ratio.

The undrained strength depends on the amount of effective normal stress or excess pore pressure generated during shearing. This may be expressed as

$$\tau_f = c'_h + \left( 1 - \frac{\Delta u_f}{\sigma'_{vc}} \right) \cdot \sigma'_{vc} \tan \phi'_h, \quad (7)$$

where  $c'_h$  is the cohesion of soil based on effective stresses on the horizontal plane, and  $\phi'_h$  is the friction angle of soil based on effective stresses on the horizontal plane.

Eq. 5 is suitable for normally consolidated or slightly over-consolidated clay, so Eq. 7, based on Eq. 5, is also applicable in the same clay but not for medium or strong over-consolidated clay.

An alternative interpretation of the simple shear test that considers the diagonal failure plane rather than the horizontal plane is given by Joer et al. (2010). Effective parameters on the

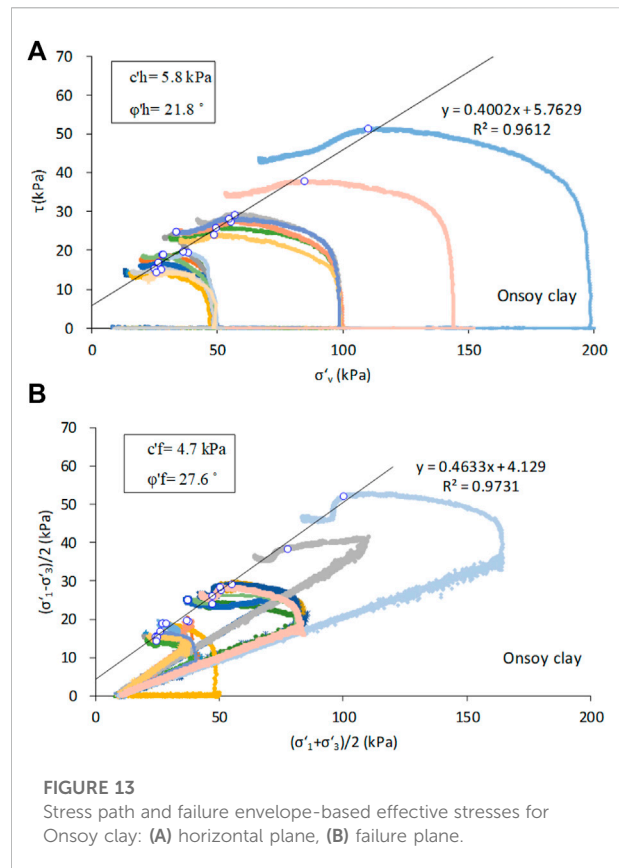
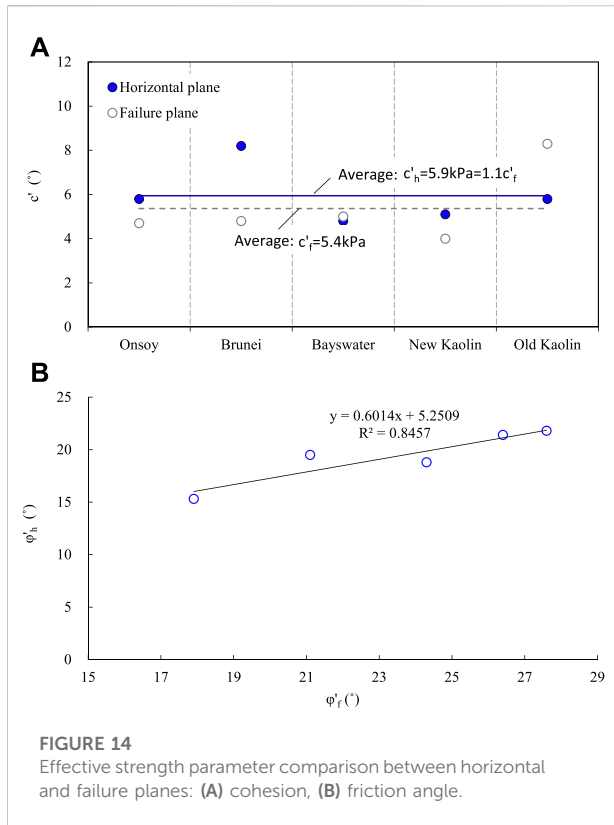


FIGURE 13

Stress path and failure envelope-based effective stresses for Onsoy clay: (A) horizontal plane, (B) failure plane.

horizontal plane can be deduced according to the traditional interpretation of horizontal failure mode (Table 4). Figure 13 gives the typical stress paths and failure envelopes on the horizontal and failure planes, respectively, which are both based on undrained simple shear tests. The failure points in the diagram are determined by the shear stress, normal stress, and pore pressure at the point of peak shear stress. The failure envelopes both show a good linear relationship, while the envelope of the failure plane is slightly more linear than that of the horizontal plane. As shown in Table 4, cohesion on the horizontal and failure planes is very close for each clay, and the friction angle on the horizontal plane is smaller than that on the failure plane.

The strength parameters of the failure plane based on effective stresses can be obtained by various methods, such as the CU and CD triaxial tests, the drained direct shear test, and the simple shear test. Effective strength parameters must be used when applying Eqs 5, 7 to predict undrained strength. It is possible to deduce effective parameters of the horizontal plane from failure plane parameters. The comparisons of effective strength parameters between the horizontal and failure planes are shown in Figure 14. The relationships of cohesion and friction angle between different planes are as follows:



**FIGURE 14**  
Effective strength parameter comparison between horizontal and failure planes: (A) cohesion, (B) friction angle.

$$c_h' = \max(1.1c_f', 6 \text{ kPa}), \quad (8)$$

$$\phi_h' = 5.3^\circ + 0.6 \cdot \phi_f', \quad (9)$$

where  $c_f'$  is the cohesion of soil based on effective stresses on the failure plane, and  $\phi_f'$  is the friction angle of soil based on effective stresses on the failure plane.

## 5 Verification of undrained strength

### 5.1 Reconstituted clay

Including the data of the old Kaolin clay used in UWA previously (Lehane et al., 2009), the undrained strength of five clays was compared with the measurement and prediction data from Eqs 4, 7, shown in Figure 15A. In addition, Leonards' method was compared in Figure 15B. Leonards (1962) gave Eq. 10 to estimate undrained strength.

$$\tau_f = \frac{c_f' \cdot \cos \phi_f' + \sigma_{vc}' \sin \phi_f' [K + A_f \cdot (1 - K)]}{1 - (2A_f - 1) \cdot \sin \phi_f'}, \quad (10)$$

where  $A_f$  is the pore pressure parameter, and its value is 0.7–1.3 for normally consolidated clays.

Figure 15A shows good agreement between predicted and measured undrained  $\tau_f$  values, including those of the old

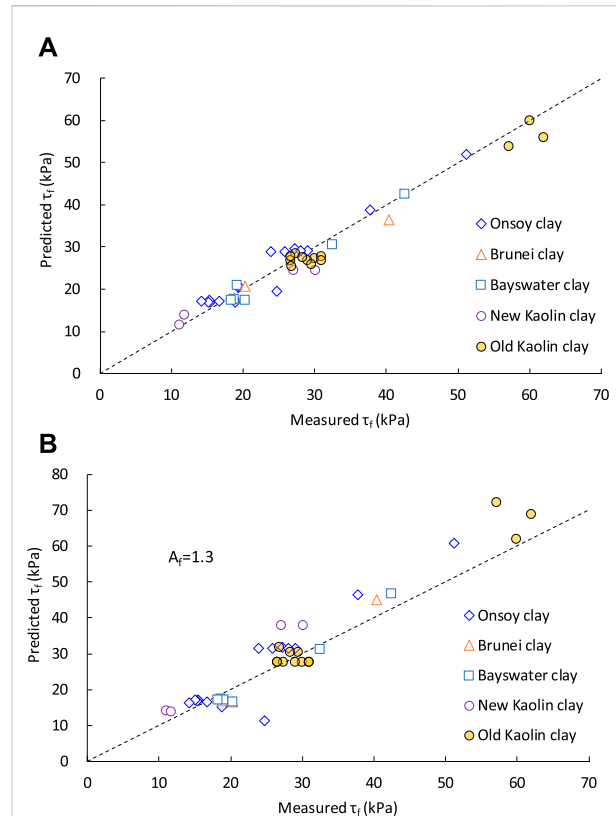


**FIGURE 15**  
Comparison between predicted and measured undrained strength for reconstituted clay: (A) method of Eqs 4, 7, (B) method of Leonards (1962).

Kaolin clay, which is not referred to in the developing formula. There is a slightly higher calculated undrained strength when using Leonards' method with the  $A_f$  value of the upper limit in Eq. 10. The lower the  $A_f$  value, the higher the strength. It is difficult to determine the pore pressure parameter properly.

Jamiolkowski et al. (1985) suggested that

$$\frac{c_u}{\sigma_{vc}} = (0.23 \pm 0.04) \cdot \text{OCR}^{0.8}. \quad (11)$$

Figure 4 shows the normalized undrained strength of Eq. 11 with the measured values for each clay. There is an obvious decreasing trend of undrained strength ratio versus vertical consolidation stress, while a trend is not clear in the Jamiolkowski equation. Jamiolkowski's strength ratio is the lower limit of the measured values. From Eqs 7, 10, the undrained strength ratio decreases with increasing vertical consolidation stress due to the existence of clay cohesion. If the cohesion is equal to 0, the undrained strength ratio is constant and would not change with the level of stress. Cohesion can be neglected for high stress levels, and the undrained strength ratio is nearly constant.

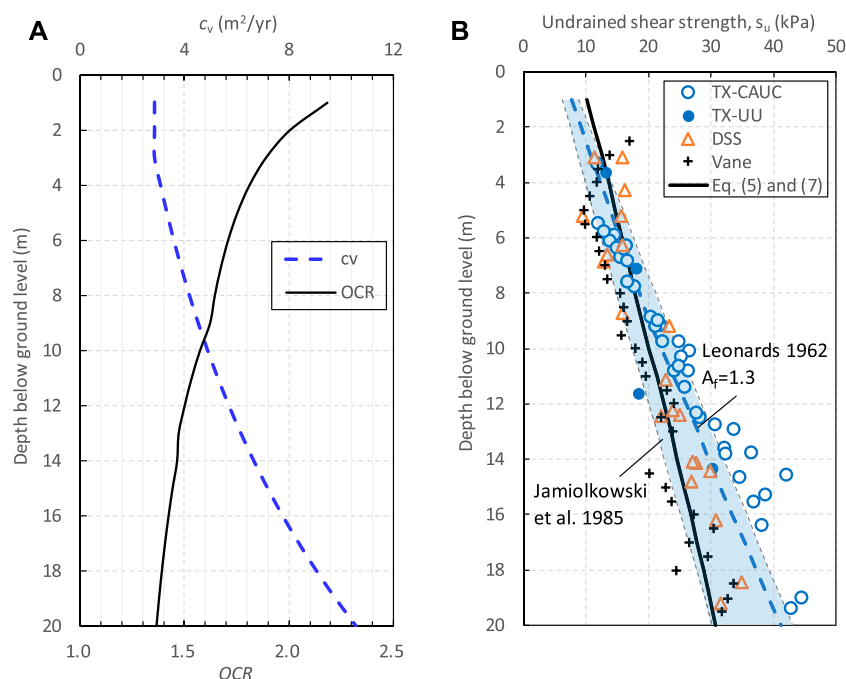


FIGURE 16

Intact Onsoy clay: (A) OCR and  $c_v$  profiles, (B) comparison between predicted and measured undrained strength.

## 5.2 Intact Onsoy clay

According to the reference of the NGI research report (2019) and Gundersen et al. (2019), the property profiles of clay at the Onsoy site are listed in Figure 16A. The OCR value of Onsoy clay is 1.3–1.9, and the  $c_v$  value is 3–11 m<sup>2</sup>/yr with a soil depth of 3–20 m. Therefore, intact Onsoy clay is slightly overconsolidated clay with an average OCR of 1.5 and has a larger coefficient of consolidation than reconstituted Onsoy clay. Soil disturbance delays the consolidation and hence reduces the coefficients of consolidation of both normally consolidated and overconsolidated clays (U.S. Navy, 1982). Holtz et al. (2011) included lightly overconsolidated deposits with an OCR < 2 in the category of normally consolidated clays. Representative values of the friction angle and cohesion are  $\phi'_{f=30^\circ}$  and  $c'_f=5$  kPa, respectively (Gundersen et al., 2019). The predictions given by Eqs 5, 7 are compared with different types of measured undrained shear strength in Figure 16B.

In direct simple shear (DSS) tests, the clay specimens were consolidated to what was believed to be a low estimate of the preconsolidation stress (approximately 75%–80%) and then unloaded to the estimated *in situ* effective vertical stress before shearing. This method was used to counteract the negative effect of stress release and other disturbance effects during sampling and extrusion (ISO 19901-8, 2015). UU triaxial tests have been performed on intact material. All consolidated undrained triaxial compression (CAUC) tests were consolidated to a best estimate of

the *in-situ* stress condition with a  $K_0$  value of 0.6 on the soft clay from the Onsoy site. The vane test is usually considered to give the best result of the undrained strength of clay.

The undrained strength of DSS tests is in the empirical range of Jamiolkowski, which is very close to UU test results and slightly lower than the strength found using CAUC tests, especially below a depth of 10 m. The undrained strength of DSS tests at a depth of 0–9 m is essentially the same as the vane strength, but its strength below 9 m is slightly higher than the vane strength. The predicted undrained strength from Eqs 5, 7 for intact Onsoy clay has a good agreement with vane and DSS test results, while the predicted strength using Leonards' method is at the upper limit of that found using the DSS tests. However, in Figure 16B, the value of  $A_f$  is the upper limit, which leads to the smallest undrained strength. For intact clay, obtaining good estimates of the pore pressure parameter  $A_f$  is often difficult because that parameter is very sensitive to sample disturbance.

## 6 Conclusion

The undrained strength of clay determined by the simple shear test is related to shearing rate  $v$ , coefficient of consolidation  $c_v$ , the height of specimen  $H_f$ , consolidation stress  $\sigma'_{vc}$  and lateral stress ratio  $K$ . Although there is some uncertainty for undrained strength, it could become much more certain with an effective stress analysis. A normalized shearing rate  $V=vH_f/c_v$  is suggested

to develop the relationship with excess pore pressure. Based on the Mohr–Coulomb failure criterion, undrained strength can be calculated from strength parameters in terms of effective stress. The equations developed with high plasticity clays are suitable for normally consolidated and slightly overconsolidated clays. In addition, the failure mode of specimens in a Berkeley simple shear device is a diagonal failure plane instead of a horizontal plane. Meanwhile, an empirical relationship of strength parameters on different planes is established.

## Data availability statement

The original contributions presented in the study are included in the article/Supplementary material; further inquiries can be directed to the corresponding author.

## Author contributions

Methodology, BH and SC; investigation and experiment, SC and JL; resources, JL and KW; writing—original draft preparation, BH and KW; writing—review and editing, SC. All authors have read and agreed to the published version of the manuscript.

## Funding

The work presented in this paper was finished at the University of Western Australia, where the first author

engaged in CSC post-doctoral research work (CSC grant No. 201906275010).

## Acknowledgments

The authors express sincere thanks to Professor Phil Watson, who leads the Shell Chair in Offshore Engineering research team and supported the simple shear testing at the University of Western Australia. The second author also thanks the State Key Laboratory of Subtropical Building Science (Grant No. 2018ZB08). The work is also supported by Undergraduate Online Courses Committee of University in Guangdong Province (Grant No. 2022ZXKC437).

## Conflict of interest

The authors declare that the research was conducted in the absence of any commercial or financial relationships that could be construed as a potential conflict of interest.

## Publisher's note

All claims expressed in this article are solely those of the authors and do not necessarily represent those of their affiliated organizations or those of the publisher, the editors, and the reviewers. Any product that may be evaluated in this article, or claim that may be made by its manufacturer, is not guaranteed or endorsed by the publisher.

## References

- Acharya, B., and Airey, D. (2017). "Effect of specimen confinement method on simple shear test of clay," in *Advances in laboratory testing and modelling of soils and shales* (Cham, Switzerland: Springer), 247–254.
- Airey, D. W., and Wood, D. M. (1987). An evaluation of direct simple shear tests on clay. *Géotechnique* 37 (1), 25–35. doi:10.1680/geot.1987.37.1.25
- Atkinson, J. H., Lau, W. H. W., and Powell, J. J. M. (1991). Measurement of soil strength in simple shear tests. *Can. Geotechnical J.* 28 (2), 255–262. doi:10.1139/t91-031
- Bjerrum, L., and Landva, A. (1966). Direct simple-shear tests on a Norwegian quick clay. *Geotechnique* 16 (1), 1–20. doi:10.1680/geot.1966.16.1.1
- Bjerrum, L. (1973). Problems of soil mechanics and construction on soft clays. Proceedings of the 8th international conference on soil mechanics and foundation engineering, Moscow, Russia, August 1973, 3, 111–159.
- Boukpeti, N., and White, D. J. (2017). Interface shear box tests for assessing axial pipe–soil resistance. *Géotechnique* 67 (1), 18–30. doi:10.1680/jgeot.15.p.112
- Budhu, M. (1985). Lateral stresses observed in two simple shear apparatus. *J. Geotechnical Eng.* 111 (6), 698–711. doi:10.1061/(asce)0733-9410(1985)111:6(698)
- Budhu, M. (1984). Nonuniformities imposed by simple shear apparatus. *Can. Geotechnical J.* 21 (1), 125–137. doi:10.1139/t84-010
- Chow, S. H., O'loughlin, C. D., and Randolph, M. F. (2014). Soil strength estimation and pore pressure dissipation for free-fall piezocone in soft clay. *Géotechnique* 64 (10), 817–827. doi:10.1680/geot.14.p.107
- Dyvik, R., Berre, T., Lacasse, S., and Raadim, B. (1987). Comparison of truly undrained and constant volume direct simple shear tests. *Geotechnique* 37 (1), 3–10. doi:10.1680/geot.1987.37.1.3
- Finnie, I. M. S., and Randolph, M. F. (1994). "Punch-through and liquefaction induced failure of shallow foundations on calcareous sediments," in Proceedings of the international conference on behaviour of offshore structures, Boston, MA, USA, July 1994, 217–230.
- Gundersen, A., Hansen, R., Lunne, T., L Heureux, J. S., Strandvik, S. O., O. Strandvik, S., et al. (2019). Characterization and engineering properties of the NGTS Onsoy soft clay site. *AIMS Geosci.* 5 (3), 665–703. doi:10.3934/geosci.2019.3.665
- Gylland, A. S., Jostad, H. P., and Nordal, S. (2014). Experimental study of strain localization in sensitive clays. *Acta Geotech.* 9 (2), 227–240. doi:10.1007/s11440-013-0217-8
- Hicher, P. Y., Wahyudi, H., and Tessier, D. (1994). Microstructural analysis of strain localisation in clay. *Comput. Geotechnics* 16 (3), 205–222. doi:10.1016/0266-352x(94)90002-7
- Holtz, R. D., Kovacs, W. D., and Sheahan, T. C. (2011). *An introduction to geotechnical engineering*. London, UK: Pearson.
- Hvorslev, H. J. (1960). "Physical components of the shear strength of cohesive soils," in Proceedings of the Research Conference on Shear Strength of Cohesive Soils ASCE, Boulder, CO, USA, June 1960, 169–273.
- Jamiolkowski, M., Ladd, C. C., Germaine, J. T., and Lancellotta, R. (1985). "New developments in field and laboratory testing of soils," in Proceedings of the 10th



International Conference on Soil Mechanics and Foundation Engineering, San Francisco, CA, USA, 57–153.1,

Joer, H. A., Erbrich, C. T., and Sharma, S. S. (2010). "A new interpretation of the simple shear test," in Proceedings of the 2nd International. Symp. On Frontiers in Offshore Geotechnics, Perth, Australia, November 2010.

Jostad, H. P., Andresen, L., and Thakur, V. (2006). Calculation of shear band thickness in sensitive clays. *6th Numer. methods geotechnical Eng.* 1, 27–32.

Ladd, C. C., and Foott, R. (1974). New design procedure for stability of soft clays. *J. Geotechnical Geoenvironmental Eng.* 100 (7), 763–786. doi:10.1061/ajgeb6.0000066

Lehane, B. M., and Jardine, R. J. (1992). Residual strength characteristics of Bothkennar clay. *Géotechnique* 42 (2), 363–367. doi:10.1680/geot.1992.42.2.363

Lehane, B. M., O'loughlin, C. D., Gaudin, C., and Randolph, M. F. (2009). Rate effects on penetrometer resistance in kaolin. *Géotechnique* 59 (1), 41–52. doi:10.1680/geot.2007.00072

Leonards, G. A. (1962). *Foundation engineering*. New York, NY, USA: McGraw-Hill.

Mahmoodzadeh, H., and Randolph, M. F. (2014). Penetrometer testing: Effect of partial consolidation on subsequent dissipation response. *J. Geotechnical Geoenvironmental Eng.* 140 (6), 04014022. doi:10.1061/(asce)gt.1943-5606.0001114

Mayne, P. W. (1985). A review of undrained strength in direct simple shear. *Soils Found.* 25 (3), 64–72. doi:10.3208/sandf1972.25.3\_64

Mayne, P. W., and Kulhawy, F. H. (1982). Ko-OCR relationships in soil. *J. Geotechnical Eng. Div.* 108 (6), 851–872. doi:10.1061/ajgeb6.0001306

Muraro, S., and Jommi, C. (2021). Experimental determination of the shear strength of peat from standard undrained triaxial tests: Correcting for the effects of end restraint. *Géotechnique* 71 (1), 76–87. doi:10.1680/jgeot.18.p.346

U.S. Navy (1982). *Soil mechanics – design manual 7.1, naval facilities engineering command*. Washington, DC, USA: U.S. Government Printing Office.

NGI research report (2019). "Norwegian GeoTest sites—field and laboratory test results from NGTS soft clay site—onsøy," Report No: 20160154-10-R (Sognsveien, Norway: Norwegian geotechnical institute).

Prevost, J. H., and Høeg, K. (1976). Reanalysis of simple shear soil testing. *Can. Geotechnical J.* 13 (4), 418–429. doi:10.1139/t76-042

Randolph, M. F., and Wroth, C. P. (1981). Application of the failure state in undrained simple shear to the shaft capacity of driven piles. *Geotechnique* 31 (1), 143–157. doi:10.1680/geot.1981.31.1.143

Randolph, M., and Gourvenec, S. (2017). *Offshore geotechnical engineering*. Boca Raton, FL, USA: CRC Press.

Rau, G. A. (1999). *Evaluation of strength degradation in seismic loading of Holocene Bay mud from Marin County, California*. PhD Thesis (Berkeley, CA, USA: University of California).

Reyno, A. J., Airey, D., and Taiebat, H. A. (2005). "Influence of height and boundary conditions in simple shear tests," in *International symposium on Frontiers in offshore geotechnics* (Boca Raton, FL, USA: Taylor & Francis/Balkema).

Richardson, A. M., and Whitman, R. V. (1963). Effect of strain-rate upon undrained shear resistance of a saturated remoulded fat clay. *Geotechnique* 13 (4), 310–324. doi:10.1680/geot.1963.13.4.310

Richardson, M. D., O'Loughlin, C. D., Randolph, M. F., and Gaudin, C. (2009). Setup following installation of dynamic anchors in normally consolidated clay. *J. Geotechnical Geoenvironmental Eng.* 135 (4), 487–496. doi:10.1061/(asce)1090-0241(2009)135:4(487)

Rutledge, P. C. (1947). *Review of 'Cooperative triaxial shear research program of the Corps of Engineers'*. Vicksburg, MS, USA: USAE Waterways Experiment Station.

Sharma, S. S., Ramsey, N., Lee, F., and Bhattarai, B. N. (2017). Challenges in assessing the shear strength of offshore sediments using simple shear tests. *Geotech. Front.* 2017, 327–336.

Verma, P., and Wijewickreme, D. (2020). Effect of different modes of lateral boundary constraints of the direct simple shear (DSS) device under monotonic and cyclic shear loading. *Geotechnical Test. J.* 43 (4), 20180357–20181070. doi:10.1520/gtj20180357

Wood, D. M., Drescher, A., and Budhu, M. (1979). On the determination of stress state in the simple shear apparatus. *Geotechnical Test. J.* 2 (4), 211–222. doi:10.1520/gtj10460j

Wroth, C. P. (1984). The interpretation of *in situ* soil tests. *Geotechnique* 34 (4), 449–489. doi:10.1680/geot.1984.34.4.449



## OPEN ACCESS

## EDITED BY

Guang-Liang Feng,  
Institute of Rock and Soil Mechanics (CAS),  
China

## REVIEWED BY

Wenjun An,  
Jiangxi University of Engineering, China  
Bangyou Jiang,  
Shandong University of Science and  
Technology, China

## \*CORRESPONDENCE

Jucai Chang,  
✉ cjcminecoal@163.com

## SPECIALTY SECTION

This article was submitted to Geohazards  
and Georisks,  
a section of the journal  
Frontiers in Earth Science

RECEIVED 26 November 2022

ACCEPTED 22 December 2022

PUBLISHED 06 January 2023

## CITATION

Yan L, Chang J, Qiao L, Shi W, Wang T,  
Pang D, Li Y and Guo Y (2023), Similar ratio  
experiment and characteristic analysis  
of quasi-sandstone.  
*Front. Earth Sci.* 10:1108582.  
doi: 10.3389/feart.2022.1108582

## COPYRIGHT

© 2023 Yan, Chang, Qiao, Shi, Wang, Pang,  
Li and Guo. This is an open-access article  
distributed under the terms of the [Creative  
Commons Attribution License \(CC BY\)](#).  
The use, distribution or reproduction in  
other forums is permitted, provided the  
original author(s) and the copyright  
owner(s) are credited and that the original  
publication in this journal is cited, in  
accordance with accepted academic  
practice. No use, distribution or  
reproduction is permitted which does not  
comply with these terms.

# Similar ratio experiment and characteristic analysis of quasi-sandstone

Lianghuan Yan, Jucai Chang\*, Longquan Qiao, Wenbao Shi,  
Tuo Wang, Dongdong Pang, Yuan Li and Yijun Guo

School of Mining Engineering, Anhui University of Science and Technology, Huainan, Anhui, China

The stability control of surrounding rock in deep roadway is becoming more and more difficult, and grouting reinforcement support has become the mainstream of roadway control. In order to obtain the ratio of quasi-sandstone material corresponding to the grouting body, this paper uses river sand as aggregate, cement and gypsum as cementing agent, retarder and defoamer as additives, and carries out orthogonal proportioning tests with three influencing factors: water-binder ratio (ratio of water to mass of cementing agent), gypsum-cement ratio (ratio of gypsum to mass of cement) and binder-aggregate ratio (ratio of cementing agent to aggregate mass), and compares and analyzes the sensitivity of each factor on the density, compressive strength, tensile strength, elastic modulus, Poisson's ratio, longitudinal wave velocity, elasticity index and brittleness index of quasi-sandstone material. The results show that 1) the Water-binder ratio has the greatest effect on the sensitivity of material compressive strength, tensile strength, elastic modulus, Poisson's ratio and longitudinal wave velocity; the gypsum-cement ratio has the greatest effect on the sensitivity of material deformation index and brittleness index; the binder-aggregate ratio has the greatest effect on the sensitivity of material density. 2) Reducing the Water-binder ratio can improve the density, compressive strength and tensile strength of the material; reducing the paste ratio can improve the modulus of elasticity, Poisson's ratio and longitudinal wave speed of the material; as the gypsum-cement ratio increases, the deformation index first decreases and then increases and then decreases; as the binder-aggregate ratio increases, the brittleness index first increases and then decreases and then increases. 3) The empirical equations between physical and mechanical properties of sandstone-like materials and Water-binder ratio, gypsum-cement ratio and binder-aggregate ratio were established based on multiple linear regression analysis, and more reasonable material ratios were quickly obtained by physical and mechanical parameters of materials. The results of the study provide theoretical references for similar material simulation tests for quasi-sandstone grouting.

## KEYWORDS

quasi-sandstone, similar proportioning, physical and mechanical properties, orthogonal test, sensitivity, multiple linear regression

## 1 Introduction

With Chinese coal resources into deep mining, deep roadway surrounding rock in high stress, strong mining of the mutual superposition of the role of deep roadway surrounding rock stability control increasingly difficult, surrounding rock grouting reinforcement support has become the mainstream of roadway control (He 2021; Jia et al., 2022a; Jia et al., 2022b; Jing et al.,

2022; Li et al., 2022; Wang et al., 2022; Zhang and Yin, 2022). In recent years, physical model tests have been widely used in the field of underground engineering because of the advantages of easy fabrication, controllable size and variables, and low price, so carrying out the raw rock similar material proportioning experiments to prepare raw rock and obtain the similar material proportioning of quasi-sandstone corresponding to the grouted body provides an experimental basis for further research on the slurry seepage diffusion law and grouting reinforcement effect in quasi-sandstone under true triaxial stress environment, which is of deep significance. The seepage flow grouting support of the tunnel surround rock has important practical significance (Lu et al., 2022; Liu et al., 2017; Kang et al., 2020; Zhang et al., 2020).

Rich results have been achieved in the proportioning of similar materials for quasi-sandstone materials, (Wang et al., 2006; Zhang et al., 2008; Zhang et al., 2019; Deng et al., 2020; Bai et al., 2021; Liu et al., 2022; Qin et al., 2022; Zhai et al., 2022), by using the similarity theory, similar specimens of the original rock were prepared using similar materials, and the physical and mechanical properties and damage laws were investigated. Optimized the ratio of rock-like materials prepared by 3D printing technology (Wu et al., 2020). Quasi-Sandstone similar materials were prepared using cement, gypsum, sand and coal dust, and it was concluded that gypsum and cement were the main controlling factors for deformation and strength of similar materials, respectively (Chen et al., 2019). Using hardener (CA), epoxy resin (ER) and rosin saturated solution (RSS) as proportional materials, the observability of this type of rock material after fracture generation was demonstrated based on physical and mechanical properties experiments (Ge et al., 2019). The quartz sand was selected as aggregate, and high-strength gypsum powder and talcum powder were used as cementing materials to prepare rock-like materials. The effects of sand-to-gel ratio, water curing, molding pressure and molding time on elastic modulus, compressive strength and permeability were investigated (Hou et al., 2022). Artificial sandstone was prepared using quartz sand as aggregate, montmorillonite and illite as clay, and epoxy resin as binder, and the effect law of clay ratio on the permeability of artificial sandstone was explored (Zhang et al., 2018). A four-factor, three-level orthogonal test was designed using ceramic sand, cement, gypsum and water as raw materials to simulate similar materials of red sandstone, and the test results of physical and mechanical properties of similar materials were subjected to extreme difference analysis and multiple linear regression analysis to obtain the degree of influence of each influencing factor on physical and mechanical properties of similar materials and empirical equations for the proportioning of similar materials of red sandstone (Hu et al., 2020). Mortar-like rock materials were prepared, and  $(E/\sigma_c)$  was introduced as the deformation index and  $(\sigma_c/\sigma_t)$  as the brittleness index, and rock-like ratios meeting the deformation index and brittleness index were selected (Song et al., 2020). In summary, previous authors have prepared quasi-sandstone similar material specimens in different ratios using different similar materials and studied the basic physical and mechanical properties with fruitful results. However, most of the current studies are limited to the selection of similar materials with quartz sand and baryte powder as the main aggregates, which are expensive and limited in wide application.

In this paper, river sand, cement and gypsum are used as raw materials, retarder and defoamer are used as additives. Density, longitudinal wave velocity, compressive strength, tensile strength,

elastic modulus, Poisson's ratio, brittleness index  $(\sigma_c/\sigma_t)$  and deformation index  $(E/\sigma_c)$  are selected as the characteristic indexes of similar materials. Through the orthogonal ratio test, the ratio of water to cementitious material quality (water-binder ratio), the ratio of cement to gypsum quality (gypsum-cement ratio), and the ratio of cementitious material to aggregate quality (binder-aggregate ratio) are used as the influencing factors of the test. The sensitivity analysis of each index is carried out by using the range analysis method, and the sensitivity of each factor to the physical and mechanical indexes of sandstone-like similar materials is obtained. Then, through multiple non-linear regression, the empirical equation of the influencing factors of the characteristics of quasi-sandstone similar materials is obtained. Finally, the optimal ratio scheme is determined according to the physical and mechanical parameters.

## 2 Raw material selection

According to previous studies, appropriate sandstone similar materials should be selected for conducting physical model tests, and the following three principles need to be followed (Li et al., 2017). 1) The physical and mechanical properties of sandstone analogues are similar to those of sandstone. 2) The raw materials of similar materials are widely available, inexpensive, non-toxic and non-hazardous, and stable in physical and mechanical properties. 3) The physical and mechanical properties of sandstone analogues can be adjusted to a larger extent by changing the proportioning scheme.

A well-prepared sandstone similar specimen must have a certain compressive strength. Ordinary silicate cement is a cementing material widely used to regulate the strength of specimens at present, and the compressive strength of sandstone similar material is mainly related to the amount of cement content. Gypsum as a cementing agent has obvious brittle characteristics, which can regulate the range of compressive strength and modulus of elasticity, and the specimens with gypsum added mainly undergo brittle deformation, and its brittle characteristics are mainly determined by the amount of gypsum content. River sand is one of the most common materials similar to sandstone, so this test used Huaihe River sand as aggregate with an average particle size of 0.125 mm–0.25 mm to reduce the effect of particle size gradation on the strength of the specimens.

In this paper, Renlou coal mine perimeter rock (sandstone mainly) is used as the research object, and ordinary silicate cement P.O 42.5 and gypsum are selected as cementing materials, which not only ensure the sandstone similar materials to better simulate the influence of gravity field under real environment, but also meet the mechanical properties of the materials. Because gypsum is added to the similar material as cemented river sand (0.125 mm–0.225 mm) as aggregate and retarder and defoamer as added materials, thus a certain proportion of retarder borax was needed to slow down the setting rate of gypsum and facilitate the fabrication of specimens.

## 3 Experiment

### 3.1 Experimental scheme

Three factors, water-cement ratio, gypsum-cement ratio and binder-aggregate ratio, are selected as the influencing factors of the test, and four levels of each factor are selected. In order to simplify the

**TABLE 1 Horizontal setting of orthogonal test factors for class 1 sandstone materials.**

Level	Water-binder ratio	Gypsum-cement ratio	Binder-aggregate ratio
I	0.40	0.1	0.5
II	0.45	0.2	1.0
III	0.50	0.3	1.5
IV	0.55	0.4	2.0

**TABLE 2 Orthogonal design combination of class 2 sandstone materials.**

Group number	Water-binder ratio	Gypsum-cement ratio	Binder-aggregate ratio
1	0.40	0.1	0.5
2	0.40	0.2	1.0
3	0.40	0.3	1.5
4	0.40	0.4	2.0
5	0.45	0.1	1.0
6	0.45	0.2	1.5
7	0.45	0.3	2.0
8	0.45	0.4	0.5
9	0.50	0.1	1.5
10	0.50	0.2	2.0
11	0.50	0.3	0.5
12	0.50	0.4	1.0
13	0.55	0.1	2.0
14	0.55	0.2	0.5
15	0.55	0.3	1.0
16	0.55	0.4	1.5

analysis process, ignoring the interaction between the factors. The specific factor level settings were determined after pre-experimental blending as shown in [Table 1](#). When designing an orthogonal table for the experiment, it is necessary to select an orthogonal table with the same number of levels and not less than the number of columns than the number of factors as a reference, so this experiment chose a 3-factor 4-level orthogonal design scheme L16 (43). The specific combination of each group is shown in [Table 2](#).

Note: The effect of defoamer and water-reducing agent on the test was not explored in the test. The amount of defoamer is 0.1% of the mass of binder, and the amount of water-reducing agent is 1% of the mass of binder.

## 3.2 Sample preparation

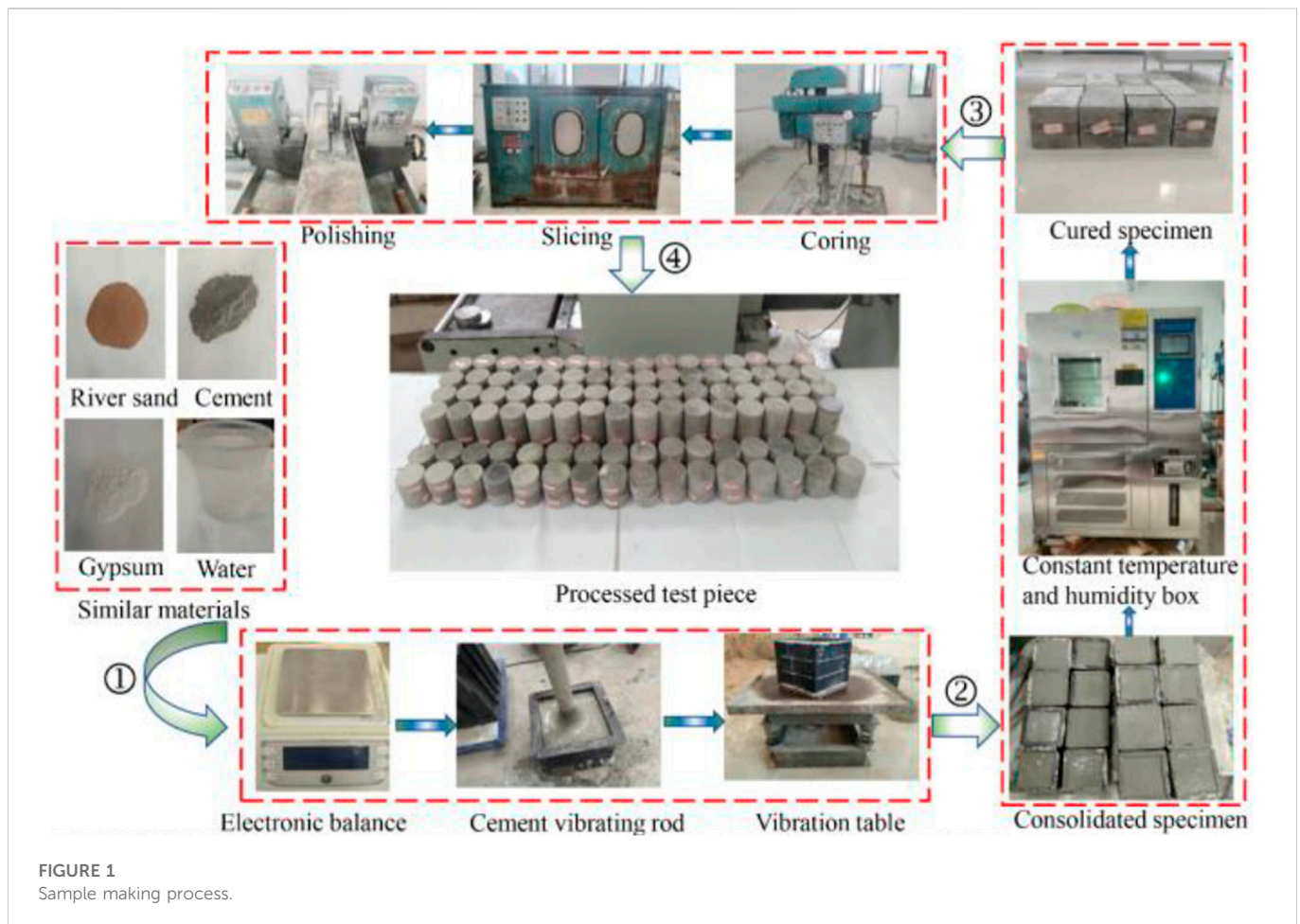
According to the orthogonal design combination table in [Table 2](#), quasi-sandstone similar material samples are made, as shown in [Figure 1](#). Weigh the quality of various raw materials using an electronic balance, the use of cement mixer raw materials will be evenly stirred into the slurry, the slurry will be poured into the

150 mm × 150 mm × 150 mm cube mold, and vibration on the shaking [Table 1](#) ~ 3 min, the use of shaking table to eliminate bubbles inside the specimen, improve the homogeneity of the specimen. The molds are placed in the constant temperature and humidity chamber for 2 days by standard maintenance. During the period, the temperature in the curing box was kept at 201°C and the relative humidity was more than 99%, and the mold was removed after the specimen is formed and continued to be placed in the constant temperature and humidity box for 28 days. The well-cared cubic specimens were cored, cut and polished into two standard cylindrical specimens: 50 mm × 25 mm for Brazilian splitting test and 50 mm × 100 mm for uniaxial compression test according to the recommended sample preparation requirements of the International Society of Rock Mechanics (ISRM) Recommended Methods for Rock Mechanics Testing (1982) ([Zhai et al., 2022](#)).

## 3.3 Physical parameters of sample

The basic physical test, ultrasonic longitudinal wave velocity test, Brazilian splitting test and uniaxial compression test are performed on





the orthogonal test group, and the natural density  $\rho_0$ , uniaxial compressive strength  $\sigma_c$ , tensile strength  $\sigma_t$ , modulus of elasticity  $E$ , longitudinal wave velocity  $v$  and Poisson's ratio  $\mu$  of the specimens is measured as shown in Table 3. The instrument used in the longitudinal wave velocity test is HC-U81 concrete ultrasonic detector, as shown in Figure 2, with a measurement range of 0–99999s and a repeatability error of 0.1s; the instruments used in the Brazilian splitting test and uniaxial compression test are both RMT rock mechanics testing machines, as shown in Figure 3, and the test process is carried out by displacement loading with a loading rate of 0.02 mm/s.

## 4 Sensitivity analysis of test results

The range analysis method commonly used in orthogonal experimental design is a more intuitive data analysis method, which usually obtains the optimal level combination under an index. Since the indexes of rock similar materials designed in this experiment are all interval values, the criterion selected is the index closest to the median value of the index range when selecting the optimal level combination. Sensitivity analysis is the analysis of the problem by calculating the average range for each factor, that is, by subtracting the minimum value from the maximum average of the test results for each influencing factor. The specific calculation methods are shown in Formula 1 and Formula 2.

$$I_i = (X_1 + X_2 + \dots + X_i) / i \quad (1)$$

$$R = I_{\max} - I_{\min} \quad (2)$$

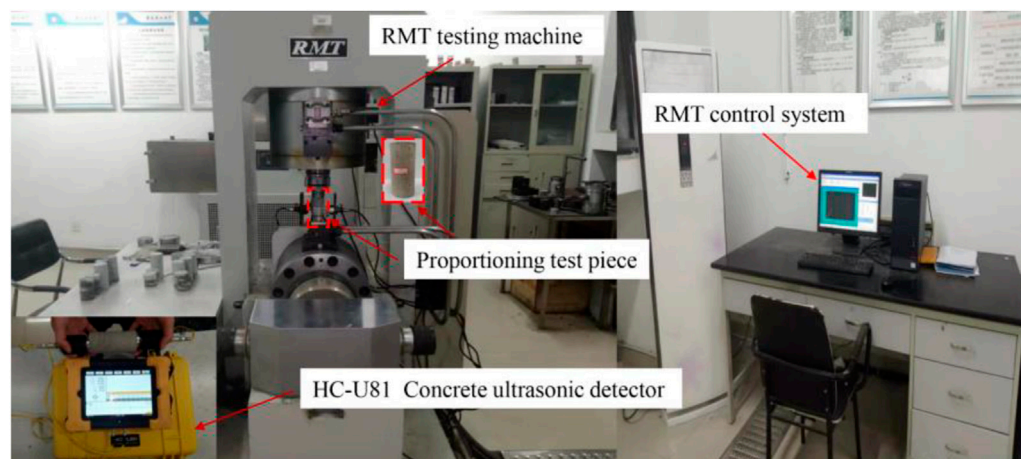
In the formula:  $I_i$  is the average value of the test results of any influencing factors;  $X_i$  is the test result of any influencing factor;  $I$  is the  $i$  test results of any influencing factor;  $R$  is range;  $I_{\max}$  is the maximum value of any influencing factor test results;  $I_{\min}$  is the minimum value of the test results for any influencing factor.

### 4.1 Density sensitivity analysis

Through the orthogonal proportional test results, the specimen density is analyzed by using the polar difference analysis method, and the polar difference and influence law of each influencing factor are shown in Table 4 and Figure 3. The binder-aggregate ratio has the greatest effect on the density, with the extreme difference of  $0.175 \text{ g cm}^{-3}$ , indicating that the ratio of cement to the total mass of aggregate had the highest effect on the density of the material, and the gypsum-cement ratio has the least effect on the density, with the extreme difference of  $0.027 \text{ g cm}^{-3}$ , indicating that the ratio of gypsum to cement in the cement has the lowest effect on the density of the material. The extreme differences of binder-aggregate ratio, water-binder ratio and gypsum-cement ratio decreased in order, and the degree of influence of each factor is binder-aggregate ratio > water-binder ratio > gypsum-cement ratio. The density of the specimens is approximately negatively correlated

**TABLE 3** Measurement results of physical and mechanical parameters.

Group number	Density (g.Cm-3)	Compressive strength (MPa)	Tensile strength (MPa)	Elastic modulus (GPa)	Poisson's ratio	Longitudinal wave velocity (km.s-1)	Elasticity index	Brittleness index
1	2.248	35.612	3.552	29.881	0.107	3.901	839.326	10.028
2	2.196	29.591	3.221	27.123	0.120	3.863	916.216	9.193
3	2.096	27.012	2.877	25.856	0.161	3.611	957.053	9.411
4	2.062	32.024	2.725	22.646	0.105	3.532	707.058	11.772
5	2.133	29.183	1.732	19.74	0.210	3.509	676.491	16.867
6	2.054	22.558	2.163	16.053	0.247	3.411	711.752	10.440
7	1.979	18.129	1.895	21.102	0.241	2.832	1164.459	9.587
8	2.154	26.452	2.376	25.343	0.272	3.76	958.034	11.160
9	2.061	24.424	1.750	29.857	0.226	3.514	1222.359	13.954
10	1.968	18.765	1.682	16.452	0.291	3.205	876.866	11.167
11	2.191	20.357	2.191	13.658	0.214	3.706	670.762	9.292
12	2.054	18.712	1.908	16.201	0.162	3.292	865.847	9.847
13	2.010	21.151	1.554	17.342	0.434	3.372	819.858	13.645
14	2.127	17.760	1.692	17.726	0.291	3.46	997.748	10.509
15	1.990	12.562	1.498	12.051	0.330	3.105	959.395	8.430
16	1.816	8.734	1.461	6.203	0.244	2.630	710.195	5.979

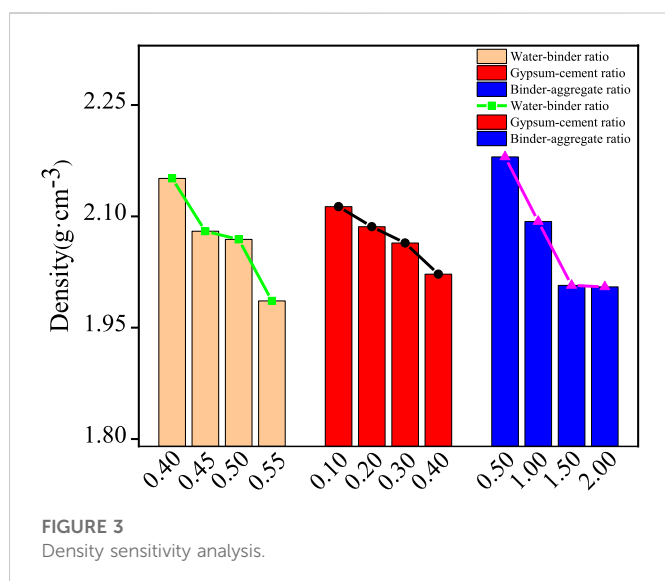
**FIGURE 2**  
Test system.

with the water-binder ratio, negatively correlated with the gypsum-cement ratio, and negatively correlated with the gypsum-cement ratio.

## 4.2 Sensitivity analysis of compressive strength

Through the orthogonal proportional test results, the specimen compressive strength is analyzed by using the polar

difference analysis method, and the polar difference and influence law of each influencing factor are shown in [Table 5](#) and [Figure 4](#). The water-binder ratio has the greatest effect on the compressive strength, with the extreme difference of 16.008 MPa, indicating that the proportion of water consumption and cementing agent had the highest degree of influence on the compressive strength of the material, and the binder-aggregate ratio has the least effect on the tensile strength, with the extreme difference of 4.363 MPa, indicating that the



proportion of cementing agent and aggregate had the lowest degree of influence on the compressive strength of the material. The extreme differences of water-binder ratio, gypsum-cement ratio and binder-aggregate ratio decreases in turn, and the degree of influence of each factor is water-binder ratio > gypsum-cement ratio > binder-aggregate ratio. The compressive strength of the specimens is approximately negatively correlated with the water-binder ratio, and the compressive strength of the specimens can be increased by decreasing the water-binder ratio and then increasing it, and the compressive strength reaches the minimum value of 19.515 MPa when the water-binder ratio is 0.3, and decreased and then increased with the increase of the binder-aggregate ratio, and the compressive strength reached the minimum value of 20.682 MPa when the binder-aggregate ratio is 1.5.

**TABLE 4** Density range analysis ( $\text{g.cm}^{-3}$ ).

Number of horizontal groups	Water-binder ratio	Gypsum-cement ratio	Binder-aggregate ratio
I	2.151	2.113	2.180
II	2.080	2.086	2.093
III	2.069	2.064	2.007
IV	1.986	2.022	2.005
Range	0.165	0.027	0.175

**TABLE 5** Compressive strength range analysis (MPa).

Number of horizontal groups	Water-binder ratio	Gypsum-cement ratio	Binder-aggregate ratio
I	31.060	27.593	25.045
II	24.081	22.169	22.512
III	20.565	19.515	20.682
IV	15.052	21.481	22.517
Range	16.008	8.078	4.363

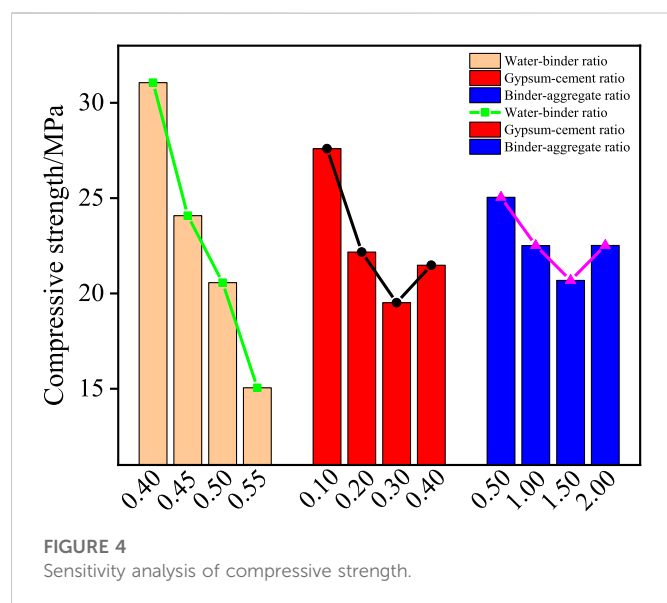
### 4.3 Tensile strength sensitivity analysis

Through the orthogonal proportional test results, the specimen tensile strength is analyzed by using the polar difference analysis method, and the polar difference and influence law of each influencing factor are shown in Table 6 and Figure 5. The water-binder ratio has the greatest influence on the tensile strength, with the extreme difference of 1.543 MPa, indicating that the proportion of water consumption and cementing agent has the highest influence on the tensile strength of the material, and the gypsum-cement ratio has the least influence on the tensile strength, with the extreme difference of 0.075 MPa, indicating that the proportion of gypsum and cement in the cementing agent has the lowest influence on the tensile strength of the material. The extreme differences of water-cement ratio, binder-aggregate ratio and gypsum-cement ratio. Decreased in order, and the degree of influence of each factor is water-cement ratio > binder-aggregate ratio > gypsum-cement ratio. The tensile strength of the sample is approximately negatively correlated with the water-binder ratio. Reducing the water-binder ratio can increase the tensile strength of the sample, has no significant correlation with the gypsum-cement ratio, and is approximately negatively correlated with the binder-aggregate ratio.

### 4.4 Elastic modulus sensitivity analysis

Through the orthogonal proportional test results, the specimen elastic modulus is analyzed by using the polar difference analysis method, and the polar difference and influence law of each influencing factor are shown in Table 7 and Figure 6. The water-binder ratio has the greatest effect on the elastic modulus with a polar difference of 13.046 GPa, indicating that the proportion of water used to the cementing agent has the highest degree of influence on the elastic modulus of the material, and the binder-aggregate ratio has the least effect on the elastic modulus with a polar difference of 2.873 GPa, indicating that the proportion of cementing agent to the aggregate has the lowest effect on the elastic modulus of the specimen. The extreme differences of water-binder ratio, gypsum-cement ratio and binder-

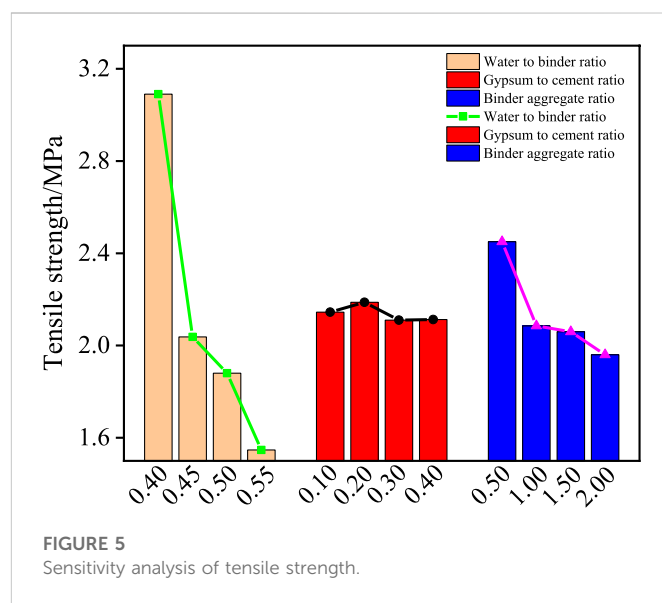




aggregate ratio decrease in order, and the degree of influence of each factor is water-binder ratio > gypsum-cement ratio > binder-aggregate ratio. The modulus of elasticity of the specimen and the water-binder ratio is approximately negatively correlated, lowering the water-binder ratio can improve the modulus of elasticity of the specimen, and the gypsum-cement ratio is approximately negatively correlated, with the increase of the binder-aggregate ratio first decreases and then increases and then decreases.

## 4.5 Poisson's ratio sensitivity analysis

Through the orthogonal proportional test results, the specimen Poisson's ratio is analyzed by using the polar difference analysis method, and the polar difference and influence law of each influencing factor are shown in Table 8 and Figure 7. The water-binder ratio has the greatest influence on Poisson's ratio, with a polar difference of 0.202, which indicates that the water consumption and the proportion of cement have the highest influence on Poisson's ratio, and the gypsum-cement ratio has the least influence on Poisson's ratio, with a polar difference of 0.048, which indicates that the proportion of gypsum and cement in the cement has the lowest influence on Poisson's ratio. The extreme differences of water-binder ratio, binder-aggregate ratio and gypsum-cement ratio decrease in order, and the degree of influence of each factor is water-binder ratio > binder-aggregate ratio > gypsum-cement ratio. The Poisson's ratio of



the specimens is approximately positively correlated with the water-binder ratio and negatively correlated with the gypsum-cement ratio, which decreased first and then increased with the increase of the binder-aggregate ratio, and reached the minimum value when the binder-aggregate ratio is 1.0.

## 4.6 Longitudinal wave speed sensitivity analysis

Through the orthogonal proportional test results, the specimen longitudinal wave speed is analyzed by using the polar difference analysis method, and the polar difference and influence law of each influencing factor are shown in Table 9 and Figure 8. The water-binder ratio has the greatest influence on the longitudinal wave speed, with the extreme difference of 0.585 km/s, which indicates that the proportion of water consumption and cement has the highest influence on the longitudinal wave speed of the material, and the gypsum-cement ratio has the least influence on the longitudinal wave speed, with the extreme difference of 0.270 km/s, which indicates that the proportion of gypsum and cement in the cement has the lowest influence on the longitudinal wave speed of the material. The extreme differences of water-binder ratio, gypsum-cement ratio and binder-aggregate ratio decrease in order, and the degree of influence of each factor is water-binder ratio > gypsum-cement ratio > binder-aggregate ratio. The longitudinal wave velocity of the specimen is approximately

**TABLE 6** Analysis of extreme differences in tensile strength (unit: MPa).

Number of horizontal groups	Water-binder ratio	Gypsum-cement ratio	Binder-aggregate ratio
I	3.094	2.147	2.453
II	2.042	2.190	2.090
III	1.883	2.115	2.063
IV	1.551	2.118	1.964
Range	1.543	0.075	0.489

TABLE 7 Range analysis of elastic modulus.

Number of horizontal groups	Water-binder ratio	Gypsum-cement ratio	Binder-aggregate ratio
I	26.377	24.205	21.652
II	20.560	19.339	18.779
III	19.042	18.167	19.492
IV	13.331	17.598	1.414
Range	13.046	4.867	2.873

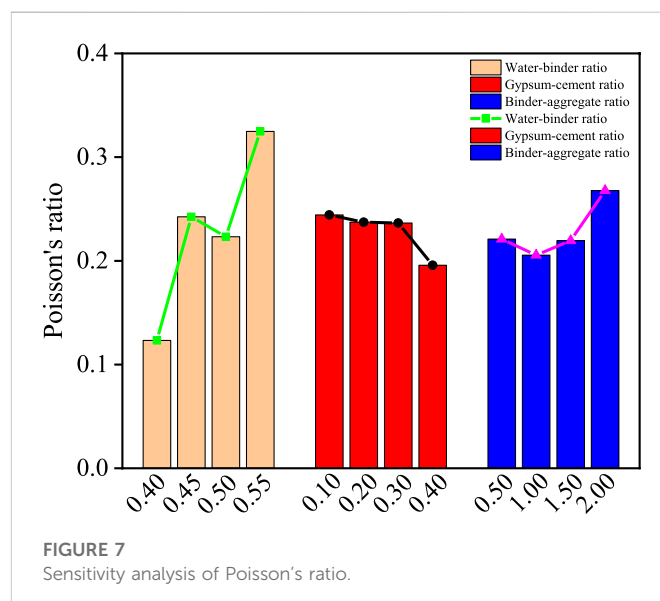
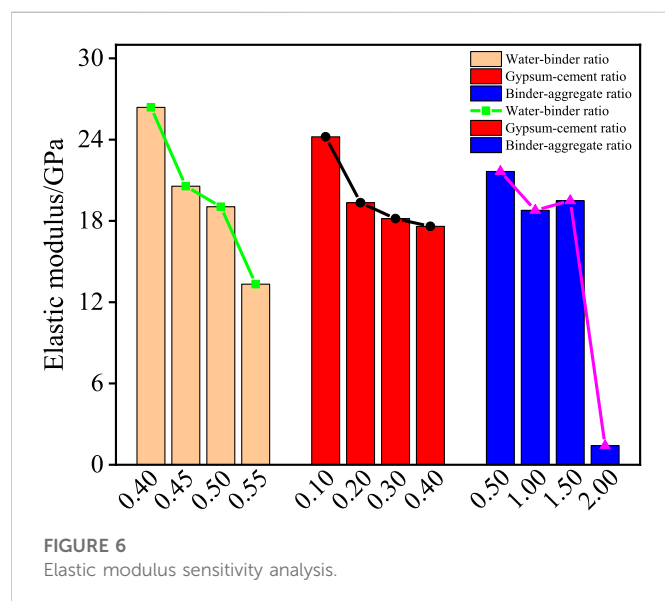


TABLE 8 Range analysis of Poisson's ratio.

Number of horizontal groups	Water-binder ratio	Gypsum-cement ratio	Binder-aggregate ratio
I	0.123	0.244	0.221
II	0.243	0.237	0.206
III	0.223	0.237	0.220
IV	0.325	0.196	0.268
Range	0.202	0.048	0.062

negatively correlated with the water-binder ratio, and is approximately negatively correlated with the gypsum-cement ratio, that is, it is approximately negatively correlated with the binder-aggregate ratio.

## 4.7 Sensitivity analysis of deformation index

Through the orthogonal proportional test results, the specimen deformation index is analyzed by using the polar difference analysis method, and the polar difference and influence law of each influencing factor are shown in Table 10 and Figure 9. The gypsum-cement ratio has the greatest effect on the deformation index with an extreme difference of 127.634, indicating that the ratio of gypsum to cement in the cementing agent has the highest degree of influence on the

deformation index of the material. The binder-aggregate ratio has the least effect on the deformation index with an extreme difference of 45.853, indicating that the ratio of cement to aggregate has the lowest effect on the elastic modulus of the specimen. The extreme differences of the gypsum-cement ratio, water-binder ratio and binder-aggregate ratio decreased in order, and the degree of influence of each factor is gypsum-cement ratio > water-binder ratio > binder-aggregate ratio. With the increase of water-binder ratio, the deformation index first increases and then decreases, when the water-binder ratio is 0.50, the deformation index reaches the maximum; with the increase of gypsum-cement ratio, the deformation index first decreases and then increases and then decreases, with the increase of binder-aggregate ratio, the deformation index first decreases and then increases and then decreases.

TABLE 9 Range analysis of longitudinal wave velocity (km/s).

Number of horizontal groups	Water-binder ratio	Gypsum-cement ratio	Binder-aggregate ratio
I	3.727	3.574	3.707
II	3.378	3.485	3.442
III	3.429	3.314	3.292
IV	3.142	3.304	3.235
Range	0.585	0.270	0.472

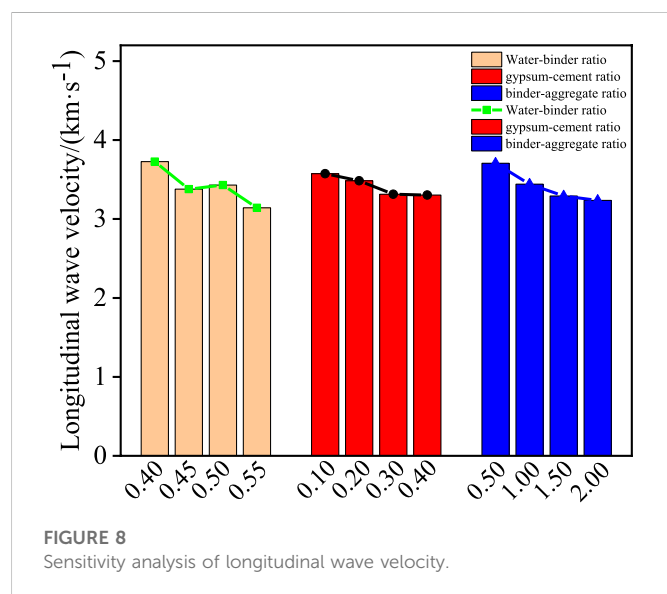
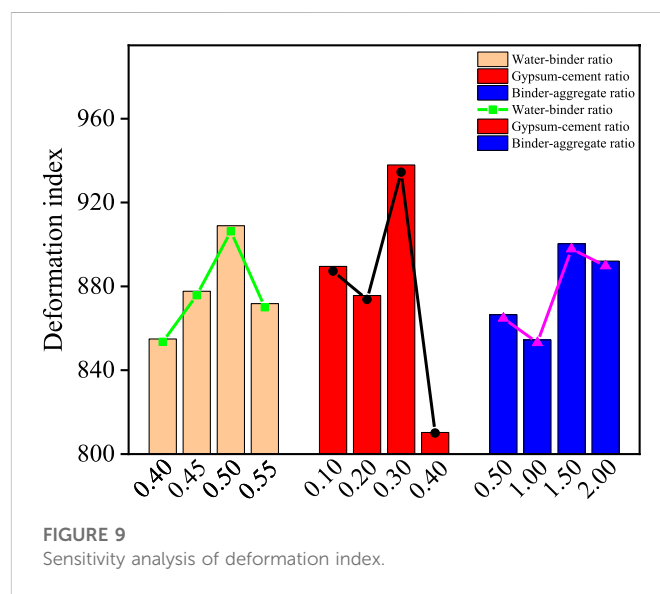
FIGURE 8  
Sensitivity analysis of longitudinal wave velocity.FIGURE 9  
Sensitivity analysis of deformation index.

TABLE 10 Range analysis of deformation index.

Number of horizontal groups	Water-binder ratio	Gypsum-cement ratio	Binder-aggregate ratio
I	854.913	889.508	866.467
II	877.684	875.645	854.487
III	908.958	937.917	900.340
IV	871.799	810.283	892.060
Range	54.045	127.634	45.853

## 4.8 Sensitivity analysis of brittleness index

Through the orthogonal proportional test results, the specimen brittleness index is analyzed by using the polar difference analysis method, and the polar difference and influence law of each influencing factor are shown in Table 11 and Figure 10.

The binder-aggregate ratio has the least effect on the brittleness index with an extreme difference of 1.597, indicating that the ratio of cement to aggregate has the lowest degree of influence on the material brittleness index. The extreme differences of the gypsum-cement ratio, water-binder ratio and binder-aggregate ratio decrease in order, and the degree of influence of each factor is gypsum-cement ratio > water-binder ratio > binder-aggregate ratio. As the water-binder ratio

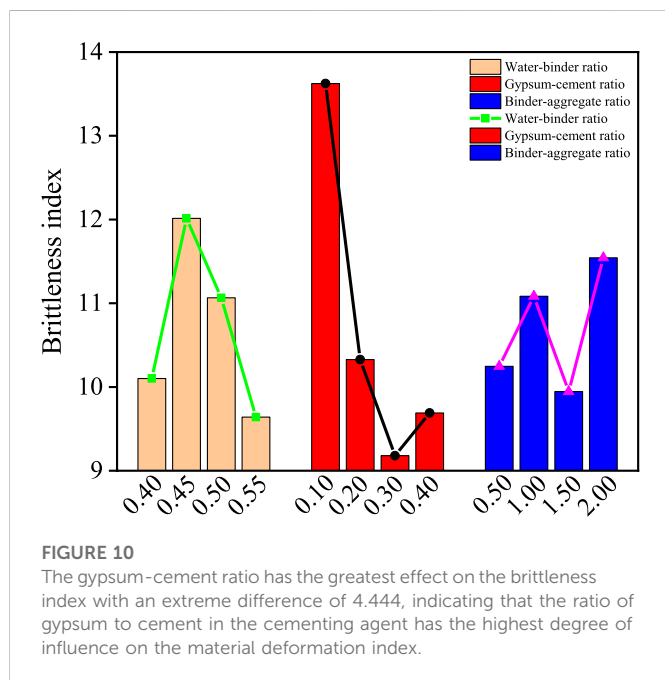
increases, the brittleness index first increases and then decreases, and the brittleness index reaches the maximum value when the water-binder ratio is 0.45. As the gypsum-cement ratio increases, the brittleness index first decreases and then increases, and the brittleness index reaches the minimum value when the gypsum-cement ratio is 0.3. As the binder-aggregate ratio increases, the index first increases and then decreases and then increases.

## 5 Multiple linear regression analysis

According to the results of quasi-sandstone similar material ratio test and the sensitivity analysis of each factor, it can be seen that except

TABLE 11 Range analysis of brittleness index.

Number of horizontal groups	Water-binder ratio	Gypsum-cement ratio	Binder-aggregate ratio
I	10.101	13.624	10.247
II	12.014	10.327	11.084
III	11.065	9.180	9.946
IV	9.641	9.690	11.543
Range	2.373	4.444	1.597



for the change of deformation index and brittleness index, each factor has obvious linear relationship with the properties of quasi-sandstone similar materials. In order to improve the efficiency of quasi-sandstone similar material ratio test, it is necessary to find the quantitative relationship between each factor and each parameter. Therefore, multiple linear regression analysis is carried out on the test results.

Assuming that  $Y$  is the dependent variable and  $X$  is the independent variable, the multiple linear regression model can be expressed as (Li and Hu, 2010):

$$Y = \begin{bmatrix} a_{11} & a_{12} & a_{13} & \cdots & a_{1m} \\ a_{21} & a_{22} & a_{23} & \cdots & a_{2m} \\ a_{31} & a_{32} & a_{33} & \cdots & a_{3m} \\ \cdots & \cdots & \cdots & \cdots & \cdots \\ a_{n1} & a_{n2} & a_{n3} & \cdots & a_{nm} \end{bmatrix} X + P \quad (3)$$

Where:  $a_{11}, a_{12}, \dots, a_{nm}$  are partial regression coefficients;  $p$  are constants.

According to the analysis of the results of quasi-sandstone similar material proportioning tests and the sensitivity of each factor, it can be seen that, except for the insignificant changes of deformation index and brittleness index, each factor has an obvious linear relationship with the properties of quasi-sandstone similar materials. In order to

improve the efficiency of quasi-sandstone similar proportioning tests, it is necessary to find the quantitative relationship between each factor and each parameter, so multiple linear regression analysis was performed on the test results.

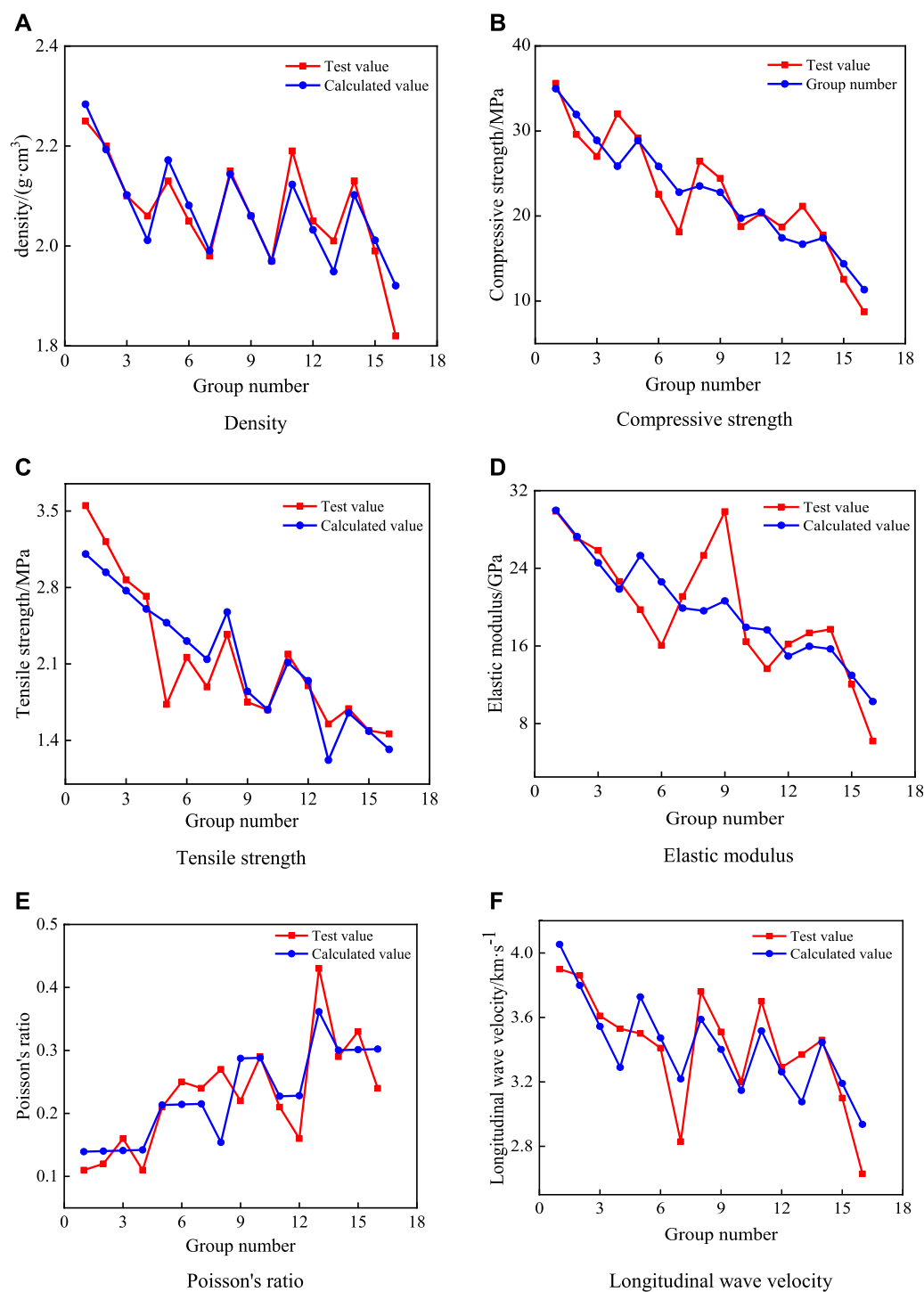
$$Y = \begin{bmatrix} -1.012 & -0.297 & -0.122 \\ -103.080 & -20.989 & -1.883 \\ -9.573 & -0.163 & -0.299 \\ -81.311 & -20.992 & -1.217 \\ 1.166 & -0.146 & 0.031 \\ -3.408 & -0.983 & -0.313 \end{bmatrix} X + \begin{bmatrix} 2.779 \\ 79.253 \\ 7.103 \\ 65.219 \\ -0.329 \\ 5.675 \end{bmatrix}; R = \begin{bmatrix} 0.917 \\ 0.915 \\ 0.913 \\ 0.801 \\ 0.821 \\ 0.832 \end{bmatrix} \quad (4)$$

For ease of description, let  $X = [x_1 \ x_2 \ x_3]^T$ , Where  $x_1$  is the Water-binder ratio,  $x_2$  is the gypsum-cement ratio,  $x_3$  is the binder-aggregate ratio, let  $Y = [y_1 \ y_2 \ y_3 \ y_4 \ y_5 \ y_6]$ , Among them,  $Y$  is the density, compressive strength, tensile strength, elastic modulus, Poisson's ratio and longitudinal wave velocity of quasi-sandstone materials, respectively. Using the analysis module of SPSS software, the optimal coefficients  $a_1, a_2$  and constant term  $b$  are obtained. The results are shown in formula 4, where  $R$  the linear correlation coefficient is obtained.

According to the analysis of the results of quasi-sandstone similar material proportioning tests and the sensitivity of each factor, it can be seen that, except for the insignificant changes of deformation index and brittleness index, each factor has an obvious linear relationship with the properties of quasi-sandstone similar materials. In order to improve the efficiency of quasi-sandstone similar proportioning tests, it is necessary to find the quantitative relationship between each factor and each parameter, so multiple linear regression analysis is performed on the test results Figure 11.

## 6 Discussion

The method described in this paper is used to prepare similar quasi-sandstone materials corresponding to the grouting body. The relationship between the physical and mechanical properties of similar materials and the three factors of water-binder ratio, gypsum-cement ratio and binder-aggregate ratio is mainly explored. Based on multiple linear regression analysis, the empirical formula of the three factors and physical and mechanical properties is obtained, which overcomes the blindness of the previous preparation of quasi-sandstone materials. The introduction of deformation index and brittleness index increases the mechanical properties of similar materials and reduces the error caused by the difference between the properties of similar materials and the original sandstone in the indoor test of replacing rock. To a certain extent, it ensures that the prepared quasi-sandstone material has a certain similarity with the natural original

**FIGURE 11**

Comparison between test results and calculation results of various parameters. (A) Density (B) Compressive strength (C) Tensile strength (D) Elastic modulus (E) Poisson's ratio (F) Longitudinal wave velocity.

sandstone, and can better carry out the test of slurry seepage diffusion law and grouting reinforcement effect of rock and rock mass under true triaxial stress environment.

However, in some indoor tests, it is sometimes necessary to select appropriate physical and mechanical parameters. Therefore, it is necessary to quickly find the corresponding material ratio based on

the empirical formula and then reversely adjust the three factors to change their properties. It can be seen from [Figure 12A](#) that the density, compressive strength and tensile strength of the material are approximately negatively correlated with the water-binder ratio, and the density, compressive strength and tensile strength of the material can be improved by reducing the water-binder ratio. It can be seen

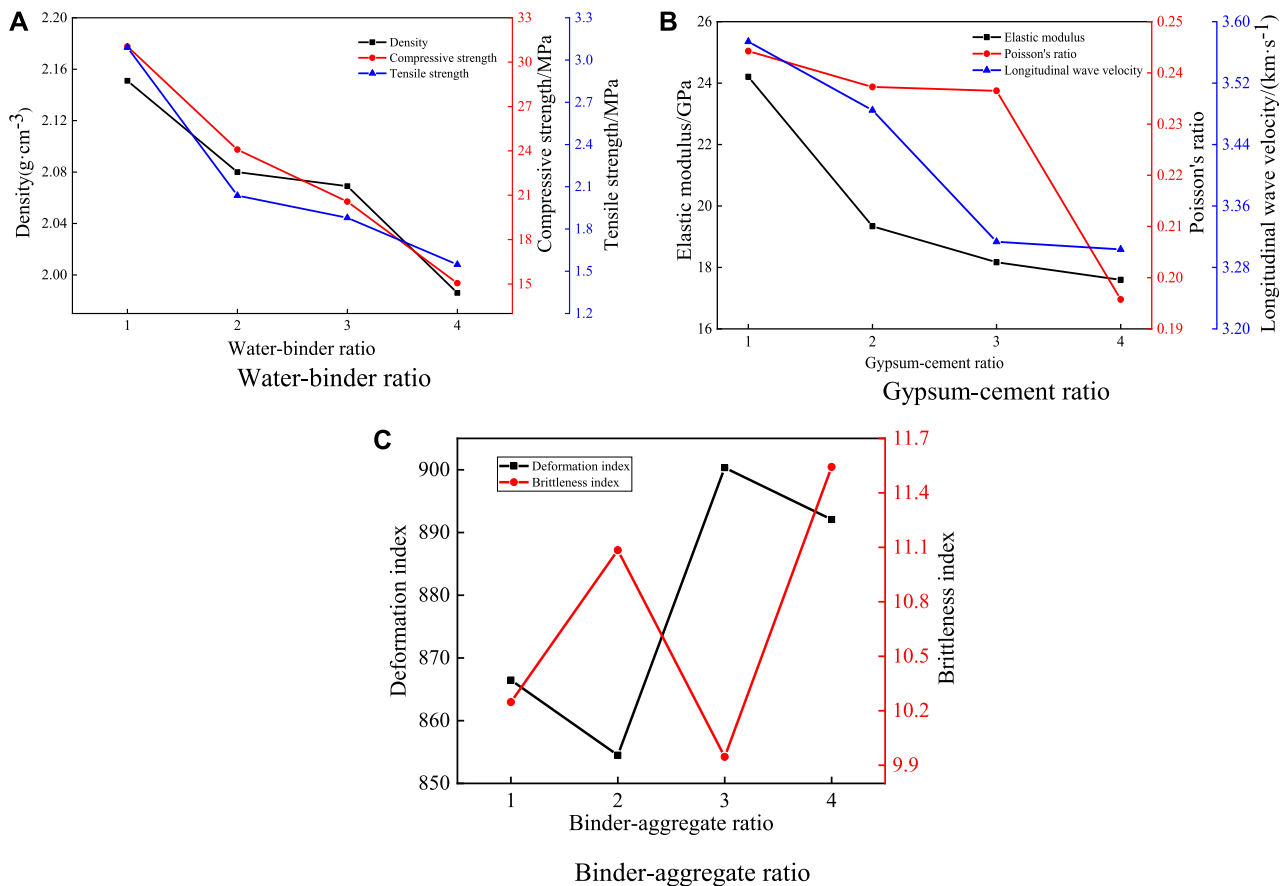


FIGURE 12

Comparative analysis of three factors and physical mechanical properties. (A) Water-binder ratio (B) Gypsum-cement ratio (C) Binder-aggregate ratio.

from Figure 12B that with the increase of gypsum-cement ratio, the elastic modulus, Poisson's ratio and longitudinal wave velocity of the material gradually decrease. The elastic modulus, Poisson's ratio and longitudinal wave velocity of the material can be improved by reducing the paste-mud ratio. It can be seen from Figure 12C that with the increase of the binder-aggregate ratio, the deformation index decreases first, then increases and then decreases. With the increase of the binder-aggregate ratio, the brittleness index increases first and then decreases.

## 7 Conclusion

In this paper, using the method of orthogonal test, three factors of water-binder ratio, gypsum-cement ratio and binder-aggregate ratio are used as the influencing factors of the test, and the sensitivity analysis of each index is carried out by using the method of extreme difference analysis, and the influence of the sensitivity degree of each factor on the physical and mechanical indexes of similar materials of quasi-sandstone is obtained, based on the multiple linear regression analysis method, the empirical equation of the influencing factors of similar material properties of quasi-sandstone is obtained, and the physical and mechanical parameters of sandstone can be indicators to determine the optimal proportioning scheme of sandstone-like material

corresponding to the grouted body. The main conclusions are as follows:

- 1) Using river sand as aggregate, cement and gypsum as cementing agent, we can prepare a density of  $1.816\text{--}2.248\text{g cm}^{-3}$ , compressive strength of  $8.734\text{--}35.642\text{ MPa}$ , modulus of elasticity of  $6.203\text{--}29.881\text{ GPa}$ , Poisson's ratio of  $0.161\text{--}0.434$ , longitudinal wave speed of  $2.630\text{ km/s}\sim 3.901\text{ km/s}$ , deformation index of  $670.762\text{--}1222.359$ , and brittleness index of  $5.979\text{--}16.867$ .
- 2) Based on the range analysis method, the effects of water-binder ratio, gypsum-cement ratio and binder-aggregate ratio on the physical and mechanical properties of sandstone-like similar materials were analyzed by orthogonal similarity ratio test. The water-binder ratio had the greatest influence on the compressive strength, tensile strength, elastic modulus, Poisson's ratio and longitudinal wave velocity sensitivity of the material. The gypsum-cement ratio has the greatest influence on the sensitivity of material deformation index and brittleness index. The binder-aggregate ratio has the greatest influence on the density sensitivity of the material.
- 3) Reducing the water-binder ratio can improve the density, compressive strength and tensile strength of the material; reducing the gypsum-cement ratio can improve the elastic modulus, Poisson's ratio and longitudinal wave velocity of the material; with the increase of Binder-aggregate ratio, the

deformation index decreases first, then increases and then decreases. With the increase of binder-aggregate ratio, the brittleness index increases first, then decreases and then increases.

- 4) The multiple linear regression analysis of the test data is carried out by using SPSS analysis software. The empirical formula between the physical and mechanical properties of quasi-sandstone materials and water-binder ratio, gypsum-cement ratio and binder-aggregate ratio is obtained. The feasibility and reliability of the empirical formula are verified by the linear correlation coefficient  $R$ , which can provide a theoretical reference for the simulation test of quasi-sandstone grouting similar materials.

## Data availability statement

The original contributions presented in the study are included in the article/supplementary material, further inquiries can be directed to the corresponding author.

## Author contributions

LY: Conceptualization, Methodology, Software, Data curation, Validation, Writing-original draft, Funding acquisition. JC: Data curation, Writing-review and editing, Funding acquisition. LQ: Supervision, Writing-review and editing, Funding acquisition. WS: Writing review and editing, Funding acquisition. TW: Funding

acquisition, Writing-review and editing. DP: Writing-review and editing. YL: Writing-review and editing. YG: Writing-review and editing.

## Funding

This work was supported by National natural science foundation of China (52174105), Key R & D project of Anhui province (202004a07020045), Collaborative Innovation Project of Anhui Universities (GXXT-2019-0294).

## Conflict of interest

The authors declare that the research was conducted in the absence of any commercial or financial relationships that could be construed as a potential conflict of interest.

## Publisher's note

All claims expressed in this article are solely those of the authors and do not necessarily represent those of their affiliated organizations, or those of the publisher, the editors and the reviewers. Any product that may be evaluated in this article, or claim that may be made by its manufacturer, is not guaranteed or endorsed by the publisher.

## References

- Bai, H., Du, W., Shou, Y. D., Chen, L. C., and Berto, F. (2021). Experimental investigation of cracking behaviors of ductile and brittle rock-like materials. *Fract. Struct. Integr. Int. J. Italian Group Fract.* 15 (56), 16–45. doi:10.3221/IGF-ESIS.56.02
- Chen, J. Z., Li, X. B., and Cao, H. (2019). Experimental investigation of coal-like materials for hydraulic fracturing based on fluid-solid interaction. *J. Nat. Gas Sci. Eng.* 69, 102928. doi:10.1016/j.jngse.2019.102928
- Deng, H. W., Tian, G. L., Yu, S. T., Jiang, Z., Zhong, Z. M., and Zhang, Y. N. (2020). Research on strength prediction model of sand-like material based on nuclear magnetic resonance and fractal theory. *Appl. SCIENCES-BASEL* 10 (18), 6601. doi:10.3390/app10186601
- Ge, J. J., Xu, Y., and Candido, F. P. (2019). A method for making transparent hard rock-like material and its application. *Adv. Mater. Sci. Eng.* 2019 (2), 1–14. doi:10.1155/2019/1274171
- He, M. C. (2021). Research progress of deep shaft construction mechanics. *J. China Coal Soc.* 46 (03), 726–746. doi:10.13225/j.cnki.jccs.YT21.0124
- Hou, X. W., Zhou, X. Z., and Pan, J. N. (2022). Similar material proportioning and preparation of ductile surrounding rocks for simulating *in situ* coalbed methane production from tectonically deformed coals. *Rock Mech. Rock Eng.* 55 (9), 5377–5392. doi:10.1007/S00603-022-02951-3
- Hu, M., Yang, X. M., and Luo, X. D. (2020). Study on mixture ratio scheme of similar materials of red sandstone based on orthogonal experiment. *J. Hefei Univ. Technol. Nat. Sci.* 43 (06), 736–740. doi:10.3969/j.issn.1003-5060.2020.06.004
- Jia, B. X., Wan, W. Y., Ma, C. Y., Liu, F. P., and Zhang, J. J. (2022a). Ratio test and characteristic analysis of similar materials in white sand rock. *Chin. J. Undergr. Space Eng.* 18 (02), 503–512. doi:10.3969/j.issn.1673-0836.2022.2.dxkj202202018
- Jia, S. P., Yang, J. W., Gao, M., Jia, L. F., Wen, C. X., and Wu, G. J. (2022b). Experimental and numerical analysis of deformation and failure behaviour for deep roadways in soft rocks. *Bull. Eng. Geol. Environ.* 81 (11), 466. doi:10.1007/S10064-022-02959-7
- Jing, W., Liu, S. X., Yang, R. S., Jing, L. W., and Xue, W. P. (2022). Mechanism of aging deformation zoning of surrounding rock in deep high stress soft rock roadway based on rock creep characteristics. *J. Appl. Geophys.* 202, 104632. doi:10.1016/j.jappgeo.2022.104632
- Kang, H. P., Jiang, P. F., Huang, B. X., Guang, X. M., Wang, Z. G., Wu, Y. Z., et al. (2020). Roadway strata control technology by means of bolting-modification-destressing in synergy in 1000 m. *J. China Coal Soc.* 45 (03), 845–864. doi:10.13225/j.cnki.jccs.SJ20.0204
- Li, G. C., Yu, S., Sun, Y. T., Xie, J. W., and Li, J. H. (2022). Research progress of roadway surrounding strata rock control technologies under complex. *Coal Sci. Technol.* 50 (06), 29–45. doi:10.13199/j.cnki.cst.2022-0304
- Li, S. G., Bie, C. F., Zhao, P. X., Li, L., and Lin, H. F. (2017). Study on influence factors of new solid-gas coupling simulation. *material J. Min. Saf. Eng.* 34 (05), 981–986. doi:10.13545/j.cnki.jmse.2017.05.023
- Li, Y. Y., and Hu, C. R. (2010). *Experiment design and data processing*. Beijing: Chemical Industry Press, 82–127.
- Liu, L. S., Yang, Y., Chai, Y. G., Zhong, S. L., Chen, H., Xia, S. M., et al. (2022). A study of the dynamic damage characteristics of Rock-Like materials with different connectivity of concealed structural surfaces. *Theor. Appl. Fract. Mech.* 121, 103497. doi:10.1016/J.TAFMEC.2022.103497
- Liu, Q. S., Lei, G. F., Lu, C. B., Peng, X. X., Zhang, J., and Wang, J. T. (2017). Experimental study of grouting reinforcement influence on mechanical properties of rock fracture. *Chin. J. Rock Mech. Eng.* 36 (1), 3140–3147. doi:10.13722/j.cnki.jrme.2016.0459
- Lu, H. F., Zhang, K., Yi, J. L., and Wei, A. C. (2022). A study on the optimal selection of similar materials for the physical simulation experiment based on rock mineral components. *Eng. Fail. Anal.* 140, 106607. doi:10.1016/J.ENGFAILANAL.2022.106607
- Qin, Y., Xu, N. X., Guo, Y. X., Li, J. Y., and Han, W. B. (2022). Physical simulation of the influence of the original rock strength on the compaction characteristics of caving rock in longwall goaf. *R. Soc. Open Sci.* 9 (9), 220558. doi:10.1098/RSoS.220558
- Song, Y., Liu, B. G., Liu, H., Sun, J. L., Yu, M. Y., and Ren, D. R. (2020). Orthogonal test method for determination of the proportion of rock-like material based on properties of deformation and brittleness. *Rock Soil Mech.* 41 (08), 2675–2684. doi:10.16285/j.rsm.2019.1711
- Wang, H. P., Li, S. C., Zhang, Q. Y., Li, Y., and Guo, X. H. (2006). Development of a new geomaterial similar material. *Chin. J. Rock Mech. Eng.* 25 (09), 1842–1847. doi:10.3321/j.issn:1000-6915.2006.09.016



- Wang, X. F., Zhang, Y. Y., Zhang, Q., Wei, Y. Y., Liu, W. G., and Jiang, T. (2022). Space-time evolution characteristics of deformation and failure of surrounding rock in deep soft rock roadway. *Sustainability* 14 (19), 12587. doi:10.3390/su141912587
- Wu, T. T., Zhao, H., Xu, Q., and Zhao, Y. X. (2020). Optimal analysis of material ratio for artificial rock by 3D printing technique. *Geomechanics Geoengin.* 17 (1), 260–268. doi:10.1080/17486025.2020.1739752
- Zhai, C., Zheng, Y. F., Yu, X., Xu, J. Z., Sun, Y., Cong, Y. Z., et al. (2022). Experimental study on the mechanical properties of coal-like materials for hydraulic fracturing simulation. *Coal Geol. Explor.* 50 (08), 16–22. doi:10.12363/issn.1001-1986.22.04.0272
- Zhang, Q. Y., Li, S. C., Guo, X. H., Li, Y., and Wang, H. P. (2008). Research and development of new typed cementitious geotechnical similar material for iron crystal sand and its application. *Rock Soil Mech.* 29 (08), 2126–2130. doi:10.16285/j.rsm.2008.08.002
- Zhang, S. K., and Yin, S. D. (2022). Analytical approach based on full-space synergy technology to optimization support design of deep mining roadway. *Minerals* 12 (6), 746. doi:10.3390/min12060746
- Zhang, Y. L., Wu, Y. P., and Xie, P. S. (2019). Orthogonal testing on ratio of physical simulation material similar to sandstone. *IOP Conf. Ser. Mater. Sci. Eng.* 688 (3), 033007. doi:10.1088/1757-899X/688/3/033007
- Zhang, Y., Zhou, H. W., Zhong, J. C., and Wang, R. (2018). An experimental study on artificial sandstone-clay proportioning on permeation behavior. *Chin. J. Rock Mech. Eng.* 37 (S1), 3253–3262. doi:10.13722/j.cnki.jrme.2016.1540
- Zhang, Z. F., Kang, H. P., Jiang, Z. Y., Li, W. Z., Jiang, P. F., Cai, R. C., et al. (2020). Study and application of high-pressure splitting grouting modification technology in coalmine with depth more than 1 000 m. *J. China Coal Soc.* 45 (03), 972–981. doi:10.13225/j.cnki.jccs.SJ19.1545



## OPEN ACCESS

## EDITED BY

Guang-Liang Feng,  
Institute of Rock and Soil Mechanics  
(CAS), China

## REVIEWED BY

Tao Wen,  
Yangtze University, China  
Houbin Liu,  
Southwest Petroleum University, China

## \*CORRESPONDENCE

Jia-Xin Sun,  
sunjiaxin@home.hpu.edu.cn

## SPECIALTY SECTION

This article was submitted to  
Geohazards and Georisks,  
a section of the journal  
Frontiers in Earth Science

RECEIVED 06 September 2022

ACCEPTED 31 October 2022

PUBLISHED 10 January 2023

## CITATION

Zhu C-X, Sun J-X, Gong J and Wang F-E  
(2023), Experimental and numerical  
research of crack propagation process  
and energy dissipation law of grouting  
specimens under radial impact load.  
*Front. Earth Sci.* 10:1037756.  
doi: 10.3389/feart.2022.1037756

## COPYRIGHT

© 2023 Zhu, Sun, Gong and Wang. This  
is an open-access article distributed  
under the terms of the [Creative  
Commons Attribution License \(CC BY\)](#).  
The use, distribution or reproduction in  
other forums is permitted, provided the  
original author(s) and the copyright  
owner(s) are credited and that the  
original publication in this journal is  
cited, in accordance with accepted  
academic practice. No use, distribution  
or reproduction is permitted which does  
not comply with these terms.

# Experimental and numerical research of crack propagation process and energy dissipation law of grouting specimens under radial impact load

Chang-Xing Zhu<sup>1</sup>, Jia-Xin Sun<sup>1\*</sup>, Jian Gong<sup>1</sup> and Feng-E Wang<sup>2</sup>

<sup>1</sup>School of Civil Engineering, Henan Polytechnic University, Jiaozuo, China, <sup>2</sup>School of Computer Science and Technology, Henan Polytechnic University, Jiaozuo, China

Different air pressures are used to conduct an impact test based on the split Hopkinson pressure bar (SHPB) test system to study the crack evolution process and energy dissipation law of the cemented rock under impact load. The failure mechanism of the specimens is analyzed from the perspective of dynamic failure process and energy dissipation. The spatial distribution of the specimen components visualized by the image reconstruction technology and the LS-DYNA mesoscopic model is established. Results show that the proportion of dissipated energy, the dynamic tensile strength and peak strain of the specimens increase with strain rate increase. The crack evolution process of the model is quantitatively described under an impact load, which is divided into four stages, namely, no crack stage, slow development stage, accelerated propagation stage and penetration stage. Compared with the indoor and simulation test result, the crack evolution process and failure modes are consistent under different strain rates. When the specimens are destroyed, the energy dissipation rate fluctuates from 10% to 13%. The dissipated energy of cement paste accounts for more than 90% of the total dissipated energy. The cement paste damages first and its strength has a great influence on the strength of the grouting specimens. This study provides a reference to evaluate the cemented rock under a dynamic load.

## KEYWORDS

grouting specimens, SHPB, crack evolution, energy evolution, Ls-Dyna

## 1 Introduction

The construction process of underground engineering faces instability problems of rock and Earth mass with the rapid development of the urban underground space (Von et al., 2020; Jong et al., 2021). The sand layer is a common, poor self-stabilization and hazardous harmful geology, and it induces frequent geological disasters, such as sand collapse, landslide, and surface collapse (Wen et al., 2020a; Ye et al., 2022). Grouting reinforcement can effectively enhance the overall mechanical properties and anti-leakage

performance of the sand beds (Liang et al., 2020; Ren et al., 2022). The tensile strength of the sand layer is far less than the compressive strength after grouting reinforcement. The sand bears not only bears quasi-static load but also earthquake, mechanical construction, explosion, and other impact loads. The crack initiation, expansion, penetration, and fracture of the grouting specimens must be studied under radial impact load. The split Hopkinson pressure bar (SHPB) system has been commonly used in dynamic compression, splitting, and fracture testing of the materials in a dynamic load test (Dai et al., 2010; Chen et al., 2014; Liao et al., 2016; Zhu et al., 2022). Most previous experimental studies have focused on strain rate effects (Liu et al., 2019; Yu et al., 2021).

During the dynamic splitting experiments, the failure process of several specimens is captured with a high-speed camera, and the crack propagation law and damage process of the concrete, sandstone, and rock materials are analyzed (Ai et al., 2019; Xing et al., 2018; Lai et al., 2022). The variation rules of the transmitted and dissipated energy of basalt and granite are studied through the SHPB test (Li et al., 2019; Liu et al., 2022). The energy utilization rate of the mortar is also studied through experiments (Sun et al., 2022). Xu et al. (2015) measured the expansion toughness and fracture energy of the rock through simulation. The influence of the angle and thickness of the joints and fractures in the rock mass on the law of energy propagation and dissipation is also explored (Huang et al., 2019; Han et al., 2022). The above-mentioned studies have analyzed the dynamic mechanics or energy dissipation characteristics of rock-like materials, while the energy dissipation characteristics of the grouting specimens under SHPB impact are rarely studied. The impact failure of the grouting specimens can be regarded as the result of energy transformation or energy dissipation among different energies. The process of energy variation reflects the evolution of internal micro-defects, and its failure mechanism can be further revealed from the perspective of energy dissipation (Gong et al., 2022).

The crack initiation and propagation in the specimens are difficult to observe due to the opaque nature of concrete materials. The crack propagation process can be observed through CT scanning, 3D printing, acoustic emission detection and other tests, but these experiments greatly increase the cost and do not scan the instantaneous failure process. The grouting specimen is a heterogeneous material with a complex internal structure, and the three-dimensional numerical model can effectively solve the problem of damage and energy dissipation of internal components, but indoor tests results don't be quantitatively analyzed (Lv et al., 2022; Sun et al., 2022). Previous research results (Li et al., 2012; Ayhan et al., 2022; Dong et al., 2021) have proven that LS-DYNA software can effectively simulate the dynamic impact process and fracture mechanical properties of cement-based materials. Yu et al. (2021) changed the parameters of the HJC constitutive model and studied the influence of the strength of

TABLE 1 Mix proportions of grout.

Groups	$m_C/\text{kg}$	$m_W/\text{kg}$	$m_{VAE}/\text{kg}$	$m_A/\text{kg}$
Grout	803.10	642.48	40.16	4.02

Notes:  $m_C$ ,  $m_W$ ,  $m_{VAE}$ , and  $m_A$  represent the quality of cement, water, VAE emulsion, and defoamer in 1 m<sup>3</sup> grout.

aggregate and mortar on the overall performance. Wang et al. (2021) established a 3D mesoscopic model to study the damage and energy dissipation process of concrete. Ai et al. (2013) simulated the mesoscopic failure mechanism of the concrete materials based on LS-DYNA software. A mesospheric aggregate model is established to study the tensile and compressive properties and failure process of concrete at high strain rates (Zhou et al., 2008; Xu et al., 2012). Few studies have reported the heterogeneous grouting-reinforced rock mass on SHPB numerical simulation.

The radial impact test of the same batch grouting specimens is conducted on the SHPB system. The failure process are recorded with a high-speed camera, which is helpful in analyzing the crack evolution law and failure mode. A 3D micro model of the standard size specimens is established by using the grid mapping method. LS-DYNA is used to simulate fracture process of the specimens under high strain rate. Based on the failure mode and the crack evolution process of the LS-DYNA model, the crack development law and its failure mechanisms are further researched to make up for the experimental deficiency. Moreover, the dynamic characteristics and energy dissipation law of the cemented rock are studied. The research results can provide reference for the grouting-reinforced rock mass of the deep roadway under an impact load.

## 2 Split Hopkinson pressure bar test

### 2.1 Preparation of the grouting specimens

The grouting specimens are mainly composed of the grouting material and graded gravel. The grouting materials include superfine cement slurry, vinyl acetate-ethylene (VAE), and defoamer. VAE is a type of polymer that serves as the binder. Some holes of the grouting specimens are minimized using the defoamer function. The mixing ratio is determined through indoor orthogonal tests and compared with the grouting injectability and effect and other factors (Avci et al., 2020), as shown in Table 1.

The graded gravel with a controllable particle size are selected as the injected material to simulate the sand layer with a large number of fine cracks. This work aims to minimize the porosity of the poured material and achieve the tightest packing state (Hwang et al., 2007). According to the Fuller gradation curve, the

TABLE 2 Grading of sand particles.

Particle size (mm)	Sorting sieve residue (%)	Accumulated sieve residue (%)	Consumption per liter (kg)
>4.75	0.00	0.00	0.000
4.75–2.36	35.87	35.87	0.534
2.36–1.18	25.10	60.97	0.373
1.18–0.60	17.42	78.39	0.259
0.60–0.30	12.66	91.05	0.189
0.30–0.15	8.95	100.00	0.133
<0.15	0.00	0.00	0.000

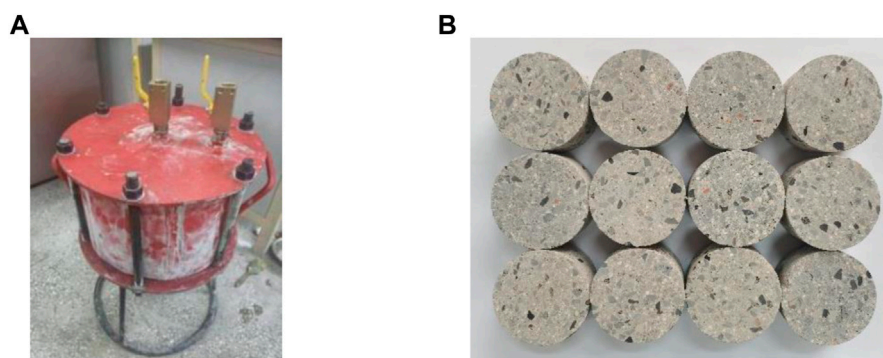


FIGURE 1  
Grouting mold and specimens. (A) Grouting mould, (B) Grouting specimens.

gravel gradation is calculated by using Eq. 1, where  $P$  is the total amount of the material less than the particle size  $D_s$ .  $D_s$  and  $D_m$  are the screen size and the maximum particle size of the material, respectively.

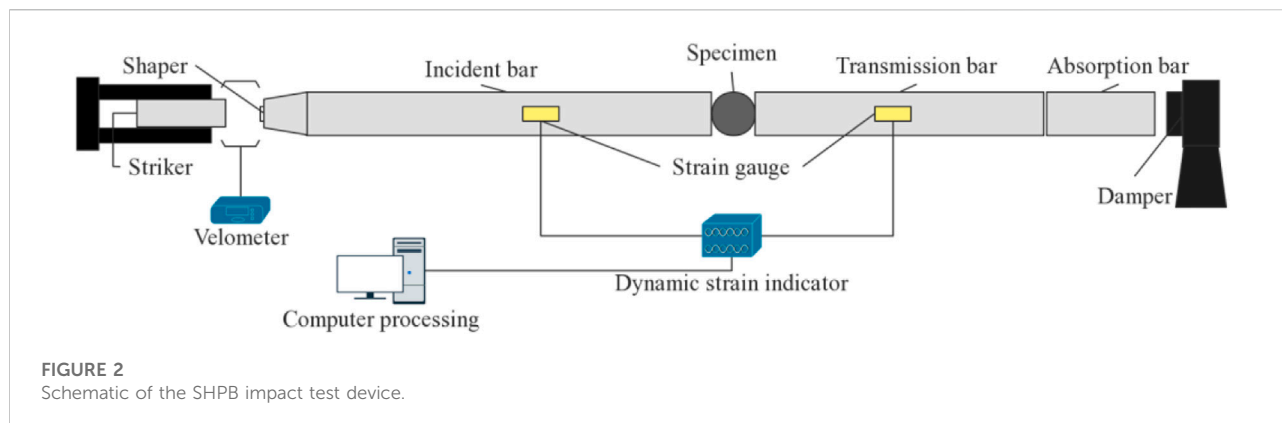
$$P = 100 \left( \frac{D_s}{D_m} \right)^h \quad (1)$$

The value of  $h$  ranges from  $1/3$  to  $1/2$ . When  $h = 1/2$ , the graded gravel theoretically reaches the maximum density. Accordingly, the value of  $h$  in the test is  $1/2$ . The particle size range is  $0.15$ – $4.75$  mm, and the detailed parameters are shown in Table 2. Given that the  $2.36$ – $4.75$  mm gravel has more impurities and poor quality, this part is replaced with crushed stone of the same particle size.

The specimens are obtained from the indoor grouting experiment. The size of the grouting mould is  $\Phi 330$  mm  $\times$  220 mm, as shown in Figure 1A. The mould is removed after the cement paste is consolidated. The specimens are cored and polished according to the requirement of the disk specimens ( $\Phi 50$  mm  $\times$  25 mm), placed into the curing box, and cured to the specified age, as shown in Figure 1B.

## 2.2 Split Hopkinson pressure bar test system and process

The impact test of the grouting specimens is conducted on the SHPB system, which is composed of a nitrogen pressure system, an elastic pressure bar system, and a data acquisition system. The schematic of the device is shown in Figure 2. The bullet, incident bar, and transmission bar are steel bars of  $\Phi 37$  mm  $\times$  400 mm,  $\Phi 50$  mm  $\times$  2,400 mm, and  $\Phi 50$  mm  $\times$  1,200 mm, respectively. The bar density is  $7,800$  kg/m<sup>3</sup>, the bar elastic modulus is 210 GPa, the bar diameter of the contact part between the incident bar and the bullet is 37 mm, and the variable section length is 170 mm. Nitrogen is used as the power source, and the strain rate of the specimen is controlled by changing air pressure. The SHPB test uses five different air pressures which are 0.15, 0.175, 0.20, 0.225, and 0.25 Mpa respectively, and the corresponding strain rates are 24.8, 29.1, 33.2, 39.3, and  $45.1$  s<sup>-1</sup>. Considering the randomness of the meso structure of the grouting specimens, the impact test of each group repeats five times, and the average values are taken as the strain rate and dynamic tensile strength of the specimens. A MIRO M310 high-speed camera of PHANTOM is used to capture the crack



evolution process of the specimens with a resolution of  $512 \times 512$  pixels and a frame rate of up to 10,800 fps.

Based on the assumption of the 1D stress waves and stress uniformity, the dynamic tensile stress, strain, and strain rate of the specimen are calculated by using Eq. 2 (KHAN et al., 2019), where  $\sigma = (P_i + P_t)/2$ . Variables  $P_i$  and  $P_t$  are the forces on the contact surface between the specimen-incident bar and the specimen-transmission bar, respectively, as shown in Eq. 3.

$$\begin{cases} \sigma_t = 2\bar{P}/\pi D_s L_s \\ \varepsilon_t = 2C_0/D_s \cdot \int_0^t (\varepsilon_i - \varepsilon_r) dt \\ \dot{\varepsilon}_t = 2C_0/D_s \cdot (\varepsilon_i - \varepsilon_r) \end{cases} \quad (2)$$

$$P_i = AE(\varepsilon_i + \varepsilon_r), P_t = AE\varepsilon_t \quad (3)$$

where  $A$ ,  $E$ , and  $C_0$  are the cross-sectional area, elastic modulus, and elastic wave velocity of the bar, respectively;  $D_s$  and  $L_s$  are the diameter and thickness of the specimens; and  $\varepsilon_i$ ,  $\varepsilon_r$ , and  $\varepsilon_t$  are the strain signals of the incident, reflected, and transmitted waves, respectively.

## 2.3 Energy calculation of the split Hopkinson pressure bar test

In the SHPB test, the energy propagates in the form of stress wave. From the perspective analysis of energy composition, the incident energy  $W_i$ , reflected energy  $W_r$ , and transmitted energy  $W_t$  are calculated to study the energy consumption law and failure characteristics of the grouting specimens in the dynamic splitting process, respectively. The calculation formula is shown in Eq. 4 (Li et al., 2020).

$$\begin{cases} W_i = AEC_0 \int_0^t \varepsilon_i^2(t) dt \\ W_r = AEC_0 \int_0^t \varepsilon_r^2(t) dt \\ W_t = AEC_0 \int_0^t \varepsilon_t^2(t) dt \end{cases} \quad (4)$$

The contact surface between the specimen and the bar is small, the interface is coated with vaseline, and the consumed energy by friction can be ignored. According to the energy conservation law, the absorbed energy  $W_s$  by the specimen can be calculated by using Eq. 5.

$$W_s = W_i - (W_r + W_t) \quad (5)$$

where  $W_s$  is mainly dissipated in crushed dissipation energy  $W_{FD}$ , crushed kinetic energy  $W_K$ , and other dissipation energy  $W_O$ .  $W_K$  only accounts for about 5% of the total absorbed energy, and the  $W_O$  dissipation energy is negligible (Wen et al., 2019; YAO et al., 2019). Thus,  $W_s = W_{FD}$ .

## 3 Numerical simulation

### 3.1 Establishment of the split Hopkinson pressure bar model

When the SHPB model was established, the specimen is composed of cement mortar and gravel. This model considers the 1.18–2.36 mm gravel and 2.36–4.75 mm crushed stone because of the limitation of computer performance. A single gravel occupies a few grids due to the small size and large number of gravel inside the model, so it is simplified as a sphere. The pre-divided mesh avoids some problems, such as high magnitude and poor quality of grids, which can meet the roughness of the grit surface. The spherical aggregate can reliably simulate the response of the cement-based materials under impact load and greatly simplify the modeling and calculation time compared with the random shape aggregate model (Zhou et al., 2007; Kim et al., 2011; Xu et al., 2012).

The CT slices of the specimen are imported into AVZIO. The processing process is shown in Figure 3A. Approximately 2.36–4.75 mm crushed stone and 1.18–2.36 mm gravel are selected, and their number and volume of are obtained (Table 3).

According to the material information extracted from the above CT images, large and small gravels are randomly placed

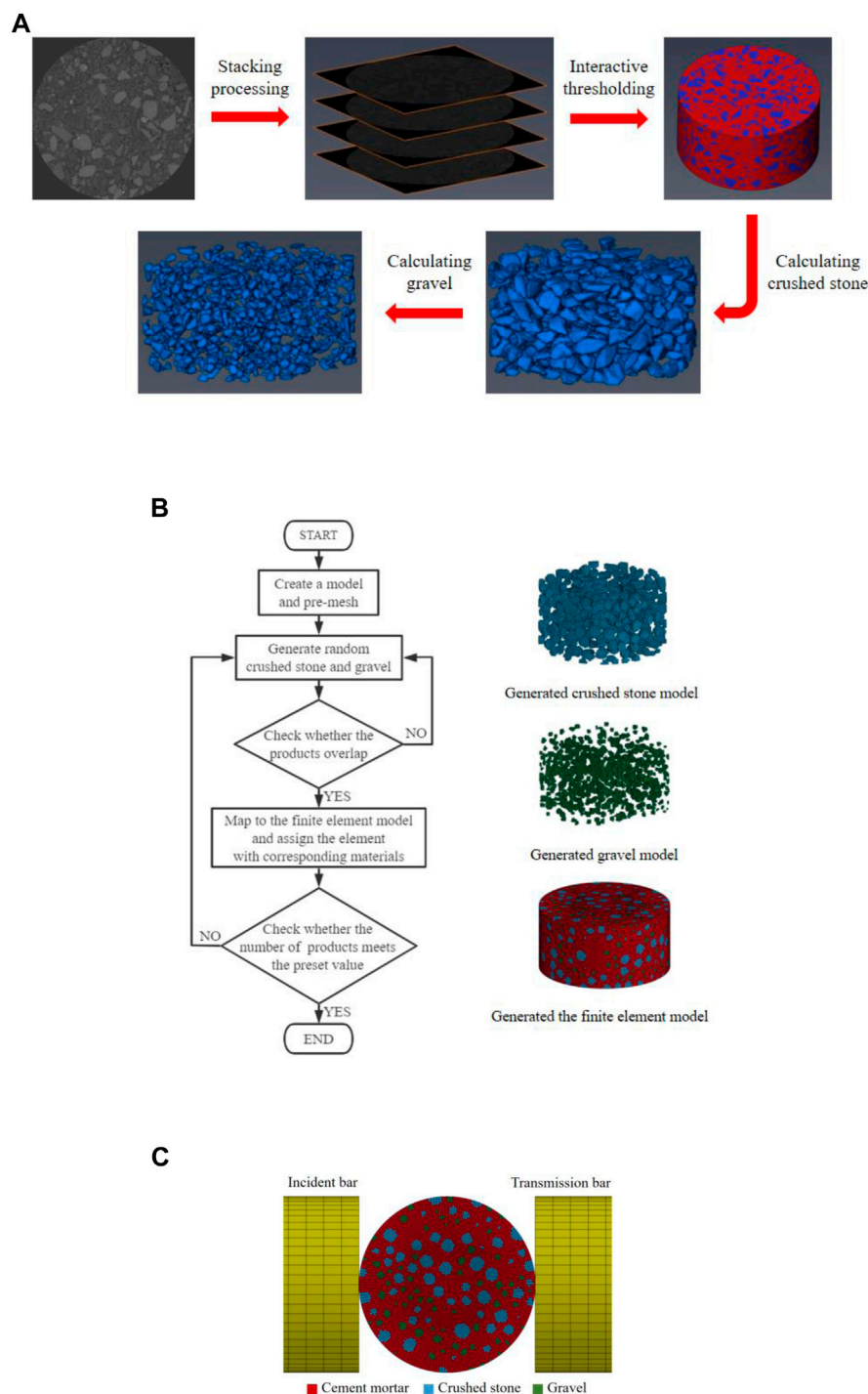


**FIGURE 3** The meso-scal FEM model of grouting specimen. **(A)** AVIZO processing, **(B)** Flow chart of generating mesoscale finite element model of the grouting specimen, **(C)** Simplified model of the SHPB simulation test.

by using the Monte Carlo method. Finally, the model places 491 crushed stones, and the number of units is 73,300, accounting for 23.27%. The model places 876 gravels, and

the number of units is 16,128, accounting for 5.12%. The placement processes of sand and gravel are shown in Figure 3B.



TABLE 3 Specimen internal component.

Component	Number	Volume/mm <sup>3</sup>	Proportion %
Crushed stone	491	11,809	24.07
Gravel	876	2,589.5	5.28

The established 3D model of the SHPB test and its physical and geometric parameters are consistent with the test. The model placement is shown in Figure 3C. The model adopts a solid164 unit, a mapping grid division, and a set of automatic surface contact between the bars and the erosion contact between bars—the specimen and its each component. The initial velocity of the bullet when loading is consistent with the test.

### 3.2 Holmquist–johnson–cook constitutive model

The HJC model can better describe the dynamic response of the materials at high strain rates. This constitutive model is proposed for the cement-based materials and comprehensively considers the damage evolution, compaction, and crushing effects and hardening characteristics (Xu et al., 2016). The HJC model includes yield surface, state, and damage evolution equations. The yield surface equation takes into account the damage and strain rate, and it is expressed by the dimensionless equivalent stress. The state equation describes the relationship between the hydrostatic pressure and the volumetric strain in a piecewise manner. The damage equation is described by the cumulative plastic strain (equivalent plastic strain  $\varepsilon_p$  and plastic volumetric strain  $\mu_p$ ), as shown in Figure 4.

The HJC model has 21 parameters. According to the method illustrated in the literature (Xie et al., 2019), the basic physical parameters of RO, G,  $F_C$ , T,  $P_{crush}$ , and  $\mu_{crush}$  are obtained from the laboratory test, and crushed stones and gravel parameters are provided by the manufacturer. The parameters of the state and damage equations can be found in the literature (Wang et al., 2021;

Lv et al., 2018). The rest of the parameters are determined through the simulation test. The material parameters are shown in Table 4.

The failure mode during calculation is controlled by using the element erosion technology to avoid the negative volume or large deformation of the element. When the element exceeds a certain threshold, it will be deleted because of failure, and the isolated failure element will manifest crack. The inherent failure criterion of the HJC model is the minimum fracture strain and the damage degree, and the maximum principal strain is set as 0.1 (LV et al., 2019). If the given value exceeds the element erosion criterion, the cement mortar, crushed stone, and gravel are considered to the failure.

## 4 Test verification and result analysis

### 4.1 Validity verification

In the SHPB and simulation tests, the measurement of the point of stress wave is set on the central unit of the incident and transmission bars, and the similarity of waveforms between them can verify the correctness of the model (Lv et al., 2022). The typical waveform of the dynamic tensile test is shown in Figure 5.

The measured waveforms through the laboratory and the simulation tests are in good agreement, and the characteristic errors of the two pulse peaks and durations are within 5%. The bearing loads at both ends of the specimen are basically the same, achieving dynamic balance and eliminating the influence of inertia effect (Dai et al., 2010). The feasibility of impact failure based on LS-DYNA is verified according to the test results.

### 4.2 Analysis of the test results

#### 4.2.1 Stress–strain curve of the specimens under three strain rates

Figure 6 shows the stress–strain curves of the specimens under three impact rates. A good correspondence can be

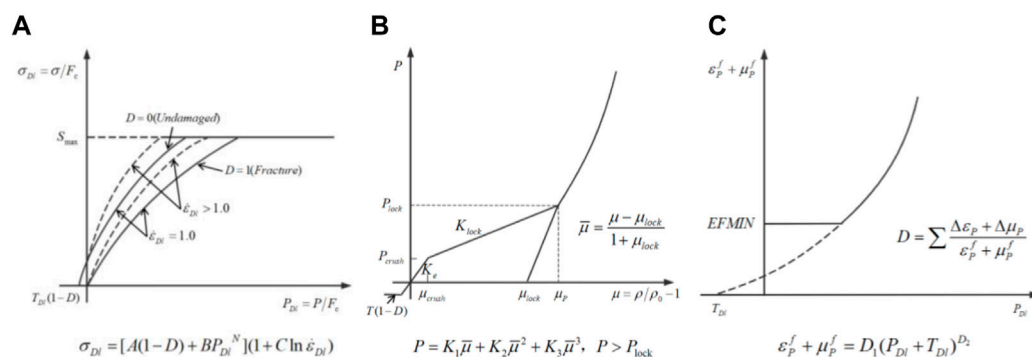
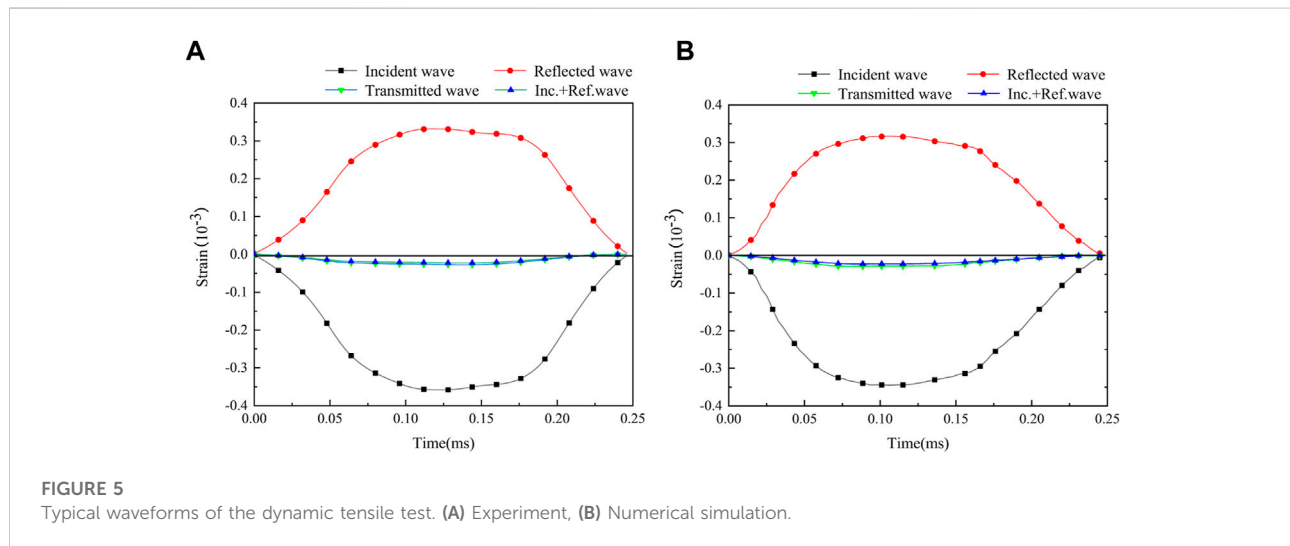


FIGURE 4  
HJC constitutive model. (A) Yield surface equation, (B) State equation, (C) Damage equation.

TABLE 4 Parameters of the HJC constitutive model.

Parameters	Cement mortar	Crushed stone	Gravel	Parameters	Cement mortar	Crushed stone	Gravel
MID	1	2	3	SFMAX	7	4	7
RO (kg/m <sup>2</sup> )	1970	2,660	1,650	PC (MPa)	5.3	40	12.4
G (GPa)	0.81	20.8	1.36	UC	0.0043	0.001	0.0075
A	0.58	0.9	0.66	PL (GPa)	0.104	3	0.255
B	1.335	1.8	1.335	UL	0.15	0.1	0.1
C	0.007	0.02	0.0023	D1	0.04	0.04	0.04
N	0.575	0.84	0.845	D2	1	1	1
FC (MPa)	15.9	120	37.2	K1 (MPa)	$8.5 \times 10^4$	$3.9 \times 10^4$	$3 \times 10^4$
T (MPa)	1.33	10	2.79	K2 (MPa)	$-1.71 \times 10^5$	$-2.23 \times 10^5$	$-2 \times 10^5$
EPSO	1	1	1	K3 (MPa)	$2.08 \times 10^5$	$5.5 \times 10^5$	$1.9 \times 10^5$
EFMIN	0.003	0.01	0.01	FS	0	0	0



observed between the test and the simulation curves. The dynamic tensile strength and peak strain of the specimens increase with the increase in the strain rate, and the envelope area of the curve gradually increases, which is a strain rate-dependent material. The high tensile performance of the specimens at a high strain rate has a close connection with the input energy. The input energy increases with the increase in strain rate, and the specimen is unable to release a large amount of energy in a short period of time, resulting in tensile strength increase.

#### 4.2.2 Crack evolution process of the specimen

In addition to the strength characteristics, the crack propagation process on the specimen surface is also the key to the dynamic damage evolution process. Figure 7 shows the whole process of dynamic splitting of the grouting specimens captured

with a high-speed camera. The stress wave of the specimen transmitters from the left side and the contact time is defined as zero. The selected pictures are used to analyze the failure process.

When  $\dot{\epsilon}$  is  $24.8 \text{ s}^{-1}$ , the center of the specimen showed a fine crack of about  $93 \mu\text{s}$ . At  $186 \mu\text{s}$ , the main crack in the center widens and expands to both ends. At  $279 \mu\text{s}$ , the main crack basically penetrates, and the failure zones of both ends are relatively small. In comparison with  $\dot{\epsilon} = 24.8 \text{ s}^{-1}$  and  $\dot{\epsilon} = 33.2 \text{ s}^{-1}$ , the crack at the center changes to about  $93 \mu\text{s}$ . At  $279 \mu\text{s}$ , the main crack expands to two ends. Meanwhile, secondary cracks appear at two ends. Furthermore, two ends appears at two wedge-shaped failure zones at  $651 \mu\text{s}$ .

In comparison with  $\dot{\epsilon} = 33.2 \text{ s}^{-1}$ , when  $\dot{\epsilon}$  is  $45.1 \text{ s}^{-1}$ , the failure law is almost the same before  $186 \mu\text{s}$ , and the

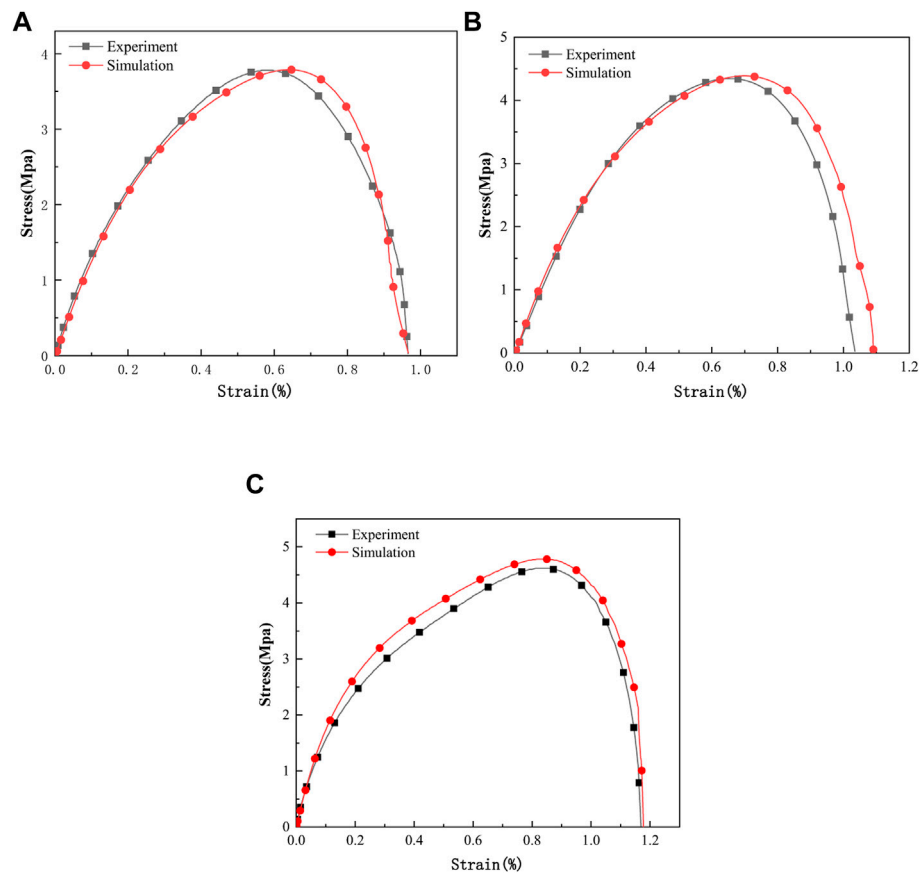


FIGURE 6

Three stress–strain curves of the experiment and simulations. (A)  $\dot{\epsilon} = 24.8 \text{ s}^{-1}$ , (B)  $\dot{\epsilon} = 33.2 \text{ s}^{-1}$ , (C)  $\dot{\epsilon} = 45.1 \text{ s}^{-1}$ .

corresponding primary crack is significantly wider at  $279 \mu\text{s}$ . The number of secondary cracks at two ends increases. At  $1,395 \mu\text{s}$ , the center failure is more serious, the wedge-shaped failure zone at two ends becomes larger, and the breakage degree is more serious. Excessive input energy induces a large number of secondary cracks, and the failure zone near the incident bar significantly increases. When  $\dot{\epsilon}$  is  $46.2 \text{ s}^{-1}$ , two penetrating cracks successively appear in the central position, the failure zones at both ends decrease, and the failure surface of the specimen increased, which are helpful to absorb more energy.

In summary, when the grouting specimens are fractured, the cracks initiate from the center to two ends, and tensile stress produced by the pulse wave is perpendicular to the loading direction at the center of the specimens. When the tensile stress exceeds its tensile strength, the crack initiates and then expands to both ends along the loading direction. The width of the main crack also increases. Before the first pulse finishes ( $279 \mu\text{s}$ ), the main crack did not fully cut-through the specimens, and the wedge failure zone is small at two ends. When the compressive and shear stresses are

combined with the specimen's contact surfaces, two ends of a secondary crack first emerge and form a wedge failure zone, which eventually connected with the main crack and penetrated the whole specimen. The crack initiation time of the high strain rate is earlier than low strain rate in the middle of the specimen. The crack width and the failure zone at two ends increase with the increase in the strain rate. When the strain rate changes from  $24.8$  to  $33.2 \text{ s}^{-1}$ , the failure mode of the specimens is similar, namely, the center split and the main crack. When  $\dot{\epsilon}$  is  $46.2 \text{ s}^{-1}$ , the failed fragment of the specimen is similar to a strip with two main cracks, consistent with the results in the literature (Khan et al., 2019).

When the path of crack expansion encounters the crushed stone and gravel, cracks mostly expand along the edge of the gravel, and rarely penetrates the crushed stone and gravel. Because the strength of crushed stone and gravel are higher than cement mortar, also the water film layer of the gravel surface results in higher water cement ratio, and the structure of interfacial transition zone is loose, which results in cracks extension along the edge of gravel.

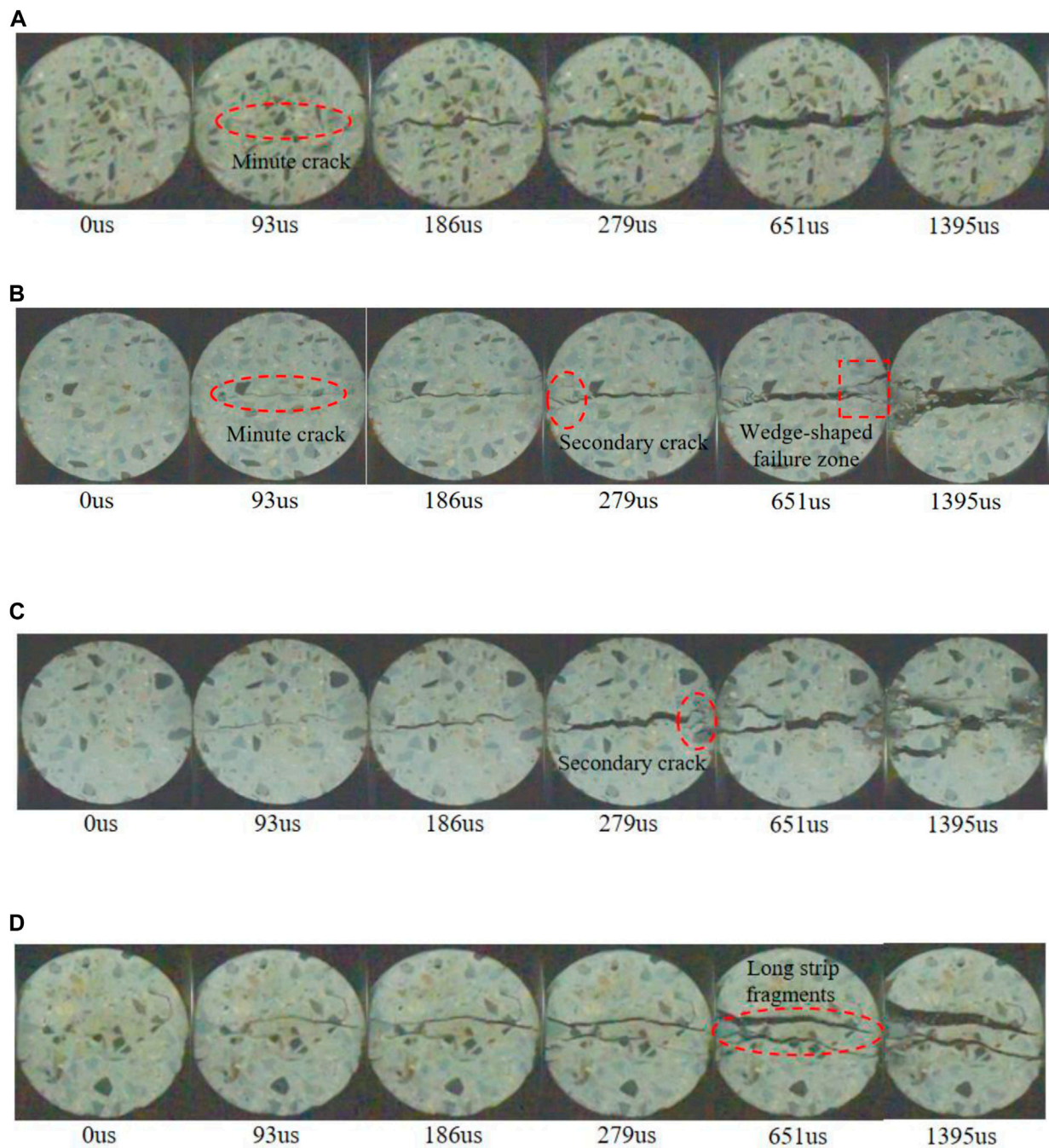


FIGURE 7

Typical failure process of the grouting specimens. (A)  $\dot{\epsilon} = 24.8 \text{ s}^{-1}$ , (B)  $\dot{\epsilon} = 33.2 \text{ s}^{-1}$ , (C)  $\dot{\epsilon} = 45.1 \text{ s}^{-1}$ , (D)  $\dot{\epsilon} = 46.2 \text{ s}^{-1}$ .

#### 4.2.3 Crack evolution process of the model

When the strain rates change from 24.8 to 33.2  $\text{s}^{-1}$ , the failure modes of the specimens are roughly similar. The strain rates of 24.8 and 45.1  $\text{s}^{-1}$  are shown in the simulation process due to the paper limitation (Figure 8). The simulation results are in good agreement with the experimental results, which verifies the

correctness of the 3D mesoscopic model. When the model is impacted, its central element first failed, and few failure elements can be observed at both ends. The crack rapidly spread from the center to both ends. After 279  $\mu\text{s}$ , the number of failure elements at both ends and the range of wedge failure zone rapidly increased. When  $\dot{\epsilon}$  is 45.1  $\text{s}^{-1}$ , the input energy is larger, and



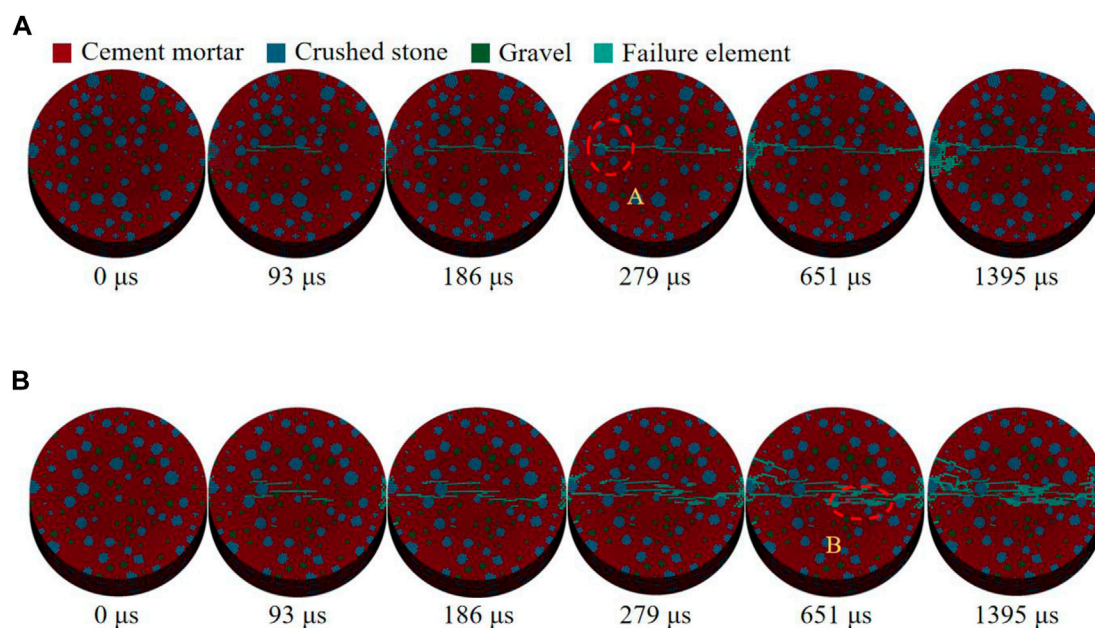


**FIGURE 8**  
Simulation failure process of the grouting specimens. (A)  $\dot{\epsilon} = 24.8 \text{ s}^{-1}$ , (B)  $\dot{\epsilon} = 45.1 \text{ s}^{-1}$ .

the number and range of central failure units are greater than  $24.8 \text{ s}^{-1}$  strain rate. According to the failure results, the main crack width in the center is wider, the number of secondary cracks is higher, and the failure zone is greater when  $\dot{\epsilon} = 45.1 \text{ s}^{-1}$ .

The cracks extend along the cement paste which is in good agreement with the experimental results (such as area A). Spreading through the gravel crack is almost perpendicular to the gravel surface, and the crack width is obviously bigger than that around the gravel. When the extension of crack encounter the gravel, a few cracks which are perpendicular to the gravel coarse gradually (such as area B). According to the theory of stress intensity factors in fracture mechanics (Cai et al., 2018), crack shape, size and the far field stress can affect the stress field intensity of crack tip. When the intensity factor of crack tip reaches the fracture toughness of gravel, the crack continues to expand through the gravel, and release energy in the form of fracture energy.

The 3D cracks inside the specimen have complex a topological structure, making it difficult to extract spatial cracks and quantitatively analyze the crack growth process. However, the numerical model is suitable for quantitative analysis of the crack growth process. The crack growth is show in Figure 9A, the cracks still expands from the center of the specimens to both ends. After the main crack is basically connected, the failure zone also expands at two ends, which is consistent with the cracks growth process on the model surface. This model is divided into 315,000 meshes, and the number of failure elements is counted at each calculation time.

The damage degree parameter is introduced to describe the damage degree of the model, namely,  $D_s = N_s/N_A$ , where  $N_s$  is the number of failure elements, and  $N_A$  is the total number of model elements at given time. The relationship is plotted between stress, strain, and crack volume base on  $45.1 \text{ s}^{-1}$ , as shown in Figures 9B,C. According to the crack evolution process curves, the damage process of the model can be divided into four stages:

Stage I (no crack stage):  $0\text{--}53 \mu\text{s}$ , the stress level of the model is low, and the model does not occur crack. At the moment, the strain of the model is small.

Stage II (slow development stage):  $53\text{--}146 \mu\text{s}$ , the model occurs few cracks at first, and it continue to expand with the stress increase. At this time, crack number and strain value are still small. At  $146 \mu\text{s}$ , the number of failure elements and  $D_s$  reaches 5,374 and 1.7% respectively.

Stage III (accelerated growth stage):  $146\text{--}190 \mu\text{s}$ , the stress exceeds  $4.03 \text{ MPa}$ , the crack rapidly expands, and the growth rate of  $D_s$  significantly increases. After reaching the peak stress, the stress rapidly declines, but the strain continues to increase. The number of internal failure elements and  $D_s$  reaches 13,583 and 4.3% at  $190 \mu\text{s}$ , respectively.

Stage IV (crack penetration stage): After  $190 \mu\text{s}$ , the stress reaches the peak and then decreases sharply, the cracks of the specimen continue to expand until failure. The number of internal failure elements gradually slows growth. At  $330 \mu\text{s}$ , the number of failure elements reaches 20,430, and  $D_s$  reaches 6.5%. The crack evolution process of the model is roughly similar

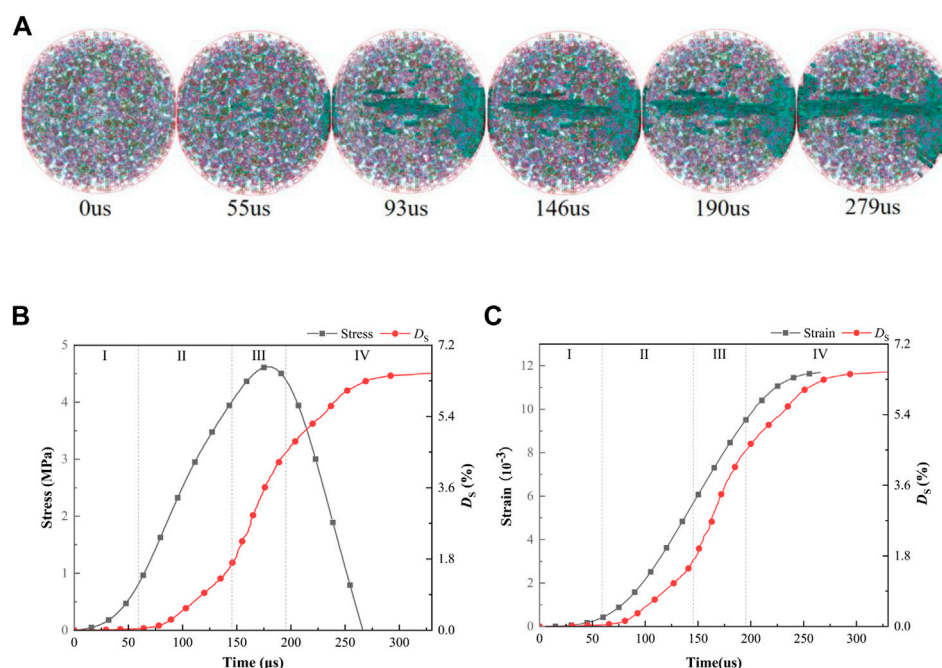


FIGURE 9

Crack extraction and variation trend of damage degree of  $45.1 \text{ s}^{-1}$ . (A) Extracted crack of the model, (B) Stress and damage degree, (C) Strain and damage degree.

to the strain curve. Thus, the crack volume can approximately reflect the strain value.

#### 4.2.4 Analysis of the energy dissipation process

Energy is the driving force behind material failure (Wen et al., 2020b; Wei et al., 2022), and energy dissipation causes everything from microscopic damage to macroscopic fragmentation of the model. The energy dissipation rate is defined as  $\lambda$ , namely,  $\lambda = W_s/W_i$ , to compare the degree of absorbed energy under different strain rates. Approximately 0.175 and 0.225 MPa impact air pressures are applied based on the original tests to comprehensively analyze the impact failure characteristics and energy change law of the model. In order to obtain the incident energy, The test parameters are substituted into Eqs 4, 5, and the absorbed energy and transmitted energy at five strain rates are obtained, as shown in Table 5.

In Table 5, the incident energy value gradually increases with the increase in strain rate. The incident energy, transmitted energy, and absorbed energy at five strain rates in Table 5 are fitted to obtain the energy relationship curves, as shown in Figure 10. The fitting curves of the incident energy and transmitted energy show increasing trends. The growth scope of the transmitted energy slows down with the increase in incident energy, as shown in Figure 10A. When the incident energy impacts on the model are low, the microcracks are less,

and the crack propagation scope is small. The crack number and damage range continuously increase with the increase in incident energy, and the cracks weakens the propagation of transmitted waves, resulting in a slow increase in transmitted energy. The energy dissipated by the crushed specimen linearly grows with the development of the incident energy, as shown in Figure 10B. The energy dissipation rate ( $\lambda$ ) is basically constant with the increase in the incident energy. The fluctuation value changes from 10% to 13%, as illustrated in Table 5, which shows the strain rate independence.

The energy curve of the model is drawn using the strain rate of  $45.09 \text{ s}^{-1}$  as an example and the three energies determined utilizing Eqs 4, 5, as shown in Figure 11A. The three energies curves show a slow growth, continuous linear growth and stabilization trend. The incident energy greatly increased. The maximum transmission energy is only 0.165 J, and the growth rate is the smallest due to the low tensile strength of the specimen (4.62 MPa). The failure process of the specimen is analyzed using the stress–strain curve and failure characteristics of the specimen. When time is 0–53  $\mu\text{s}$ , the incident energy slowly increases, and the stress pulse wave enters the rising elastic deformation stage. The dissipated energy of this stage is almost zero, no crack initiated, and the model stores a large amount of elastic energy. From 53 to 190  $\mu\text{s}$ , the incident energy and reflected energy rapidly increase, but the transmitted energy slightly increases. When the stress of the model is greater than the tensile strength,



TABLE 5 Calculation results of energy.

Impact pressure (MPa)	Strain rate (s <sup>-1</sup> )	Tensile strength (MPa)	$W_I$ (J)	$W_R$ (J)	$W_T$ (J)	$W_S$ (J)	$\lambda$
0.15	24.8	3.78	15.713	13.867	0.068	1.778	0.113
0.175	29.1	4.07	22.333	19.678	0.109	2.546	0.114
0.2	33.2	4.35	30.817	27.059	0.141	3.617	0.117
0.225	39.3	4.50	36.435	32.180	0.157	4.098	0.112
0.25	45.1	4.62	40.608	35.755	0.165	4.688	0.115

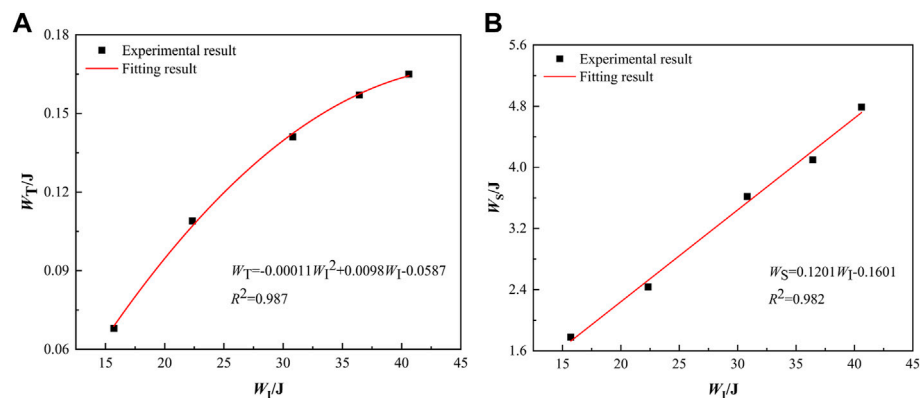


FIGURE 10

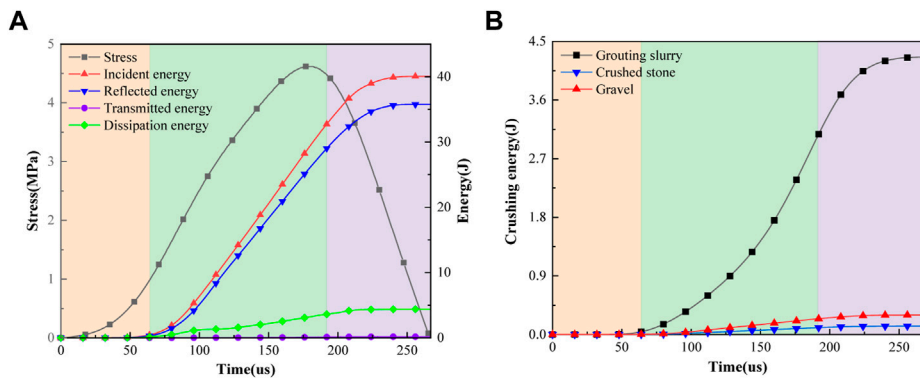
Energy relation curve. (A) Relationship between  $W_I$  and  $W_T$ , (B) Relationship between  $W_I$  and  $W_S$ .

FIGURE 11

Energy curve of the grouting specimen. (A) Energy dissipation curve of the specimen, (B) Breakup energy curves of each component.

the dissipated energy of the specimen increases due to crack growth. From 190 to 267  $\mu$ s, the stress of the model decreases after reaching the peak strength, and the original and new cracks in the specimen continued to expand. The release of elastic energy also aggravates the failure of the model, and the

dissipation energy slightly increases and then tended to a constant value.

The energy evolution process of each material component of the specimen model cannot be measured in a laboratory. However, the dissipated energy of the different components

can be described by using a 3D meso-numerical model. Take  $\dot{\epsilon} = 45.1 \text{ s}^{-1}$  as an example, as shown in Figure 11B. The dissipation energy in the model is 4.78 J, which is within 5% of the experimental value of 4.69 J. Before 53  $\mu\text{s}$ , each component of the model is in the elastic stage and basically did not consume energy. From 53 to 190  $\mu\text{s}$ , the dissipated energy of the cement mortar increases. Internal cracks and fine cracks start to appear when the local stress in the cement mortar exceeds its tensile strength. The strength of the crushed stone and gravel is higher than that of the cement mortar, and most of the particles are not failure, so the number of failure units is few. The dissipation energy of the crushed stone and gravel slowly increases, and the dissipation energy of the gravel is slightly greater than that of the crushed stone. From 190 to 267  $\mu\text{s}$ , the model significantly breaks, and the dissipated energy of the cement mortar, gravel and crushed stone accounted for 90.8%, 6.5%, and 2.7% of the dissipated energy of the model, respectively.

When the strain rate is 24.8–45.1  $\text{s}^{-1}$ , the proportion of dissipated energy of the cement mortar is above 90%. When the specimen fails, the cement mortar is the first to be significantly damaged. Crushed stone and gravel are bonded by using a cement mortar. Thus, the strength of the cemented specimen is most affected by the strength of the cement mortar.

## 5 Conclusion

Different strain rate dynamic splitting tensile tests of the cemented specimens are carried out by using the SHPB test device. The dynamic failure process and energy dissipation law of the cemented specimens are studied. A 3D mesoscopic numerical model is established by using the SHPB, and the accuracy of the numerical simulation is verified by comparing with the SHPB test result. The main conclusions are as follows:

- (1) The dynamic tensile strength and peak strain of the cemented specimens increase with the increase in strain rate. It is a strain rate-related material.
- (2) When the specimens are destroyed by impact load, the cracks initiated at the center and spread to both ends of the specimen along the load direction. The wedge-shaped failure zone at both ends expands after the first pulse wave completed. When the strain rates changed from 24.8 to 33.2  $\text{s}^{-1}$ , the failure morphology of the specimens is similar with the splitting failure and the main crack at the center. When the strain rate is 46.2  $\text{s}^{-1}$ , the failure mode of the specimens is a strip fragment with two main cracks at the center.
- (3) The crack growth process in the model is quantitatively describe based on LS-DYNA software. The damage of the specimen is divided into four stages: no crack stage, slow crack development stage, accelerated crack growth stage and

crack penetration stage. When the specimen broke, the energy dissipation rate fluctuates from 10% to 13%, and the dissipated energy of the cement mortar accounts for more than 90% of the total dissipated energy. The cement mortar is destroyed first and most severely, and its strength has a great influence on the strength of the grouting specimen.

- (4) In comparison with the indoor SHPB test result, the 3D meso-model of the grouting specimens established based on the 3D reconstruction technology and LS-DYNA software can better simulate the crack evolution process and failure mode of the specimen, which can quantitatively analyze the energy consumption of the internal components. (XU and WEN, 2016), (LI and XU, 2009).

## Data availability statement

The raw data supporting the conclusion of this article will be made available by the authors, without undue reservation.

## Author contributions

C-XZ proposed the research methods and ideas of this article, J-XS completed the experiment of this article, JG and F-EW completed the writing of this article.

## Funding

This work was supported by the National Natural Science Foundation of China (51874119), the Department of Education Project of Henan Province (2011A440003) and the Doctorate Fund of Henan Polytechnic University (B2009-96).

## Conflict of interest

The authors declare that the research was conducted in the absence of any commercial or financial relationships that could be construed as a potential conflict of interest.

## Publisher's note

All claims expressed in this article are solely those of the authors and do not necessarily represent those of their affiliated organizations, or those of the publisher, the editors and the reviewers. Any product that may be evaluated in this article, or claim that may be made by its manufacturer, is not guaranteed or endorsed by the publisher.

## References

- Ai, D. H., Zhao, Y. C., Wang, Q. F., and Li, C. W. (2019). Experimental and numerical investigation of crack propagation and dynamic properties of rock in SHPB indirect tension test. *Int. J. Impact Eng.* 126, 135–146. doi:10.1016/j.ijimpeng.2019.01.001
- Ai, S. G., Tang, L. Q., Mao, Y. Q., Liu, Y., and Fang, D. (2013). Numerical analysis on failure behaviour of polyurethane polymer concrete at high strain rates in compression. *Comput. Mater. Sci.* 69, 389–395. doi:10.1016/j.commatsci.2012.12.018
- Avcı, E., and Mollamahmutoglu, M. (2020). Strength and permeability characteristics of superfine cement and fine fly ash mixture grouted sand[J]. *ACI Mater. J.* 117 (6), 293–304.
- Ayhan, B., and Lale, E. (2022). Modeling strain rate effect on tensile strength of concrete using damage plasticity model. *Int. J. Impact Eng.* 162, 104132. doi:10.1016/j.ijimpeng.2021.104132
- Cai, X. J., Xia, R., Huo, M. C., and Xu, J. (2018). A threshold formula for fatigue crack growth with mean stress intensity factors. *Int. J. Mech. Sci.* 135, 639–645. doi:10.1016/j.jimecs.2017.12.014
- Chen, X. D., Wu, S. X., and Zhou, J. K. (2014). Quantification of dynamic tensile behavior of cement-based materials. *Constr. Build. Mater.* 51, 15–23. doi:10.1016/j.conbuildmat.2013.10.039
- Dai, F., Xia, K. W., and Tang, L. Z. (2010). Rate dependence of the flexural tensile strength of Laurentian granite. *Int. J. Rock Mech. Min. Sci.* 47 (3), 469–475. doi:10.1016/j.jrmms.2009.05.001
- Dong, C. L., Lu, X. Y., Zhao, G. M., Meng, X., Li, Y., and Cheng, X. (2021). Experiment and applications of dynamic constitutive model of tensile and compression damage of sandstones. *Adv. Mater. Sci. Eng.* 2021, 1–13. doi:10.1155/2021/2492742
- Gong, F. Q., Si, X. F., Li, X. B., and Wang, S. Y. (2019). Dynamic triaxial compression tests on sandstone at high strain rates and low confining pressures with split Hopkinson pressure bar. *Int. J. Rock Mech. Min. Sci.* 113, 211–219. doi:10.1016/j.jrmms.2018.12.005
- Han, Z. Y., Li, D. Y., Zhou, T., Zhu, Q., and Ranjith, P. (2020). Experimental study of stress wave propagation and energy characteristics across rock specimens containing cemented mortar joint with various thicknesses. *Int. J. Rock Mech. Min. Sci.* 131, 104352. doi:10.1016/j.jrmms.2020.104352
- Huang, J., Liu, X. L., Song, D. Q., Zhao, J., Wang, E., and Zhang, J. (2022). Laboratory-scale investigation of response characteristics of liquid-filled rock joints with different joint inclinations under dynamic loading. *J. Rock Mech. Geotechnical Eng.* 14 (2), 396–406. doi:10.1016/j.jrmge.2021.08.014
- Hwang, C. L., and Hsieh, S. L. (2007). The effect of fly ash/slag on the property of reactive powder mortar designed by using Fuller's ideal curve and error function. *Comput. Concr.* 4 (6), 425–436. doi:10.12989/cac.2007.4.6.425
- Jong, S. C., Ong, D. E. L., and Oh, E. (2021). State-of-the-art review of geotechnical-driven artificial intelligence techniques in underground soil-structure interaction. *Tunn. Undergr. Space Technol.* 113, 103946. doi:10.1016/j.tust.2021.103946
- Khan, M. Z. N., Hao, Y. F., Hao, H., and Shaikh, F. u. A. (2019). Mechanical properties and behaviour of high-strength plain and hybrid-fiber reinforced geopolymer composites under dynamic splitting tension. *Cem. Concr. Compos.* 104, 103343. doi:10.1016/j.cemconcomp.2019.103343
- Kim, S. M., and Abu Al-Rub, R. K. (2011). Meso-scale computational modeling of the plastic-damage response of cementitious composites. *Cem. Concr. Res.* 41 (3), 339–358. doi:10.1016/j.cemconres.2010.12.002
- Lai, D. D., Demartino, C., and D. D. Y. X. (2022). High-strain rate tension behavior of fiber-reinforced rubberized concrete[J]. *Cem. Concr. Compos.* 131, 104554.
- Li, W. M., and Xu, J. Y. (2009). Mechanical properties of basalt fiber reinforced geopolymeric concrete under impact loading. *Mater. Sci. Eng. A* 505 (1), 178–186. doi:10.1016/j.msea.2008.11.063
- Li, X. J., Zhang, Y. Y., Shi, C., and Chen, X. (2020). Experimental and numerical study on tensile strength and failure pattern of high performance steel fiber reinforced concrete under dynamic splitting tension. *Constr. And Build. Mater.* 259, 119796. doi:10.1016/j.conbuildmat.2020.119796
- Liang, Y., Chen, X. Y., Yang, J. S., Zhang, J., and Huang, L. (2020). Analysis of ground collapse caused by shield tunnelling and the evaluation of the reinforcement effect on a sand stratum. *Eng. Fail. Anal.* 115, 104616. doi:10.1016/j.engfailanal.2020.104616
- Liao, Z. Y., Zhu, J. B., Xia, K. W., and Tang, C. A. (2016). Determination of dynamic compressive and tensile behavior of rocks from numerical tests of split Hopkinson pressure and tension bars. *Rock Mech. Rock Eng.* 49 (10), 3917–3934. doi:10.1007/s00603-016-0954-8
- Liu, L., Wang, Y., and An, H. M. (2022). Fractal characteristics and energy dissipation of granite after high-temperature treatment based on SHPB experiment. *Front. Earth Sci. (Lausanne)*. 10, 861847. doi:10.3389/feart.2022.861847
- Liu, P. F., Zhou, X. P., Qian, Q. H., Berto, F., and Zhou, L. (2019). Dynamic splitting tensile properties of concrete and cement mortar. *Fatigue Fract. Eng. Mat. Struct.* 43 (4), 757–770. doi:10.1111/ffe.13162
- Lv, N., Wang, H. B., Rong, K., Chen, Z., and Zong, Q. (2022). The numerical simulation of large diameter split Hopkinson pressure bar and Hopkinson bundle bar of concrete based on mesoscopic model. *Constr. Build. Mater.* 315, 125728. doi:10.1016/j.conbuildmat.2021.125728
- Lv, T. H., Chen, X. W., and Chen, G. (2018). The 3D meso-scale model and numerical tests of split Hopkinson pressure bar of concrete specimen. *Constr. Build. Mater.* 160, 744–764. doi:10.1016/j.conbuildmat.2017.11.094
- Ren, L. W., He, P. F., Zou, Y. F., Dun, Z. L., Zou, Z. s., and Wang, S. r. (2022). A new classification method of mine goaf ground activation considering high-speed railway influence. *Front. Earth Sci. (Lausanne)*. 10, 896459. doi:10.3389/feart.2022.896459
- Sun, B., Chen, R., Ping, Y., Zhu, Z., Wu, N., and Shi, Z. (2022). Research on dynamic strength and inertia effect of concrete materials based on large-diameter split Hopkinson pressure bar test. *Materials* 15 (9), 2995. doi:10.3390/ma15092995
- Sun, J. Y., Xie, J. B., Zhou, Y., and Zhou, Y. (2022). A 3D three-phase meso-scale model for simulation of chloride diffusion in concrete based on ANSYS. *Int. J. Mech. Sci.* 219, 107127. doi:10.1016/j.jimecs.2022.107127
- Von Der Tann, L., Sterling, R., Zhou, Y. X., and Metje, N. (2020). Systems approaches to urban underground space planning and management – a review. *Undergr. Space* 5 (2), 144–166. doi:10.1016/j.undsp.2019.03.003
- Wang, S. R., Zhao, J. Q., Wu, X. G., Yang, J. H., and Liu, A. (2021). Meso-Scale simulations of lightweight Aggregate concrete under impact loading. *Int. J. Simul. Model.* 20 (2), 291–302. doi:10.2507/ijimm20-2-558
- Wei, L. K., Yuan, Q., Ren, Y. W., al, er, Zhang, D., Liu, Y., et al. (2022). Analysis of failure mechanics and energy evolution of sandstone under uniaxial loading based on DIC technology. *Front. Earth Sci. (Lausanne)*. 10, 814292. doi:10.3389/feart.2022.814292
- Wen, T., Tang, H. M., Huang, L., Wang, Y., and Ma, J. (2020a). Energy evolution: A new perspective on the failure mechanism of purplish-red mudstones from the three gorges reservoir area, China. *Eng. Geol.* 264, 105350. doi:10.1016/j.enggeo.2019.105350
- Wen, T., Tang, H. M., Ma, J. W., and Liu, Y. (2019). Energy analysis of the deformation and failure process of sandstone and damage constitutive model. *KSCE J. Civ. Eng.* 23 (2), 513–524. doi:10.1007/s12205-018-0789-9
- Wen, T., Tang, H. M., Wang, Y. K., and Ma, J. (2020b). Evaluation of methods for determining rock brittleness under compression. *J. Nat. Gas Sci. Eng.* 78, 103321. doi:10.1016/j.jngse.2020.103321
- Xie, B. J., Yan, Z., Du, Y. J., Zhao, Z., and Zhang, X. (2019). Determination of holmquist-johnson-cook constitutive parameters of coal: Laboratory study and numerical simulation. *Processes* 7 (6), 386. doi:10.3390/pr7060386
- Xing, H. Z., Zhang, Q. B., Ruan, D., Dehkhoda, S., Lu, G., and Zhao, J. (2018). Full-field measurement and fracture characterisations of rocks under dynamic loads using high-speed three-dimensional digital image correlation. *Int. J. Impact Eng.* 113, 61–72. doi:10.1016/j.ijimpeng.2017.11.011
- Xu, H., and Wen, H. M. (2016). A computational constitutive model for concrete subjected to dynamic loadings. *Int. J. Impact Eng.* 91, 116–125. doi:10.1016/j.ijimpeng.2016.01.003
- Xu, Y., Dai, F., Xu, N. W., and Zhao, T. (2015). Numerical investigation of dynamic rock fracture toughness determination using a semi-circular bend specimen in split Hopkinson pressure bar testing. *Rock Mech. Rock Eng.* 49 (3), 731–745. doi:10.1007/s00603-015-0787-x
- Xu, Z., H., H., and Li, H. (2012). Mesoscale modelling of fibre reinforced concrete material under compressive impact loading. *Constr. And Build. Mater.* 26 (1), 274–288. doi:10.1016/j.conbuildmat.2011.06.022
- Yao, W., and Xia, K. W. (2019). Dynamic notched semi-circle bend (NSCB) method for measuring fracture properties of rocks: Fundamentals and applications. *J. Rock Mech. Geotechnical Eng.* 11 (5), 1066–1093. doi:10.1016/j.jrmge.2019.03.003
- Ye, F., Liang, S., Liang, X. M., Zhang, W., Liu, C., and Feng, H. (2022). Grouting technology and construction schemes of a tunnel in aeolian stratum: A case study of shenmu No. 1 tunnel. *Sci. Rep.* 11 (1), 23552. doi:10.1038/s41598-021-03021-4
- Yu, Q., Chen, Z. Y., Yang, J., and Rong, K. (2021). Numerical study of concrete dynamic splitting based on 3D realistic aggregate mesoscopic model. *Materials* 14 (8), 1948. doi:10.3390/ma14081948
- Zhou, X. Q., and Hao, H. (2008). Mesoscale modelling of concrete tensile failure mechanism at high strain rates. *Comput. Struct.* 86 (21–22), 2013–2026. doi:10.1016/j.compstruc.2008.04.013
- Zhu, C. X., Li, W. D., and An, Y. M. (2022). Split Hopkinson pressure bar test and its numerical analysis based on transparent rock samples. *KSCE J. Civ. Eng.* 26 (9), 4128–4135. doi:10.1007/s12205-022-1743-4



## OPEN ACCESS

## EDITED BY

Jun Zhao,  
Anhui University of Science and  
Technology, China

## REVIEWED BY

Yi Chang,  
East China University of Technology,  
China  
Feng Xu,  
University of South China, China

## \*CORRESPONDENCE

Mingxin Zheng,  
✉ 294817459@qq.com

## SPECIALTY SECTION

This article was submitted to  
Geohazards and Georisks,  
a section of the journal  
Frontiers in Earth Science

RECEIVED 13 November 2022

ACCEPTED 05 December 2022

PUBLISHED 11 January 2023

## CITATION

Fan Y, Zheng M and Wu J (2023), A study  
on the shear strength characteristics  
and microscopic mechanism of coal-  
bearing soil under dry-wet cycles.  
*Front. Earth Sci.* 10:1096980.  
doi: 10.3389/feart.2022.1096980

## COPYRIGHT

© 2023 Fan, Zheng and Wu. This is an  
open-access article distributed under  
the terms of the [Creative Commons  
Attribution License \(CC BY\)](https://creativecommons.org/licenses/by/4.0/). The use,  
distribution or reproduction in other  
forums is permitted, provided the  
original author(s) and the copyright  
owner(s) are credited and that the  
original publication in this journal is  
cited, in accordance with accepted  
academic practice. No use, distribution  
or reproduction is permitted which does  
not comply with these terms.

# A study on the shear strength characteristics and microscopic mechanism of coal-bearing soil under dry-wet cycles

Yakun Fan<sup>1,2</sup>, Mingxin Zheng<sup>1\*</sup> and Junhua Wu<sup>2</sup>

<sup>1</sup>School of Transportation Engineering, East China Jiaotong University, Nanchang, China, <sup>2</sup>School of Civil Engineering and Architecture, Nanchang Hangkong University, Nanchang, China

The slope of coal-bearing strata distributed along the high-speed highway (railway) is affected by the atmospheric dry-wet cycles (DWC), and the collapse occurs many times during the construction of such highways, in Pingxiang city, in the province of Jiangxi. The DWC affect the strength characteristics of the unsaturated coal-bearing soil (CBS). In order to study the shear-strength characteristics of the unsaturated CBS under the DWC, the relationship between the shear strength and matric suction was analyzed by using direct shear test of the unsaturated CBS, the filter paper method of the matrix suction measurement, and the scanning electron microscope test. The internal reasons of shear strength attenuation of unsaturated CBS under DWC are revealed from microscopic perspective. The results show that the DWC at 0 to 4 times, with an increase in the water content, the clay domains expanded unevenly. Further, the clay minerals that served as the cementing junctions and soluble salts were softened and dissolved, and the bonding strength between the basic units and the cohesion of the samples decreased, so that the shear strength of unsaturated CBS samples decreased with an increase in the water content, and increased with the increase of matric suction. Under the influence of the DWC, the CBS samples slaked, the quartz matrix between the fissures slaked, and produce fragments and debris which reduced the size of large particles, and the bonding strength between the basic units was low. Therefore, the matric suction and the shear strength of the unsaturated CBS samples with the same moisture content, under the same normal pressure, decreased gradually with an increase in the number of the DWC. It is feasible to study the strength characteristics of unsaturated CBS by combining the test methods of macroscopic strength, matric suction and microstructure of soil.

## KEYWORDS

dry-wet cycles, unsaturated coal-bearing soil, shear strength, matric suction, microstructure characteristics

# 1 Introduction

There are many coal-measure strata along the expressway (iron) road in Pingxiang City, in Jiangxi Province. Under the action of the atmospheric DWC, the slope of coal measure strata in expressway (railway) has collapsed many times during construction (YANG and ZHENG, 2018). The coal-measure strata and its weathered materials are generally referred to as the CBS, which are characterized by uneven soft and hard soil layers, poor interlayer cementation, loose structure, fast weathering speed after excavation, softening, disintegration, and loss of strength in the event of water-saturation (Han et al., 2019). Therefore, it is of great theoretical and practical significance to study the engineering properties of the unsaturated CBS under the DWC for slope stability and soil and water conservation.

The shear strength theory of the unsaturated soil has been studied for several decades, amongst which the most accepted shear strength formulae for the unsaturated soil are the Bishop effective stress strength formula (BISHOP and BLIGHT, 1963) and the Fredlund double stress variable strength formula (FREDLUND et al., 1978), both of which reflect the contribution of the matric suction against the shear strength. Due to the difficulties in measuring and calculating the matric suction, many studies have chosen the water content or the saturation to replace matric suction in the study of the unsaturated soil strength (Cui and Si, 2014; Aqtash and Bandini, 2015; Hassan Marwan Adil and Mohamad Ismail Mohd Ashraf, 2018; Qian et al., 2020; Ma, Huang, Hu, Yang; Chou and Wang, 2021). However, some studies have pointed out that there is no one-to-one single value relationship between the matric suction and the water content in unsaturated soil strength. Chengren (XIONG et al., 2005) discussed the variation characteristics of matric suction in the unsaturated soil water-density state space, and discovered that there was neither direct correlation nor definite corresponding relationship between the matric suction and saturation, but that water and the soil structure were two very important factors affecting the matric suction. Therefore, matric suction is a combination of water content and soil structure, which is more suitable for the analysis of the shear properties of the unsaturated soils. Changguang et al. (ZHANG et al., 2012) divided the various unsaturated soil shear strength formulas into five categories, among which the formula index of the total stress shear strength has been widely used in practical engineering. Therefore, with a change in the moisture content and the soil structure of the CBS, the filter-paper method could be used to transform the measured matric suction into the total stress shear strength of the soil, which has high application value in engineering practices.

The macroscopic physical and mechanical properties of the rock and soil as well as their specific engineering properties all depend on their microscopic structure (Zuo et al., 2016; NOWAMOOZ et al.,

2016; Zhao et al., 2018; Zhou et al., 2021). However, most studies have focused on the micro-structure of the red clay, expansive soil, loess, and silty sand (ALDAOOD et al., 2014; Jiang et al., 2014; AHMED, 2015; Lin and Amy, 2015; Sun and Cui, 2018; Xiao et al., 2020; Wang et al., 2021), for instance. Some studies had also investigated the slope protection and the reinforcement of the CBS, the physical and the mechanical properties of the soil, and the micro-structure parameters (Hang et al., 2019; Huang and Zheng, 2021; Zhang et al., 2021). There are few studies, however, on the relationship between the microstructure and the macroscopic strength of the unsaturated CBS under the wetting and drying cycles. In this paper, the remolded samples of the CBS along the Changli Expressway were taken as the research object. Based on the total stress strength, the shear strength, and the microstructure characteristics, the unsaturated CBS under the dry and wet cycling conditions were studied by the direct shear test of the unsaturated CBS, matrix suction test by the filter-paper method, and the microscopic scanning electron microscope test. The relationship between the shear strength and the matric suction of the unsaturated CBS was analyzed, and the cause of the shear-strength attenuation of the unsaturated CBS under the three DWC was revealed from the microscopic point of view, which provided some important and beneficial supplements for the study of engineering properties of the unsaturated CBS and slope stability.

## 2 Methods

### 2.1 Basic characteristics of the test soil samples

The CBS used in this test was taken from the landslide soil in K213 section of the Changli Expressway in Jiangxi Province. The specific physical and mechanical indexes are shown in Table 1.

The particle composition of the CBS is shown in Table 2. According to the classification of soil of the Highway Geotechnical Test Regulations, the CBS belongs to clay-sand.

### 2.2 Testmethod

#### 2.2.1 Soil samplepreparation

According to the compaction degree of the 93% of the maximum dry density of the compaction test, the CBS sample with the dry density of  $669.1 \text{ g/cm}^3$  was prepared. In this paper, the particles of the remolded samples were all passed through a 2 mm screen, and the prepared soil was pressed into a large round sample with a diameter of 100 mm, and a height of 40 mm by the sample pressing method. Then the samples were placed on a water tray, and soaked and saturated with the water absorption by using the principle of the capillary water absorption. In the indoor constant temperature ( $20^\circ\text{C}$ )



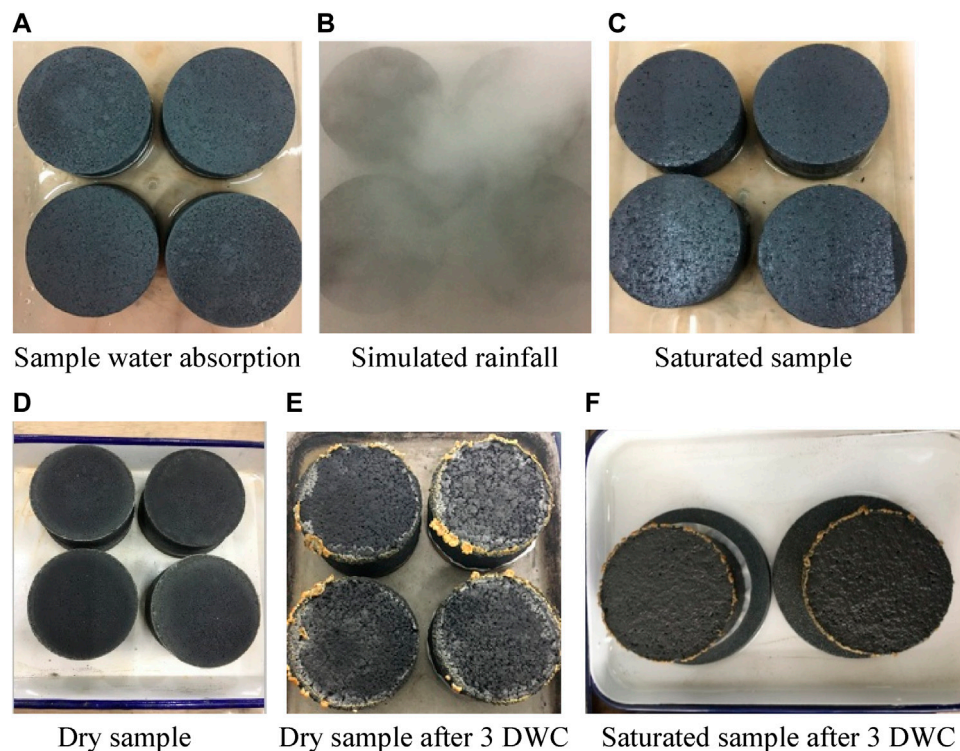
**TABLE 1** The main physical and mechanical indices of the CBS as used in this study.

Specific gravity	Liquid limit	Plastic limit	Maximum dry density (g/cm <sup>3</sup> )	Optimum moisture content (%)
2.68	31.8	17.8	1.795	18.36

**TABLE 2** The particle gradation of the CBS.

Particle size/mm	2	1	0.5	0.25	0.075
The percentage of particles smaller than the particle size to the total weight (%)	100	94.8	78.3	64.6	29.5

X-ray diffraction analysis showed that the mineral composition of the sample is mainly quartz, muscovite, and calcium carbonate, but also contains a small amount of kaolinite and chlorite (about 18%).

**FIGURE 1**

The surface morphology of the large round samples with the hygroscopic, dehumidifying, and after three DWC. (A) Sample water absorption (B) Simulated rainfall (C) Saturated sample (D) Dry sample (E) Dry sample after three DWC (F) Saturated sample after three DWC.

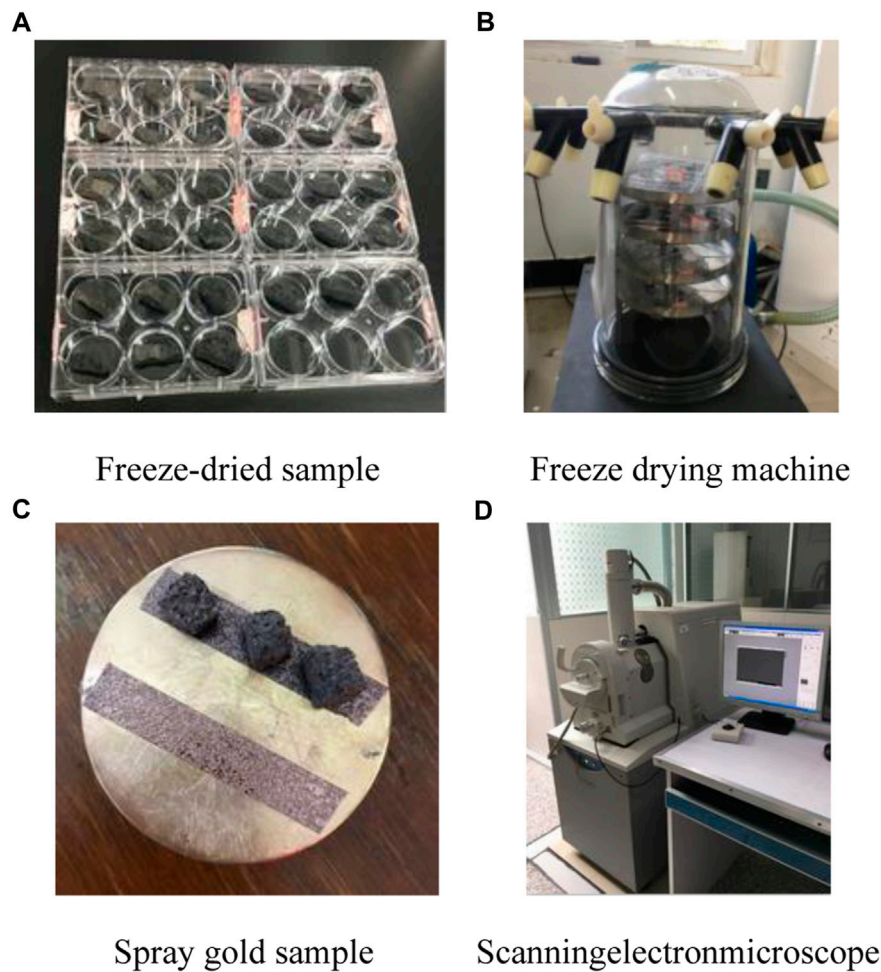
environment, the water loss was simulated by blowing the saturated sample surface with miniature electric fan. The mass of the unchanged CBS sample indicated that the dehumidification was finished. Then in the test, a humidifier was used to spray the surface of the sample, and the capillary action was used to make the bottom surface of the sample absorb water to simulate the process of the rain-moisture absorption. When the mass of the CBS sample did not increase, the water spraying was stopped, and the plastic

film was used to seal it for at least 24 h. The repeat cycles of DWC were also performed. Figure 1 shows the surface morphology of the large round sample of the CBS prepared by the sample pressing method after hygroscopicity, dehumidification, and three DWC.

### 2.2.2 Test plan and procedure

There were five DWC in this study, and the moisture content of the coal-measure soil samples in each DWC were 21%, 17%, 13%,



**FIGURE 2**

The matric suction test sample (A). Freeze-dried sample (B). Freeze drying machine (C). Spray gold sample (D). Scanning electron microscope.

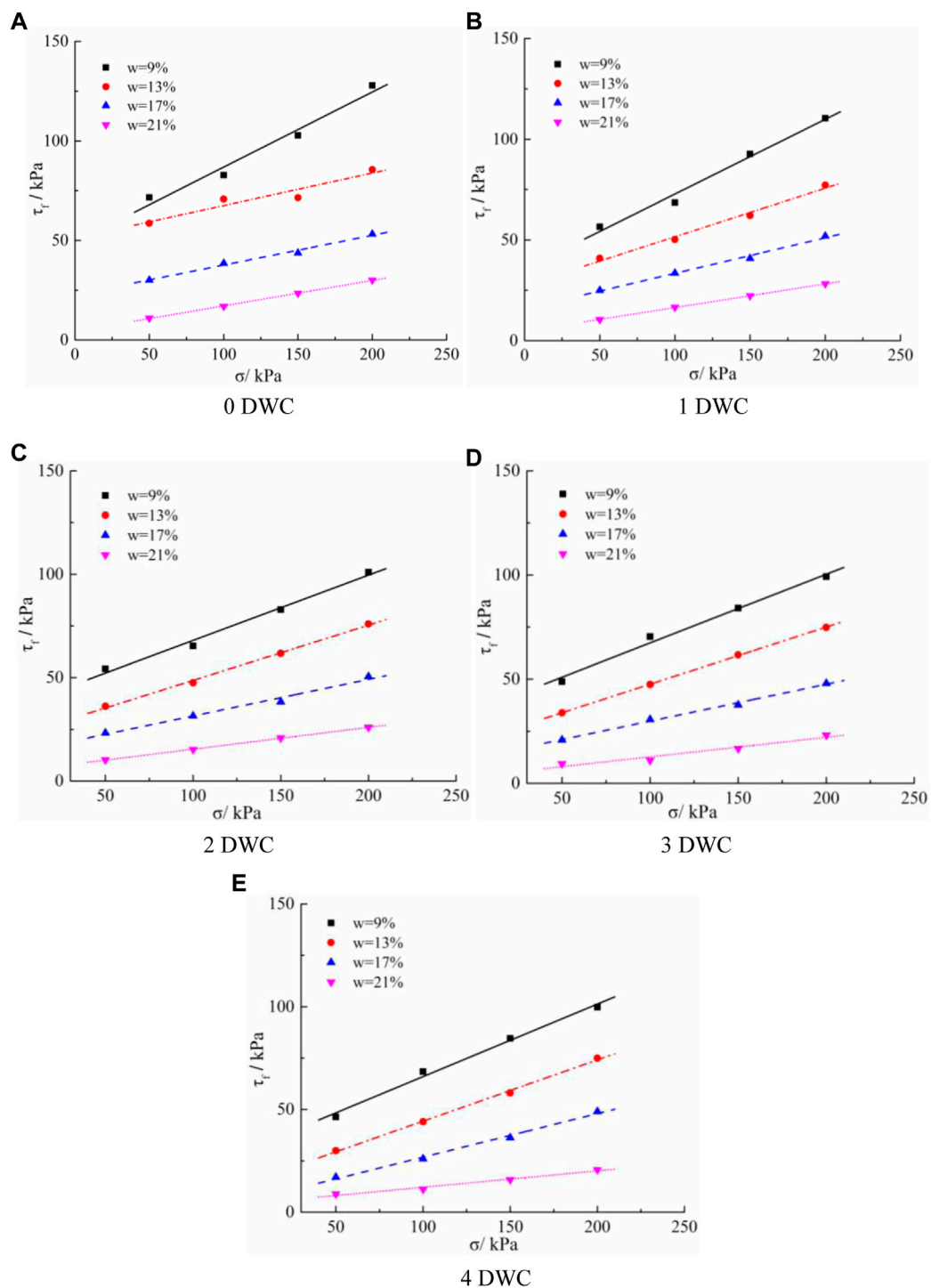
and 9%, with four samples in each group. A small ring knife was used to take samples from the large round samples, and the remaining intact samples were preserved with plastic film for the scanning electron microscope test. The samples were placed in the direct-shear instrument, and the overlaying loads of 50 kPa, 100 kPa, 150 kPa, and 200 kPa were applied until the deformation was stabilized, and the undrained, fast shear was carried out at the constant shear rate of 0.013 mm/s. After the direct shear test, the matrix suction value was measured by the filter-paper method, along the shear plane, which was approximately the average suction of the sample in the shear process. The soil samples retained for the scanning electron microscopy tests were gently broken into strips of soil about 15 mm and 10 mm wide, and then frozen in a  $-80^{\circ}\text{C}$  refrigerator for more than 36 h to make the pore water in the soil become amorphous ice without the volume expansion. The samples were then treated by the freeze-vacuum sublimation drying method, and the dried samples were sprayed with gold before the scanning electron microscope test. The soil samples and instruments were

tested in each step, as shown in Figure 2. Images with magnification of 2000 times were uniformly selected for this study.

## 3 Test results and analysis

### 3.1 The shear strength

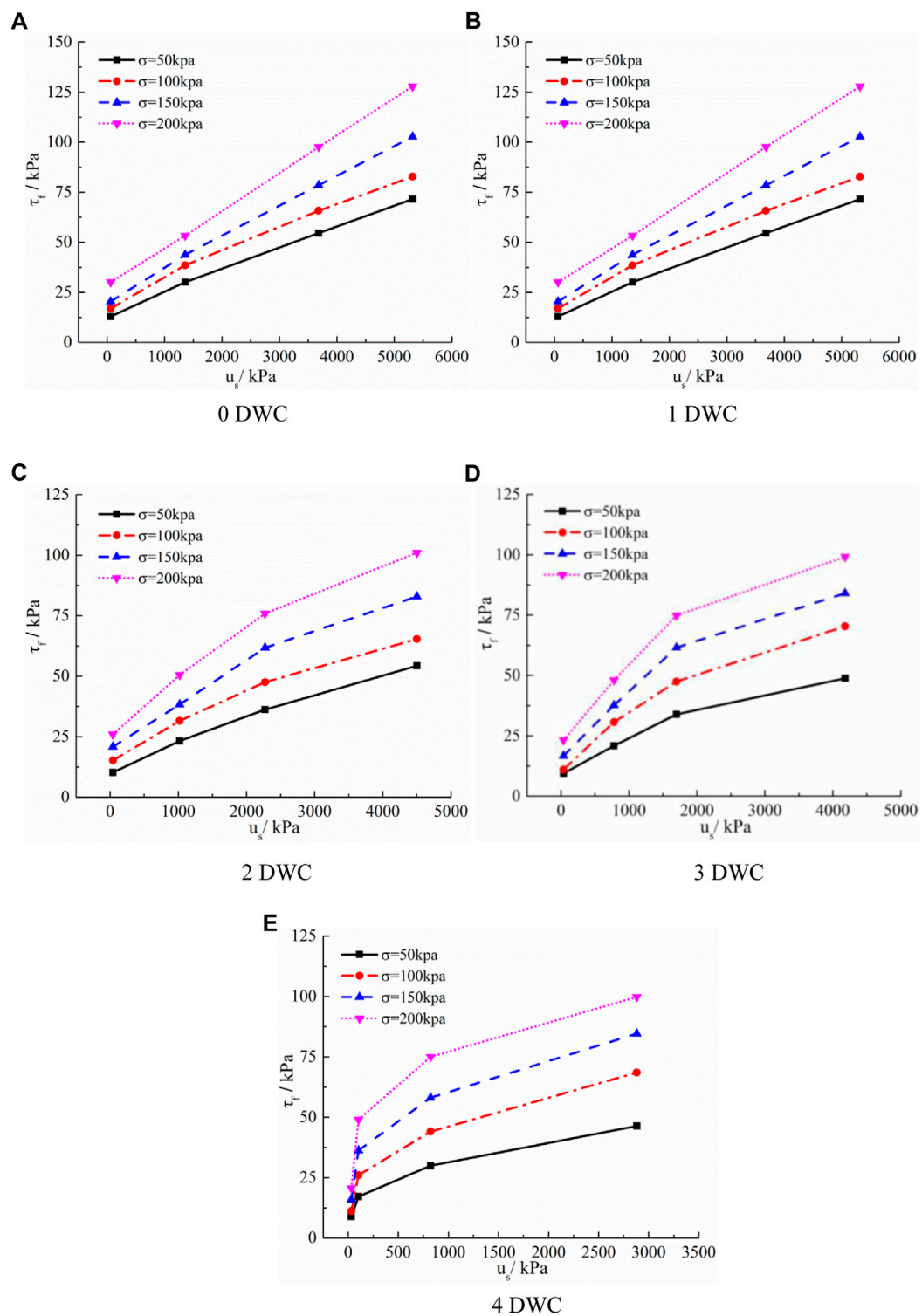
In this test, the unsaturated CBS samples were subjected to undrained fast shear, so the shear strength obtained was the total stress strength. Figure 3 shows that there is a linear relationship between the shear strength and the normal stress of the unsaturated CBS samples under the different wetting and drying cycles. In the same drying-wetting cycles, the shear strength of the unsaturated CBS samples decreases gradually with the increase of the moisture content. When the normal stress of the 0 drying-wetting cycle was 200 kPa, and the moisture content increased from 9% to 21%, the shear strength of the

**FIGURE 3**

Relationship between the shear strength and the normal stress of samples with the different water contents (A). 0 DWC (B). One DWC (C). Two DWC (D). Three DWC (E). Four DWC.

unsaturated CBS samples decreased from 128 kPa to 30 kPa, respectively, which reflects a reduction by 77%. In addition, the shear strength of the soil increased with the increase of the

normal stress under the same drying-wetting cycles and the same moisture content. For example, when the normal stress increased from 50 kPa to 200 kPa, the shear strength of the soil with 9%

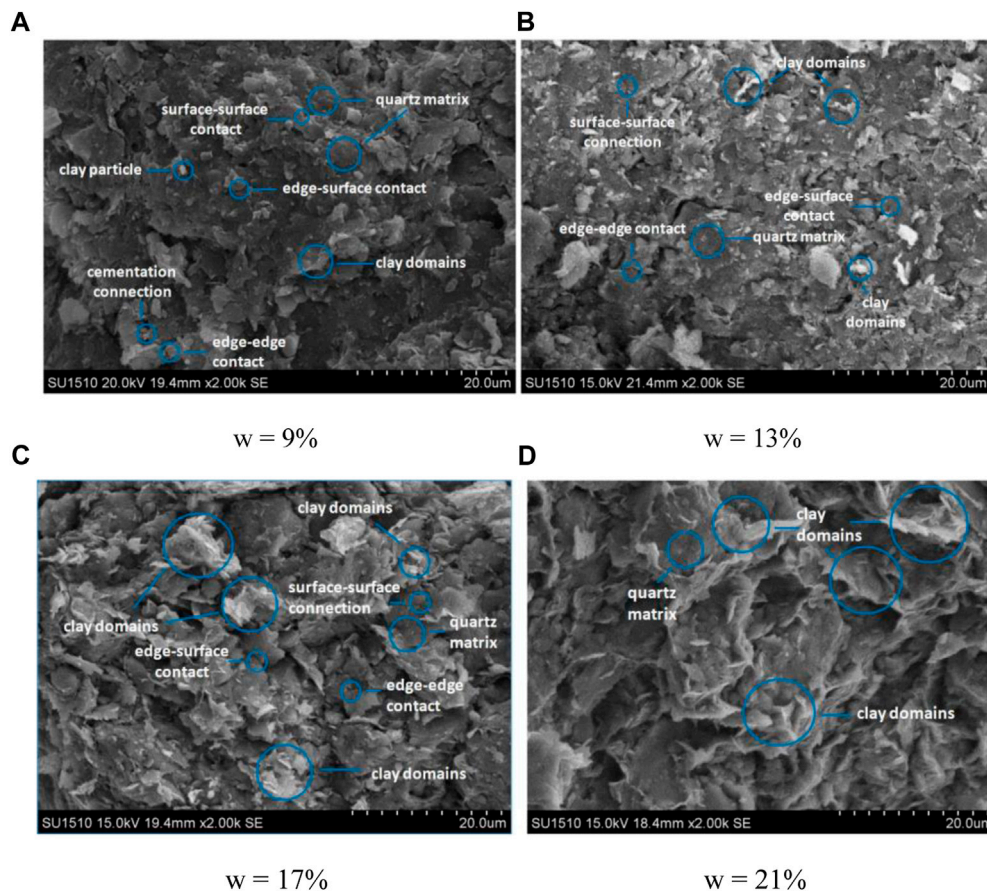
**FIGURE 4**

Relationship between the shear strength and the matric suction of the samples under the different DWC (A). 0 DWC (B). One DWC (C). Two DWC (D). Three DWC (E). Four DWC.



**TABLE 3** The total stress shear strength indices and the matrix suction of the samples under the different DWC.

The number of wet and dry cycles/ <i>n</i>	The moisture content /%	$c_{\text{total}}/(kPa)$	$\phi_{\text{total}}/(^{\circ})$	The matrix suction /( <i>kPa</i> )
1	9	30.7	19.4	2,880.6
	13	14.5	16.6	821.8
	17	5.6	12.0	103.3
	21	4.1	4.6	31.0

**FIGURE 5**

The 0 DWC microcosmic structures of the CBS with the different moisture contents. (A)  $w = 9\%$  (B)  $w = 13\%$  (C)  $w = 17\%$  (D)  $w = 21\%$ .

moisture content for 0 drying-wetting cycles increased from 72 kPa to 128 kPa. The shear strength of the unsaturated CBS samples, with the same moisture content, decreased with the increase of the number of the drying and wetting cycles. For example, for the unsaturated CBS samples with a moisture content of 9% undergoing 0–4 drying-wetting cycles, when the normal stress was 200 kPa, the shear strength was 128 kPa, 110 kPa, 101 kPa, 99 kPa, 100 kPa.

### 3.2 The influence of the matrix suction on the shear strength

Linchang et al. (MIAO et al., 2000) reformulated the expression for the shear strength of the unsaturated soil, into a strength formula similar to Mohr-Coulumb (Eq. 1, as follows):

$$\tau_f = c_{\text{total}}(u_s) + \sigma \tan \psi_{\text{total}}(u_s) \quad (1)$$

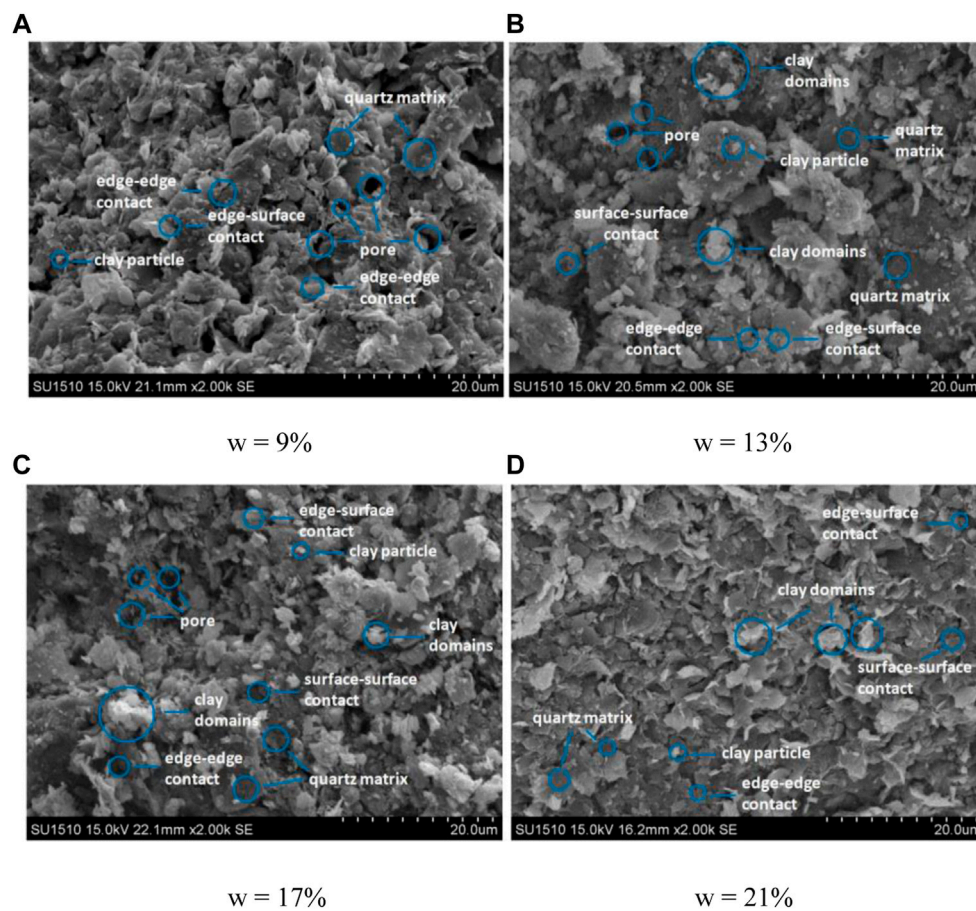


FIGURE 6

The three DWC microcosmic structures of the CBS with the different moisture contents. (A)  $w = 9\%$  (B)  $w = 13\%$  (C)  $w = 17\%$  (D)  $w = 21\%$ .

where,  $\tau_f$  is the total stress shear strength;  $c_{\text{total}}$  is total cohesion;  $\psi_{\text{total}}$  is the total internal friction angle;  $u_s$  is the matrix suction. The shear strength obtained in this test is the total stress shear strength, the cohesion of soil is the total cohesion, and the friction angle is the total internal friction angle. Figure 4 shows the relationship between the total stress shear strength and the matrix suction of the coal-measure soil samples under the different normal stress conditions and different DWC. Over the DWC conditions at the same time, the sample shear strength which increased with the increase of the matrix suction, including the zero DWC, when the increase of the matrix suction influence on the strength of soil increased more clearly, the approximate to linear, the influence of matrix suction on the soil strength increases gradually during one to four DWC. In addition, in the same DWC, the corresponding shear strength of the matrix suction was different when the matrix suction was the same, indicating that the contribution of the matrix suction to the shear strength was different when the stress environment was different. The shear strength increased

with the increase of the normal stress applied to the coal measure soil sample. Under the different drying and wetting cycles, the matrix suction and the shear strength of the soil samples with the same moisture content, under the same normal pressure, gradually decreased with the increase of the number of drying and wetting cycles, indicating that there was no definite one-to-one correspondence between the water content or the saturation and the matrix suction. The contribution of the matrix suction to shear strength was influenced by the change of the soil structure and the water content after the repeated DWC. And along with the rise of DWC times, the coal-soil structure changed in the matrix suction and the influence of the shear strength, than the effects of the moisture content, change was bigger, which makes it consistent with the conclusions as in a previous study (Fu et al., 2019). The changes, namely, in the DWC and the repeated wetting and drying cycles, affect the wetting shear strength of the soil more than the water content, which, in turn, is only caused due to the changes brought about in the structure of the soil.

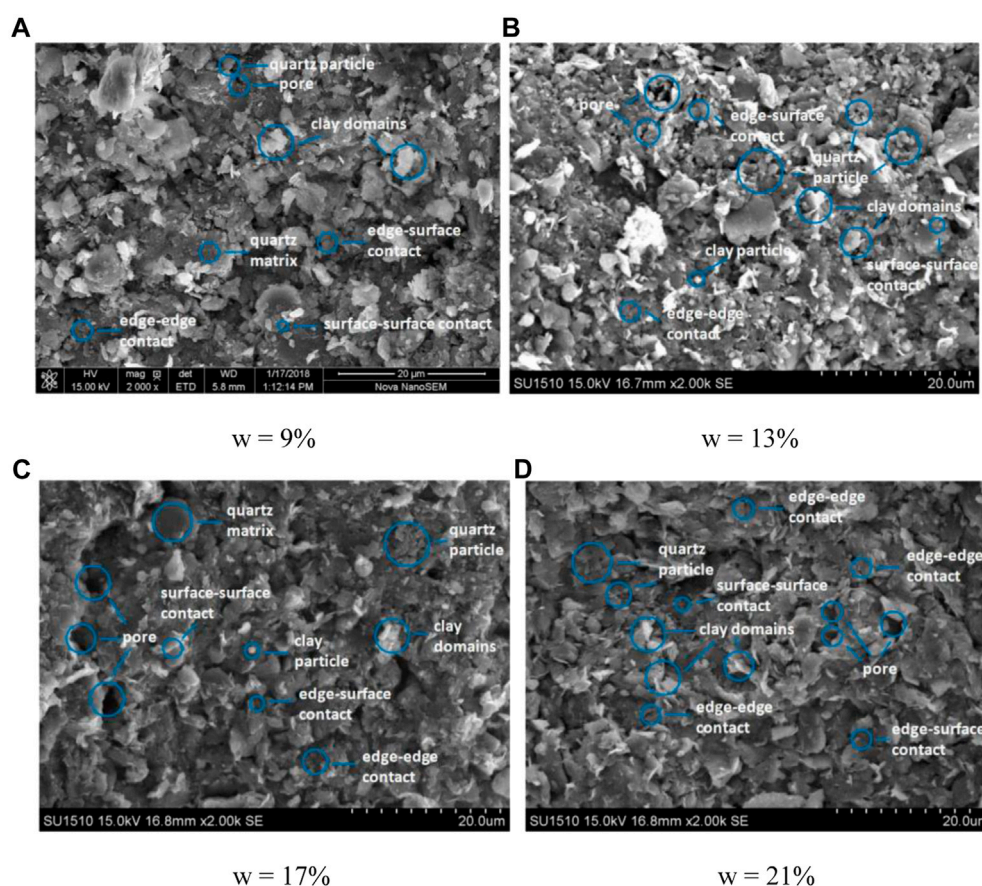


FIGURE 7

The four DWC microcosmic structures of the CBS with the different moisture contents. (A)  $w = 9\%$  (B)  $w = 13\%$  (C)  $w = 17\%$  (D)  $w = 21\%$ .

Table 3 shows the total stress shear strength index and matric suction of coal measure soil under different drying and wetting cycles. It can be seen that there is a linear relationship between the total stress shear strength index and the logarithm value of matric suction under each drying and wetting cycle. Therefore, the shear strength model of unsaturated coal measure soil under drying and wetting cycle is as follows (Eq. 2):

$$\tau_f = (a + b \lg u_s) + \sigma \tan(c + d \lg u_s) \quad (2)$$

where,  $a$ ,  $b$ ,  $c$ ,  $d$  are the fitting parameters of  $c_{\text{total}}$ ,  $\psi_{\text{total}}$  and matrix suction respectively.

### 3.3 Analysis of microstructure characteristics

The influence of the soil structure on the matric suction and shear strength of the CBS is greater than that of water content

under the DWC. The change in the soil structure at the macro level is reflected in the change of soil structure at micro level. The DWC with the zero moisture content 9% of the coal-soil sample in the scanning electron microscope (SEM) image (Figure 5) show that the quartz-particle plate-shaped structure form the soil sample matrix, the matrix surface has cracks, and form a particle size difference than that of the quartz grains, the kaolinite and the chlorite form the clay particles in the clay domain, which are in the form of surface to surface connection attached to the surface of the quartz substrate, or in the form of surface to surface connection in the quartz matrix in the cracks and in the quartz-particle joints. The lamellar quartz particles are mainly edge to edge, edge to surface, and surface to surface contact. The interface between the aggregates formed by the clay domain surface to surface contact and the quartz particles is mainly edge to surface, surface to surface contact. The connection is cemented by clay minerals and soluble salts, or the contact connection is formed by the direct contact between the basic



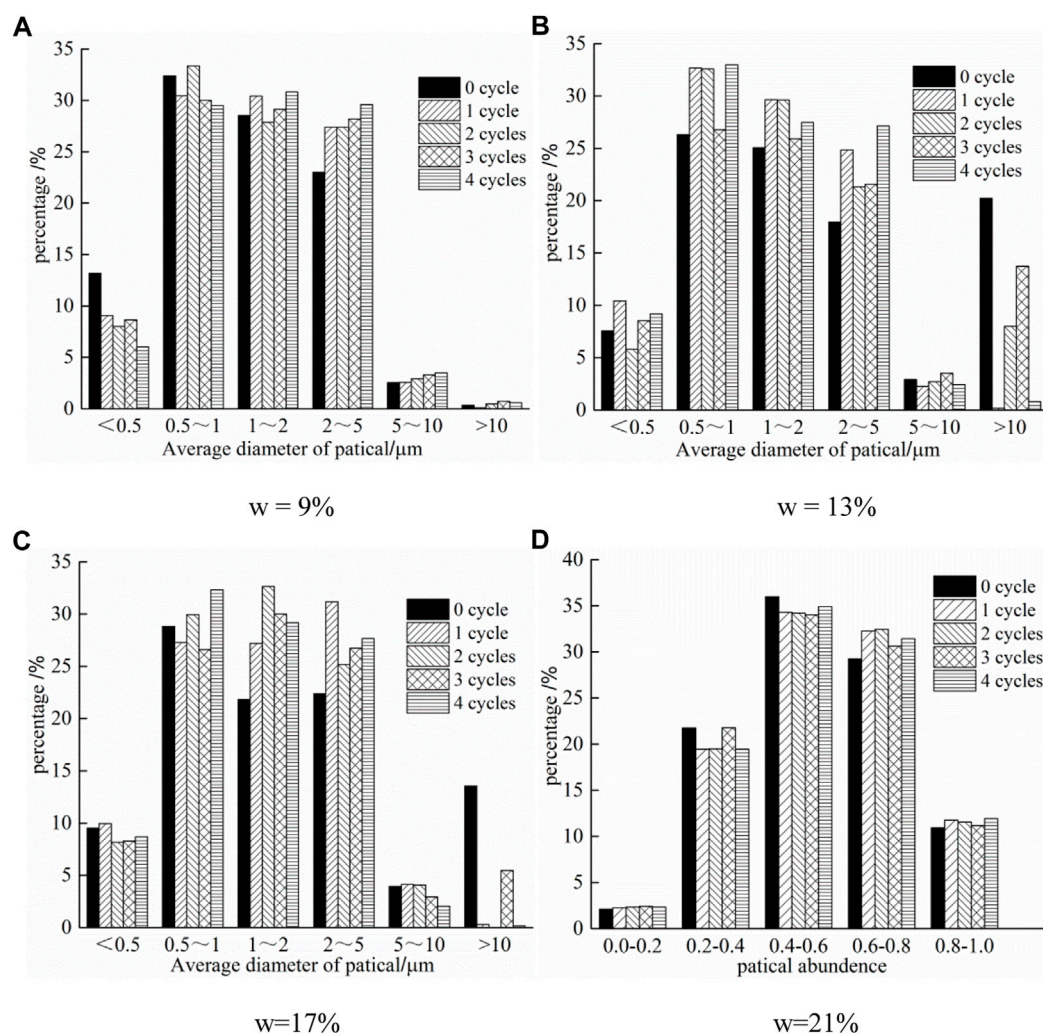


FIGURE 8

The variation of average diameter percentage of the soil particles under different DWC (A)  $w = 9\%$  (B)  $w = 13\%$  (C)  $w = 17\%$  (D)  $w = 21\%$ .

units. At this time, the cementation strength between the basic units is not high, and the particle connection is relatively loose. The SEM images (Figure 5) of the CBS samples with the moisture contents of 9%, 13%, 17%, and 21% during the 0 cycle of wetting and drying show that with the increase of the moisture content, the particle morphology, and the connection between the particles of the samples changed. The overlap formed by the facetoface contact of the clay expands with the increase of water content in the soil. Long, flat, clay domains with thick middle and thin edges are observed on the surface of the quartz matrix, between the cracks, and the quartz grains. This happened because the surface of the clay domain is generally negatively charged, while the connection between the surface-and-surface of the clay domain is mainly ion-electrostatic. As the water in the soil increased, the water film thickened, the diffusion-double electric layer thickened,

and the repulsion between the surface-and-surface predominated, resulting in the expansion of the polymer. With the increase of the water content, the cemented clay minerals, and the soluble salts at the junction of the basic unit body softened and dissolved. At this time, the cementation strength between the basic unit body decreased greatly, and the cohesion of the sample somewhat decreased. In the scanning electron microscope images of the samples with different moisture content in the first, second, third, and the fourth drying and wetting cycles (see Figures 6, 7 for the third and fourth dry and wet cycles), it can also be observed that the uneven volume expansion of the clay domain occurs with the increase of the water content, and the clay minerals and soluble salts that play the role of cementing connection softened and dissolve. Further, the basic unit body and the change of the pore volume caused the gas-liquid interface in the change of the

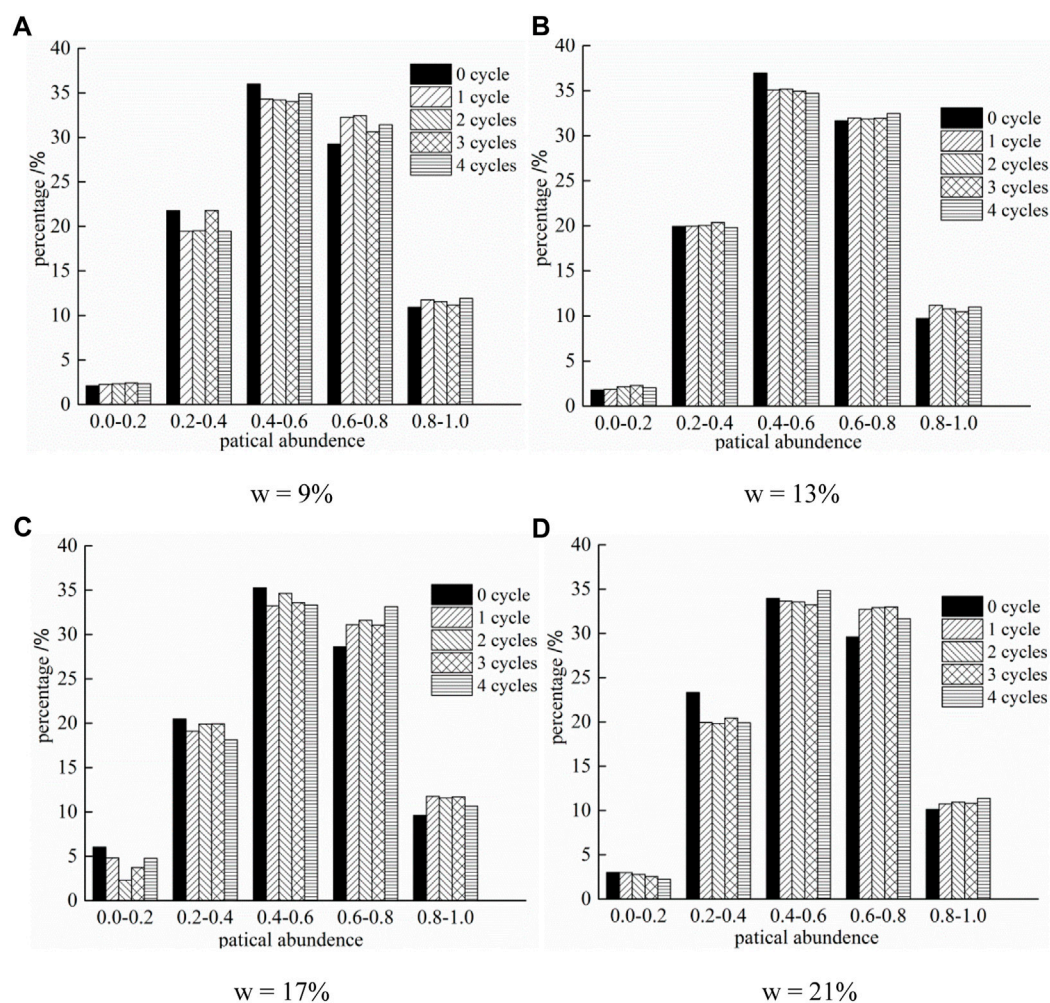


FIGURE 9

The variations of the soil particle abundances under the different DWC. (A)  $w = 9\%$  (B)  $w = 13\%$  (C)  $w = 17\%$  (D)  $w = 21\%$ .

meniscus water film, which caused the change of the matrix suction. It was at the same time during the drying-wetting circulation process, that the soil specimen macro performance of the shear strength of the unsaturated coal decreased gradually with the increase of the moisture content, and with the increase of the matrix suction, which can all be seen microscopically.

With the 0, 1, 2, and 3 times of the DWC, the moisture content is 9%, 4 times of the coal-soil sample in the electron microscope scanning figures. With the increase of the DWC, collapse happened in the coal soil sample, the cracks of the quartz substrate collapse happened, the magnitude of the large particle size decreased, and the clay minerals content in the DWC under the influence of particle size reduced. Further, the cementation strength between the basic units decreased, the particle connections became looser, and there were more pores. This is also the microscopic reason that the matric suction and the shear strength of the unsaturated CBS samples with the same

moisture contents, and under the same normal pressure gradually decreased with the increase of the number of DWC.

### 3.4 The influence of the drying and wetting cycles on the characteristic parameters of the microstructure

The image processing software IPP (Image-Pro Plus) was used to analyze and process the SEM images of the CBS with different water contents after 0–4 DWC, and the microstructure information was extracted to analyze the average particle average of the CBS after different DWC. The changes in the microstructural characteristic parameters, such as the diameter, particle abundance, and the particle orientation frequency were examined.



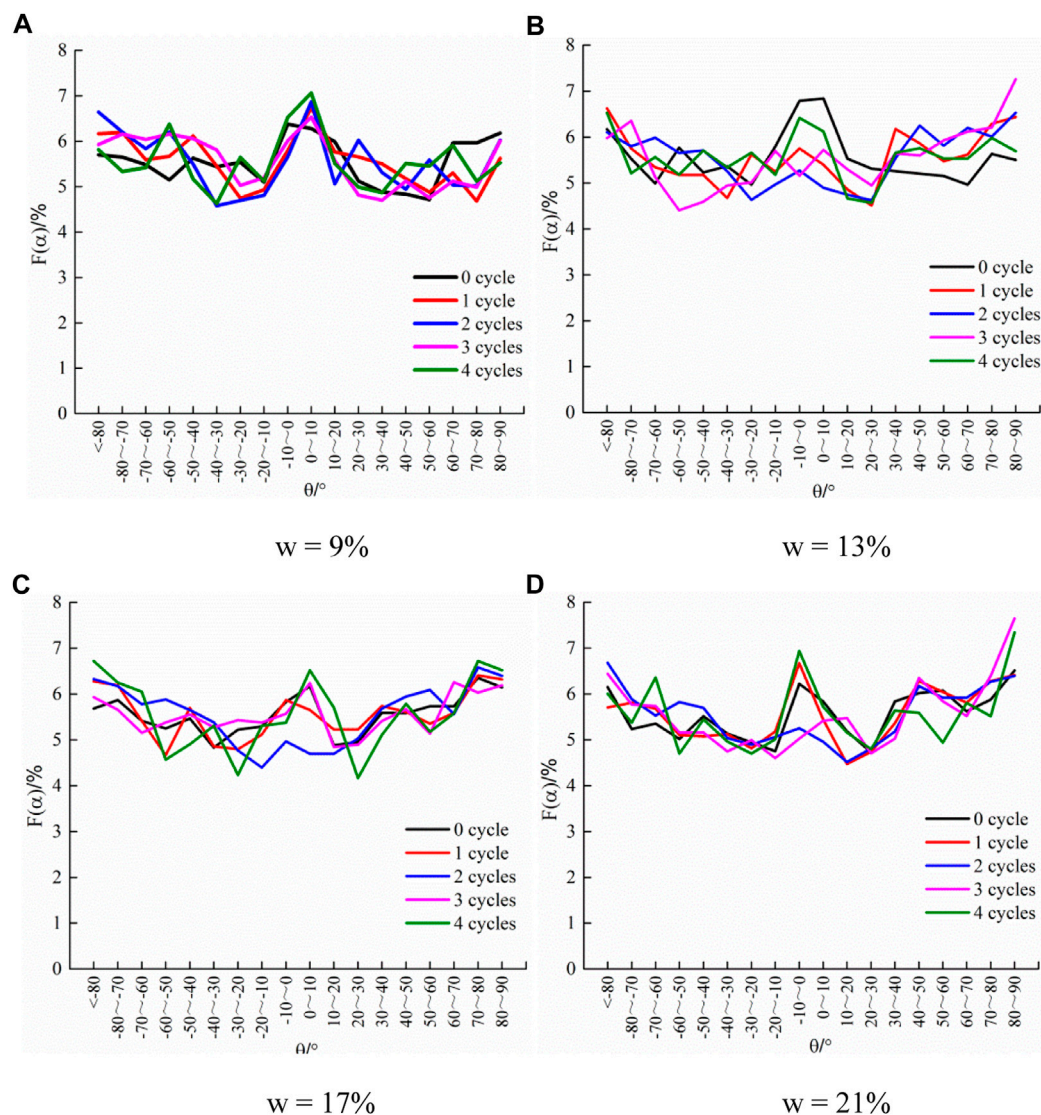


FIGURE 10

The directional frequency of the soil particles under the different DWC. (A)  $w = 9\%$  (B)  $w = 13\%$  (C)  $w = 17\%$  (D)  $w = 21\%$ .

### 3.4.1 The average particle diameter

The average particle diameter was used to represent the particle size. The diameter of the circle is equal to the particle area,  $S$ , and where  $D$  is the average diameter of the particle unit body. The calculation formula is (Eq. 3):

$$D = \sqrt{\frac{4S}{\pi}} \quad (3)$$

The average particle diameter was classified over a certain range, and the percentage of the number of particles in each interval of the soil samples with the different moisture contents under the

different DWC was counted, and the results are shown in Figure 8.

For the CBS with the moisture content of 9% and 13% under the different drying and wetting cycles, and with the increase of the drying and wetting cycles, the particle size was less than  $0.5 \mu\text{m}$  and between  $0.5 \sim 1 \mu\text{m}$ , respectively. The content of the particles between  $1 \sim 2 \mu\text{m}$  and  $2 \sim 5 \mu\text{m}$ , however, was in an increasing state, the content of particles between  $5 \sim 10 \mu\text{m}$  did not change much, and the content of particles larger than  $10 \mu\text{m}$  decreased. For the CBS with the moisture content of 17% and 21%, under the different DWC, and with the increase of DWC, the content of particles with the particle size of less than  $5 \mu\text{m}$  was in an

increasing state, and the content of particles with the particle size over five to 10  $\mu\text{m}$  did not change much. The content of the particles with the diameter greater than 10  $\mu\text{m}$  decreased. This was mainly related to the disintegration of the CBS samples after the multiple DWC. As the number of DWC increases, the content of particles with a particle size of less than five increased, the disintegration and the dispersion of the large particles reduced their contents. The contents of the small particles increased when the moisture content was lower, however, and the smaller particles adhered to the larger particles, which formed a larger particle, and which reduced the percentage of the smaller particles over this range. Yet, when the same is high, the number of the DWC and the high water content weakened the cementation between the basic units, the particle connection was weaker, and the particles were more loose, so that the content of particles in the range of less than 5  $\mu\text{m}$  particles increased.

### 3.4.2 Particle abundance

The ratio of the short axis to the long axis of the particle is the particle abundance  $C$ , and its calculation formula is (Eq. 4):

$$C = \sqrt{\frac{B}{L}} \quad (4)$$

where  $B$  is the short axis of the particle, and  $L$  is the long axis of the particle. The value of  $C$  ranges from 0 to 1, and the closer  $C$  is to 1, the more circular the particles tend to be on the plane, and the more elongated they tend to be.

Figure 9 shows the particle abundance of the reconstituted CBS with the different water contents under the different DWC. With the increase of the number of DWC, the abundance percentage of the particles with abundance less than 0.6 gradually decreased, while the abundance percentage of the particles with abundance greater than 0.6 showed an increasing trend, indicating that the effect of the DWC gradually changed the shape of the particles. From long strips to that of approaching the circle. Under the action of the multiple DWC, the quartz matrix of the CBS sample disintegrated, and the clay minerals dispersed and disintegrated, so that the size of large particles decreased more, the number of the small particles increased, and the particles with the complex shapes tended to be simple, which resulted in the soil erosion.

### 3.4.3 The particle orientation frequency

The particle orientation frequency is the frequency at which the angle between the long axis and the  $X$  axis of the particle is calculated into each equally divided orientation angle interval. The orientation angle interval is at  $\Delta\theta = 20^\circ$ , divide  $180^\circ$  into nine orientation angle intervals, and  $F_i(\alpha)$  represents the orientation

frequency of the particle unit in  $i$ th orientation angle interval (Eq. 5):

$$F_i(\alpha) = \frac{n_i}{n} \quad (5)$$

where  $n_i$  is the number of particles whose long axis direction falls in  $i$ th orientation angle interval, and  $n$  is the total number of particles.

It can be seen from Figure 10 that the orientation angle of the reshaped coal measures soil particle unit has a certain distribution in each interval, but it is mainly concentrated in the interval of  $-10^\circ$ – $10^\circ$ , that is, the particles are mainly arranged in the horizontal direction and have a certain orientation. With the increase of the number of the drying and wetting cycles, the orientation frequency of the particle units increased significantly in the range of  $-10^\circ$ – $10^\circ$ . The percentage content was the highest, while the variation law of orientation frequency in other orientation angle ranges is not apparent. The remolded CBS was prepared by the compaction method. During the compaction process, the soil particles were arranged in the horizontal direction under the action of the vertical force, that is, the angle between the main axis of the particle unit and the  $X$  axis was in the horizontal direction and  $-10^\circ$ – $10^\circ$  range. Under the action of the DWC, the disintegration and the dissolution of the coal-measure soil increased the number of the soil particles, decreased the average particle diameter, weakened the inter-particle cementation, and changed the contact mode between the particles, which affected the soil mass to a large extent. Cohesion, soil particles are more loose, and the arrangement of particle units tends to be simpler and orderly.

## 4 Conclusion

- 1) In 0 to four DWC, the clay domain expands unevenly with the increase of water content, the clay minerals and soluble salts that play the role of cementation and connection soften and dissolve, the cementation strength between basic units decreases greatly, the cohesion of the sample decreases, and the changes of water, basic units and pores cause the changes of meniscus water film at the gas-liquid interface, thus causing the changes of matrix suction. The shear strength of unsaturated CBS sample decreases with the increase of water content in the same DWC, and increases with the increase of matrix suction.
- 2) The CBS samples disintegrated under the action of DWC, and the quartz matrix in the cracks disintegrated to produce fragments and debris, and the particle size of large particles decreased more. The diameter was also reduced, the disintegrated and dispersed particles were scattered on the surface of the quartz matrix and around the other particles

and in the pores. The same was more loose and had more pores, so that the matrix suction and the shear strength of the unsaturated CBS samples with the same water content under the same normal pressure condition gradually decreased with the increase of the number of DWC.

- 3) Under the action of the DWC, the disintegration and dissolution of the CBS increased the number of the soil particles, reduced the average particle diameter, changed the particle shape, weakened the inter-particle cementation, and changed the contact mode between the particles. It is shown here that the content of the particles with the average diameter of less than 5  $\mu\text{m}$  increased, while the content of the particles larger than 10  $\mu\text{m}$  decreased. The shape of the particles gradually approached from a strip to a circle, while the particle orientation was slightly more apparent.

## Data availability statement

The original contributions presented in the study are included in the article/supplementary material, further inquiries can be directed to the corresponding author.

## Author contributions

YF: Investigation, Methodology, Writing—original draft; MZ: Formal analysis, Writing—review and editing, Supervision; JW: Resources, Writing—review and editing; All

authors have read and agreed to the published version of the manuscript.

## Funding

This work was supported by the National Natural Science Foundation of China (51568022), the Key Project of Jiangxi Natural Science Foundation (20202ACB202005), the National Natural Science Foundation of China (51869013), the Project of the Science and Technology of Jiangxi Education Department (GJJ210924), and the Key Laboratory of Hydraulic and Waterway Engineering of the Ministry of Education, Chongqing Jiaotong University (SLK2021B01).

## Conflict of interest

The authors declare that the research was conducted in the absence of any commercial or financial relationships that could be construed as a potential conflict of interest.

## Publisher's note

All claims expressed in this article are solely those of the authors and do not necessarily represent those of their affiliated organizations, or those of the publisher, the editors and the reviewers. Any product that may be evaluated in this article, or claim that may be made by its manufacturer, is not guaranteed or endorsed by the publisher.

## References

- Ahmed, A. (2015). Compressive strength and microstructure of softclay soil stabilized with recycled bassanite. *Appl. Clay Sci.* 104, 27–35. doi:10.1016/j.clay.2014.11.031
- Aldood, A., Bouasker, M., and Al-Mukhtar, M. (2014). Impact of wetting-drying cycles on the microstructure and mechanical properties of lime-stabilized gypseous soils. *Eng. Geol.* 174, 11–21. doi:10.1016/j.enggeo.2014.03.002
- Aqtash, Umama Al, and Bandini, Paola (2015). Prediction of unsaturated shear strength of an adobe soil from the soil–water characteristic curve. *Constr. Build. Mater.* 98, 892–899. doi:10.1016/j.conbuildmat.2015.07.188
- Bishop, A. W., and Blight, G. E. (1963). Some aspects of effective stress in saturated and partly saturated soils. *Géotechnique* 13 (3), 177–197. doi:10.1680/geot.1963.13.3.177
- Chou, Y. L., and Wang, L. J. (2021). Soil-water characteristic curve and permeability coefficient prediction model for unsaturated loess considering freeze-thaw and dry-wet. *Sci. Rep.* 11, 1–11. doi:10.1038/s41598-021-05832-0
- Cui, S. L., and Si, D. D. (2014). Experimental research of swelling behaviors with initial water content and matric suction of bentonite-sand mixtures. *Geosystem Eng.* 17 (6), 317–324. doi:10.1080/12269328.2014.994788
- Fredlund, D. G., Morgenstern, N. R., and Widger, R. A. (1978). The shear strength of unsaturated soils. *Can. Geotech. J.* 15 (3), 313–321. doi:10.1139/t78-029
- Fu, H. Y., Liu, J., Zeng, L., Bian, H. B., and Shi, Z. N. (2019). Deformation and strength tests of pre-disintegrating carbonaceous mudstone under loading and soaking condition. *Rock Soil Mech.* 40 (4), 1273–1280. doi:10.16285/j.rsm.2017.2307
- Han, B., Lu, G. Y., Zhu, Z. Q., Guo, Y. J., and Zhao, Y. W. (2019). Microstructure features of powdery coal-bearing soil based on the digital image measurement Technology and fractal theory. *Geotech. Geol. Eng. (Dordr.)* 37 (3), 1357–1371. doi:10.1007/s10706-018-0691-8
- Hassan Marwan Adil and Mohamad Ismail Mohd Ashraf (2018). Effect of soil types on the development of matric suction and volumetric water content for dike embankment during overtopping tests. *CivileJournal*. 4 (3), 668. doi:10.28991/cej-0309124
- Huang, Gang, and Zheng, Mingxin (2021). Strength of vegetated coal-bearing soil under dry-wet cycles: An experimental study. *Int. J. Corros.* 2021,6657160–13. doi:10.1155/2021/6657160
- Jiang, Mingjing, Zhang, F., Hu, H., Cui, Y., and Peng, J. (2014). Structural characterization of natural loess and remolded loess under triaxial tests. *Eng. Geol.* 181, 249–260. doi:10.1016/j.enggeo.2014.07.021
- Lin, Botao, and Amy, B. (2015). Shear strength of shale weathered expansive soils along swell-shrink paths: Analysis based on microscopic properties. *Environ. Earth Sci.* 74 (9), 6887–6899. doi:10.1007/s12665-015-4691-1
- Ma, Shao-kun, Huang, M. s., Hu, P., and Yang, C. (2013). Soil-water characteristics and shear strength in constant water content triaxial tests on Yunnan red clay. *J. Cent. South Univ.* 20 (5), 1412–1419. doi:10.1007/s11771-013-1629-1
- Miao, L. C., Yin, Z. Z., and Liu, S. Y. (2000). Research of the strength characteristics of UnsaturatedExpansive soils based on general tri-axial test. *J. Southeast University Nat. Sci. Ed.* 30 (1), 121–125. in Chinese.

- Nowamooz, H., Jahangir, E., Masrouri, F., and Tisot, J. P. (2016). Effective stress in swelling soils during wetting drying cycles. *Eng. Geol.* 210, 33–44. doi:10.1016/j.enggeo.2016.05.021
- Qian, Zhai, Rahardjo, H., Satyanaga, A., Dai, G. L., and Du, Y. J. (2020). Effect of the uncertainty in soil-water characteristic curve on the estimated shear strength of unsaturated soil. *J. Zhejiang Univ. Sci. A* 21 (8), 317–330. doi:10.1631/jzus.a1900589
- Sun, W.-J., and Cui, Y.-J. (2018). Investigating the microstructure changes for silty soil during drying. *Géotechnique* 68 (4), 370–373. doi:10.1680/jgeot.16.p.165
- Wang, Yongwei, Li, K., Li, J., and Tang, S. (2021). Influence of soil particle size on the engineering properties and microstructure of a red clay. *Appl. Sci.* 11 (22), 10887. doi:10.3390/app112210887
- Xiao, Xie, Li, P., Hou, X., Li, T., and Zhang, G. (2020). Microstructure of compacted loess and its influence on the soil-water characteristic curve. *Adv. Mater. Sci. Eng.* 2020, 1–12. doi:10.1155/2020/3402607
- Xiong, C. R., Liu, B. C., and Zhang, J. S. (2005). Relation of matric suction with moisture state and density state of remolded cohesive soil. *Chin. J. Rock Mech. Eng.* 24 (2), 321–327. in Chinese.
- Yang, Jikai, and Zheng, Mingxin (2018). Effects of density and drying-wetting cycle on soil water characteristic curve of coal soil. *J. East China Jiaot. Univ.* 35 (3), 91–96. in Chinese.
- Zhang, Changguang, Zhao, Junhai, and Zhu, qian (2012). Classification and summary of shear strength for unsaturated soils. *J. Archit. Civ. Eng.* 29 (2), 74–82. in Chinese.
- Zhang, Hong, Zhang, B., Wu, C., and Chen, K. (2021). Macro and micro analysis on coal-bearing soil slopes instability based on CFD-DEM coupling method. *PLoS one* 16 (9), e0257362. doi:10.1371/journal.pone.0257362
- Zhao, X. L., Zhang, C., Luan, Y., and Xiao, Z. (2018). Stereological analyses of microstructure of granular soils using the numerical method. *Bull. Eng. Geol. Environ.* 77 (3), 1103–1115. doi:10.1007/s10064-017-1086-4
- Zhou, Cuiying, Cui, G., Liang, W., Liu, Z., and Zhang, L. (2021). A coupled macroscopic and mesoscopic creep model of soft marine soil using a directional probability entropy approach. *J. Mar. Sci. Eng.* 9 (2), 224. doi:10.3390/jmse9020224
- Zuo, C. Q., Liu, D. G., Ding, S. L., and Chen, J. P. (2016). Micro-characteristics of strength reduction of tuff residual soil with different moisture. *KSCE J. Civ. Eng.* 20 (2), 639–646. doi:10.1007/s12205-015-0408-y





## OPEN ACCESS

## EDITED BY

Lijie Guo,  
Beijing Mining and Metallurgy  
Technology Group Co., Ltd., China

## REVIEWED BY

Xiao Wang,  
Southeast University, China  
Lixiang Xie,  
China University of Mining and  
Technology, China

## \*CORRESPONDENCE

Shuyin Ma,  
402362325@qq.com

## SPECIALTY SECTION

This article was submitted to  
Geohazards and Georisks,  
a section of the journal  
Frontiers in Earth Science

RECEIVED 23 September 2022

ACCEPTED 01 November 2022

PUBLISHED 13 January 2023

## CITATION

Ma S, Xue S and Pan C (2023), Numerical  
simulations of fatigue failure processes  
in intermittent jointed rock masses  
under the action of repeated  
stress waves.  
*Front. Earth Sci.* 10:1051639.  
doi: 10.3389/feart.2022.1051639

## COPYRIGHT

© 2023 Ma, Xue and Pan. This is an  
open-access article distributed under  
the terms of the [Creative Commons  
Attribution License \(CC BY\)](https://creativecommons.org/licenses/by/4.0/). The use,  
distribution or reproduction in other  
forums is permitted, provided the  
original author(s) and the copyright  
owner(s) are credited and that the  
original publication in this journal is  
cited, in accordance with accepted  
academic practice. No use, distribution  
or reproduction is permitted which does  
not comply with these terms.

# Numerical simulations of fatigue failure processes in intermittent jointed rock masses under the action of repeated stress waves

Shuyin Ma<sup>1,2,3,4\*</sup>, Sheng Xue<sup>1,5</sup> and Cheng Pan<sup>6</sup>

<sup>1</sup>School of Safety Science and Engineering, Anhui University of Science and Technology, Huainan, Anhui, China, <sup>2</sup>State Key Laboratory of Mining Response and Disaster Prevention and Control in Deep Coal Mines, Anhui University of Science and Technology, Huainan, Anhui, China, <sup>3</sup>China Coal Technology Engineering Group Chongqing Research Institute, Chongqing, China, <sup>4</sup>State Key Laboratory of the Gas Disaster Detecting, Preventing and Emergency Controlling, Chongqing, China, <sup>5</sup>Joint National-Local Engineering Research Centre for Safe and Precise Coal Mining, Anhui University of Science and Technology, Huainan, Anhui, China, <sup>6</sup>School of Civil Engineering and Architecture, Anhui University of Science and Technology, Huainan, Anhui, China

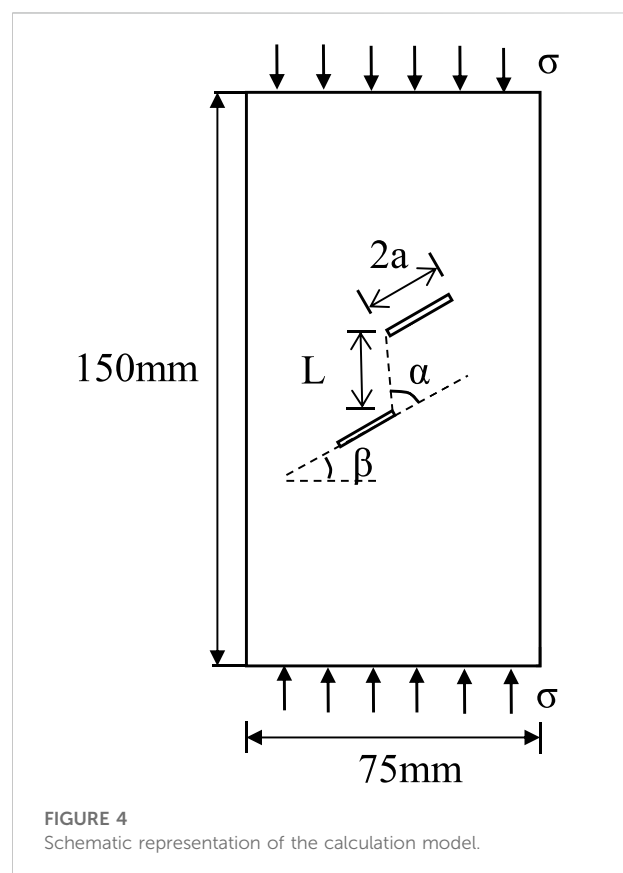
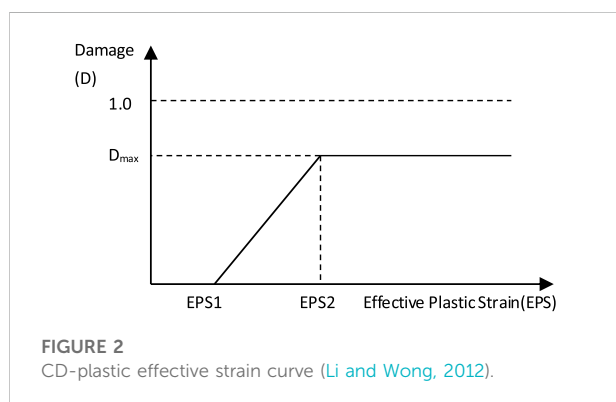
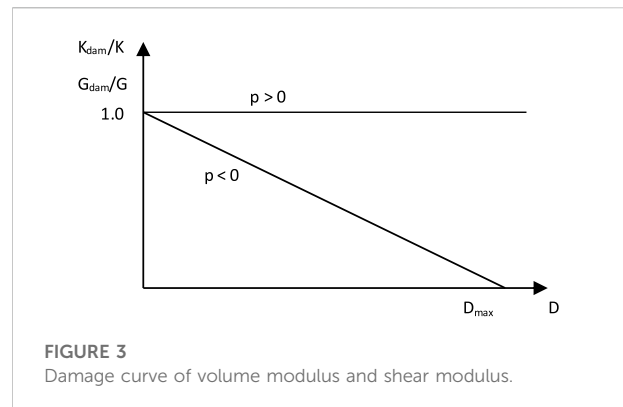
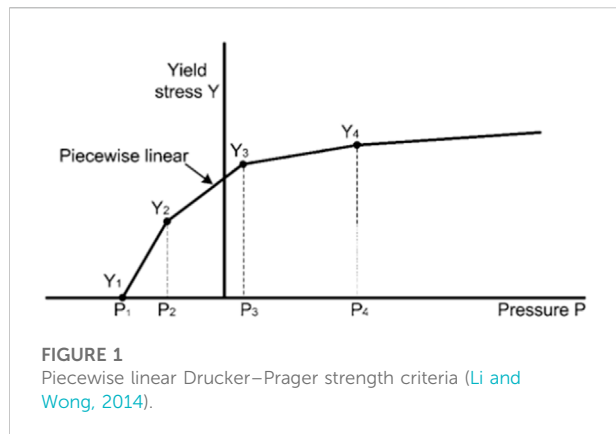
To study the fatigue failure of an intermittent jointed rock mass under repeated stress waves, numerical models of jointed rock masses with different joint angles were created using Autodyne software, and crack propagation behavior was simulated using the Drucker–Prager strength model and cumulative damage failure criteria. In this numerical simulation, the influence of stress wave amplitude and the mode of disturbance on fatigue failure of the rock mass were analyzed. The simulation results showed a significant difference between the failure process of jointed rock masses subjected to repeated stress waves and those exposed to a single stress wave, including crack initiation locations, propagation paths, and rock mass failure patterns. With increasing angles of inclination, the fatigue life of the rock mass first decreased and then increased under repeated stress waves. As the joint inclination angle,  $\beta$ , increased from 20° to 50°, it had a significant influence on the fatigue life of the rock mass, which decreased rapidly with increases in  $\beta$ . The variation in the disturbance form (the change in amplitude of the stress waves from small to large, or from large to small) did not affect the final macro failure pattern of the rock mass; but the extent of damage to the rock mass was affected.

## KEYWORDS

rock mechanics, stress wave, intermittent jointed rock mass, fatigue failure, numerical simulation

## 1 Introduction

Different sizes of fractures, joints, beddings, and other discontinuous surfaces exist universally in natural rock masses. These discontinuous surfaces influence the mechanical properties and control the stability of a rock mass. Many geotechnical engineering tests demonstrated that the propagation and connection of joint fissures in a rock mass under an external load resulted in the instability and failure of geotechnical engineering (Tang



et al., 2022). Many scholars have discussed the initiation, propagation, and evolution of cracks into macro-cracks through physical tests (Lin et al., 2000; Sagong and Bobet, 2002; Prudencio and van Sint Jan, 2007; Yang et al., 2019; Haeri et al., 2020; Wang M et al., 2020) and numerical modeling (Vergara et al., 2016; Wang and Tian, 2018; Wang X et al., 2020; Li et al., 2022; Yuan et al., 2022; Zou et al., 2022). Using physical tests, Lin et al. (2000) determined the influences of joint distribution, joint length, and rock bridge length in a jointed rock mass on connection modes, failure modes, and peak strength. They found that the number of joints, joint length, rock bridge length, and side pressure could significantly influence the connection modes, failure modes, and peak strength of a jointed rock mass. Sagong and Bobet (2002) conducted a comparative study on the connection modes of multi-fracture rock mass specimens and double-fracture rock mass specimens under uniaxial compression conditions. They discovered that the failure mode of a multi-fracture rock mass was similar to that of a double-fracture rock mass and identified nine double-fracture connection modes. Prudencio and Van Sint Jan (2007) carried out a biaxial compression test on discontinuous joint specimens formulated with cement mortar and summarized four failure

modes of discontinuous jointed rock masses, namely, plane failure, block rotational failure, stepwise failure, and mixed failure. Haeri et al. (2020) conducted uniaxial compression tests to investigate the effect of joint number and angle on both compression behavior and joint tensile strength.

Recently, numerical software, such as UDEC (Pan et al., 2021; Li et al., 2022), PFC (Wang X et al., 2020; Yuan et al., 2022), and Autodyn (Li and Wong 2014; Zhao et al., 2020; Zou et al., 2022), were extensively compared as methods to simulate the crack

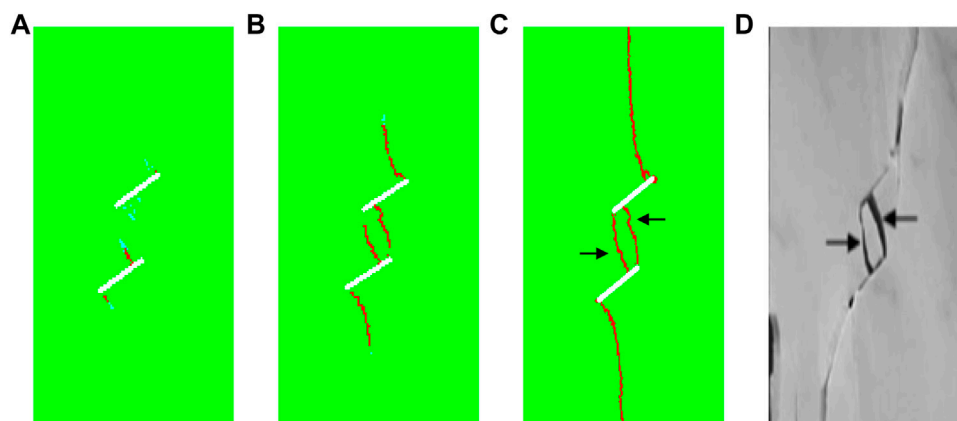


**FIGURE 5**  
Comparison between numerical simulation and experimental results.

propagation process. Compared with physical tests, numerical simulations can more easily obtain the mechanical information of crack initiation and propagation. For example, [Li and Wong \(2014\)](#) found 11 connection modes of double-fracture rock masses under uniaxial loading by using the nonlinear dynamic software, Autodyn. These connection modes were divided into tensile, shear, and mixed tensile-shear connection modes according to the mechanism of crack formation. Studies by [Zhao et al. \(2020\)](#) and [Zou et al. \(2022\)](#) also demonstrated that the combined use of the Drucker–Prager (DP) strength model and cumulative damage (CD) failure criteria could describe the macroscopic inelastic behavior of geotechnical materials and the evolution of CD-induced macro-cracks. It is worth noting that most existing research focused on the failure behavior of a jointed rock mass under static loading or single-impact loading.

As the literature shows, drilling and blasting are still the main methods of tunnel excavation ([Pan et al., 2022](#)). However, the cyclical footage of 3–5 m is often used during tunneling, indicating that the surrounding rocks within this range were also disturbed by multiple blasting excavations ([Ji et al., 2021a, b](#)). Although a single disturbance is insufficient to cause the instability of a rock mass, multiple disturbances can cause progressive failure of discontinuous jointed rock masses through the cumulative effects of repeated damage. These disturbances can lower bearing capacity and stability, thereby accelerating failure. Therefore, studying the fatigue failure process of discontinuous jointed rock masses under the action of repeated stress waves has practical significance for the long-term qualitative analysis of rock mass engineering. Based on this information, the fatigue failure process of a discontinuous jointed rock mass with different incidence angles under the action of repeated stress waves was investigated by using the DPCD model and Autodyn, and compared with that occurring under single

impact loading. The influence of stress wave amplitudes and disturbance mode on the fatigue failure process of a discontinuous jointed rock mass was discussed.

## 2 Numerical methodology and verification

### 2.1 Rock material model

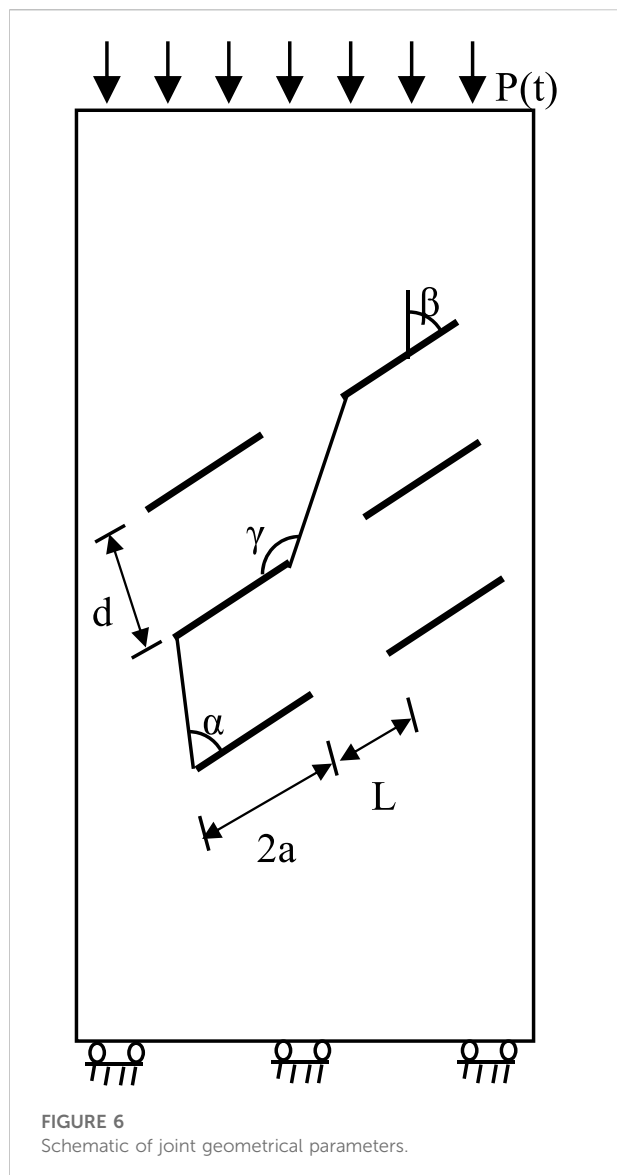
The material model in Autodyn is mainly composed of state equation, strength model, and failure criteria.

The state equation belongs to a problem of small deformation dynamics because the stress wave amplitude in the simulation is small. Therefore, the state equation of the jointed rock mass can be described by the linear state equation ([Zhao et al., 2020](#)):

$$p = k \left( \frac{\rho}{\rho_0} - 1 \right), \quad (1)$$

where  $p$  is the pressure,  $k$  is the bulk modulus,  $\rho$  is the current density of materials, and  $\rho_0$  is the density of materials at the initial moment. The parameters of the state equation of rock mass involved in the simulation ([Li and Wong 2014](#)) include initial density  $\rho_0 = 2.44 \text{ g/cm}^3$  and bulk modulus  $k = 27 \text{ GPa}$ .

A piecewise linear DP strength model was selected as the rock strength model ([Li and Wong 2014](#)). This model is applicable to granular materials, such as soils, rocks, and concretes and can accurately describe the cracking phenomena of materials. By defining the pressure–yield strength points, it was shown that the yield strength increased with hydrostatic pressure after giving consideration to compression ([Figure 1](#)). Using a scanning electron microscope, [Wong and Einstein \(2009a\)](#) observed that macro-cracks produced in marble under compression conditions were formed by the initiation, propagation, and



connection of micro-cracks. Therefore, the initiation of macro-cracks is a cumulative process rather than the result of a single unexpected event. Thus, the CD failure criteria were chosen as the failure criteria in the numerical simulation. CD failure criteria pertain to the reduction in strength during the progressive failure process of materials by defining the damage factor,  $D$ , which is related to the deformation of materials. Its value is zero when the effective plastic strain (EPS) is smaller than a certain value (EPS1). When EPS is higher than EPS1,  $D$  increases linearly with the strains to a maximum  $D_{\max}$  ( $<1$ ). At this moment, a corresponding effective plastic strain (EPS2) exists (Figure 2).  $D$  is expressed as (Li and Wong 2012)

$$D = D_{\max} \left( \frac{\text{EPS} - \text{EPS1}}{\text{EPS2} - \text{EPS1}} \right). \quad (2)$$

TABLE 1 Parameters for joint layout.

No.	2a/mm	L/mm	d/mm	k/%	$\beta/(^\circ)$	$\alpha/(^\circ)$	$\gamma/(^\circ)$
A	20	20	20	50	20	90	133
B	20	20	20	50	30	90	133
C	20	20	20	50	40	90	133
D	20	20	20	50	50	90	133
E	20	20	20	50	60	90	133
F	20	20	20	50	70	90	133
G	20	20	20	50	80	90	133
H	20	20	20	50	90	90	133

After applying the calculation, the current value of  $D$  was used to modify the bulk modulus ( $k$ ), shear modulus ( $G$ ), and yield strength ( $Y$ ) of materials. According to Li and Wong (2012), materials still retain some residual strength in the compression process when they reach maximum damage, but they have no residual strength in the tensile process. Hence, the reduction in  $Y$  involves two conditions. When the hydrostatic pressure is positive,

$$Y_{\text{dam}} = Y(1 - D). \quad (3)$$

When the hydrostatic pressure is negative,

$$Y_{\text{dam}} = Y \left( 1 - \frac{D}{D_{\max}} \right). \quad (4)$$

The bulk modulus and shear modulus are not influenced by compression. However, under tensile stress, the bulk modulus and shear modulus decrease to zero at the rate of  $(1 - D/D_{\max})$  when  $D$  decreases to  $D_{\max}$  (Figure 3). The CD failure criteria parameters involved in the simulation were EPS1 =  $10^{-4}$ , EPS2 =  $10^{-3}$ , and  $D_{\max} = 0.6$  (Li and Wong 2014).

## 2.2 Model validity verification

The feasibility of the numerical simulation was verified according to the compression test results of uniaxial jointed rock masses (Wong and Einstein 2009b). The 150 mm  $\times$  75 mm two-dimensional plane model was applied in the numerical simulation, and the calculation model is shown in Figure 4. The model contains two parallel open joints. The lengths of the joints and the rock bridge were  $2a = 12.7$  mm and  $L = 12.7$  mm, respectively. The angles between the rock bridge and the joint were  $\alpha = 30^\circ$  and  $\beta = 90^\circ$ , respectively. During the simulation, loads were applied at the top and bottom of the specimens. The loading rate was controlled at 12.5 MPa/ms.

The numerical simulation results of the joint connection are shown in Figures 5A–C. The initiation points, propagation paths, and connection modes of cracks were easily observed,

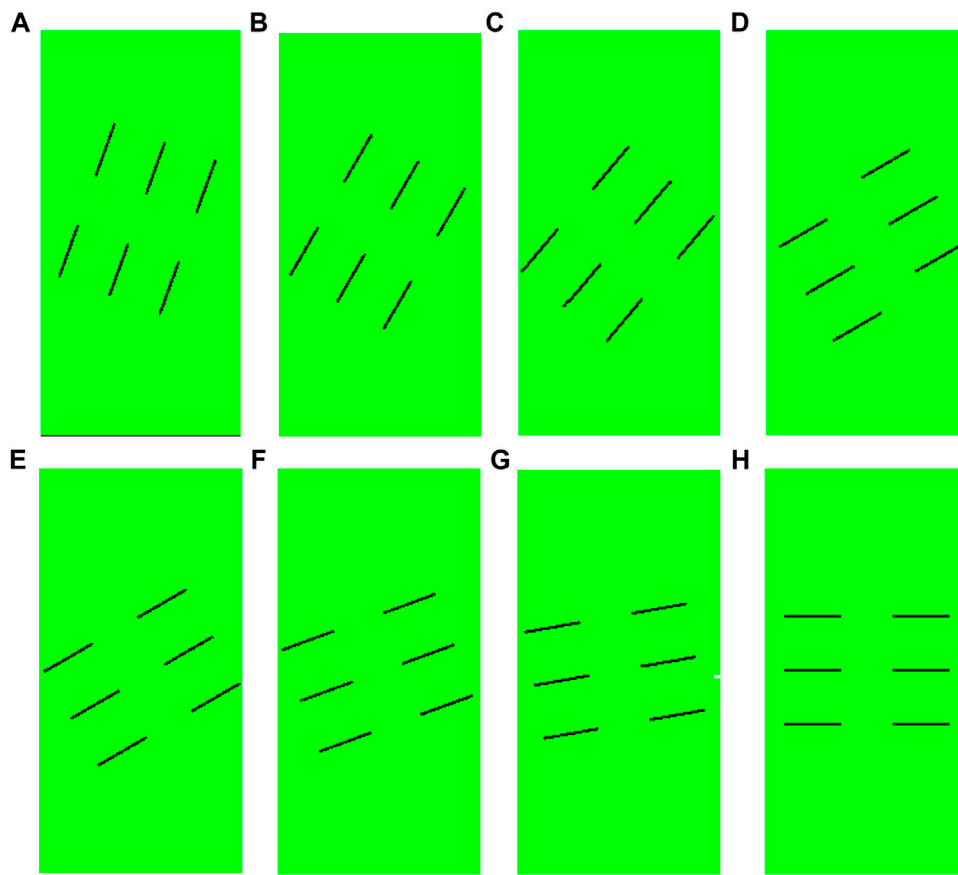


**FIGURE 7**  
Joint geometry layout of the numerical model.

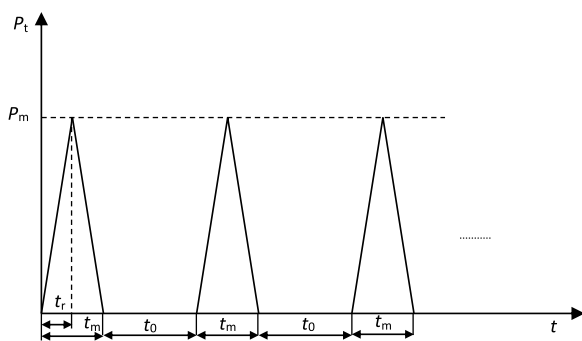


**FIGURE 8**  
Mode of action of repeated stress waves.

and the simulation results agreed well with the crack connection modes (Figure 5D), which are summarized according to test results by Wong and Einstein (2009b). On

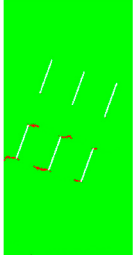
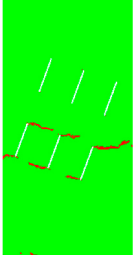
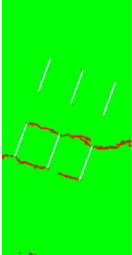
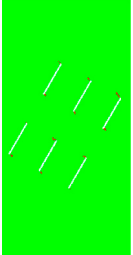
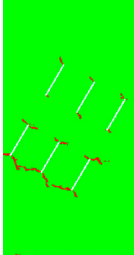
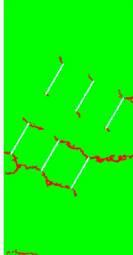
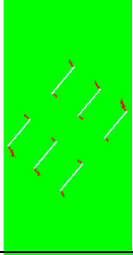
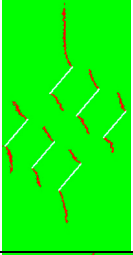
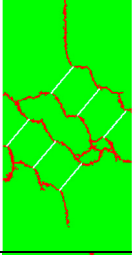
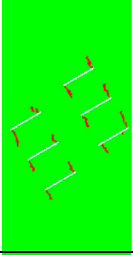
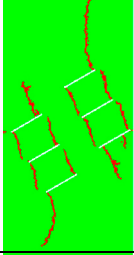
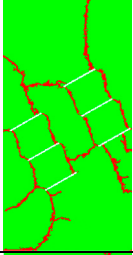
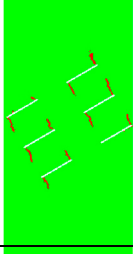
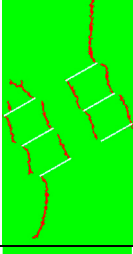
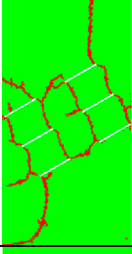
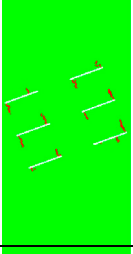
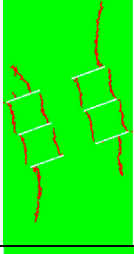
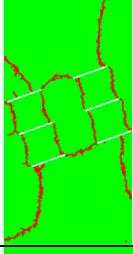
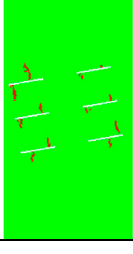
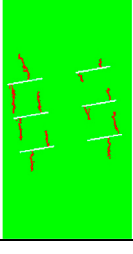
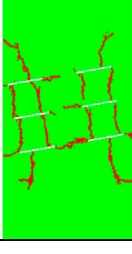
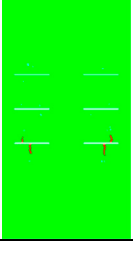
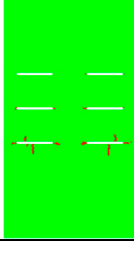
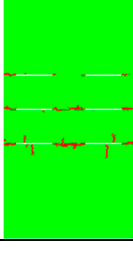
this basis, the DPCD model is feasible in simulating the failure process of a jointed rock mass.

### 3 Numerical analysis of the jointed rock mass failure process

#### 3.1 Numerical model

The failure process of a discontinuous jointed rock mass under different incidence angles was studied using the 150 mm × 75 mm two-dimensional plane model. Loads were applied at the top of the model and a fixed constraint was applied at the bottom. The geometrical parameters of the joint mainly included joint length ( $2a$ ), length of rock bridge ( $L$ ), angle of steps ( $\gamma$ ), angle of joint ( $\beta$ ), and joint spacing ( $d$ ). The definitions of these parameters are shown in Figure 6. The joint geometric parameters involved in this model are listed in Table 1, and the joint geometry layout is shown in Figure 7.

TABLE 2 Failure processes of jointed rock masses under single impact loading.

Failure mode	Crack initiation	Crack propagation	Connection failure	Failure mode	Crack initiation	Crack propagation	Connection failure
A  Block rotational failure				B  Block rotational failure			
C  Block rotational failure				D  Block rotational failure			
E  Block rotational failure				F  Block rotational failure			
G  Block rotational failure				H  Plane failure			

### 3.2 Mode of action of repeated stress waves

The action of repeated stress waves is different from ordinary cyclic loading. The dynamic stress field generated by the action of repeated stress waves is a pulsating stress field rather than an alternating stress field (Shao, 2005). During simulation, the time interval between two adjacent stress waves was set at  $t_0$  to prevent the influence of previous stress waves on the rock mass responses on follow-up. Hence, the action of repeated stress waves was simplified to repeated impact loading in Figure 8.

### 3.3 Numerical simulation results and analysis

#### 3.3.1 Action of a single stress wave

The amplitude, the pressure rising time, and the action time under the influence of a single stress wave were set to 5 MPa, and  $t_r = 100 \mu s$ , and  $t_m = 200 \mu s$ , respectively. The failure processes of discontinuous jointed rock masses with different incidence angles under single stress wave are shown in Table 2. Clearly, the initiation positions of the cracks in the joints were controlled by the incidence angle,  $\beta$ . When  $\beta$  was  $< 70^\circ$ , the cracks began at the two ends of the joint. When  $\beta$  reached  $70^\circ$ , the cracks were



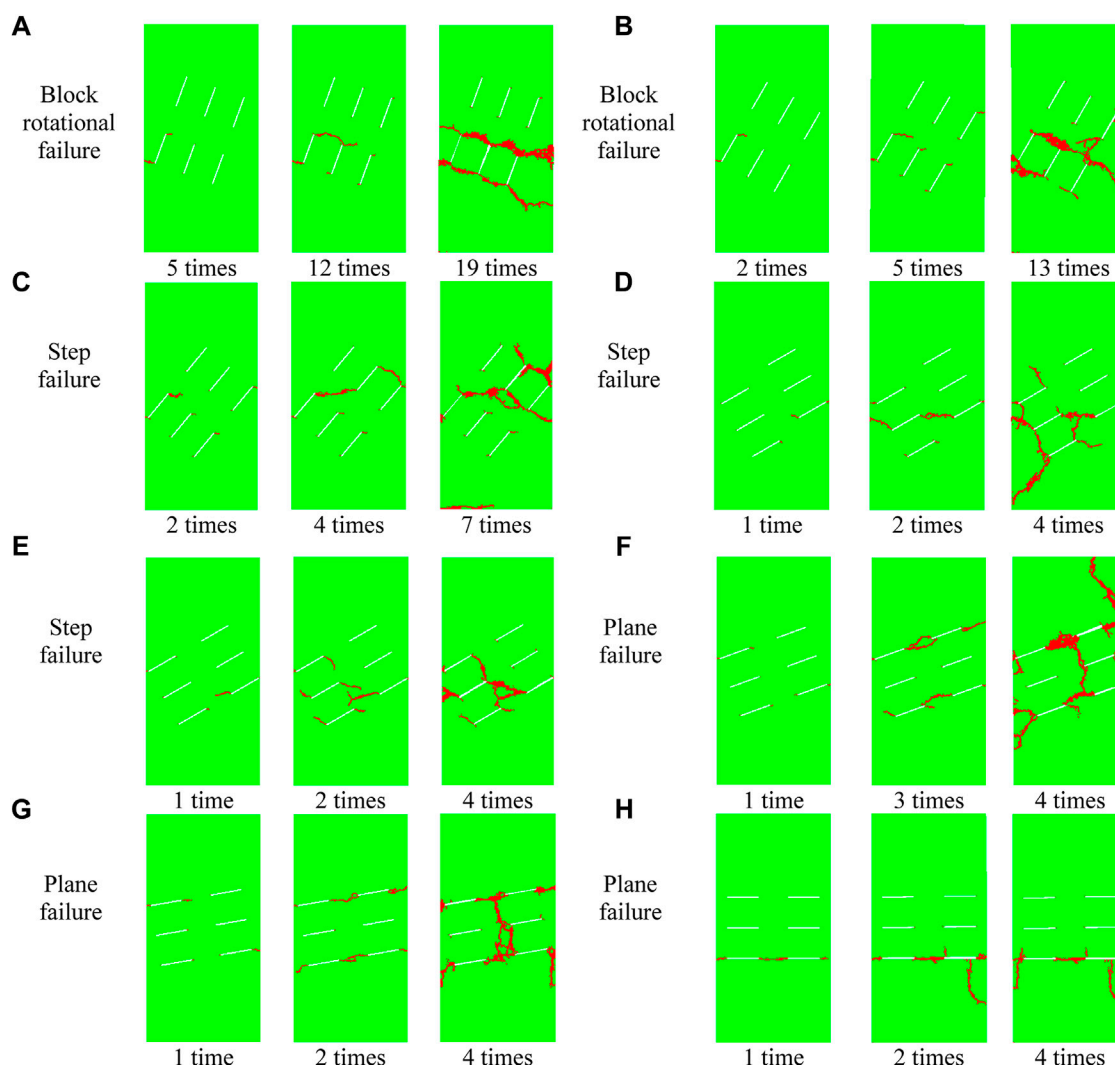


**FIGURE 9**  
Failure process of a jointed rock mass under repeated impact loading.

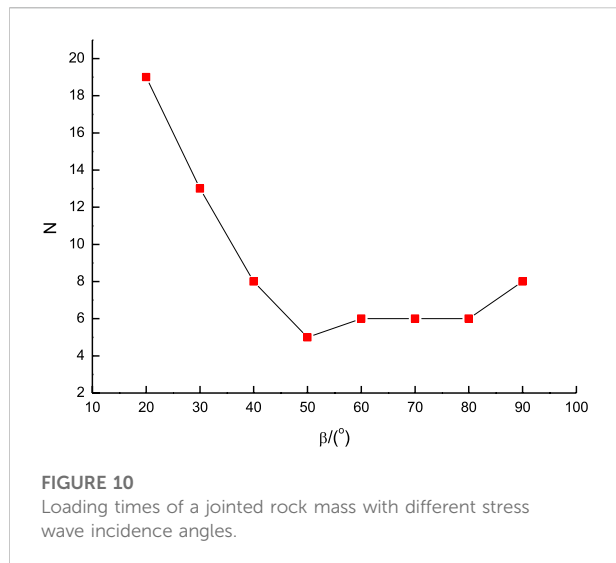
initiated at points far away from the joint. The initiation positions of cracks on the upper and lower surfaces of the same joint were gradually approaching with the increase in the incidence angle of joints.

As the loading process continued, wing cracks continued to propagate (except at  $\beta = 90^\circ$ ), and the propagation paths of cracks were influenced by adjacent joints. When  $\beta = 20^\circ$ , wing cracks propagated along the initiation direction continuously, but none was deflected toward the direction of major principal stress. This finding indicated that the influences of adjacent joints on wing cracks were weakened with the increase in the incidence angle of the joints. When  $\beta = 90^\circ$ , the wing cracks produced secondary coplanar cracks rather than propagating continuously and were connected to adjacent collinear joints, ultimately causing plane failure. Plane failure refers to a failure mode wherein wing cracks

began at joint ends, propagated under external loads, and connected with adjacent collinear joints. The failure surface presented a plane or approximate plane. Failure modes A–G were manifested as block rotational failures. Block rotational failure refers to a failure mode wherein wing cracks initiate at joint ends or surfaces, propagate under external loads, and connect with adjacent non-collinear joints to cut rock mass into numerous blocks that allow shear sliding or rotational displacement under external load.

### 3.3.2 Action of repeated stress waves

The amplitude, the pressure rising time, the action time, and the time interval under the action of repeated stress waves were set to 1 MPa,  $t_r = 100 \mu\text{s}$ ,  $t_m = 200 \mu\text{s}$ , and  $t_0 = 2,800 \mu\text{s}$ , respectively. The failure processes of discontinuous jointed



rock masses with different incidence angles under the action of repeated stress waves are shown in Figure 9. Cracks all initiated at the two ends of the joints under the action of repeated stress waves and changed with the variations of  $\beta$ . Moreover, the initiated cracks easily propagated toward the original initiation direction. The failure modes of the jointed rock mass with incidence angles other than  $\beta = 20^\circ$ ,  $30^\circ$ , and  $90^\circ$  all changed compared with those under the action of a single stress wave. Plane and step failures were the predominant modes under the action of repeated stress waves. Step failures resulted from connections between wing cracks and adjacent nonlinear joints in a stepwise distribution. In contrast, the block rotational failure was the major failure mode under the action of a single stress wave. The fatigue failure processes of a jointed rock mass under repeated stress waves, including initiation

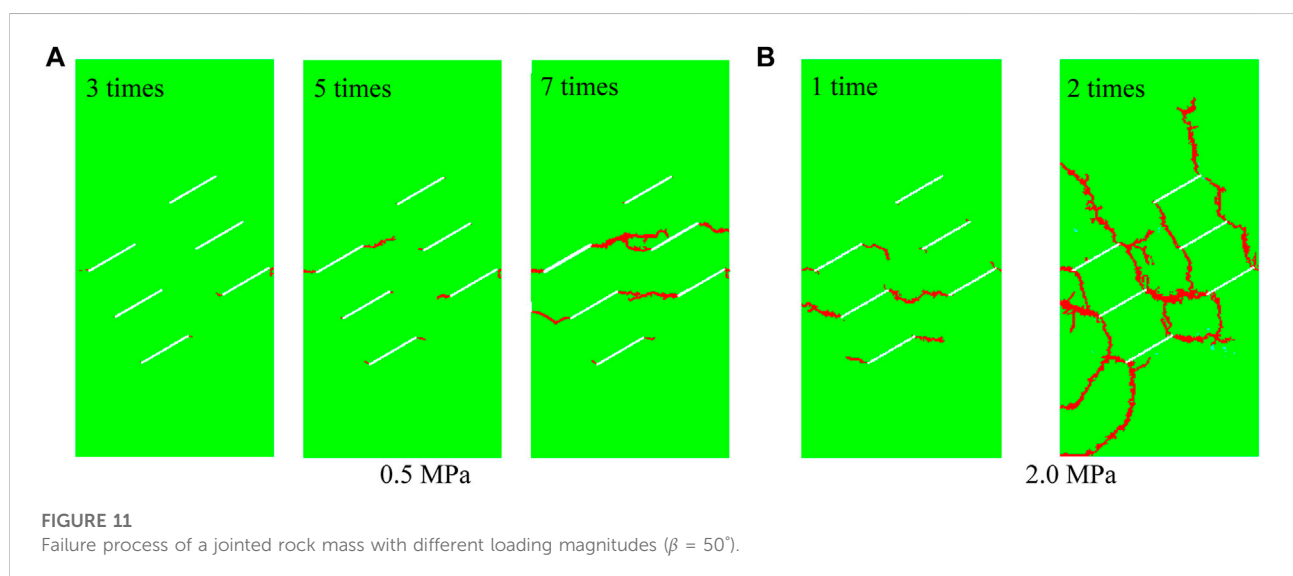
positions of cracks, propagation paths of cracks, and failure modes of rock mass, were significantly different from those resulting from a single stress wave. This result is related to the angle of incidence of the joints.

The curve showing the relationship between the fatigue life of a discontinuous jointed rock mass (loading times,  $N$ , and incidence angle of joints,  $\beta$ ) is shown in Figure 10. The fatigue life of a jointed rock mass presented a V-shaped variation trend with increasing incidence angle. When  $\beta$  was between  $20^\circ$  and  $50^\circ$ , the fatigue life of the rock mass was significantly influenced by the incidence angle of the joint and was significantly decreased with the increase of  $\beta$ . When  $\beta$  was between  $50^\circ$  and  $90^\circ$ , the fatigue life of the rock mass increased continuously with the incidence angle. When  $\beta$  was between  $60^\circ$  and  $80^\circ$ , the fatigue life of the rock mass was relatively stable and only slightly influenced by  $\beta$ .

### 3.3.3 Effects of stress wave amplitude

According to previous studies, a stress threshold exists for the fatigue failure of a rock mass. Under conditions of cyclic impacts, each stress event would intensify the internal damage to the rock mass only when its loading strength reached 80%–90% of static peak strength (Li et al., 2005). Thus, load amplitudes have important influences on the fatigue life of the rock mass. However, the mechanism of how loading amplitude affects the fatigue failure mode of a rock mass is still unclear and requires further investigation. In this study, a model with  $\beta = 50^\circ$  was selected as the research subject to investigate the effects of repeated stress waves of different amplitude on the fatigue failure modes of a discontinuous jointed rock mass.

Figures 11A and B show the simulation results for stress wave amplitudes of 0.5 MPa and 2 MPa, respectively. When the stress wave amplitude was 0.5 MPa (Figure 11A), short cracks were only seen initiating from the joint ends after three loading events.



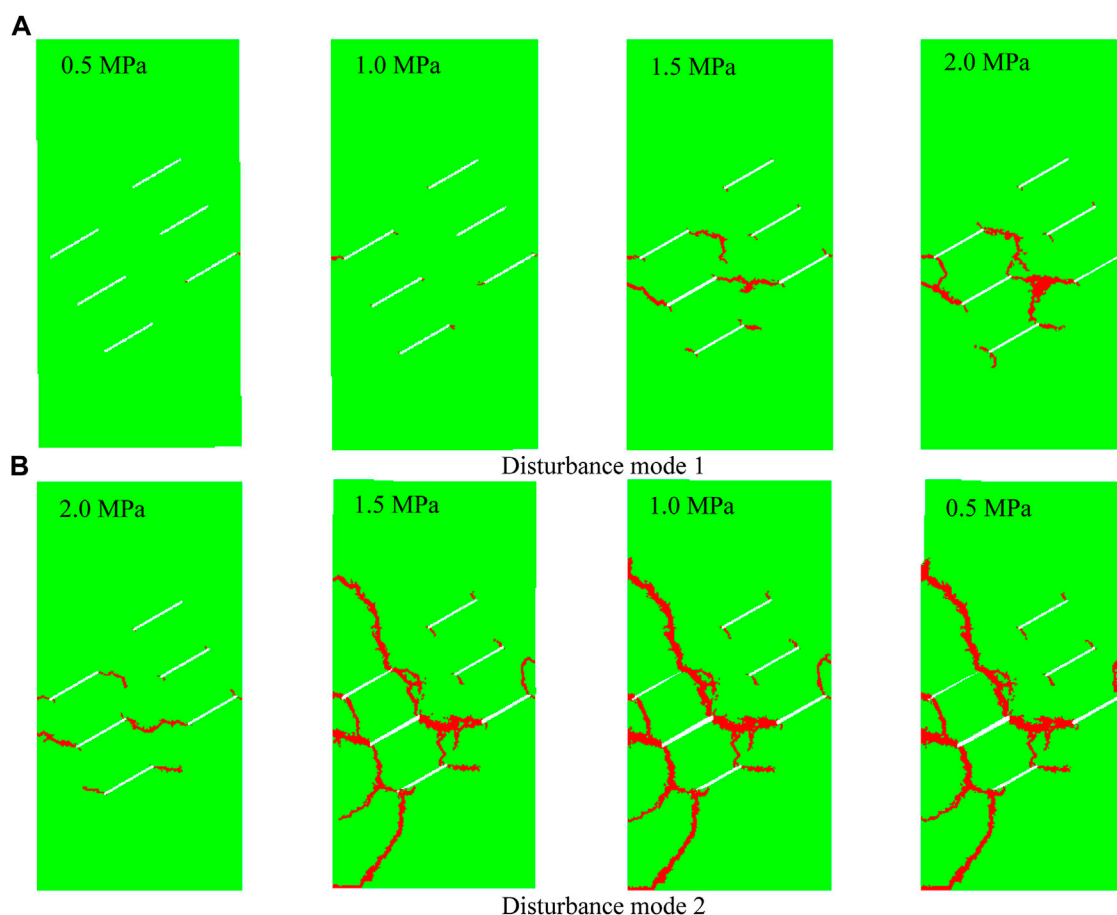


**FIGURE 12**  
Failure process of jointed rock mass with different load modes ( $\beta = 50^\circ$ ).

The wing cracks were connected to the adjacent non-collinear joints in a stepwise distribution after seven loading events. Wing cracks were generally straight, but there were local bifurcation phenomena, which ultimately led to step failure. [Figure 11B](#) shows that when the stress wave amplitude was increased to 2 MPa, wing cracks connected to adjacent non-collinear joints in stepwise distribution after only a single loading. The crack propagation path was relatively zigzag, and obvious bifurcation of wing cracks occurred after two loading times. The failure modes of a jointed rock mass were complex, with local X-shaped connections; hence, variations in stress wave amplitude could influence not only the fatigue life but also the failure mode of a jointed rock mass.

This study proved the importance of the critical stress value under the action of repeated stress waves. When the stress wave amplitude was higher than the threshold but smaller than the critical value, the jointed rock mass developed a single failure point under repeated stress waves. However, the failure modes of the rock mass were complicated by the continued increase in stress wave amplitude.

### 3.3.4 Effects of disturbance modes

In a practical engineering situation, the disturbance intensity at the same position of a rock mass changes as the tunnel face is advanced forward; thus, the influence of disturbance modes on the failure modes of a jointed rock mass must be considered. A model with  $\beta = 50^\circ$  was chosen as the research subject, and two disturbance modes were considered: (1) stress wave amplitude increased with a loading order of 0.5, 1, 1.5, and 2 MPa, and (2) stress wave amplitude decreased with a loading order of 2, 1.5, 1, and 0.5 MPa. Other conditions were fixed. The failure processes of a jointed rock mass under the two disturbance modes are shown in [Figures 12A and B](#), respectively. Under disturbance mode 1 ([Figure 12A](#)), only extremely short cracks were initiated at the joint ends in the first two loadings because of the small amplitude. After three loading events, wing cracks propagated and connected with adjacent non-collinear joints in a stepwise distribution. As the loading increased, wing cracks were connected with adjacent non-collinear joints, and a trend of mixed failure occurred. Under disturbance mode 2 ([Figure 12B](#)),

wing cracks were connected with adjacent non-collinear joints in a stepwise distribution after one loading event. Some adjacent non-collinear joints were connected after two loading times, with general mixed failure.

By comparing the failure modes under the two disturbance modes, it is obvious that they were similar, but the failure degree of a rock mass under disturbance mode 2 was far higher than that under disturbance mode 1. This result occurred most likely because the different disturbance modes caused different initial damage to the rock mass. Given stronger initial damages, the rock mass could reach the peak failure point by absorbing less energy, and the degree of post-peak rock fracture was higher. Thus, the type of disturbance mode did not affect the final macroscopic failure mode of the rock mass, but it did influence the failure degree.

## 4 Conclusion

In this study, a numerical simulation analysis on the failure processes of discontinuous jointed rock masses was carried out using the Autodyn element software. Some major conclusions can be drawn as follows:

- 1) The fatigue failure modes of a jointed rock mass under repeated stress waves, including the initiation positions of cracks, propagation paths of cracks, and failure modes of rock masses, were significantly different from those under a single stress wave. The differences were influenced by the incidence angle of the joints.
- 2) The fatigue life of a rock mass as a function of increase in the incidence angle presents a V-shaped variation trend. When  $\beta$  was between  $20^\circ$  and  $50^\circ$ , the fatigue life of the rock mass was significantly influenced by the incidence angle of joints, and it decreased significantly with increasing  $\beta$ . When  $\beta$  was between  $50^\circ$  and  $90^\circ$ , the fatigue life of the rock mass increased continuously with the incidence angle.
- 3) The stress wave amplitude can influence not only the fatigue life but also the failure mode of a jointed rock mass. A critical stress value is under the influence of repeated stress waves. When the stress wave amplitude is higher than the threshold but smaller than the critical value, the jointed rock mass develops a single failure under repeated stress waves. However, the failure modes of rock mass become more complex with the continued increase in stress wave amplitude.
- 4) The different disturbance modes had no effect on the final macroscopic failure mode of the rock mass, but they did affect the failure degree of the rock mass. The failure degree of a jointed rock mass under the disturbance mode with decreasing stress wave amplitude was far higher than that under the disturbance mode with the increasing stress wave amplitude.

## Data availability statement

The datasets presented in this study can be found in online repositories. The names of the repository/repositories and accession number(s) can be found in the article/Supplementary Material.

## Author contributions

SM contributed to the overall conception, writing, and data analysis of the article. SX reviewed the rationality of the overall conception of the article. CP carried out numerical simulation experiments.

## Funding

This research was supported by the National Natural Science Foundation of China Key Project (51934007), the Regional Innovation and Development Joint Fund of the National Natural Science Foundation of China (U21A20110), the Key R&D Projects in Shandong Province (2019SDZY02), the Chongqing Municipal Technology Innovation and Application Development Special Key Project (cstc2019jscx-gksbX0076), and the Technological Innovation and Entrepreneurship Fund Special Project of Tiandi Technology Co., Ltd. (2022-2-TD-ZD008).

## Acknowledgments

The authors would like to express sincere thanks to those researchers whose techniques have contributed to this research.

## Conflict of interest

The authors declare that this study received funding from Tiandi Technology Co., Ltd. The funder was not involved in the study design, collection, analysis, interpretation of data, the writing of this article, or the decision to submit it for publication.

## Publisher's note

All claims expressed in this article are solely those of the authors and do not necessarily represent those of their affiliated organizations, or those of the publisher, the editors, and the reviewers. Any product that may be evaluated in this article, or claim that may be made by its manufacturer, is not guaranteed or endorsed by the publisher.

## References

- Haeri, H., Sarfarazi, V., Ebneabbasi, P., Nazari maram, A., Shahbazian, A., Fatehi Marji, M., et al. (2020). XFEM and experimental simulation of failure mechanism of non-persistent joints in mortar under compression. *Constr. Build. Mater.* 236, 117500. doi:10.1016/j.conbuildmat.2019.117500
- Ji, L., Zhou, C., Lu, S., Jiang, N., and Gutierrez, M. (2021a). Numerical studies on the cumulative damage effects and safety criterion of a large cross-section tunnel induced by single and multiple full-scale blasting. *Rock Mech. Rock Eng.* 54 (12), 6393–6411. doi:10.1007/s00603-021-02630-9
- Ji, L., Zhou, C., Lu, S., Jiang, N., and Li, H. (2021b). Modeling study of cumulative damage effects and safety criterion of surrounding rock under multiple full-face blasting of a large cross-section tunnel. *Int. J. Rock Mech. Min. Sci.* 147, 104882. doi:10.1016/j.ijrmms.2021.104882
- Li, H. Q., and Wong, L. N. Y. (2014). Numerical study on coalescence of pre-existing flaw pairs in rock-like material. *Rock Mech. Rock Eng.* 47 (6), 2087–2105. doi:10.1007/s00603-013-0504-6
- Li, H., and Wong, L. N. Y. (2012). Influence of flaw inclination angle and loading condition on crack initiation and propagation. *Int. J. Solids Struct.* 49 (18), 2482–2499. doi:10.1016/j.ijsolstr.2012.05.012
- Li, X. B., Lok, T. S., and Zhao, J. (2005). Dynamic characteristics of granite subjected to intermediate loading rate. *Rock Mech. Rock Eng.* 38 (1), 21–39. doi:10.1007/s00603-004-0030-7
- Li, X., Pan, C., Li, X., Shao, C., and Li, H. (2022). Application of a synthetic rock mass approach to the simulation of blasting-induced crack propagation and coalescence in deep fractured rock. *Geomech. Geophys. Geo. Energy. Ge. Resour.* 8 (2), 57. doi:10.1007/s40948-022-00376-4
- Lin, P., Wong, R. H. C., Chau, K. T., and Tang, C. A. (2000). Multi-crack coalescence in rock-like material under uniaxial and biaxial loading. *Key Eng. Mat.* 187 PART 2, 809–814. doi:10.4028/www.scientific.net/kem.183-187.809
- Pan, C., Li, X., Li, J., and Zhao, J. (2021). Numerical investigation of blast-induced fractures in granite: Insights from a hybrid LS-DYNA and UDEC grain-based discrete element method. *Geomech. Geophys. Geo. Energy. Ge. Resour.* 7 (2), 49. doi:10.1007/s40948-021-00253-6
- Pan, C., Xie, L. X., Li, X., Liu, K., Gao, P. F., and Tian, L. G. (2022). Numerical investigation of effect of eccentric decoupled charge structure on blasting-induced rock damage. *J. Cent. South Univ.* 29 (2), 663–679. doi:10.1007/s11771-022-4947-3
- Prudencio, M., and van Sint Jan, M. (2007). Strength and failure modes of rock mass models with non-persistent joints. *Int. J. Rock Mech. Min. Sci.* 44 (6), 890–902. doi:10.1016/j.ijrmms.2007.01.005
- Sagong, M., and Bobet, A. (2002). Coalescence of multiple flaws in a rock-model material in uniaxial compression. *Int. J. Rock Mech. Min. Sci.* (1997). 39 (2), 229–241. doi:10.1016/s1365-1609(02)00027-8
- Shao, P. (2005). *Study on the dynamic effect of elastic wave in intermittently jointed rock mass*. Xuzhou: China University of Mining and Technology Press.
- Tang, X., Tao, S., Li, P., Rutqvist, J., Hu, M., and Sun, L. (2022). The propagation and interaction of cracks under freeze-thaw cycling in rock-like material. *Int. J. Rock Mech. Min. Sci.* 154, 105112. doi:10.1016/j.ijrmms.2022.105112
- Vergara, M. R., van Sint Jan, M., and Lorig, L. (2016). Numerical model for the study of the strength and failure modes of rock containing non-persistent joints. *Rock Mech. Rock Eng.* 49 (4), 1211–1226. doi:10.1007/s00603-015-0824-9
- Wang, X., and Tian, L. G. (2018). Mechanical and crack evolution characteristics of coal-rock under different fracture-hole conditions: A numerical study based on particle flow code. *Environ. Earth Sci.* 77 (8), 297. doi:10.1007/s12665-018-7486-3
- Wang, M. M., Wan, W., and Zhao, Y. (2020). Experimental study on crack propagation and the coalescence of rock-like materials with two preexisting fissures under biaxial compression. *Bull. Eng. Geol. Environ.* 79, 3121–3144. doi:10.1007/s10064-020-01759-1/
- Wang, X. X., Yuan, W., Yan, Y., and Zhang, X. (2020). Scale effect of mechanical properties of jointed rock mass: A numerical study based on particle flow code. *Geomechanics Eng.* 21 (3), 259–268. doi:10.12989/GAE.2020.21.3.259
- Wong, L. N. Y., and Einstein, H. H. (2009a). Crack coalescence in molded gypsum and carrara marble: Part 1. Macroscopic observations and interpretation. *Rock Mech. Rock Eng.* 42 (3), 475–511. doi:10.1007/s00603-008-0002-4
- Wong, L. N. Y., and Einstein, H. H. (2009b). Crack coalescence in molded gypsum and carrara marble: Part 2 - microscopic observations and interpretation. *Rock Mech. Rock Eng.* 42 (3), 513–545. doi:10.1007/s00603-008-0003-3
- Yang, S. Q., Yin, P. F., Zhang, Y. C., Chen, M., Zhou, X. P., Jing, H. W., et al. (2019). Failure behavior and crack evolution mechanism of a non-persistent jointed rock mass containing a circular hole. *Int. J. Rock Mech. Min. Sci.* 114, 101–121. doi:10.1016/j.ijrmms.2018.12.017
- Yuan, W., Wang, X., and Wang, X.-B. (2022). Numerical investigation on effect of confining pressure on the dynamic deformation of sandstone. *Eur. J. Environ. Civ. Eng.* 26 (9), 3744–3761. doi:10.1080/19648189.2020.1816217
- Zhao, G., Liu, C., Pan, C., and Meng, X. (2020). Researches on crack propagation of the two filled noncoalescent coplanar flaws under the high strain rate loading by means of AUTODYN-based simulation. *Geofluids* 2020, 1–10. doi:10.1155/2020/8875734
- Zou, C., Maruvanchery, V., Zhao, X., and He, L. (2022). Change of crack mode in rock cracking process under quasi-static and dynamic loadings. *Geomech. Geophys. Geo. Energy. Ge. Resour.* 8 (1), 20. doi:10.1007/s40948-021-00313-x



## OPEN ACCESS

## EDITED BY

Jun Zhao,  
Anhui University of Science and  
Technology, China

## REVIEWED BY

Qi Yao,  
China Earthquake Administration, China  
Feng Du,  
China University of Mining and  
Technology, China  
Zou Quanle,  
Chongqing University, China  
Zhengzheng Cao,  
Henan Polytechnic University, China  
Ke Yang,  
Anhui University of Science and  
Technology, China

## \*CORRESPONDENCE

Jinrong Cao,  
jin-rongcao@cumt.edu.cn  
Linming Dou,  
lmdou@126.com

## SPECIALTY SECTION

This article was submitted to  
Geohazards and Georisks,  
a section of the journal  
Frontiers in Earth Science

RECEIVED 12 September 2022

ACCEPTED 31 October 2022

PUBLISHED 13 January 2023

## CITATION

Cao J, Dou L, He J, Zhu G, Wang Z, Bai J  
and Han Z (2023), Failure mechanism  
and control of coal bursts triggered by  
mining induced seismicity in steeply  
inclined and extra thick coal seam.  
*Front. Earth Sci.* 10:1042539.  
doi: 10.3389/feart.2022.1042539

## COPYRIGHT

© 2023 Cao, Dou, He, Zhu, Wang, Bai  
and Han. This is an open-access article  
distributed under the terms of the  
[Creative Commons Attribution License  
\(CC BY\)](https://creativecommons.org/licenses/by/4.0/). The use, distribution or  
reproduction in other forums is  
permitted, provided the original  
author(s) and the copyright owner(s) are  
credited and that the original  
publication in this journal is cited, in  
accordance with accepted academic  
practice. No use, distribution or  
reproduction is permitted which does  
not comply with these terms.

# Failure mechanism and control of coal bursts triggered by mining induced seismicity in steeply inclined and extra thick coal seam

Jinrong Cao<sup>1\*</sup>, Linming Dou<sup>1,2\*</sup>, Jiang He<sup>1</sup>, Guangan Zhu<sup>3</sup>,  
Zhengyi Wang<sup>4</sup>, Jinzheng Bai<sup>1</sup> and Zepeng Han<sup>1</sup>

<sup>1</sup>School of Mines, China University of Mining and Technology, Xuzhou, China, <sup>2</sup>Jiangsu Engineering Laboratory of Mine Earthquake Monitoring and Prevention, Xuzhou, China, <sup>3</sup>School of Energy Engineering, Xi'an University of Science and Technology, Xi'an, China, <sup>4</sup>School of Civil Engineering and Architecture, Changzhou Institute of Technology, Changzhou, China

With the increase in mining depth, coal bursts have become a major challenge in the safe mining of steeply inclined and extra thick coal seams (SIETCSs). Based on a typical mining induced seismicity triggered coal burst (MSTCB) in SIETCS, a large-scale numerical model was developed using the Universal Distinct Element Code. The numerical model was calibrated and validated by laboratory results and field observations. The stress evolution, crack development and ejection velocity patterns in the MSTCB were analysed, and the effect of mining induced seismicity vibration velocity on the MSTCB was discussed. The results show that a triangular static stress concentration zone is formed in the coal on the roof side. And the high-energy mining induced seismicity leads to high dynamic stresses in the coal at the roof side rib and top of the headentry. Coal bursts occur under the superposition of static and dynamic stresses. The MSTCB results in tensile failure near the headentry surface and shear failure in the depth. The vibration velocity has a significant effect on the roof side rib and top of the headentry, while it has only a slight effect on the working face rib and bottom of the headentry. The dynamic stress and ejection velocity in the roof side rib and top of the headentry are positively correlated with the vibration velocity. Finally, measures for MSTCB prevention were proposed. The findings presented in this study can provide guidance for the prevention and control of MSTCBs in SIETCSs.

## KEYWORDS

steeply inclined and extra thick coal seam, coal burst, mining induced seismicity, UDEC, crack development



# 1 Introduction

As a violent dynamic failure in underground coal mining, coal bursts occurred worldwide with the increasing mining depth (Jiang et al., 2017; Ptáček, 2017; Mark, 2018), causing many casualties (Zhang et al., 2017) and other disasters (Du et al., 2020; Wang and Du, 2020). Coal bursts can be classified into self-initiated and remotely mining-induced seismicity triggered based on its mechanisms (Dou and He, 2001; Mottahedi and Ataei, 2019). Seismic events occur frequently in large-scale mining due to roof breakage, fault slip, coal pillar failure, etc. (Dou and He, 2001; Stec, 2007). Compared to self-initiated coalburst, mining-induced seismicity triggered coal bursts (MSTCBs) are more likely to occur in coal mines (Dou and He, 2001). In recent years, MSTCBs have been reported during horizontal section mining of steeply inclined and extra thick coal seams (SIETCSs) in China (Wang et al., 2019b; He et al., 2020). It is significant to investigate the mechanism and control of MSTCBs in SIETCSs.

To reveal the mechanism of MSTCBs, (Dou et al., 2015) proposed the coupled theory of static and dynamic stresses from the perspective of stress changes during coal bursts. He et al. (2017) analyzed the stress distribution during rockburst triggered by mine tremors and proposed a method to evaluate rockburst risk in mining. According to Cai et al. (2021), the dynamic stress from fault activation is a key factor in the coal burst triggered by fault. Dai et al. (2021) investigated the MSTCB theoretically and developed a critical index system to describe the remotely triggered coal bursts quantitatively. And many prevention measures had been applied in the field to control MSTCBs, such as optimization of mining design (Dou and He, 2001; Jiang et al., 2017), destress blasting in the roof (Konicek et al., 2011; Konicek et al., 2013), as well as hydraulic fracturing of hard and thick rock (Shapiro et al., 2006; He et al., 2012a). However, current studies mainly focus on horizontal and gently inclined coal seams. Due to the special geological conditions and mining methods, MSTCBs caused by horizontal section mining of SIETCSs are significantly different from those of horizontal and gently inclined coal seams. (Wang et al., 2019c). reported an MSTCB occurred on the working face in SIETCS and mechanically investigated its mechanism, results showed that abutment pressure near the roof was the main source of static stress. Xie et al. (2019) observed the roof deformation caused by mining two adjacent working faces in SIETCS based on physical simulation and found that mining of the lower working face led to a secondary movement of the roof. Yang et al. (2020b). analyzed the temporal-spatial evolution characteristics of dynamic failure in SIETCS and identified the stress concentration areas around the roadway. Wang et al. (2022) studied the stress redistribution caused by horizontal section mining in SIETCS, and found that there is high shear stress in the bottom coal under the effect of “shear-clamping”. Dynamic stress plays a critical role in MSTCBs (He et al., 2012; Dou et al., 2014). Yun et al. (2017) performed field monitoring of support pressure

in the working face and observed that the dynamic load coefficients caused by roof breakage varied between 1.45 and 1.52 during mining of the SIETCS. He et al. (2020) investigated the rock burst mechanism of two adjacent working faces in SIETCS, and the results indicated that fractures of the roof and rock pillar were the main dynamic stress sources of rock bursts. Yang et al. (2019) concluded that topping-slumping failure would occur after mining in SIETCS, resulting in strong dynamic loads. Lai et al. (2021) found that the roof structure in SIETCS would experience periodic “balance-instability” during mining, which is accompanied by energy accumulation and release. Cao et al. (2020) used numerical simulation to study the development of roof structure and the evolution of stress during mining in SIETCS, and concluded the sources of static and dynamic stress. Cui et al. (2019) proposed a surface filling technology to reduce the risk of dynamic hazards caused by mining of SIETCS. In addition, there are also some studies on precursory warnings for coal bursts in SIETCSs based on field monitoring (He et al., 2019; Wang et al., 2020; Li et al., 2021b).

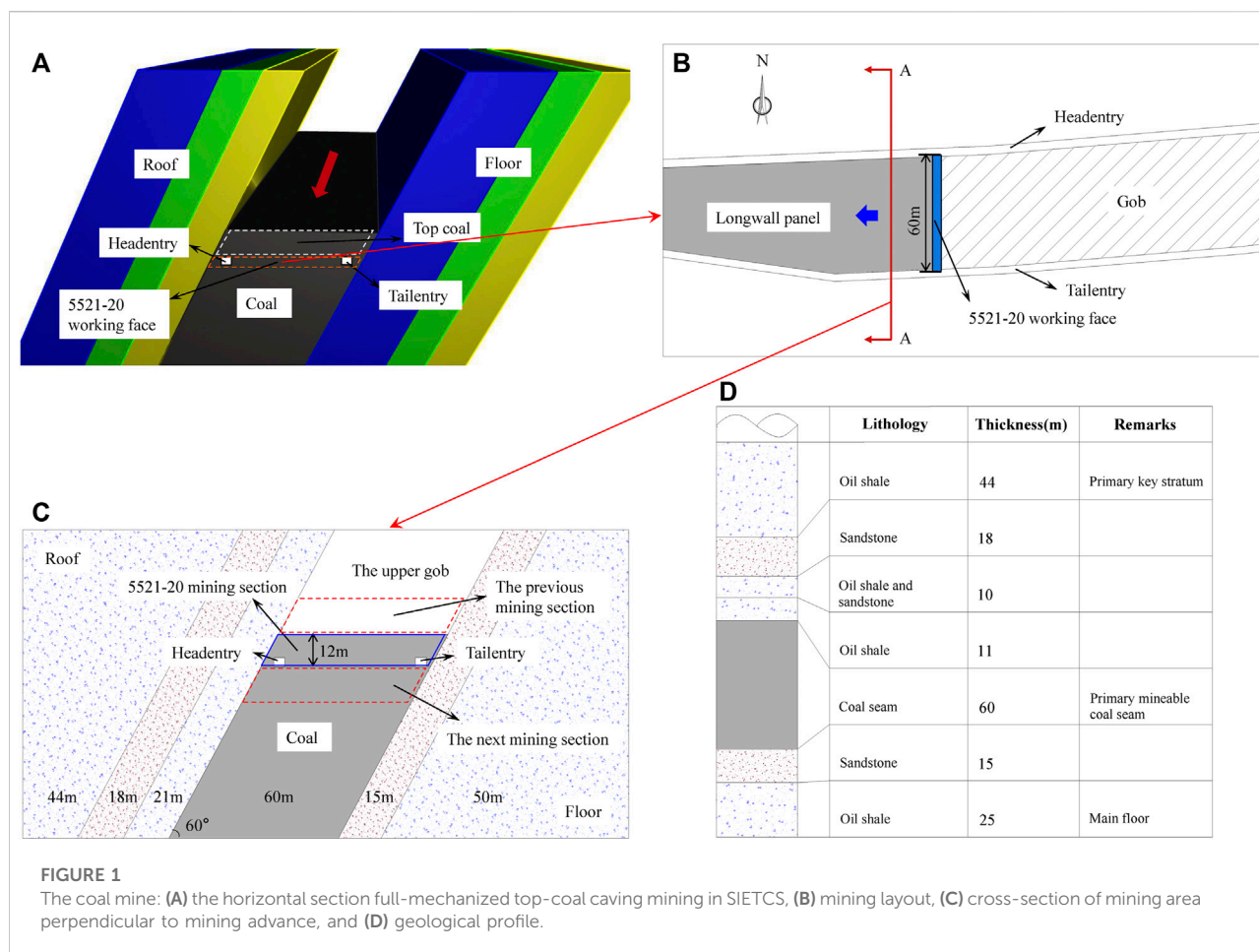
The above-mentioned studies have enriched our understanding of MSTCBs in SIETCSs. At present, many meaningful results have been derived, such as the asymmetric distribution of mining-induced stresses, the periodicity breakage of the steeply inclined roof, as well as the identification of static and dynamic stress sources, etc. However, more details of the dynamic failure process of MSTCBs in SIETCSs need to be further investigated, including stress evolution, the development of cracks, ejection velocity patterns, and the effect of the mining induced seismicity strength on MSTCBs. Studies in these aspects also are important for the prevention and control of MSTCBs in SIETCSs.

Taking an MSTCB that occurred in a typical SIETCS as the engineering background, this paper investigates the mechanism and control of MSTCBs in SIETCSs by using the Universal Distinct Element Code (UDEC) software (Itasca 2014). First, the engineering background and damage characteristics of the MSTCB were present. Second, a large-scale numerical model to reproduce the complete process of the MSTCB was developed. Third, the stress evolution, crack development and ejection velocity during the MSTCB were analysed, and the effect of the vibration velocity of mining induced seismicity on the MSTCB was studied. Finally, the mechanism and prevention measures of the MSTCB in SIETCS were proposed. Field monitoring indicates that the measures significantly decrease the risk of MSTCB in SIETCS.

## 2 Engineering background and damage characteristics

### 2.1 Engineering overview

The thickness of the SIETCS in Yaojie No.3 Coal Mine is in the range of 36–115 m, with an inclination angle of about 60°.



According to the classification standard of coal seams in China, coal seams with a thickness greater than 8 m are classified as extra thick coal seams. Coal seams with an inclination angle greater than  $45^\circ$  are classified as steeply inclined coal seams. Thus, the coal seam in Yaojie No.3 Coal Mine is a typical SIETCS. The horizontal section full-mechanized top-coal caving mining technology is adopted, and a longwall working face is arranged in each horizontal section. As shown in Figure 1A, the 5,521-20 working face is located in a section with a height of 12 m, and the mining to caving height ratio is 1:3. The design of the 5,521-20 working face is shown in Figures 1B,C, the width of the 5,521-20 working face is variable due to the change in coal seam thickness, the maximum width is about 60 m. The 5,521-20 headentry and the 5,521-20 tailentry are set in the coal seam near the roof and floor respectively and there is a coal pillar with a width of 6 m between the headentry and the roof. The mining depth of the 5,521-20 working face is 470–530 m. *In-situ* stress measurements were carried out, and the results showed that the initial horizontal and vertical stresses were 22 MPa and 13 MPa, respectively. The geological profile is shown in Figure 1D, there are thick sandstone and oil shale in the roof,

and a 44 m thick oil shale is the main key layer according to the key layer theory (Qian et al., 2000). With the increase of mining depth, the upper gob became larger, and the number of mine tremors caused by the roof breakage increased, which eventually caused a serious coal burst in the headentry.

## 2.2 Coal burst in the headentry

On June 29, 2016, accompanied by a high-energy seismic event in the roof, an MSTCB occurred in the headentry of the 5,521-20 working face. Figure 2 shows the location of the MSTCB and some *in situ* recorded photos. As shown in Figure 2A, a total of 44 m of the headentry in front of the working face was damaged, including a 10 m area near the working face that was severely damaged. Under the effect of the seismic event on the roof, some equipment overturned, and some artificial support units failed, as shown in Figure 2B, and it is worth noting that both the rollover of equipment and the sliding of support units have the same direction from the roof side to the working face side. As illustrated in Figure 2C, the MSTCB resulted in large

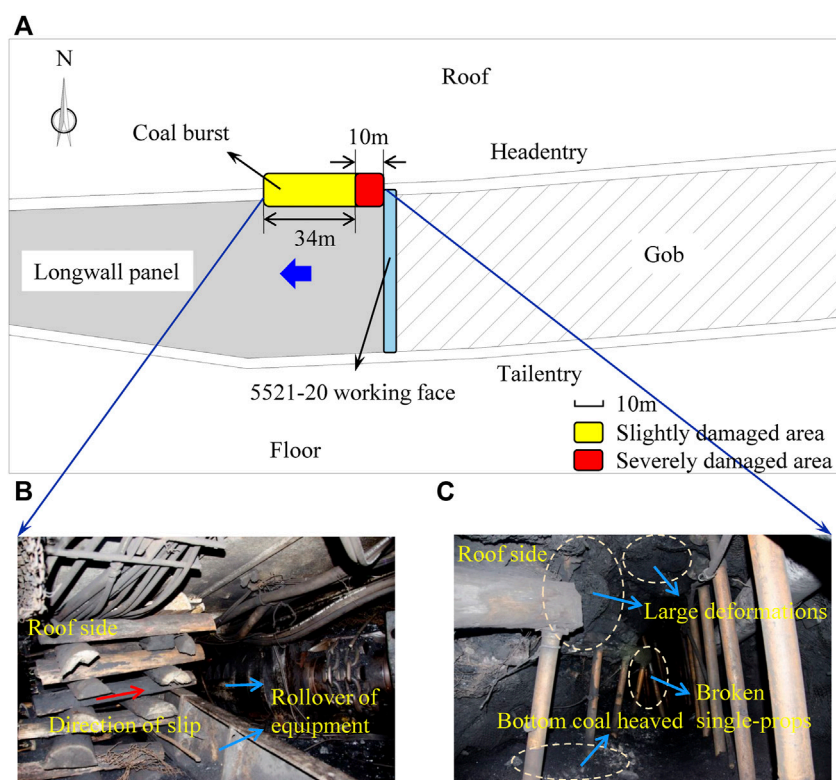


**FIGURE 2**  
The MSTCB in the 5,521–20 headentry: (A) location of coal burst, (B) rollover of equipment, and (C) typical failures in the headentry.

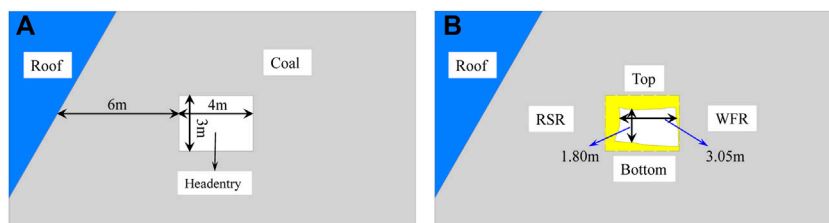


**FIGURE 3**  
Cross-section of the headentry: (A) before the MSTCB, and (B) after the MSTCB.

deformation on the roof side and top of the headentry, and the cables and wire mesh were damaged by the fractured coal, and it can be seen that the deformation of the roof side wall was mainly concentrated on the upper part. The bottom coal was heaved. In addition, a large number of single-props failed. After the MSTCB occurred, field measurements were carried out on the headentry. A sketch (see Figure 3) of the headentry before and after the MSTCB illustrates the damage and deformation pattern. Before the MSTCB, the width and height of the headentry were 4 m and 3 m respectively, as shown in Figure 3A. The sketch of the

headentry after the MSTCB is shown in Figure 3B, we divided the coal around the headentry into four zones, they are the top, bottom, roof side range (RSR), and working face range (WFR). According to the field measurement results, the maximum deformation of the top, bottom, RSR, and WFR were 0.7, 0.5, 0.8, and 0.15 m respectively, and the convergence of the roof to the bottom and the RSR to the WFR reached 1.2 and 0.95 m respectively. It is also notable that the maximum deformation of the bottom is located on the roof side. It can be concluded that the damage to the headentry caused by the MSTCB has

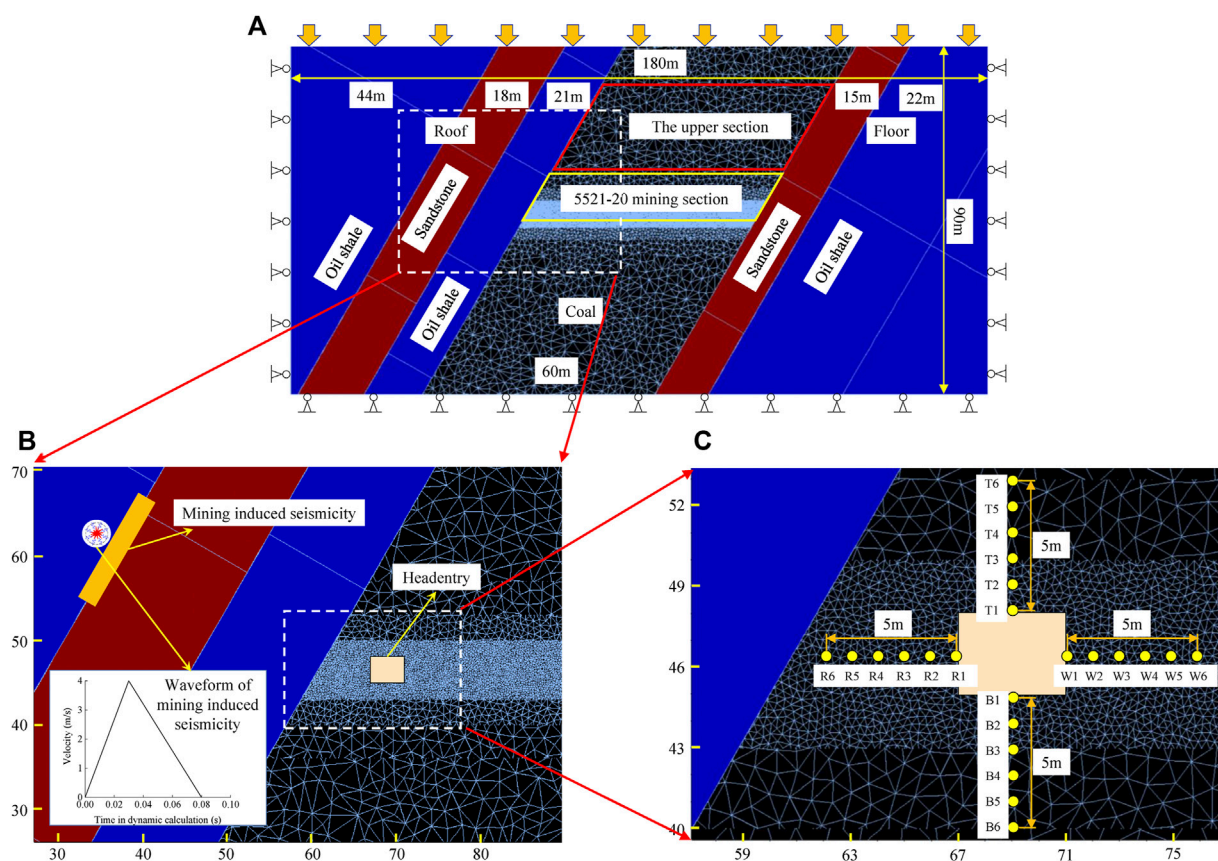


FIGURE 4

UDEC numerical model: (A) overview of the model, (B) detail incl. hypocentre of mining induced seismicity, and (C) detail of 5,521–20 headentry area (T, R, B, and W indicate the locations of monitoring).

significant asymmetric characteristics, and the main large deformation areas are the RSR, top, and bottom of the headentry. Compared with the area on the WFR, more severe dynamic damage occurred in the area near the roof. When the MSTCB occurred, the pressures of the hydraulics arranged near the roof were observed to increase significantly. The pressures of 25# and 30# hydraulic were up to 46 and 44 MPa, respectively. In comparison with the previous day, the pressures increased by 360% and 340%, respectively, indicating that strong dynamic stress was developed in the coal on the roof side.

### 3 Numerical simulation

#### 3.1 Modelling method

UDEC, a two-dimensional numerical program, simulates the quasi-static or dynamic response to the loading of a discontinuous medium. The simulated coal and rock consist of a number of deformable blocks and contacts between the

blocks. The failures of the contacts are controlled by the stresses acting at the contact and the failure criterion (Itasca 2014). There are two main failure modes for the contacts: shear cracking and tensile cracking. The penetration of contact cracks leads to the formation of macroscopic failure. In this study, the blocks were divided into triangles according to the UDEC-Trigon method (Gao and Stead, 2014). It was shown that the UDEC-Trigon model can successfully reproduce the failure processes including conventional brittle damages or nonlinear dynamic failures caused by mining at the field scale (Gao et al., 2014; Gao and Yang, 2021).

#### 3.2 Model configuration and modelling procedure

Based on the geological data of the 5,521-20 working face, a large-scale numerical model was developed using UDEC. The width of the numerical model is 160 m and the height is 80 m, which consists of the roof, coal and floor, as shown in Figure 4A. The



inclination angle and thickness of the coal seam were set to 60° and 60 m respectively. In the UDEC simulation, if a larger size of the block is chosen, it will be possible to get the wrong failure pattern and mechanism. However, a small block size will be a high computational requirement and time-consuming. To solve this problem, different block sizes were used in different areas in this study, and the small block sizes were used in the areas that need attention. Triangular blocks were used in the coal seam, while rectangular blocks were used in the roof and floor. The average size of the smallest block around the headentry was 0.3 m, which was similar to the size used in the simulation at the field scale (Gao and Stead, 2014), and the size of the blocks in the outer area gradually increased. The gravitational acceleration was set to 9.8 m/(s<sup>2</sup>). The static and dynamic calculation modes were employed in order to simulate mining and the MSTCB, respectively. The boundary conditions in the two calculation modes are different. In the static calculation, initial horizontal stress of 22 MPa and initial vertical stress of 13 MPa was applied to the numerical model according to the *in-situ* stress measurements. The boundaries on both sides as well as the bottom were fixed. Vertical stress of 12 MPa was applied to the upper boundary considering the gravity of the overlying rock layers. In the dynamic calculation, the boundary conditions were changed to viscous boundaries to avoid incorrect results caused by the wave reflection on outer boundaries. The stress increase in the surrounding rock caused by the mine tremor is due to the propagation of seismic waves. In addition, the velocity and duration of the seismic waves can be obtained by a microseismic monitoring system in the field. Therefore, a triangular vibration wave is used in this study, and it should be noted that the structural changes caused by the mine tremor are not considered. As shown in Figure 4B, a triangular vibration wave was applied to the roof to simulate the disturbance caused by roof breakage with a peak velocity of 4 m/s and duration of 0.08 s. In this study, Rayleigh damping was adopted. A small value of the damping ratio (e.g., 0.5%) is recommended when large deformation may occur (Itasca 2014). As we know, coal bursts result in large displacement and ejection of coal. Therefore, Rayleigh damping of 0.5 % is employed. In order to quantitatively investigate the stress, velocity, and displacement changes around the headentry during the MSTCB, a large number of monitoring points were set up, as shown in Figure 4C. There are six monitoring points in the top, bottom, RSR, and WFR of the headentry, respectively, and the distance between adjacent monitoring points is 1 m.

A combination of static and dynamic calculation modes was adopted to reproduce the MISTCB in SIETCS. The simulation was divided into two stages. The first stage was carried out in the static calculation mode, in which the upper section located above the 5,521–20 mining section was first excavated after the model was calculated to equilibrium under the given initial conditions, and then, the headentry was excavated. This part focuses on studying the redistribution of stresses and micro-cracking caused by mining. In the second stage, the calculation mode was changed to dynamic, and the vibration wave was applied to the roof. In

this section, the MSTCB process is investigated to identify its failure characteristics and mechanisms, including stress evolution, crack development, and velocity patterns.

### 3.3 Model calibration

The micro-properties of simulated rocks and coal were calculated theoretically and calibrated by laboratory results. First, we obtained the mechanical properties of the rocks and coal in the laboratory, which were referred to as the intact rock properties. Then, considering the difference between the properties of the rock mass and the intact rock, the mechanical properties of the rock mass were estimated theoretically and were the target value for calibration. In this study, the elastic modulus of the rock mass was calculated by the RQD method (Zhang and Einstein, 2004), as shown in Eq. 1, and the uniaxial compressive strength of the rock mass was calculated by the empirical formula proposed by Singh and Seshagiri Rao (2005), and the tensile strength of the rock mass was estimated as 1/10 of the uniaxial compressive strength, as shown in Eq. 2. The properties are shown in Table 1. After obtaining the mechanical properties of the rock mass, two critical micro-properties of the rock mass, normal stiffness and shear stiffness, were calculated by Eqs. 3, 4 (Itasca 2014). Finally, the micro-properties obtained from the above theoretical calculations were calibrated by performing a series of simulated uniaxial compressive tests (UCS-test) and Brazilian tensile tests (BT-test). The UCS-test model was 10 m long and 5 m wide, and the diameter of the BT-test model was 5 m, as shown in Figure 5. The average size of the blocks in the calibration numerical model was also set to 0.3 m, which was same as that of the region of interest. The calibrated micro-properties are presented in Table 2. The rock mass properties obtained from the calibrated simulation tests with the target values are shown in Table 3. It can be seen that the errors between the numerical results, including elastic modulus, uniaxial compressive strength and tensile strength, and the target values do not exceed 4%, indicating that the calibrated micro-properties are reasonable.

$$\frac{E_m}{E_r} = 10^{0.186RQD-1.91} \quad (1)$$

where  $E_m$  and  $E_r$  are the elastic modulus of rock mass and intact rock, respectively.

$$\frac{\sigma_{cm}}{\sigma_c} = \left(\frac{E_m}{E_r}\right)^n, \sigma_{tm} = \frac{1}{10}\sigma_{cm} \quad (2)$$

where  $\sigma_{cm}$ ,  $\sigma_c$  and  $\sigma_{tm}$  are the uniaxial compressive strength of rock mass, the uniaxial compressive strength of intact rock, and the tensile strength of rock mass, respectively.  $n=0.63$  was used in this study.

$$K_m = \frac{E_m}{3(1-2\mu)}, G_m = \frac{E_m}{2(1+\mu)} \quad (3)$$

where  $K_m$  and  $G_m$  are the bulk and shear moduli of rock mass.  $\mu$  is Poisson's ratio.



TABLE 1 Properties of intact rocks and rock masses.

Rock Strata	Intact Rock $E_r$ (GPa)	$\sigma_c$ (MPa)	RQD	Rock Mass $E_m$ (GPa)	$\sigma_{cm}$ (MPa)	$\sigma_{tm}$ (MPa)
sandstone	9.5	61.2	90	5.5	43.5	3.62
Siltstone	6.9	45.4	85	3.2	28.2	2.35
Sandy mudstone	3.8	26.4	82	1.5	15.1	1.26
Coal	3.1	25.3	79	1.12	13.4	1.12

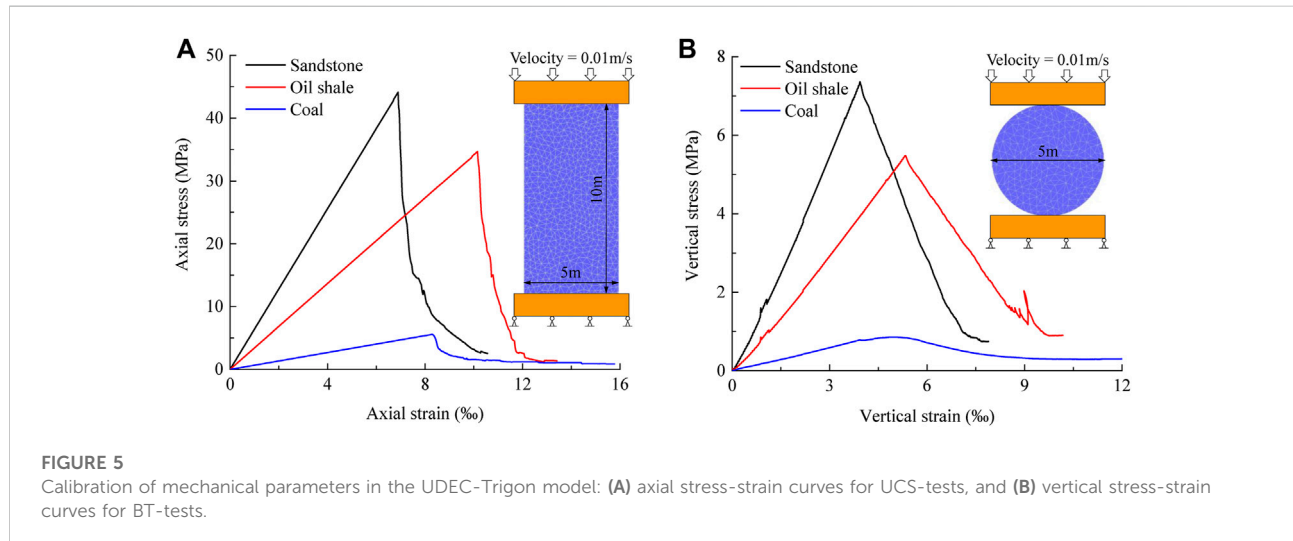


TABLE 2 Calibrated micro-properties for UDEC-Trigon model.

Rock Strata	Matrix Properties $E$ (GPa)	Contact Properties Poisson's Ratio	$k_n$ (GPa/m)	$k_s$ (GPa/m)	Cohesion (MPa)	Friction Angle (°)	Tensile Strength (MPa)
sandstone	9.5	0.26	225.0	67.5	14.1/0*	43/31*	3.30/0*
Siltstone	6.9	0.25	129.0	32.3	10.3/0*	39/32*	2.20/0*
Sandy mudstone	3.8	0.21	58.8	21.2	5.6/0*	37/31*	1.16/0*
Coal	3.1	0.21	84.3	30.4	5.1/0*	36/31*	0.98/0*

Peak and residual value.

$$k_n = n \left[ \frac{K_m + (4/3)G_m}{\Delta Z_{\min}} \right] \quad (1 \leq n \leq 10), \quad k_s = (0.25 - 0.4)k_n \quad (4)$$

where  $k_n$  and  $k_s$  are the normal stiffness and shear stiffness, respectively,  $\Delta Z_{\min}$  is the smallest width of zone.

### 3.4 Model validation

The numerical model was validated by comparing the simulation results with the field measurements. Three important aspects are included in the validation: (1)

deformation caused by the headentry excavation, (2) displacement of the top, bottom, RSR, and WFR of the headentry due to the MSTCB, and (3) failure characteristics of the headentry induced by the MSTCB. The simulated deformation caused by the excavation of the headentry was compared with the results measured during the field development, as shown in Figure 6A. It can be seen that they have the same trend, the rate of deformation decreased gradually, and the convergence between the top and bottom is greater than that between RSR and WFR. Deformation characteristics of the headentry after excavation are different from those in horizontal coal seams (Li et al., 2022). This is due to the fact that the top and bottom of the

TABLE 3 Target values and final simulation results for rock mass for UDEC-Trigon model.

Rock strata	$E_m$ (GPa)			$\sigma_{cm}$ (MPa)		$\sigma_{tm}$ (MPa)		Calibrated	Error (%)
	Target	Calibrated	Error (%)	Target	Calibrated	Error (%)	Target		
sandstone	5.5	5.2	5	43.5	44.2	2	3.62	3.73	3
Siltstone	3.2	3.1	3	28.2	27.9	1	2.35	2.31	2
Sandy mudstone	1.5	1.5	0	15.1	15.7	4	1.26	1.28	2
Coal	1.12	1.05	6	13.4	13.7	2	1.12	1.15	3

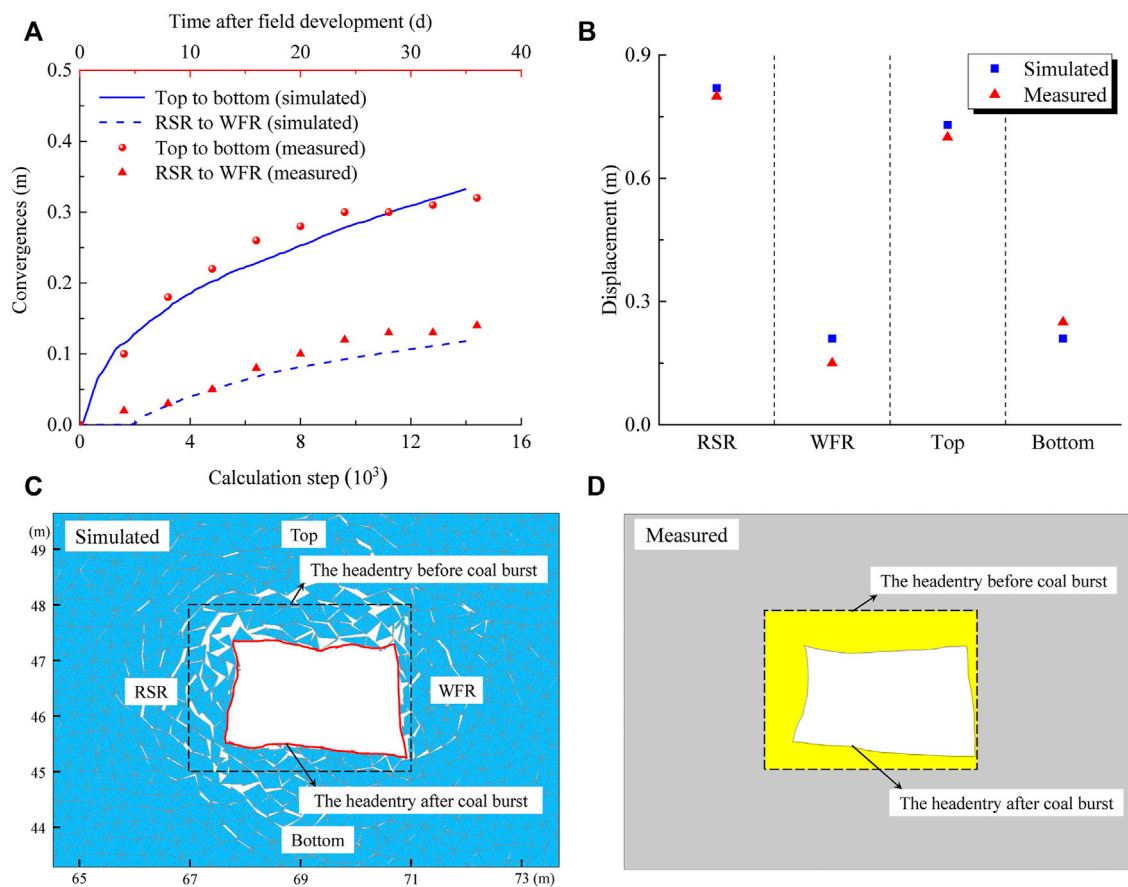


FIGURE 6 Validation of the UDEC-Trigon model: (A) convergence of the headentry, (B) displacement in the MSTCB, (C) simulated results of the MSTCB, and (D) measured results of the MSTCB.

headentry in this study are coal, rather than rock. The thickness of the top coal is greater than the width of the coal pillar in the RSR. Large deformation will occur in the top and bottom coal with increasing stress. As shown in Figure 6B, the simulated and measured results for the displacements of the top, bottom, RSR, and WFR of the headentry induced by the MSTCB are also very close, with the largest displacement of coal in the RSR. The failure

characteristics of the simulated and *in-situ* coal burst are shown in Figures 6C, D, respectively. The same failure characteristics are shown with severe dynamic damage mainly at the top and RSR, and only minor damage in the WFR. The simulation results are in good agreement with the field measurements, indicating that the numerical model and simulation procedures adopted in this study can well reproduce the MSTCB process.

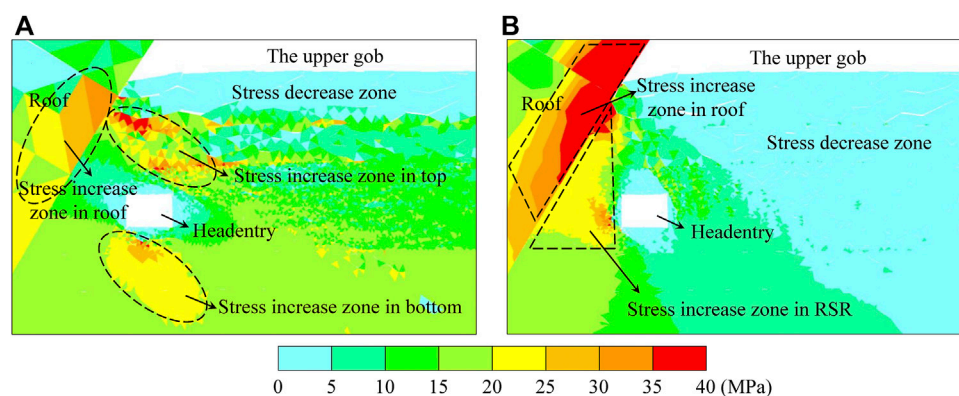


FIGURE 7

The stresses after the excavation of the upper mining section and the headentry: (A) horizontal stresses, and (B) vertical stresses.

## 4 Results and analysis

### 4.1 Stress evolution

The horizontal stresses and vertical stresses after the excavation of the upper mining section and the headentry are shown in Figure 7A and 7B. The mining of the upper section resulted in a large stress decrease zone in the coal seam. However, the stress increase zone appeared in the roof due to the gradual falling and deforming of the roof caused by mining, and there were three stress increase zones in the coal around the headentry under the compression of the roof, they were the horizontal stress increase zone at the top, the horizontal stress increase zone at the bottom and the vertical stress increase zone located in the RSR. A large amount of elastic energy would accumulate in the stress concentration zone in the roof and coal, resulting in a potentially high risk of coal bursts. The above high coal burst risk zones have been validated by the MSTCB that occurred on June 29.

The propagation of the mining induced seismicity will cause stress changes in the rock or coal. As expected, the stresses in the coal around the headentry were changed under the action of the mining induced seismicity. Figure 8 presents the stress records of all the monitoring points after the dynamic calculation mode is activated, including the seismic wave propagation stage before the dynamic time of 0.06 s and the MSTCB stage after the dynamic time of 0.06 s. During the propagation stage, most of the monitoring points were recorded the stress increase caused by the seismic wave. These increased stresses are called dynamic stresses. As shown in Figures 9A,C, large dynamic stresses were recorded at each monitoring point at the top of the headentry and in the RSR, indicating that the mining induced seismicity in the roof had a significant effect on these two regions. The largest dynamic stresses were observed in the RSR, and accordingly, the most severe coal burst damage occurred in the RSR. The dynamic stresses at the bottom and shallow WFR (e.g., W1, W2 and W3)

were small, indicating that the mining induced seismicity in the roof had a minor effect on these areas. However, the stresses at the monitoring points located in the deep part of the WFR (e.g., W4, W5 and W6) were not increased, indicating that the action range of the mining induced seismicity in the roof was limited in the WFR. As we know, the stresses will decrease significantly after a failure occurs. The stress drop is associated with the sudden penetration of cracks (Xue et al., 2020). During the MSTCB, the stresses at most of the monitoring points decreased, except for T3, B3, W4, W5, and W6. The stresses at W4, W5, and W6 increased because the coal burst occurred only in a limited shallow area in the WFR, causing the stresses to be transferred to the deeper part. The stresses in T3 and B3 did not decrease, probably due to some individual stress concentrations that occurred in localized areas during the MSTCB.

### 4.2 Cracking development

Many studies have shown that the microstructure of coal is influenced by many factors, resulting in a complex process of crack development (Xue et al., 2022; Zou et al., 2022; Xue et al., 2023). Figure 9A illustrates the distribution of cracks after mining of the upper section, with blue colour indicated tensile cracks and red colour shear cracks. The coal can be divided into two zones according to the majority of crack types: (1) shallow zone and (2) deep zone. In the shallow zone, most of the cracks were of the tensile failure type, which was due to the deformation of the coal in the shallow zone towards the upper mining area. However, in the deep zone, the coal was not only clamped by the roof and floor, but also constrained by the coal in the shallow zone. Therefore more shear slip occurred in the deep coal, resulting in most of the cracks being of shear failure type. In addition, it should be noted that the cracks did not extend to the area where the headentry is located, forming a

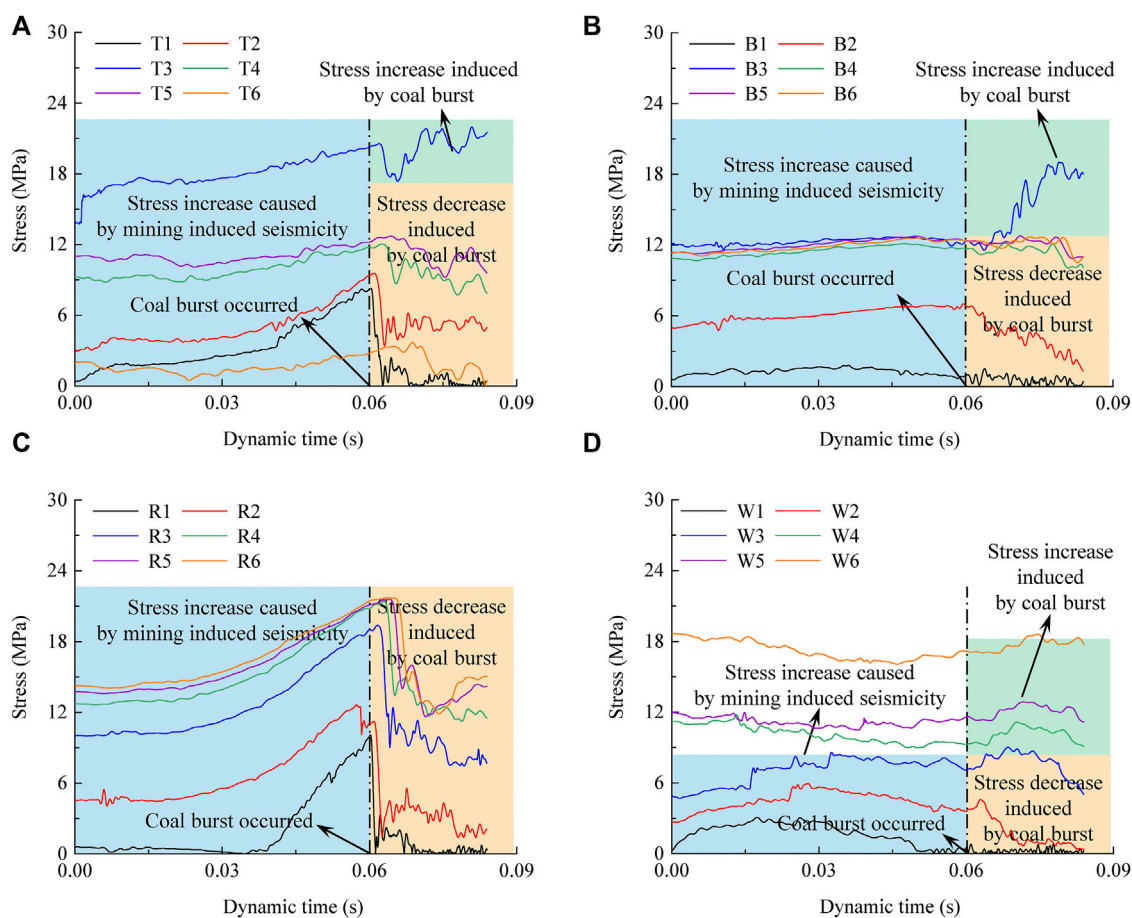


FIGURE 8

Stress changes around the 5,521–20 headentry during the MSTCB: (A) at the top, (B) at the bottom, (C) at RSR, and (D) at WFR.

triangular area where cracks are not developed. This is because the coal in the triangular area is subjected to compressive stresses under the clamping of the roof and floor, which has a higher strength.

Figures 9B–E present the crack development in the coal around the headentry during the MSTCB. As shown in Figure 9B, at the beginning of the MSTCB, a large number of shear cracks appeared first in the coal under the superposition of the initial high static stress and dynamic stress. When the dynamic time is 0.072 s, the shear cracks developed from the area near the headentry surface to the deeper part, as shown in Figure 9C. The dominant direction of crack development was west-east, which was the area of the top and RSR crossover, and this is because the static stress and dynamic stress in this area are both higher. In addition, the number of tensile cracks near the headentry surface gradually increased. Coal plate bending started to appear. As time increased, tensile cracks developed from the area near the headentry surface to the deeper part, as shown in Figure 9D. Eventually, the tensile failure zone near the headentry

surface and the shear failure zone located at the deeper part were formed.

### 4.3 Ejection velocity patterns

Figure 10 illustrates the velocity vectors around the headentry at different dynamic times during the MSTCB, including the amplitude and direction of the ejection velocities. When the dynamic time was 0.066 s, the main high-velocity areas were the top and the RSR of the headentry, and the direction of the velocity vector radiated from the top to the headentry, indicating that the initial coal burst occurred at the top and the RSR under the action of the seismic wave from the roof. When the dynamic time was 0.072 s, the velocity of the headentry bottom located near the roof started to increase. As time increased, the range of the bottom coal burst and the amplitude of the ejection velocity gradually increased, indicating that the bottom coal burst occurred. There was no significant change in the velocity of the WFR during the MSTCB. Despite the small

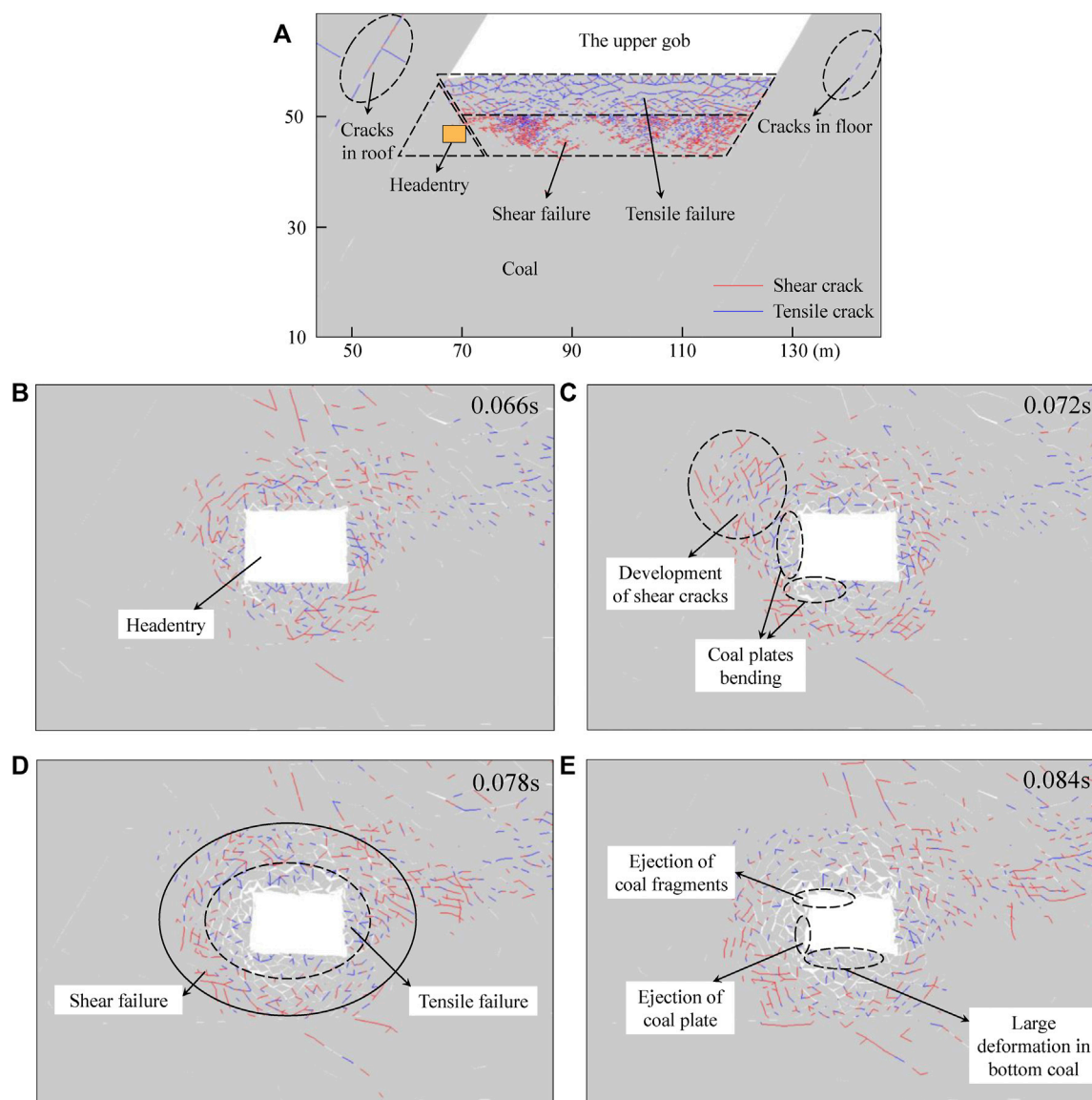


FIGURE 9

Crack development: (A) the cracks after mining of the upper section, (B) dynamic time is 0.066s in the MSTCB, (C) dynamic time is 0.072s in the MSTCB, (D) dynamic time is 0.078s in the MSTCB, and (E) dynamic time is 0.084s in the MSTCB.

time interval, the bottom coal burst occurred later than the top and RSR coal bursts in the MSTCB.

Figures 11A,B show the horizontal velocity and vertical velocity of the MSTCB obtained from the simulation. The high horizontal velocity region was the RSR and was larger compared to the WFR. The high vertical velocity regions were the top and the bottom near the roof. The regions of high ejection velocity due to the MSTCB were mainly the RSR, the top, and the bottom near the roof, which is consistent with the regions where severe dynamic failures were observed to occur in the field.

## 5 Discussion

### 5.1 Effect of the mining induced seismicity

Many studies have shown that high-energy mining induced seismicity plays an important role in coal bursts (He et al., 2012b; Wang et al., 2019a; Si et al., 2020). The vibration velocity of mining induced seismicity increases with the increase of its energy (He et al., 2015). In this study, numerical simulation results and analysis confirm that the dynamic stress caused by the mining induced



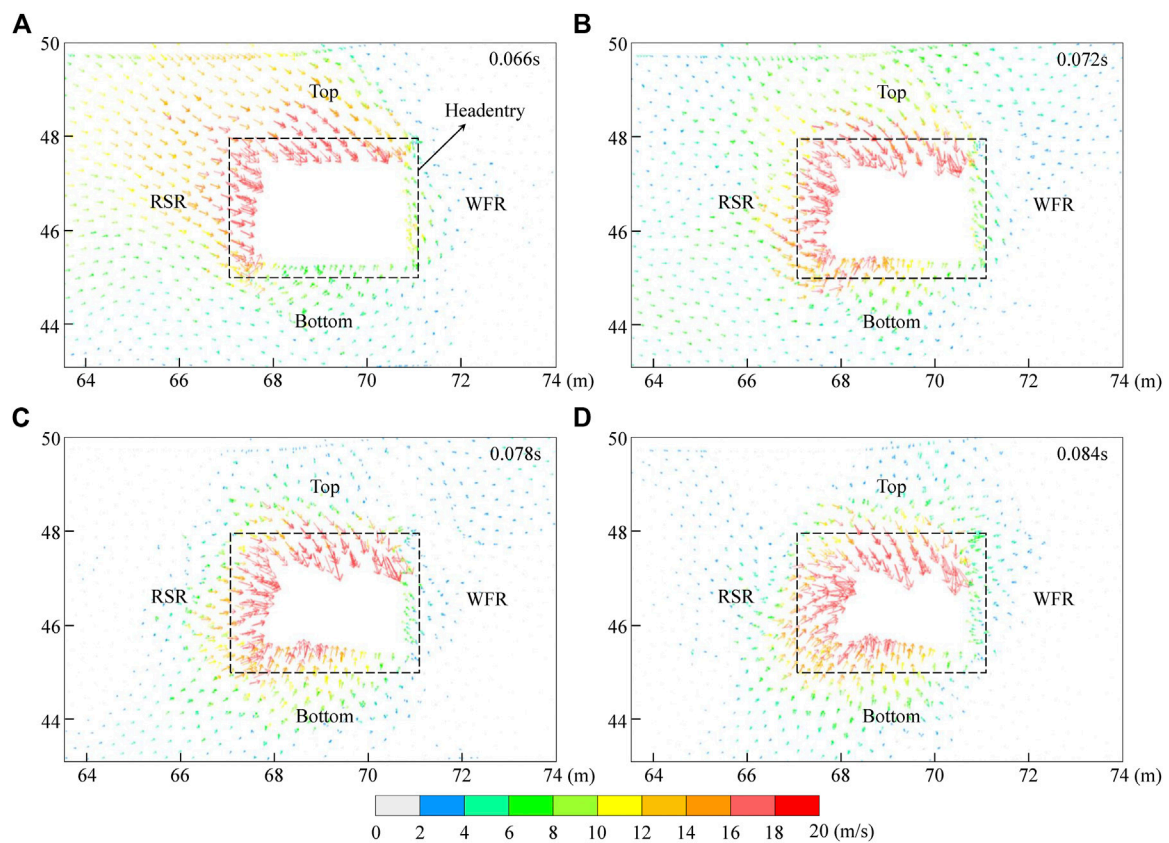


FIGURE 10

Velocity vectors around the headentry at different dynamic times: (A) dynamic time is 0.066s in the MSTCB, (B) dynamic time is 0.072s in the MSTCB, (C) dynamic time is 0.078s in the MSTCB, and (D) dynamic time is 0.084s in the MSTCB.

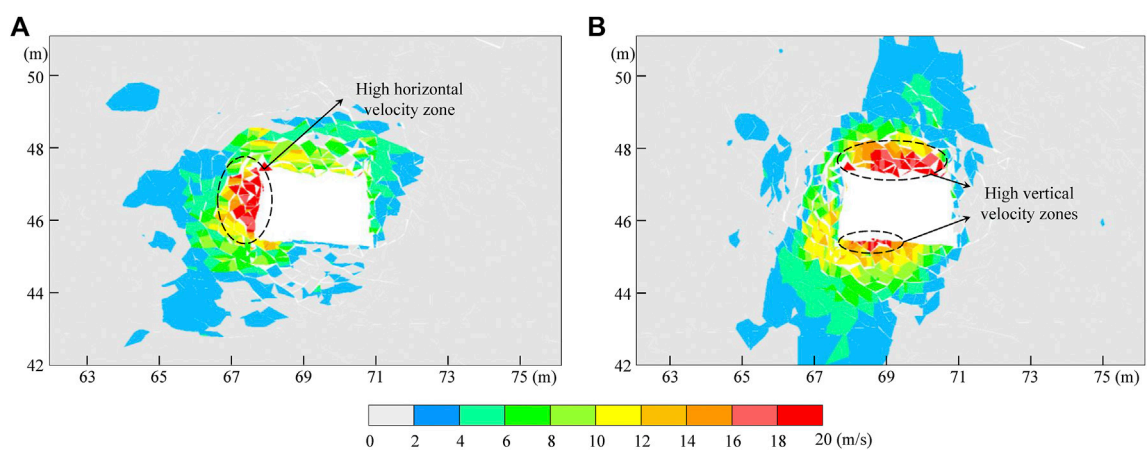


FIGURE 11

Ejection velocities of fragments in the MSTCB: (A) the horizontal ejection velocity, and (B) the vertical ejection velocity.

seismicity has an important effect on the MSTCB. It can be predicted that the dynamic stress will increase with the increase of the mining induced seismicity vibration velocity. However, the MSTCB in

different areas of the headentry had significantly different failure characteristics. For example, quite severe coal bursts occurred at the top and in the RSR, while only a small amount of low-velocity

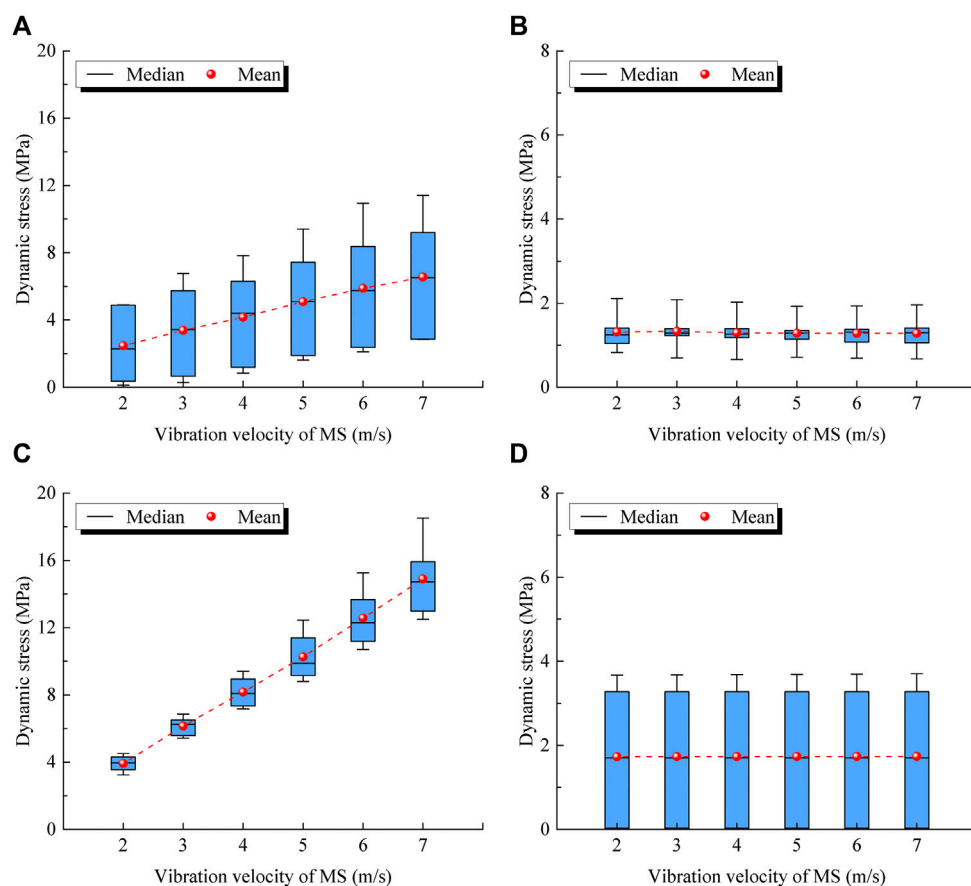


FIGURE 12

Dynamic stresses around the headentry considering different vibration velocities: (A) at the top, (B) at the bottom, (C) at RSR, and (D) at WFR.

ejections occurred in the WFR. Therefore the effect of the mining induced seismicity on coal bursts in different areas of the headentry needs to be further discussed. This can provide guidance for the determination of the critical areas for the MSTCB control in the headentry.

Figure 12 illustrates the relationship between dynamic stresses in different areas of the headentry and the vibration velocity of the mining induced seismicity, for any area, all six monitoring points are included. As shown in Figures 12A,C, the dynamic stresses in the top and RSR increased with the vibration velocity, indicating that the mining induced seismicity in the roof has a significant effect on the dynamic stresses in the top and RSR of the headentry. In addition, the growth rate of dynamic stress in the RSR is greater than that in the top. Therefore, the risk of the MSTCB in the RSR will increase significantly with the increase of vibration velocity. It is worth to be noted that the dynamic stresses in the bottom and WFR did not increase with increasing vibration velocity, and there was no significant change in the dynamic stresses in the bottom and WFR under different vibration velocities, as shown in Figures 12B,D. This is

probably because the dynamic stresses in the bottom and WFR are mainly caused by the coal bursts in the top and RSR, rather than propagation of the seismic wave.

Figure 13 illustrates the relationship between ejection velocity and the vibration velocity in different areas of the headentry, for any area, all six monitoring points are included. As shown in Figures 13A and 13C, the injection velocity in the top and RSR increased with increasing vibration velocity, which is consistent with the results obtained in the laboratory (Li et al., 2021a). The result indicates that the mining induced seismicity in the roof is a key factor affecting the occurrence of coal bursts in the top and RSR of the headentry. However, the ejection velocity in the bottom and WFR did not increase significantly with increasing vibration velocity, as shown in Figures 13B and 13D. The reasons for the failures in the bottom and the WFR may be the transfer of stress and energy due to the development of the coal bursts at the top and the RSR. The maximum ejection velocity always occurs in the RSR, indicating that the RSR is the most dangerous area in the MSTCB.

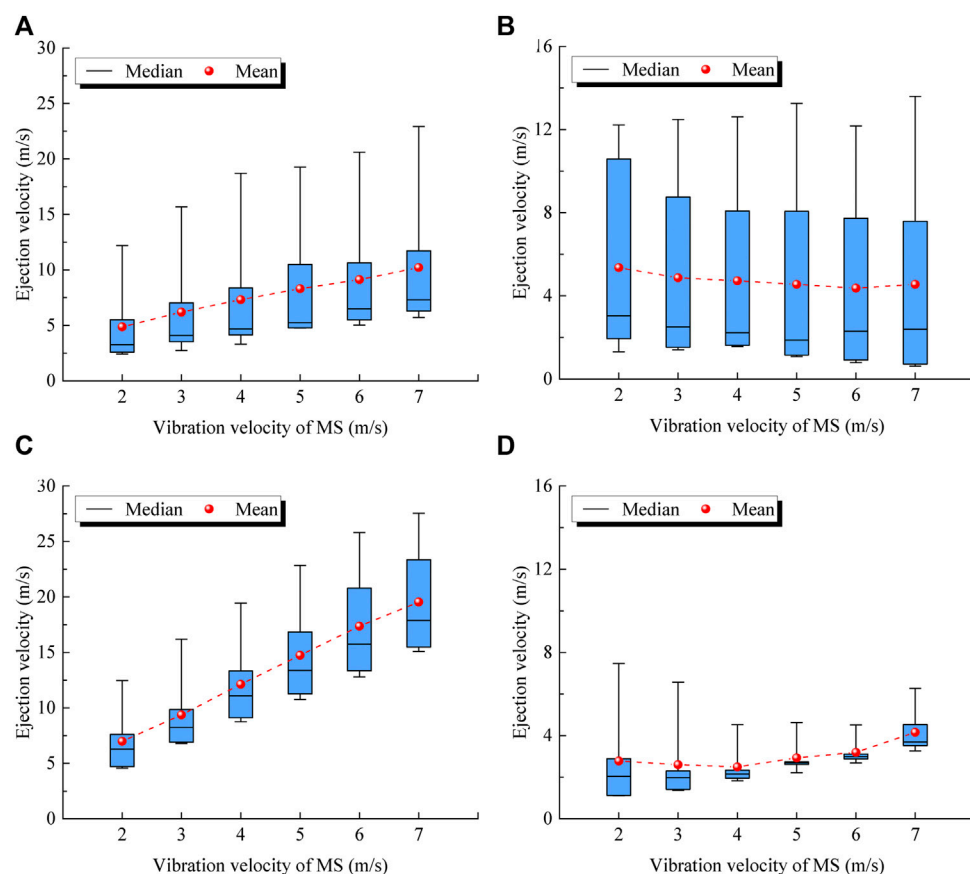


FIGURE 13

Ejection velocities around the headentry considering different vibration velocities: (A) at the top, (B) at the bottom, (C) at RSR, and (D) at WFR.

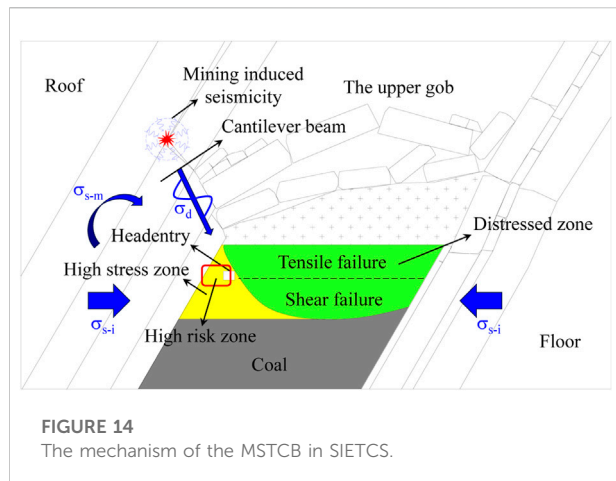
Many studies have reported the ejection velocity of coal fragments in coal bursts based on experimental observations or theoretical analysis. For example, (Yang et al., 2020a) proposed an ejection velocity estimation method and applied it to analyze a coal burst in an Australian coal mine, and found that the ejection velocity of fragments in the coal burst ranged from 26.55 to 26.62 m/s. Frith et al. (2020) analyzed a development coal burst and concluded that  $3.8 \times 10^4$  kg of coal was ejected at a velocity of 22 m/s during the coal burst. (Li et al., 2021a). measured the ejection velocity of fragments during coal bursts in the laboratory, and the results showed that most of the ejection velocities were in the range of 10–30 m/s. In this study, the maximum ejection velocities of coal fragments in MSTCBs under different vibration velocities were 12.47, 16.18, 19.45, 22.84, 25.82, and 27.53 m/s. The simulation ejection velocities are in good agreement with the mentioned findings.

## 5.2 Failure mechanism

As shown in Figure 14, a large destress zone is formed except for a triangular zone on the roof side. The coal burst

risk in the destress zone is significantly reduced. There is a high initial static stress  $\sigma_{s-i}$  in the triangular zone under the clamping of the roof and floor, causing a high risk of coal bursts. A steeply inclined cantilever beam is formed in the roof and the length of the cantilever beam gradually increases with the section mining, resulting in a tendency for the cantilever beam to rotate toward the gob. However, the rotation is restricted by the coal in the triangular zone. Therefore, additional static stress will be formed in the triangular zone, which is called mining-induced static stress  $\sigma_{s-m}$ . The superposition of the initial static stress and the mining-induced static stress leads to the formation of high static stresses in the coal on the roof side. In addition, high-energy mining induced seismicity often occurs during the mining of SIETCS. The propagation of high-energy mining induced seismicity causes dynamic stress  $\sigma_d$ . The MSTCBs occur when the superposition of the initial static stress, the mining-induced static stress and the dynamic stress exceeds the ultimate strength of the coal  $\sigma_u$ , as shown in Eq. 5.

$$\sigma_{s-i} + \sigma_{s-m} + \sigma_d \geq \sigma_u \quad (5)$$



where  $\sigma_{s-i}$ ,  $\sigma_{s-m}$ , and  $\sigma_d$  are the initial static stress, the mining-induced static stress and the dynamic stress. And  $\sigma_u$  is the ultimate strength of the coal.

### 5.3 Coal burst control in the headentry

The high risk areas for MSTCBs in the headentry were identified as the top, RSR, and the bottom near the roof. Accordingly, the MSTCB prevention measures were proposed, as shown in

**Figure 15A.** High-energy mining induced seismicity in the roof plays a critical role for MSTCBs. Therefore, pre-splitting blasting was applied to the roof to avoid the occurrence of high-energy mining induced seismicity caused by a large-scale breakage of the roof. In addition, a number of measures including large diameter drilling and blasting in the coal were employed to create distress zones. It should be noted that the spacing of the boreholes in the RSR is smaller compared to the WFR. The design parameters are shown in [Table 4](#).

Mining induced seismicity monitoring was performed at the 5,521-20 working face through a micro-seismic monitoring system. As shown in **Figure 15B**, the change in total energy presents a periodical characteristic, which is related to the periodic adjustment of the structure in the roof. The total energy increases significantly when the structure experiences change. After the application of pre-splitting, the number of seismic events with energy greater than  $10^4$  J decreased significantly and the number of low-energy seismic events increased. This is because pre-cracks formed in the roof after pre-splitting blasting, which will develop under abutment pressure. The sudden large scale fracturing is replaced by the development of pre-cracks. The stress in the coal will increase under the effect of high-energy seismic events. In addition, the failure of the structure is more likely to be triggered by high-energy seismic events. Thus, the decrease in high-energy seismic events indicates a reduction in coal burst risk. Mining practice at the 5521-20 working face demonstrates that the measures are effective for the prevention and control of MSTCBs in SIETCSs.

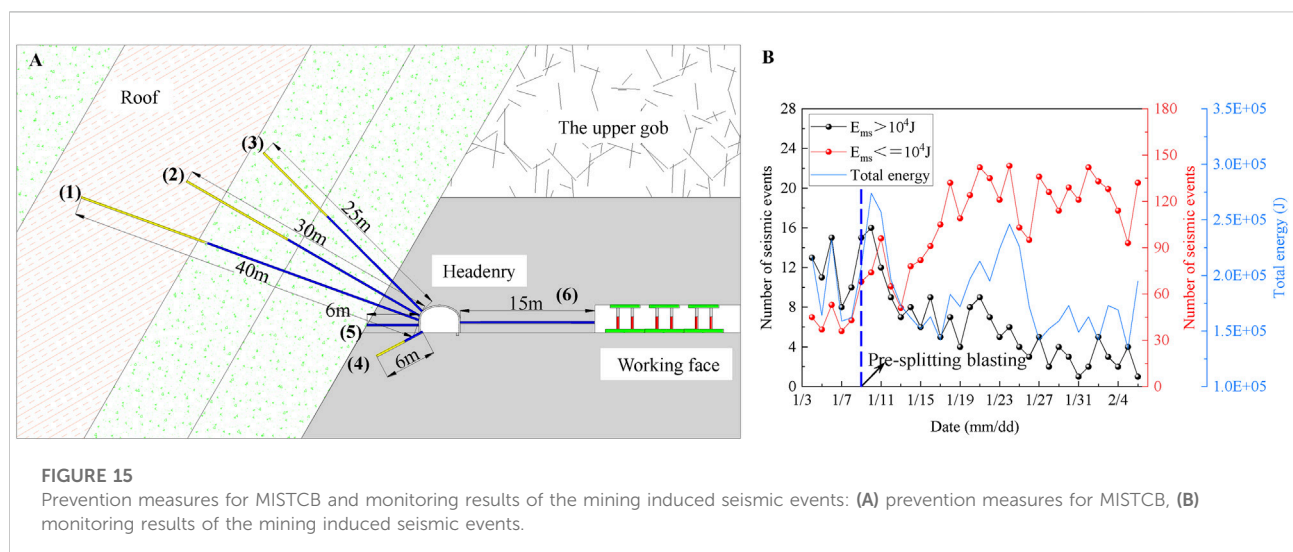


**TABLE 4** Design parameters for boreholes 1#–6# (see [Figure 15A](#)).

Number	Angle (°)	Distance between Boreholes (m)	Diameter of Borehole (mm)	Length of Borehole (m)	Explosive Charge Length (m)	Sealing Length (m)
1	20	20	75	40	15	25
2	30	20	75	30	13	17
3	45	20	75	25	10	15
4	30	5	75	6	3.5	2.5
5	0	5	110	6	/	/
6	0	10	110	15	/	/

## 6 Conclusion

In this paper, the dynamic failure process of the MSTCB in SIETCS is investigated using UDEC simulation based on a coal burst accident. And the effect of mining induced seismicity vibration velocity on MSTCBs in SIETCSs is discussed. The main conclusions are as follows.

- 1) A large destress zone is formed in the SIETCS after section mining, except for a triangular area on the roof side. The triangular area is undeveloped with cracks and has a good capacity for storing stress and energy, which causes a high coal burst risk. During the MSTCB, a large number of shear cracks appear first near the roadway surface. Then, the cracks develop rapidly to the depth. Eventually, the MSTCB leads to the formation of a tensile failure zone near the roadway surface and a shear failure zone at the deeper part, respectively.
- 2) The mechanism of the MSTCB is: under the effect of the cantilever beam rotation, as a pivot point, the coal on the roof side in SIETCS is in high static stress. And high-energy mining induced seismicity in the roof causes additional dynamic stress on the coal, especially at the RSR and top of the roadway. MSTCB occurs as the superposition of the static stress and the dynamic stress exceeds the ultimate strength of the coal.
- 3) The vibration velocity of mining induced seismicity in the roof has a significant and asymmetric effect on the MSTCB in SIETCS. The dynamic stress and mean ejection velocity in the RSR and top of the roadway are positively correlated with the vibration velocity. However, the vibration velocity only has a weak effect on the WFR and bottom of the roadway.

## Data availability statement

The original contributions presented in the study are included in the article/supplementary material, further inquiries can be directed to the corresponding authors.

## Author contributions

All authors listed have made a substantial, direct, and intellectual contribution to the work and approved it for

publication. Conceptualization: JC, LD, and JH; Methodology: JC and GZ; Software: LD; Validation: JC and JH; Formal Analysis: JC, JH, and ZW; Investigation: JC, GZ, and JB; Data curation: JC, ZH, and ZW; Writing-Original Draft Preparation: JC; Writing-Review & Editing: ZH and JB; Supervision: JC, LD, and GZ; Project Administration: LD and GZ; Funding Acquisition: LD and GZ. All authors have read and agreed to the published version of the manuscript.

## Funding

This work was conducted with support from the National Natural Science Foundation of China (Grant Nos. 51934007, 51874292, and 51904235).

## Acknowledgments

The first author JC would like to express his sincere thanks to the China Scholarship Council (CSC) for the financial support for his study at TU Bergakademie Freiberg, Germany.

## Conflict of interest

The authors declare that the research was conducted in the absence of any commercial or financial relationships that could be construed as a potential conflict of interest.

## Publisher's note

All claims expressed in this article are solely those of the authors and do not necessarily represent those of their affiliated organizations, or those of the publisher, the editors and the reviewers. Any product that may be evaluated in this article, or claim that may be made by its manufacturer, is not guaranteed or endorsed by the publisher.

## References

- Cai, W., Dou, L., Si, G., and Hu, Y. (2021). Fault-induced coal burst mechanism under mining-induced static and dynamic stresses. *Engineering* 7 (5), 687–700. doi:10.1016/j.eng.2020.03.017
- Cao, J., Dou, L., Zhu, G., He, J., Wang, S., and Zhou, K. (2020). Mechanisms of rock burst in horizontal section mining of a steeply inclined extra-thick coal seam and prevention technology. *Energies* 13 (22), 6043. doi:10.3390/en13226043
- Cui, F., Lei, Z., Chen, J., Bo, C., Yang, Y., Changlu, L., et al. (2019). Research on reducing mining-induced disasters by filling in steeply inclined thick coal seams. *Sustainability* 11 (20), 5802. doi:10.3390/su11205802
- Dai, L., Pan, Y., Li, Z., Wang, A., Xiao, Y., Liu, F., et al. (2021). Quantitative mechanism of roadway rockbursts in deep extra-thick coal seams: Theory and case histories. *Tunn. Undergr. Space Technol.* 111, 103861. doi:10.1016/j.tust.2021.103861



- Dou, L., and He, X. (2001). *Theory and technology of rock burst prevention*. Xuzhou: China University of Mining and Technology Press.
- Dou, L., Mu, Z., Li, Z., Cao, A., and Gong, S. (2014). Research progress of monitoring, forecasting, and prevention of rockburst in underground coal mining in China. *Int. J. Coal Sci. Technol.* 1 (3), 278–288. doi:10.1007/s40789-014-0044-z
- Dou, L., He, J., Cao, A., Gong, S., and Cai, W. (2015). Rock burst prevention methods based on theory of dynamic and static combined load induced in coal mine. *J. China Coal Soc.* 40 (7), 1469–1476. doi:10.13225/j.cnki.jccs.2014.1815
- Du, F., Wang, K., Zhang, X., Xin, C., Shu, L., and Wang, G. (2020). Experimental study of coal–gas outburst: Insights from coal–rock structure, gas pressure and adsorptivity. *Nat. Resour. Res.* 29 (4), 2481–2493. doi:10.1007/s11053-020-09621-7
- Frith, R., Reed, G., and Jones, A. (2020). A causation mechanism for coal bursts during roadway development based on the major horizontal stress in coal: Very specific structural geology causing a localised loss of effective coal confinement and Newton's second law. *Int. J. Min. Sci. Technol.* 30 (1), 39–47. doi:10.1016/j.ijmst.2019.12.018
- Gao, F. Q., and Stead, D. (2014). The application of a modified Voronoi logic to brittle fracture modelling at the laboratory and field scale. *Int. J. Rock Mech. Min. Sci.* 68, 1–14. doi:10.1016/j.ijrmms.2014.02.003
- Gao, F., and Yang, L. (2021). Experimental and numerical investigation on the role of energy transition in strainbursts. *Rock Mech. Rock Eng.* 54 (9), 5057–5070. doi:10.1007/s00603-021-02550-8
- Gao, F., Stead, D., and Kang, H. (2014). Numerical simulation of squeezing failure in a coal mine roadway due to mining-induced stresses. *Rock Mech. Rock Eng.* 48 (4), 1635–1645. doi:10.1007/s00603-014-0653-2
- He, J., Dou, L.-M., Cai, W., Li, Z.-L., and Ding, Y.-L. (2015). *In situ* test study of characteristics of coal mining dynamic load. *Shock Vib.* 2015, 1–8. doi:10.1155/2015/121053
- He, J., Dou, L., Gong, S., Li, J., and Ma, Z. (2017). Rock burst assessment and prediction by dynamic and static stress analysis based on micro-seismic monitoring. *Int. J. Rock Mech. Min. Sci.* 93, 46–53. doi:10.1016/j.ijrmms.2017.01.005
- He, S., Song, D., Li, Z., He, X., Chen, J., Li, D., et al. (2019). Precursor of spatio-temporal evolution law of MS and AE activities for rock burst warning in steeply inclined and extremely thick coal seams under caving mining conditions. *Rock Mech. Rock Eng.* 52 (7), 2415–2435. doi:10.1007/s00603-018-1690-z
- He, S., Song, D., He, X., Chen, J., Ren, T., Li, Z., et al. (2020). Coupled mechanism of compression and prying-induced rock burst in steeply inclined coal seams and principles for its prevention. *Tunn. Undergr. Space Technol.* 98, 103327. doi:10.1016/j.tust.2020.103327
- He, H., Dou, L., Fan, J., Du, T., and Sun, X. (2012a). Deep-hole directional fracturing of thick hard roof for rockburst prevention. *Tunn. Undergr. Space Technol.* 32, 34–43. doi:10.1016/j.tust.2012.05.002
- He, J., Dou, L., Cao, A., Gong, S., and Lü, J. (2012b). Rock burst induced by roof breakage and its prevention. *J. Cent. South Univ.* 19 (4), 1086–1091. doi:10.1007/s11771-012-1113-3
- Jiang, Y., Zhao, Y., Wang, H., and Zhu, J. (2017). A review of mechanism and prevention technologies of coal bumps in China. *J. Rock Mech. Geotechnical Eng.* 9 (1), 180–194. doi:10.1016/j.jrmge.2016.05.008
- Konicek, P., Saharan, M. R., and Mitri, H. (2011). Destress blasting in coal mining – state-of-the-art review. *Procedia Eng.* 26, 179–194. doi:10.1016/j.proeng.2011.11.2157
- Konicek, P., Soucek, K., Stas, L., and Singh, R. (2013). Long-hole destress blasting for rockburst control during deep underground coal mining. *Int. J. Rock Mech. Min. Sci.* 61, 141–153. doi:10.1016/j.ijrmms.2013.02.001
- Lai, X., Yang, Y., and Zhang, L. (2021). Research on structural evolution and microseismic response characteristics of overlying strata during repeated mining of steeply inclined and extra thick coal seams. *Lithosphere* 2021 (4), 8047321. doi:10.2113/2021/8047321
- Li, Y., Yang, R., Fang, S., Lin, H., Lu, S., Zhu, Y., et al. (2022). Failure analysis and control measures of deep roadway with composite roof: A case study. *Int. J. Coal Sci. Technol.* 9 (1), 2. doi:10.1007/s40789-022-00469-1
- Li, J., Zhao, J., Gong, S. Y., Wang, H. C., Ju, M. H., Du, K., et al. (2021a). Mechanical anisotropy of coal under coupled biaxial static and dynamic loads. *Int. J. Rock Mech. Min. Sci.* 143, 104807. doi:10.1016/j.ijrmms.2021.104807
- Li, Z., He, S., Song, D., He, X., Dou, L., Chen, J., et al. (2021b). Microseismic temporal-spatial precursory characteristics and early warning method of rockburst in steeply inclined and extremely thick coal seam. *Energies* 14 (4), 1186. doi:10.3390/en14041186
- Mark, C. (2018). Coal bursts that occur during development: A rock mechanics enigma. *Int. J. Min. Sci. Technol.* 28 (1), 35–42. doi:10.1016/j.ijmst.2017.11.014
- Mottahedi, A., and Ataei, M. (2019). Fuzzy fault tree analysis for coal burst occurrence probability in underground coal mining. *Tunn. Undergr. Space Technol.* 83, 165–174. doi:10.1016/j.tust.2018.09.029
- Ptáček, J. (2017). Rockburst in ostrava-karvina coalfield. *Procedia Eng.* 191, 1144–1151. doi:10.1016/j.proeng.2017.05.289
- Qian, M., Miao, X., and Xu, J. (2000). *Key strata theory in ground control*. Xuzhou: China University of Mining and Technology Press.
- Shapiro, S. A., Dinske, C., and Rothert, E. (2006). Hydraulic-fracturing controlled dynamics of microseismic clouds. *Geophys. Res. Lett.* 33 (14), L14312. doi:10.1029/2006gl026365
- Si, G., Cai, W., Wang, S., and Li, X. (2020). Prediction of relatively high-energy seismic events using spatial-temporal parametrisation of mining-induced seismicity. *Rock Mech. Rock Eng.* 53 (11), 5111–5132. doi:10.1007/s00603-020-02210-3
- Singh, M., and Seshagiri Rao, K. (2005). Empirical methods to estimate the strength of jointed rock masses. *Eng. Geol.* 77 (1–2), 127–137. doi:10.1016/j.enggeo.2004.09.001
- Stec, K. (2007). Characteristics of seismic activity of the upper silesian coal basin in Poland. *Geophys. J. Int.* 168 (2), 757–768. doi:10.1111/j.1365-246x.2006.03227.x
- Wang, K., and Du, F. (2020). Coal-gas compound dynamic disasters in China: A review. *Process Saf. Environ. Prot.* 133, 1–17. doi:10.1016/j.psep.2019.10.006
- Wang, C., Cao, A., Zhang, C., and Canbulat, I. (2019a). A new method to assess coal burst risks using dynamic and static loading analysis. *Rock Mech. Rock Eng.* 53 (3), 1113–1128. doi:10.1007/s00603-019-01968-5
- Wang, S., Dou, L., Mu, Z., Cao, J., and Li, X. (2019b). Study on roof breakage-induced roadway coal burst in an extrathick steeply inclined coal seam. *Shock Vib.* 2019, 1–14. doi:10.1155/2019/2969483
- Wang, Z., Dou, L., and Wang, G. (2019c). Coal burst induced by horizontal section mining of a steeply inclined, extra-thick coal seam and its prevention: A case study from Yaojie No. 3 coal mine, China. *Shock Vib.* 2019, 1–13. doi:10.1155/2019/8469019
- Wang, S.-C., Dou, L.-M., Wang, Z.-Y., Bai, J.-Z., and Chai, Y.-J. (2020). Mechanism of coal bursts induced by horizontal section mining of steeply inclined coal seams and application of microseismic multiparameter monitoring in early warning. *Adv. Civ. Eng.* 2020, 1–14. doi:10.1155/2020/1048624
- Wang, S., Cao, A., Wang, Z., Cao, J., Liu, Y., Xue, C., et al. (2022). Study on mechanism of rock burst in horizontal section mining of a steeply inclined extra-thick coal seam. *Lithosphere* 2022 (11), 7058797. doi:10.2113/2022/7058797
- Xie, P., Luo, Y., Wu, Y., Gao, X., Luo, S., and Zeng, Y. (2019). Roof deformation associated with mining of two panels in steeply dipping coal seam using subsurface subsidence prediction model and physical simulation experiment. *Min. Metallurgy Explor.* 37 (2), 581–591. doi:10.1007/s42461-019-00156-x
- Xue, D., Zhou, J., Liu, Y., and Gao, L. (2020). On the excavation-induced stress drop in damaged coal considering a coupled yield and failure criterion. *Int. J. Coal Sci. Technol.* 7 (1), 58–67. doi:10.1007/s40789-020-00299-z
- Xue, Y., Liu, J., Ranjith, P. G., Gao, F., Xie, H., and Wang, J. (2022). Changes in microstructure and mechanical properties of low-permeability coal induced by pulsating nitrogen fatigue fracturing tests. *Rock Mech. Rock Eng.* doi:10.1007/s00603-022-03031-2
- Xue, Y., Ranjith, P. G., Chen, Y., Cai, C., Gao, F., and Liu, X. (2023). Nonlinear mechanical characteristics and damage constitutive model of coal under CO<sub>2</sub> adsorption during geological sequestration. *Fuel* 331, 125690. doi:10.1016/j.fuel.2022.125690
- Yang, S., Li, L., and Deng, X. (2019). Disaster-causing mechanism of roof “toppling-slumping” failure in a horizontal sublevel top-coal caving face. *Nat. Hazards (Dordr.)* 100 (2), 757–780. doi:10.1007/s11069-019-03841-8

Yang, X., Ren, T., and Tan, L. (2020a). Estimation of average ejection velocity generated by rib burst under compression load. *Int. J. Rock Mech. Min. Sci.* 128, 104277. doi:10.1016/j.ijrmms.2020.104277

Yang, Y., Lai, X., Shan, P., and Cui, F. (2020b). Comprehensive analysis of dynamic instability characteristics of steeply inclined coal-rock mass. *Arab. J. Geosci.* 13 (6), 241. doi:10.1007/s12517-020-5217-z

Yun, D., Liu, Z., Cheng, W., Fan, Z., Wang, D., and Zhang, Y. (2017). Monitoring strata behavior due to multi-slicing top coal caving longwall mining in steeply dipping extra thick coal seam. *Int. J. Min. Sci. Technol.* 27 (1), 179–184. doi:10.1016/j.ijmst.2016.11.002

Zhang, L., and Einstein, H. H. (2004). Using RQD to estimate the deformation modulus of rock masses. *Int. J. Rock Mech. Min. Sci.* 41 (2), 337–341. doi:10.1016/s1365-1609(03)00100-x

Zhang, C., Canbulat, I., Hebblewhite, B., and Ward, C. R. (2017). Assessing coal burst phenomena in mining and insights into directions for future research. *Int. J. Coal Geol.* 179, 28–44. doi:10.1016/j.coal.2017.05.011

Zou, Q., Zhang, T., Ma, T., Tian, S., Jia, X., and Jiang, Z. (2022). Effect of water-based SiO<sub>2</sub> nanofluid on surface wettability of raw coal. *Energy* 254, 124228. doi:10.1016/j.energy.2022.124228



## OPEN ACCESS

## EDITED BY

Guang-Liang Feng,  
Institute of Rock and Soil Mechanics (CAS),  
China

## REVIEWED BY

Jiawei Xie,  
The University of Newcastle, Australia  
Luqi Wang,  
Chongqing University, China  
Paraskevas Tsangaratos,  
National Technical University of Athens,  
Greece

## \*CORRESPONDENCE

Anyu Hong,  
✉ honganyu@ncu.edu.cn

## SPECIALTY SECTION

This article was submitted to Geohazards  
and Georisks,  
a section of the journal  
Frontiers in Earth Science

RECEIVED 06 December 2022

ACCEPTED 05 January 2023

PUBLISHED 17 January 2023

## CITATION

Chen Y, Zhang X, Yang K, Zeng S and  
Hong A (2023), Modeling rules of regional  
flash flood susceptibility prediction using  
different machine learning models.  
*Front. Earth Sci.* 11:1117004.  
doi: 10.3389/feart.2023.1117004

## COPYRIGHT

© 2023 Chen, Zhang, Yang, Zeng and  
Hong. This is an open-access article  
distributed under the terms of the [Creative  
Commons Attribution License \(CC BY\)](#).  
The use, distribution or reproduction in  
other forums is permitted, provided the  
original author(s) and the copyright  
owner(s) are credited and that the original  
publication in this journal is cited, in  
accordance with accepted academic  
practice. No use, distribution or  
reproduction is permitted which does not  
comply with these terms.

# Modeling rules of regional flash flood susceptibility prediction using different machine learning models

Yuguo Chen, Xinyi Zhang, Kejun Yang, Shiyi Zeng and Anyu Hong\*

School of Civil Engineering and Architecture, Nanchang University, Nanchang, China

The prediction performance of several machine learning models for regional flash flood susceptibility is characterized by variability and regionality. Four typical machine learning models, including multilayer perceptron (MLP), logistic regression (LR), support vector machine (SVM), and random forest (RF), are proposed to carry out flash flood susceptibility modeling in order to investigate the modeling rules of different machine learning models in predicting flash flood susceptibility. The original data of 14 environmental factors, such as elevation, slope, aspect, gully density, and highway density, are chosen as input variables for the MLP, LR, SVM, and RF models in order to estimate and map the distribution of the flash flood susceptibility index in Longnan County, Jiangxi Province, China. Finally, the prediction performance of various models and modeling rules is evaluated using the ROC curve and the susceptibility index distribution features. The findings show that: 1) Machine learning models can accurately assess the region's vulnerability to flash floods. The MLP, LR, SVM, and RF models all predict susceptibility very well. 2) The MLP (AUC=0.973, MV=0.1017, SD=0.2627) model has the best prediction performance for flash flood susceptibility, followed by the SVM (AUC=0.964, MV=0.1090, SD=0.2561) and RF (AUC=0.975, MV=0.2041, SD=0.1943) models, and the LR (AUC=0.882, MV=0.2613, SD=0.2913) model. 3) To a large extent, environmental factors such as elevation, gully density, and population density influence flash flood susceptibility.

## KEYWORDS

flash flood susceptibility prediction, uncertainty analysis, machine learning, multilayer perceptron, support vector machine, random forest

## 1 Introduction

A flash flood is defined as rapid flooding within the distribution of drainage basins in hilly areas (Bobrowsky, 2013), and it is characterized by rapid disaster generation, strong ring-breaking, and unpredictability, as well as the potential for a large number of casualties (Marchi et al., 2010). China has paid close attention in recent years to the predictive study of geological hazard susceptibility. Because China has many hilly areas, flash floods affect a wide range of areas, and regional flash floods are easy to produce under short-term heavy rainfall (Bobrowsky, 2013). With China's elevated level of climate risk and an increase in extreme weather, such as heavy rainfall, regional research on flash flood susceptibility is becoming increasingly important.

With the continuous development of GIS and machine learning methods in recent years, an increasing number of researchers have cross-fertilized the engineering geology analogy method across disciplines to obtain more accurate susceptibility prediction models (István et al., 2022). Processing preliminary data, obtaining information on required environmental factors, selecting basic environmental factors, dividing prediction units, distributing training and

test datasets, selecting susceptibility prediction models, plotting accuracy curves, and testing results are typical steps in susceptibility prediction modeling (Huang et al., 2021a). Choosing machine learning models is critical to modeling uncertainty, according to the susceptibility prediction modeling steps. Different machine learning models have different effects on regional susceptibility prediction results; thus, the prediction performance of different machine learning models varies (Ha et al., 2021). According to existing studies, machine learning models are widely used in susceptibility prediction modeling due to their powerful ability to handle non-linear data with different scales and from different types of sources (Zhang et al., 2022). Recently, the research field of machine learning models has been rapidly expanding, with models such as multilayer perceptron (MLP) (Haribabu et al., 2021), support vector machine (SVM) (Xiong et al., 2019), logistic regression (LR) (Nguyen and Bouvier, 2019; Huang et al., 2020a), random forest (RF) (Abedi et al., 2022), decision trees (Ngo et al., 2021), and artificial neural networks (Dahri et al., 2022).

Numerous studies have demonstrated that the susceptibility prediction results of the aforementioned machine learning models are highly credible. In other words, it is possible to assess the vulnerability of actual geological hazards (Jiang et al., 2018; Huang et al., 2021b). However, the selection of susceptibility prediction models is currently not well defined, and the weights of input variables and analysis methods differ between machine learning models (Ha et al., 2021). Meanwhile, the machine learning models are regional, which means that the prediction accuracy of each model varies from district to district (Huang et al., 2020b). Roy et al. (2020) used machine learning models, for example, to predict the impact of climate and soil characteristics on flash flood susceptibility. They concluded that the RF model outperforms SVM in prediction performance and has the advantages of a simple implementation process, strong data mining capability, and broad applicability. Zhao et al. (2018) classified and evaluated flash flood susceptibility using multiple machine learning models. They discovered that the RF model outperformed other models such as SVM and ANN in identifying flash flood-prone areas. Elkhachy (2022) investigated flood depth using machine learning models based on remotely sensed data and concluded that the ML model outperformed the RFR. Wang et al. (2021) demonstrated the multilayer perceptron-probability density hybrid model's excellent prediction performance in their study of flash flood susceptibility in Poyang County.

The MLP model has excellent non-linear mapping capabilities in performing susceptibility prediction compared to deterministic models or general linear statistical methods (Li et al., 2019). The LR model is controlled by multiple variables, and the algorithm has the advantage that the independent variables do not need to satisfy a normal distribution (Das and Lepcha, 2019). The SVM model has many unique advantages, which are reflected in solving large sample, non-linear, and high-dimensional pattern recognition problems (Wang et al., 2019). Based on statistical analysis, the RF model has the characteristics of simplicity, ease of calculation, and high accuracy (Demir et al., 2013). Consequently, to analyze and compare the prediction performance of different categories of machine learning models, the above four widely used machine learning models, MLP, LR, SVM, and RF, are chosen for flood susceptibility prediction modeling in this study.

The study of a standardized process for constructing flash flood susceptibility prediction models using machine learning models,

comparing and analyzing the prediction performance of different machine learning models, and carrying out practical engineering applications in Longnan County is of great practical importance for flash flood and geological hazard prevention and control, road planning, and development of appropriate risk mitigation strategies in the southwest and southern China (Sheng et al., 2022). Longnan County, in the southernmost part of Jiangxi Province, is used as an example in this study. ArcGIS 10.2 software and the remotely sensed imagery website are used to extract 14 environmental factors such as topographic and geomorphological factors, hydrological factors, land cover factors, and human activities as input variables for the machine learning model. Denoted as 1 and 0, the flash flood and non-flash flood are considered the output variables. The MLP, LR, SVM, and RF models are then used to predict flash flood susceptibility. Besides, the model's predicted flash flood susceptibility index is imported into ArcGIS 10.2 software to map flash flood susceptibility. Finally, each model's prediction performance is compared and analyzed to verify its applicability and reliability using the receiver operation characteristic (ROC) curve and susceptibility index distribution features.

## 2 Study area and data sources

### 2.1 Study area

Longnan County has a total area of 1,640.55 km<sup>2</sup> and is located in the zone of 114°23'–114°59' E longitude and 24°29'–25°01' N latitude (Figure 1). Longnan County has a typical subtropical humid monsoon climate with an annual average temperature of 19.2°C, according to the data. It has seasonal rainfall, with the wet season lasting from March to August, and the annual average precipitation is approximately 1,506 mm. The Longnan stratum spans the Upper Proterozoic Sinian stratum to the Cenozoic Quaternary stratum. Other strata exist except for the Ordovician and Silurian strata in the middle stratum. The strata in the study area are classified as sedimentary rock, metamorphic rock, intrusive rock, Quaternary alluvial layer, and magmatic rock based on their lithology. Denuded hills are in the middle, where expose Cretaceous and Jurassic thin siltstone, magmatic rocks, and volcanic clastic rocks. The county's surroundings are the Quaternary alluvial layer, which has loose soil. Longnan is high in the southwest and low in the northeast, with folds and fractures as the primary tectonic features (Cui et al., 2016; Zhang et al., 2015). The most common landform types are eroded moderate and low mountainous areas, as well as eroded and denuded hilly areas. Furthermore, the county has a dense population distribution, engages in a variety of engineering activities, and the territory is primarily dependent on the mountains for self-built houses and roads. Because of the lack of slope support measures and means of protection, as well as the high rainfall in the study area, flash floods and other geological hazards are easily triggered. As a result, the predictive modeling of flash floods in this study area is important.

As of 2014, there were 127 geological hazard sites in the study area. The eroded low mountainous area and the eroded and denuded hilly area have the highest hazard sites in each geomorphological area. At the same time, flash floods are primarily distributed in Longnan County's central eroded and denuded hilly area, which is primarily located in the distribution range of metamorphic rocks. Based on previous studies and extensive literature (Guzzetti et al., 1999; Zhao et al., 2018; Roy et al., 2020; Wang et al., 2021; Elkhachy, 2022), the

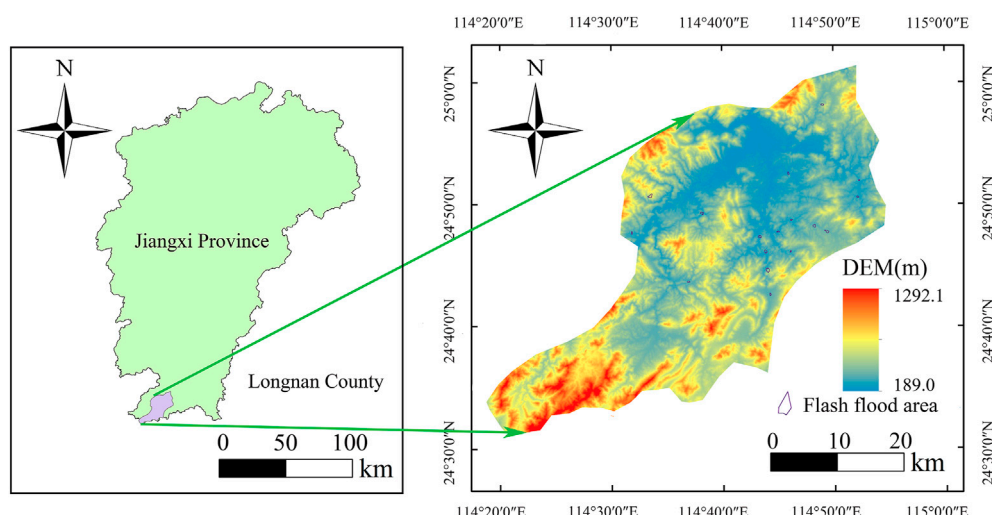


**FIGURE 1**  
Overview of the study area and flash flood inventory.

difficulty of extracting environmental factors, the weight and effect of each type of environmental factor, the topographic and geomorphological characteristics of the study area, and the model's accuracy, 14 environmental factors such as elevation, rainfall, and highway density are chosen as input variables for flood susceptibility prediction modeling. Figure 1 depicts an overview of the study area as well as a flash flood inventory.

## 2.2 Data sources and the classification of grid units

The sources of the flash flood basic data for the study area include: 1) The flood flash inventory investigated by Longnan County Land and Resources Bureau and specific information by field survey; 2) The geodata cloud platform is used to download digital elevation model (DEM) data with a spatial resolution of 30 m. Then, using ArcGIS 10.2 software's spatial analysis tools, extract environmental factors such as elevation, aspect, slope, profile curvature, and plan curvature; 3) Landsat-8 remote sensing images with a spatial resolution of 30 m downloaded from the Chinese Academy of Sciences' Earth Observation Center are used to obtain land cover factors such as the normalized difference vegetation index (NDVI) and modified normalized difference water index (MNDWI); 4) The lithology factor in the study area is derived from a 1:50,000 scale China Hydrogeological map; 5) The rainfall factor is derived by downloading China's average annual rainfall from 1975 to 2015 from the China Meteorological Data Sharing Network (Huang et al., 2022a; Li et al., 2020).

Regional, slope, grid, terrain, and uniform condition units are some of the most commonly used evaluation units (Huang et al., 2021a). Because the grid unit is simple, efficient, and widely used (Xiao et al., 2022), the flash flood inventory chooses a grid with a 30 m resolution as the flash flood prediction unit for this study. The entire research area is divided into 1,842,345 units.

## 3 Research framework

This study compares and analyzes the modeling results of MLP, LR, SVM, and RF models to estimate their susceptibility prediction performance. The following are the main contents.

- (1) Based on the information from the flash flood inventory and the geological environment, 14 basic environmental factors that are highly correlated with flood occurrence are identified. The correlation between the factors is then evaluated using Pearson's correlation coefficients in SPSS Statistics software, and basic environmental factors with absolute correlation coefficients greater than 0.7 are eliminated (Cao et al., 2020; Lee et al., 2020).
- (2) The original data of three environmental factors, NDVI, MNDWI, and surface radiation, are normalized and the other factors are kept constant. Then the original data of 14 environmental factors is directly used as the input variables of four classical machine learning models, MLP, LR, SVM, and RF, and the flash flood and non-flash flood (denoted as 1 and 0) are considered the output variables. The combined flash flood and non-flash flood samples are then randomly divided into two sets, the training dataset and the test dataset, in a 7:3 ratio (Huang et al., 2022b).
- (3) To achieve the best prediction accuracy, the model parameters are adjusted by cross-validation (Yao et al., 2022).
- (4) The model's predicted flash flood susceptibility index is imported into ArcGIS 10.2 software to generate flash flood susceptibility maps. Furthermore, based on the natural break method, the predicted flash flood susceptibility index is divided into five levels: very low, low, moderate, high, and very high (Pham et al., 2020).
- (5) The prediction performance of the four machine learning models discussed above is evaluated using the receiver operation characteristic (ROC) curve and susceptibility index distribution (Haoran et al., 2019).



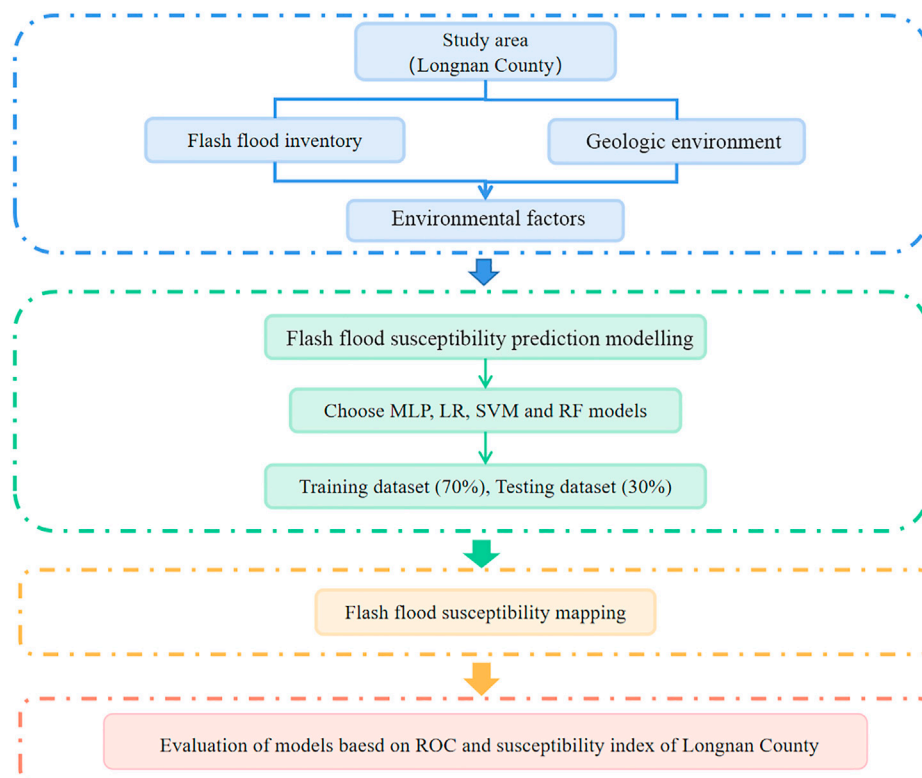


**FIGURE 2**  
The flow chart of the research framework.

## 4 Flash flood-related environmental factors

### 4.1 Environmental factors

The interaction of basic and externally induced environmental factors can result in geological hazards, and the selection of environmental factors can affect the reliability and accuracy of prediction results (Varnes, 1984; Abedi et al., 2022). As a result, identifying the effective environmental factors influencing flood occurrence is critical for flood susceptibility mapping (Rahmati et al., 2016). Based on researches on the causes of flash floods, an analysis of the study area's topographic and geomorphological features, and a review of relevant literature on geological hazard susceptibility, Figure 2 it can be concluded that the occurrence of geological hazards such as flash floods is primarily related to basic environmental factors such as geology, hydrology, and topography, as well as externally induced environmental factors such as rainfall and human activity (Guzzetti et al., 1999; Zhao et al., 2018; Roy et al., 2020; Wang et al., 2021; Elkhachy, 2022). As a result, 14 representative environmental factors, such as elevation, slope, and aspect, are chosen as input variables for the models in this study, as illustrated in Figure 3 and Table 1. The original data of each environmental factor are obtained by using the conversion tool of the spatial analysis tool in ArcGIS software to perform grid turning point, and NDVI, MNDWI, and surface radiation are normalized. The various environmental factors are then used as input variables in predictive modeling to assess flash flood

susceptibility, yielding a more accurate flash flood prediction model.

- (1) Topographic and geomorphological factors: Based on the DEM data obtained through downloading, ArcGIS 10.2 software is used to extract topographic and geomorphological factors such as elevation, slope, aspect, plan curvature, and profile curvature (Sun et al., 2020; Huang et al., 2022c). Elevation is defined as the distance along the plumb line from the grid unit to the earth's ellipsoid (Chang et al., 2020). Furthermore, elevation serves as an indirect proxy for regional climate, land cover distribution, and the impact of rock weathering at different elevations on flash flood evolution (Marjanović et al., 2011). The slope denotes how steep the land surface is. The flow velocity increases as the slope increases (Mahmoud and Gan, 2018). However, on steep slopes, infiltration is less and runoff is more. Excessive runoff can cause flash floods in downslope flat areas. Therefore, the probability of flash floods is generally higher in flat areas near and adjacent to high-gradient side slopes (Pham et al., 2020). Having an effect on soil moisture and weathering, the aspect refers to the direction of the projection of the slope normal on the horizontal plane (Chang et al., 2020; Huang et al., 2020c). Plan curvature is obtained as a representation of flow convergence and divergence using the ArcGIS tool to extract the slope from the aspect (Panahi et al., 2021a). Profile curvature is an extraction of slope from the slope that is primarily concerned with delineating areas of active and weak water runoff (Abedi et al., 2022). The magnitude of ground cutting and fragmentation is conveyed by gully density

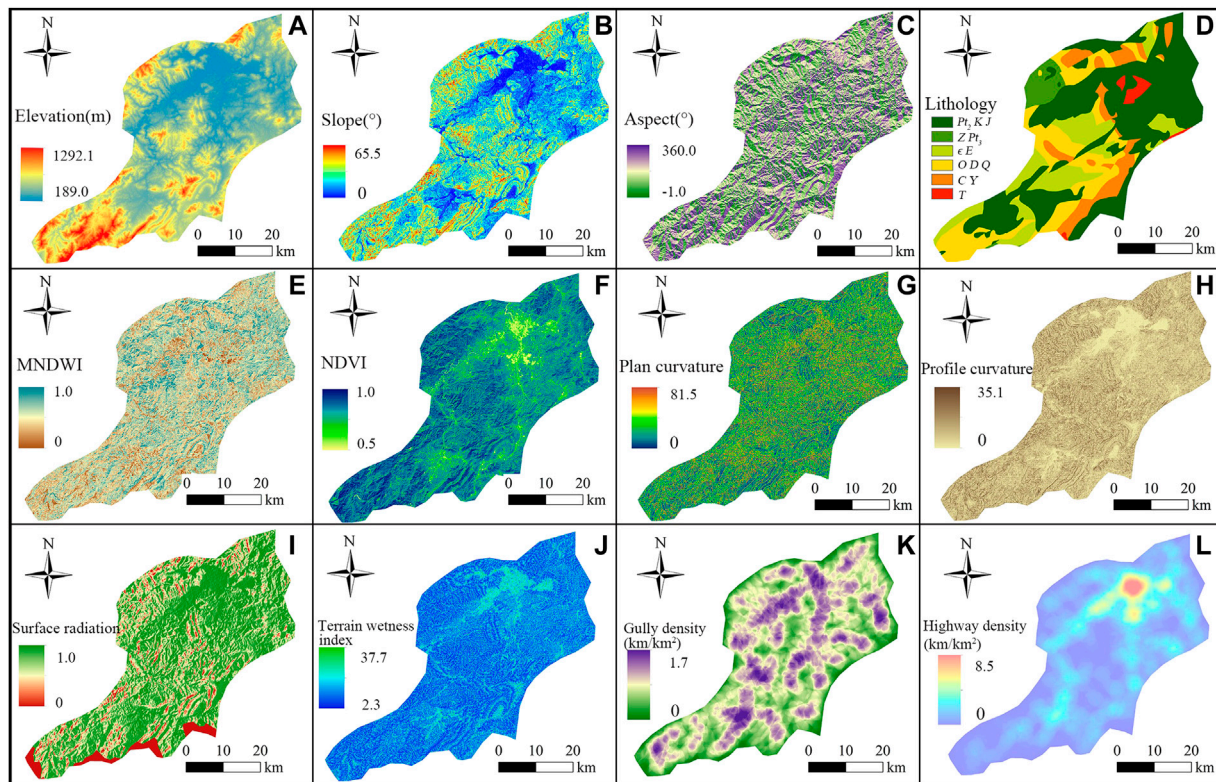


FIGURE 3

Part of the basic environmental factors of flash floods in Longnan County: (A) Elevation, (B) Slope, (C) Aspect, (D) Lithology, (E) MNDWI, (F) NDVI, (G) Plan curvature, (H) Profile curvature, (I) Surface radiation, (J) Terrain wetness index, (K) Gully density, (L) Highway density.

(Sheng et al., 2022). Using the hydrology function of ArcGIS 10.2 Spatial Analyst Toolbox, streams in the study area are extracted from the DEM. The gully density is also calculated using the ArcGIS Spatial Analyst tool, which is the total length of the streams per unit area (Liu et al., 2022). The distribution of all of the above environmental factors has a significant impact on flash flood development.

- (2) Hydrological environmental factors: Water not only accelerates the erosion of geotechnical bodies, but it also causes loosening and deformation of the interbedded layers in the soil, which promotes the development of flash floods in the event of heavy rainfall (Liu et al., 2019a). Flow analysis, depression determination, depression filling, confluence analysis, and river network analysis of DEM data by ArcGIS 10.2 software characterize hydrological environmental factors (Chang et al., 2022). The MNDWI is based on the normalized difference water index with a modification of the wavelength combinations that make up the index and is commonly used to represent surface hydrological information (Sheng et al., 2022). Using MNDWI, you can better reveal the microscopic characteristics of water bodies, such as the distribution of suspended sediments and changes in water quality, and identify water bodies in urban areas with high accuracy (Shu et al., 2022). As an indicator of water accumulation in a watershed, the terrain wetness index implies the likelihood of any area within the watershed approaching saturation and reflects geotechnical wetness (Chapi et al., 2017). Its values are positively correlated with the occurrence of flash floods (Liu et al., 2021). The rainfall factor is calculated by using the interpolation method to extract the grid of China's average annual rainfall from 1975 to 2015 downloaded from the China Meteorological Data Sharing Network. Because flash floods are defined as rapid flooding in a region within a short period of time (Bobrowsky, 2013), they are closely related to rainfall within each region. Using rainfall factors as input variables has a significant impact on flash flood susceptibility model prediction results (Criss, 2022; Dai et al., 2021; Li et al., 2021a).
- (3) Basic geological and land cover factors: The lithology factor can reveal mechanical properties of soil in each area and has a significant impact on the occurrence of geological hazards (Liu et al., 2019b). Longnan County's stratigraphic rocks include sedimentary rocks, metamorphic rocks, intrusive rocks, and Quaternary alluvial layers, according to geological data and previous studies. The vegetation growth and vegetation cover is represented by NDVI (Xiao et al., 2022). Vegetation acts as a soil consolidator and retainer, which helps to prevent erosion. The larger the NDVI value, the larger the vegetation cover and the lower the probability of flooding (Liu et al., 2021). As a result of studying the effect of different vegetation cover on flash flood susceptibility, a more accurate model of flash flood susceptibility can be derived.
- (4) Human activity factors: Highway and population distribution zones are often accompanied by extensive engineering activities, which change the study area's geological characteristics, soil structure, and stress characteristics, thus contributing to the occurrence of geological hazards (Guo et al., 2021; Xiao et al., 2022). Surface radiation is related to

TABLE 1 Original data of each basic environmental factor.

Environmental factors	Variable value	Type	Grids in the study area	Grids in a flash flood
Elevation (m)	[189.038,288.535)	Continuous	321655	571
	[288.535,375.054)		447009	827
	[375.054,457.247)		363067	222
	[457.247,543.766)		281319	187
	[543.766,634.611)		187893	18
	[634.611,738.434)		129592	0
	[738.434,868.213)		82452	0
	[868.213,1292.156]		29358	0
Slope (°)	[0,4.627)	Continuous	303351	365
	[4.627,8.997)		376257	475
	[8.997,13.110)		362859	325
	[13.110,16.965)		296030	318
	[16.965,20.821)		227282	184
	[20.821,24.934)		156110	136
	[24.934,29.818)		90137	18
	[29.818,65.548]		30319	4
Aspect (°)	−1	Continuous	213	0
	[0,22.5),[337.5,360]		225668	185
	[22.5,67.5)		203275	63
	[67.5,112.5)		234841	52
	[112.5,157.5)		261363	185
	[157.5,202.5)		224726	206
	[202.5,247.5)		202983	194
	[247.5,292.5)		226164	433
Lithology	Pt <sub>2</sub> , K, J	Discrete	888416	834
	Z, Pt <sub>3</sub>		72738	244
	ε, E		294991	319
	O, D, Q		366906	122
	C, Y		187841	245
	T		31357	61
MNDWI	[0,0.157)	Continuous	79291	91
	[0.157,0.294)		171110	177
	[0.294,0.408)		278621	232
	[0.408,0.518)		313888	237
	[0.518,0.627)		308717	268
	[0.627,0.745)		303827	314
	[0.745,0.878)		230441	277
	[0.878,1]		156450	229

(Continued on following page)

TABLE 1 (Continued) Original data of each basic environmental factor.

Environmental factors	Variable value	Type	Grids in the study area	Grids in a flash flood
NDVI	[0.480,0.681)	Continuous	33841	17
	[0.681,0.728)		56183	92
	[0.728,0.767)		111291	203
	[0.767,0.797)		227631	445
	[0.797,0.824)		347136	459
	[0.824,0.853)		436101	385
	[0.853,0.885)		405218	159
	[0.885,0.979]		224944	65
Plan curvature	[0,9.907)	Continuous	335955	397
	[9.907,18.535)		405874	344
	[18.535,27.803)		290259	271
	[27.803,37.709)		215758	213
	[37.709,48.256)		162764	184
	[48.256,59.121)		128860	128
	[59.121,70.946)		119318	94
	[70.946,81.492]		183557	194
Profile curvature	[0,1.791)	Continuous	434806	443
	[1.791,3.444)		470627	578
	[3.444,5.235)		378849	386
	[5.235,7.164)		256694	228
	[7.164,9.368)		159318	108
	[9.368,11.986)		88119	57
	[11.986,15.567)		41880	19
	[15.567,35.131]		12054	6
Surface radiation	0	Continuous	0	0
	(0,0.580)		38329	0
	[0.580,0.667)		91940	0
	[0.667,0.741)		131302	19
	[0.741,0.812)		196488	97
	[0.812,0.882)		304086	124
	[0.882,0.941)		309820	184
	[0.941,1]		770380	1401
Terrain wetness index	[2.342,5.259)	Continuous	575455	477
	[5.259,6.880)		719772	756
	[6.880,8.824)		335400	352
	[8.824,11.255)		133303	184
	[11.255,14.496)		59228	30
	[14.496,23.733)		18976	26
	[23.733,33.294)		85	0

(Continued on following page)

TABLE 1 (Continued) Original data of each basic environmental factor.

Environmental factors	Variable value	Type	Grids in the study area	Grids in a flash flood
	[33.294,43.665]		126	0
Gully density (km/km <sup>2</sup> )	[0,0.335]	Continuous	130468	0
	[0.335,0.512]		251649	0
	[0.512,0.670]		304011	177
	[0.670,0.827]		326880	67
	[0.827,0.984]		304533	774
	[0.984,1.141]		243056	336
	[1.141,1.319]		190752	402
	[1.319,1.742]		90996	69
Highway density (km/km <sup>2</sup> )	[0,0.233]	Continuous	300064	0
	[0.233,0.731]		522923	219
	[0.731,1.329]		499043	573
	[1.329,2.060]		286928	809
	[2.060,3.024]		130962	224
	[3.024,4.319]		68302	0
	[4.319,6.114]		20460	0
	[6.114,8.473]		13663	0
Population density (km/km <sup>2</sup> )	[78,126.039]	Continuous	20156	243
	[126.039,148.686]		116000	164
	[148.686,163.784]		199033	228
	[163.784,178.882]		286524	331
	[178.882,196.039]		322175	553
	[196.039,215.941]		298677	251
	[215.941,236.529]		319857	34
	[236.529,253]		279923	21
Rainfall (mm)	[0.280,0.307]	Continuous	524252	157
	[0.307,0.330]		680084	1610
	[0.330,0.359]		364758	58
	[0.359,0.393]		273251	0

absolute surface temperature, which can reflect regional temperature changes, and human activities will also shape surface radiation distribution (Li et al., 2022).

## 4.2 Correlation analysis among environmental factors

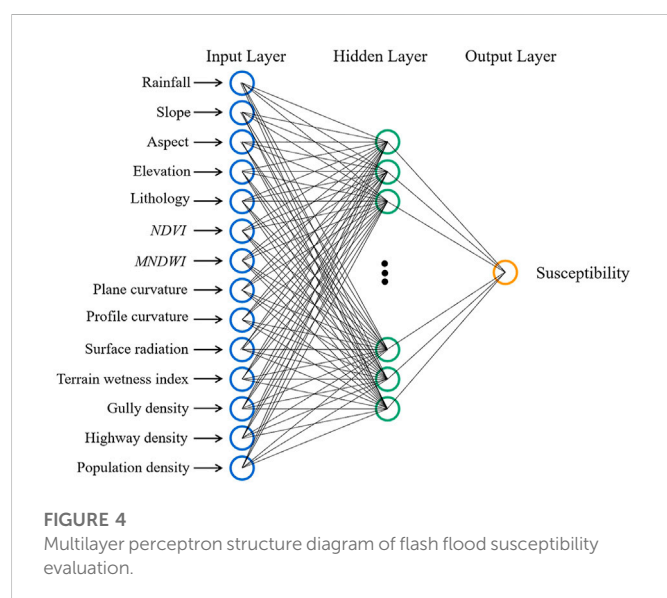
The issue of multi collinearity arises in flash flood susceptibility prediction when there is a high correlation between environmental factors, which leads to an increase in error and a decrease in the prediction accuracy of machine learning models (Erener, 2009; Tehrani et al., 2019). To avoid this effect, Pearson's correlation

coefficient is used in SPSS Statistics software to calculate the correlation between the factors. The environmental factors with absolute correlation coefficient values greater than 0.7 are then eliminated. Furthermore, because the lithology factor is a disordered multi-categorical discrete variable, in order to intuitively reflect the influence of different attributes of this independent variable on flash flood susceptibility and improve the model's accuracy and precision, this study set the lithology factor as six types of dummy variables, namely Mesoproterozoic Erathem (Pt<sub>2</sub>), Jurassic and Cretaceous (J, K); Neoproterozoic Erathem (Z, Pt<sub>3</sub>); Cambrian (e) and Tertiary (E); Ordovician (O), Devonian (D) and Quaternary (Q); Carboniferous (C) and magmatic rock group (Y); Triassic (T). In SPSS Statistics software, the dummy variables of Pt<sub>2</sub>, J, and K are



TABLE 2 Correlation coefficient matrix diagram of some environmental factors.

	Elevation	Aspect	Rainfall	Gully density	Slope	NDVI	Population density	Highway density	Surface radiation
Elevation	1								
Aspect	−0.030	1							
Rainfall	0.522	−0.029	1						
Gully density	−0.627	0.006	−0.166	1					
Slope	0.473	0.129	0.174	−0.375	1				
NDVI	0.382	−0.250	0.180	−0.277	0.275	1			
Population density	−0.009	−0.340	0.257	0.076	−0.094	0.050	1		
Highway density	−0.585	0.033	−0.319	0.549	−0.435	−0.448	0.095	1	
Surface radiation	−0.225	0.516	−0.177	0.204	−0.252	−0.390	−0.460	0.284	1



first valued as 1, and the values of other categories are 0. Secondly, the dummy variables of  $Z$  and  $Pt_3$  are valued as 1, and the other categories are valued as 0. Then and so on. Table 2 shows the results, which show that the absolute values of the correlation coefficients among the environmental factors are less than 0.7. It shows that there is no significant relationship between the factors, and all of them can be used as input variables for flash flood susceptibility modeling.

## 5 Research methods

### 5.1 Machine learning models

MLP, LR, SVM, and RF are four classic machine learning models chosen for modeling.

#### 5.1.1 Multilayer perceptron (MLP)

Rosenblatt's MLP neural network concept, first proposed in 1952, is a multilayer feed forward artificial neural network model used to predict data regression. The MLP structure is divided into three layers: input, hidden, and output. The basic units of the MLP model are neurons, which are located in the layers. The basic units between each layer are fully connected, and weights are used to represent the strength of their connection. All inputs are weighted and added together with bias. The activation function then realizes the non-linear mapping output so that the output amplitude of the basic units is limited to a specific range, typically  $(-1, 1)$  or  $(0, 1)$  (Alimi et al., 2019; Janizadeh et al., 2019). The formula is as follows:

$$n_{i,j} = f \left( \sum_j n_{i-1,j} \times w_j + b_j \right) \quad (1)$$

where,  $w$  is the connection weight between two adjacent layers of neurons,  $b$  is the bias value of the neuron, and  $f$  is the activation function. Figure 4.

#### 5.1.2 Logistic regression (LR)

The LR model, as a binomial classification-based regression analysis model, can use discrete or continuous variables as independent variables without the need for a normal distribution (Do et al., 2020). The dependent variable in the analysis of flash flood susceptibility is a binary variable representing the absence (0) or presence (1) of flash floods. The environmental factor is used as the independent variable ( $X_n$ ), and the probability of flash flood occurrence is solved using a logistic regression function. The formula is as follows:

$$Z = B_0 + B_1X_1 + B_2X_2 + \dots + B_nX_n, (i = 0, 1, 2, \dots, n) \quad (2)$$

$$P = 1 / (1 + e^{-Z})$$

where  $Z$  is the weighted sum of variables,  $P$  is the probability of flash flood occurrence with a value between 0 and 1,  $B_i$  is the regression coefficient, and  $X_i$  is the independent variable influencing flash flood occurrence.

### 5.1.3 Support vector machine (SVM)

The SVM works on the principle of mapping an instance's feature vector to a higher dimensional feature space based on certain rules and then seeking the optimal hyperplane that maximizes the classification interval of the data in this space. Finally, the output variables can be separated linearly (Cortes and Vapnik, 1995; Amol et al., 2021). Assume a set of training data and then use the SVM decision function to define its decision boundary, as shown in Eq. 3:

$$f(x) = \omega^T X + b \quad (3)$$

where  $\omega^T$  is the normal vector determining the optimal hyperplane's direction,  $X$  is the non-linear mapping function, and  $b$  is the hyperplane's offset from the origin. Eq. 4 can be used to calculate  $\omega$  and  $b$ :

$$\begin{aligned} \text{Minimization function: } g(\omega, \xi) &= \|\omega\|^2 + c \sum_{i=1}^N \xi_i \\ \text{Constrained to: } y_i((\omega, x) + b) &\geq 1 - \xi_i, \xi_i \geq 0 \end{aligned} \quad (4)$$

where  $\xi_i$  is the relaxation variable, and  $c > 0$  indicates the regularization variable of error.

### 5.1.4 Random forest (RF)

The RF model is a classifier made up of several decision trees. The model typically employs the Bootstrap method to draw samples at random as a training set with put-back and select feature variable subspace randomly. The decision tree modeling is then carried out. Finally, voting is used to classify the modeling results of all decision trees (Mohammady et al., 2019; He et al., 2021; Deng et al., 2022). The RF makes use of an ensemble learning method that makes use of multiple independent decision trees. As a result, its accuracy is higher than that of most single algorithms. Furthermore, because the training samples for each tree and the feature variable subspace are chosen at random, the model is unlikely to overfit (He et al., 2021).

## 5.2 Accuracy and uncertainty evaluation of flood flash susceptibility

Evaluation is an important step in prediction modeling because without it, the results are unreliable (Panahi et al., 2021b).

### 5.2.1 Assessment of modeling accuracy based on ROC curve

This study uses ROC curves and the area under the curve (AUC) to analyze the prediction results of four machine learning models: MLP, LR, SVM, and RF. The ROC curve's x-axis represents the false positive rate (FPR), and the y-axis represents the true positive rate (TPR), which can be calculated using Eqs. 5, 6, respectively. AUC, a performance metric that measures the merit and prediction accuracy of machine learning models, typically ranges between 0.5 and 1. The closer the value is to one, the more accurate the corresponding machine-learning model algorithm is (Tien Bui et al., 2016; Khosravi et al., 2018).

$$TPR = \frac{TP}{TP + FN} \quad (5)$$

$$FPR = \frac{FP}{FP + TN} \quad (6)$$

where, TP represents the number of flood points that can be correctly classified as a flood class, TN represents the number of non-flood points that can be correctly classified as a non-flood class, FN represents the number of flood points misclassified as a non-flood class, and FP represents the number of non-flood points misclassified as a flood class.

### 5.2.2 Distribution characteristics of susceptibility index

The susceptibility index's distribution characteristics are primarily quantified in terms of the mean value (MV) and standard deviation (SD). The MV represents the central tendency of the regional flood susceptibility index distribution, whereas the SD represents its degree of dispersion (Li et al., 2020). The lower the MV, the lower the likelihood of a flash flood in the region. The higher the SD, the better the susceptibility index discrimination and the lower the uncertainty of the corresponding machine-learning model prediction results (Huang et al., 2020a). When the MV of a model's susceptibility index is small and the SD is large, it is considered more reliable (Huang et al., 2022d).

### 5.2.3 Significance difference of susceptibility indexes

In this study, the Kendall synergy coefficient test is used to analyze the significance difference between the predicted susceptibility indexes of the models, and the null hypothesis of this test is that the susceptibility results of different models are consistent (Li et al., 2021). The formula of its rank correlation coefficient  $W$  is as follows:

$$W = \frac{12}{m^2(n^3 - n)} \sum_{i=1}^n \left[ R_i - \frac{m(n+1)}{2} \right]^2 \quad (7)$$

where  $m$  is the evaluation model,  $n$  is the sample number,  $R_i$  is the sum of the rank of the  $i$ th sample, and  $W \in [0, 1]$ . When the susceptibility prediction results are consistent,  $W$  is taken as 1. When the value of  $W$  is less than 1, the Kendall synergy coefficient should reject the null hypothesis. The significance difference between modeling results is evaluated using a chi-square test at a 5% level of significance. Therefore, if the calculated significance level is less than or equal to 5%, the null hypothesis is rejected as the modeling performance is significantly different and *vice versa* (Li et al., 2021b).

## 6 Assessment of flash flood susceptibility

### 6.1 Sample selection

The environmental factors in Longnan County are divided into 1,842,345 grids and 17 flash flood surfaces based on the 30 m resolution, and potential flash flood areas that have occurred are taken and transformed into 1,825 grids. All flash flood grid units are converted into flash flood points and their susceptibility is assigned to 1, while 1,825 non-flood grid units are chosen at random from the entire study area and converted into non-flood points and their susceptibility is assigned to 0. The assigned flash flood and non-flood susceptibility values are taken as the output variables of the model. A total of 3650 flash flood points and non-flood points are linked with their corresponding environmental factor original data. The flash flood and non-flood points are further randomly divided into a training dataset and a test dataset in a 7:3 ratio. The training dataset is used for model training and construction, and the test dataset is used to evaluate the generalization ability of the final model.

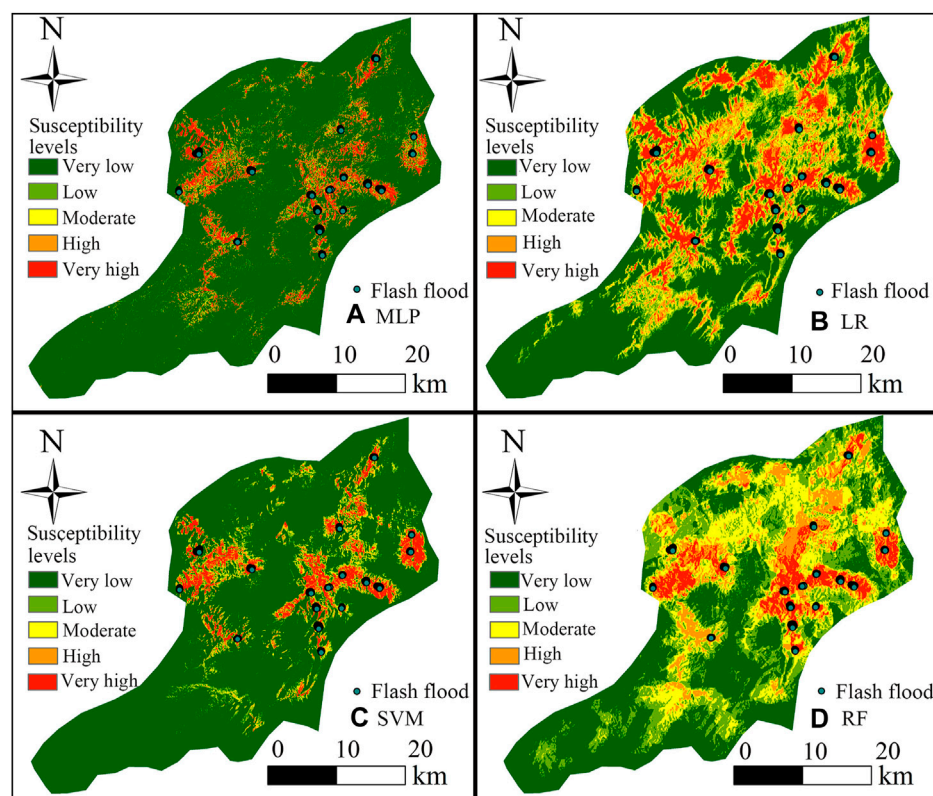


**FIGURE 5**  
Flash flood susceptibility diagram of each model: (A) MLP, (B) LR, (C) SVM, (D) RF.

## 6.2 Flash flood susceptibility prediction

### 6.2.1 Machine learning modeling and parameter setting

The MLP, LR, SVM, and RF models are trained and tested using a training dataset of 2,555 flash flood-non-flash flood grid samples and a test dataset of 1,095 flash flood-non-flash flood grid samples. The trained models are then used to predict flash flood susceptibility for 1,842,345 points in the study area.

To obtain the most accurate prediction results from the model, the model's parameters are adjusted one by one using the out-of-bag error screening method and cross-validation. Finally, the SVM model's regularization parameter  $C$  is set to 10, the regression accuracy  $\epsilon$  to 0.1, and the RBF kernel function parameter to 0.3; all other models are left alone (Chen et al., 2021).

### 6.2.2 Flash flood susceptibility mapping

The predicted flash flood susceptibility data from SPSS Modeler 18.0 software are imported and converted into grid units in ArcGIS 10.2 software. The predicted flash flood susceptibility index is then classified into five levels based on the natural break method in the classification method: very low, low, moderate, high, and very high. The results of flash flood susceptibility predicted by MLP, LR, SVM, and RF models in Longnan County are shown in Figure 5 and Table 3, and it can be concluded that the majority of Longnan County is in very low and low flood-prone areas. The very low and low flood-prone areas predicted by MLP and SVM models, on the other hand, are significantly larger than those predicted by LR and RF models, and the high and very

high flood-prone areas predicted by LR and RF models are more prominent than those predicted by MLP and SVM models.

Longnan County's very low and low flood-prone areas are mostly concentrated in the southwest, while the high and very high flood-prone areas are mostly concentrated in the center and extend in a strip-like pattern in all directions. The primary reason for this is that tectonic erosion hills dominate the central part of Longnan County, where gullies and ravines can be found. Furthermore, the county's surroundings are the Quaternary alluvium layer, whose soil is relatively loose, and the likelihood of flash floods is higher during the heavy rainfall period in the subtropical humid monsoon climate. Longnan County also has a relatively dense population distribution and engages in a variety of engineering activities. The area is primarily dependent on mountains for self-built houses and roads, and the study area's high-intensity engineering activities contribute to flash floods.

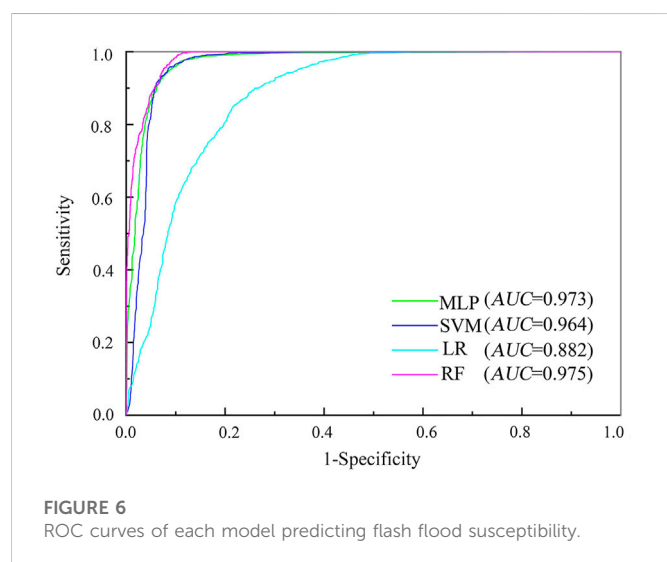
## 7 Discussion

### 7.1 Evaluation of susceptibility prediction accuracy

The ROC curve and its AUC value are used to estimate the accuracy of flash flood susceptibility prediction. The closer the ROC curve is to the upper left corner of the graph, the more sensitive the model is and the lower the likelihood of error. The larger the distance between two adjacent ROC curves, the greater the difference in prediction performance of two corresponding machine

**TABLE 3** Classification results of flash flood susceptibility index.

Machine learning models	Susceptibility levels	Grids in the study area	Ratio of grids in the study area (%)
MLP	Very low	1558322	84.58
	Low	71675	3.89
	Moderate	46069	2.50
	High	48445	2.63
	Very High	117834	6.40
LR	Very low	862680	46.83
	Low	310515	16.85
	Moderate	249722	13.55
	High	223552	12.13
	Very High	195876	10.63
SVM	Very low	1489470	80.85
	Low	110841	6.02
	Moderate	67058	3.64
	High	64012	3.47
	Very High	110964	6.02
RF	Very low	709172	38.49
	Low	436183	23.68
	Moderate	369373	20.05
	High	206100	11.19
	Very High	121517	6.60



learning models. The AUC can be used to quantify prediction accuracy; that is, the one-dimensional curve is mirrored by the two-dimensional area, making model prediction accuracy judgment more intuitive (Pradhan and Lee, 2010; Youssef et al., 2016). The AUC value is proportional to the model's prediction accuracy. [Figure 6](#)

shows how the ROC curve is used to assess the accuracy of the MLP, LR, SVM, and RF models in predicting flash flood susceptibility in Longnan County. The AUC values of each model are ranked from largest to smallest, as shown in the figure:  $AUC(RF) > AUC(MLP) > AUC(SVM) > AUC(LR)$ , implying that the RF model has the best prediction accuracy for flash flood susceptibility, followed by the MLP and SVM models, and the LR model has the worst. However, all four machine learning models perform well in terms of prediction.

## 7.2 Distribution rule of susceptibility index

The standard deviation and mean value measure the dispersion and central trend of the flood susceptibility index distribution, respectively. The model is more reliable when the mean value is smaller and standard deviation is larger. The results of flash flood susceptibility prediction revealed that the four models' mean values of the susceptibility index are ranked from largest to smallest:  $LR > RF > SVM > MLP$  ([Figure 7](#)). The MLP and SVM models predict a susceptibility index that is primarily distributed at a very low susceptibility level. The index shows a decreasing trend from very low to high susceptibility levels, with a slight increase in the very high susceptibility level. The susceptibility index predicted by the LR and RF models is concentrated in the very low and low susceptibility levels, with the index overall decreasing from very low to very high susceptibility. Furthermore, the mean values of the predicted

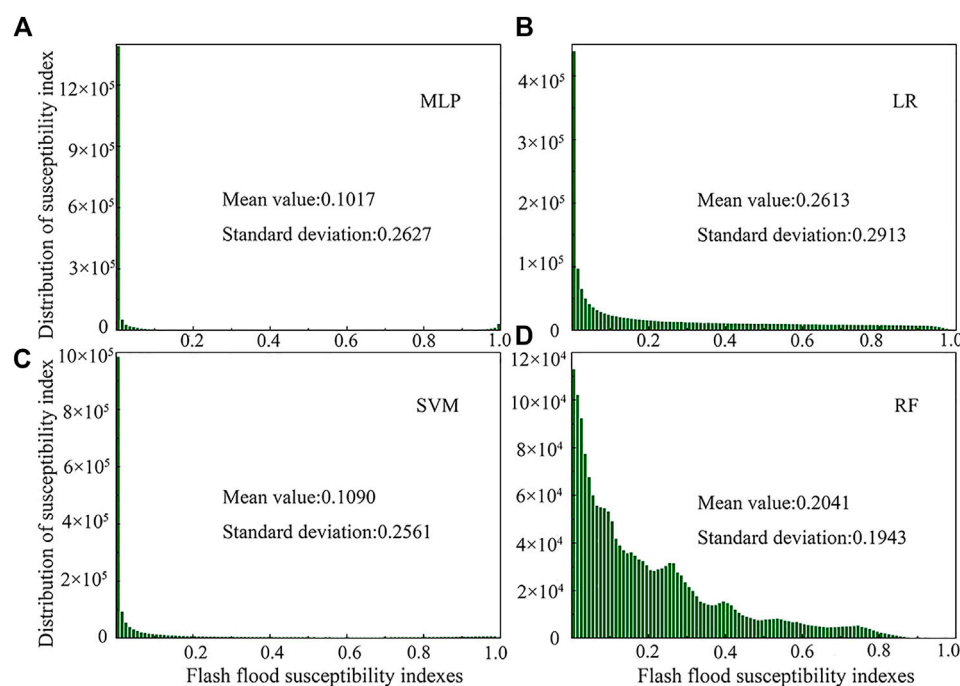


**FIGURE 7**  
Distribution rule of flash flood susceptibility index: (A) MLP, (B) LR, (C) SVM, (D) RF.

susceptibility index for all four models are in the low susceptibility range. When combined with the AUC values of the models, it is clear that the MLP model has the lowest mean value of susceptibility index while maintaining high prediction accuracy. At the same time, the LR model not only has the lowest prediction accuracy but also the highest mean value of susceptibility index, implying that the MLP model has the lowest prediction uncertainty, the SVM and RF models have the second highest, and the LR model has the highest prediction uncertainty.

Furthermore, [Figure 7](#) shows that the LR model has the greatest dispersion of the predicted susceptibility index, followed by the MLP and SVM models, and the RF model has the smallest. Overall, all four models have small mean values and large standard deviations, allowing differences in susceptibility index to be more accurately reflected. Furthermore, a low susceptibility index can represent as much known flash flood inventory information as possible. When the above ROC curves and their AUC values, mean value, and standard deviation of the susceptibility index are combined, it is concluded that the MLP model has the best prediction performance for flash flood susceptibility, followed by the SVM and RF models, and the LR model has poor prediction performance.

### 7.3 Significance difference analysis of flash flood susceptibility indexes

The Kendall synergy coefficient test is used to test the significant difference between the flash flood susceptibility indexes under any two groups of different models. If the Kendall rank correlation coefficient  $W$  is less than 1 and the significance of the test result is less than 0.05, the difference between the flash flood susceptibility indexes under

these two groups of models is significant and the null hypothesis should be rejected.

The test results show that the significance level between the flash flood susceptibility indexes of each model is less than 0.05 and the value of  $W$  is 0.449. Thus, it is clear that the difference between the susceptibility indexes under each model is significant and the null hypothesis should be rejected. Therefore, it is necessary to explore the modeling uncertainty under different machine learning model work conditions to find a reliable and stable susceptibility prediction model.

### 7.4 The contributing environmental factors of flash flood susceptibility

The top contributing environmental factors of flash flood susceptibility are the most important environmental factors in controlling the occurrence of flash floods. Their significance can be used as a theoretical reference for studying flash flood susceptibility ([Li et al., 2022c](#)). SPSS Modeler and R Studio software are used to analyze 14 environmental factors of MLP, LR, SVM, and RF models in this study. The importance ranking of each environmental factor is derived ([Figure 8](#)), revealing that elevation, gully density, and population density are the top contributing factors of flash flood susceptibility in Longnan County. MNDWI, plan curvature, profile curvature, and other environmental factors, on the other hand, have minor effects on flash flood susceptibility.

Although the importance ranking and magnitude of environmental factors differ between machine learning models, they are generally similar. As shown in [Figure 8](#), the environmental factors with a higher importance in the MLP and RF models are elevation, highway density, gully density, rainfall, and population



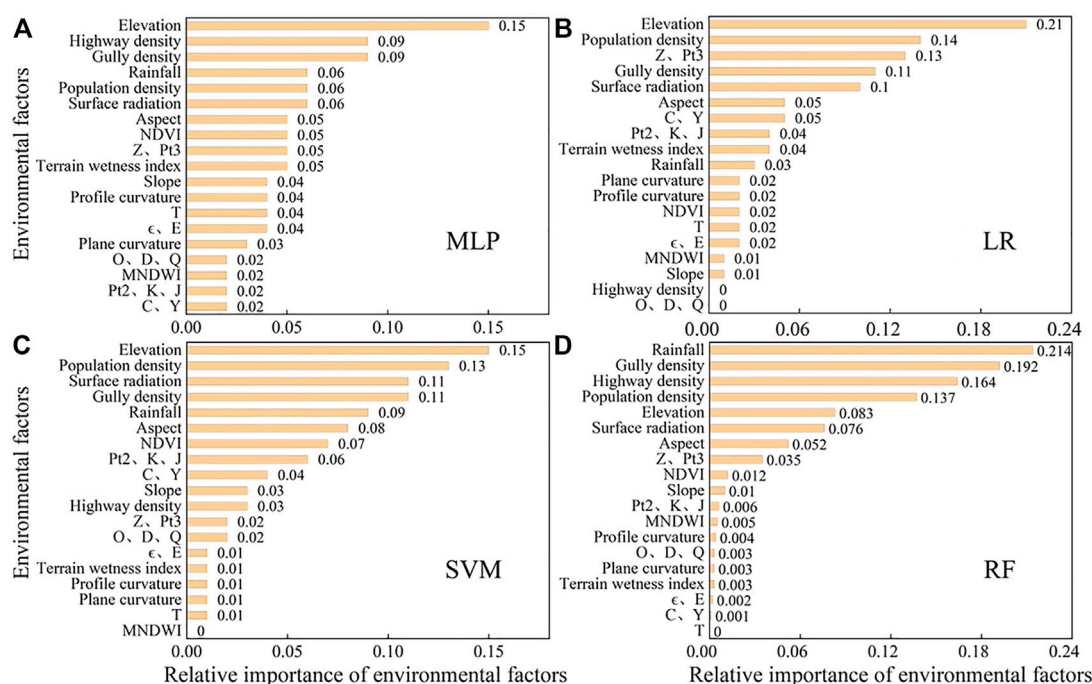


**FIGURE 8**  
Importance ranking of environmental factors: (A) MLP, (B) LR, (C) SVM, (D) RF.

density. The top five environmental factors are the same for the MLP and RF models. However, elevation is more important in the MLP model, and rainfall is more important in the RF model. Besides, only four of the top five environmental factors in the SVM model are the same as the MLP and RF models, while the LR model has only three. This leads to the difference in the model's susceptibility prediction mapping and indirectly proves that MLP and RF models have similar and highest prediction accuracy, followed by SVM and LR models.

## 7.5 Problems and frontiers of machine learning model prediction susceptibility

Li et al. (2022) proposed a combination of LR and RF models with embedded feature selection for flash flood susceptibility prediction in the mainstream basin of the Songhua River and concluded that both models exhibited accurate and reliable performance. However, the RF model had better prediction performance than the LR model. Sellami et al. (2022) compared the flash flood susceptibility prediction performance of several machine learning models and found that the RF model had the highest performance, followed by the ANN and SVM models. Janizadeh et al. (2019) used five machine learning methods to estimate flash flood susceptibility in the Tafresh watershed of Iran and revealed that the ADT method was the best. The FT method ranked second, followed by KLP, MLP, and QDA. While the results of this study are that the MLP model has the best prediction performance, followed by the SVM, RF, and LR models, respectively. However, the results of this study are generally the same as the results of the above-mentioned literature analysis. The MLP, SVM, and RF models are relatively accurate and reliable models for predicting flash flood susceptibility, and the LR model has poor prediction

performance. Thus, it can be seen that the prediction performance of different machine learning models is characterized by variability and regionality due to the differences in the weights of the input variables and the analysis methods.

In this study, the non-flood grid units are randomly selected in the whole study area. Although there is no artificial interference, the non-flood grid units selected by this method may be the potential units of flash floods, and their stability is not high, which will lead to errors in the susceptibility prediction results. In addition, due to the limitation of basic data sources, the flash flood data in this study is limited. Therefore, further research can focus on how to reasonably select non-flood grid units to improve the prediction accuracy of machine learning models. In the next research, we will collect more basic data on flash floods, strive to expand the data source of flash floods, and improve the modeling accuracy.

## 8 Conclusion

- (1) Machine learning models can accurately predict regional flash flood risk. The MLP, LR, SVM, and RF models all perform well in terms of flood susceptibility prediction, and their flash flood susceptibility maps and susceptibility index distribution maps are generally similar. Longnan County's very low and low flood-prone areas are mostly concentrated in the southwest, while the high and very high flood-prone areas are mostly concentrated in the center and extend in a strip in all directions.
- (2) It is determined that the MLP model has the best prediction performance for flash flood susceptibility, followed by the SVM and RF models, and the LR model has poor prediction performance by comparing and analyzing the ROC curves and

susceptibility index distribution maps of different machine learning models.

- (3) According to SPSS Modeler and R Studio software, the top contributing environmental factors of flash flood susceptibility in Longnan County are elevation, gully density, and population density. In contrast, environmental factors such as MNDWI, plan curvature, and profile curvature have a much lower impact on flash flood susceptibility.

## Data availability statement

The original contributions presented in the study are included in the article/supplementary material, further inquiries can be directed to the corresponding author.

## Author contributions

Writing—original draft preparation, XZ, KY, and SZ; data collection, KY and YC; data processing, XZ and KY; writing—review and editing, XZ, KY, SZ, and YC; writing—polish, XZ and AH.

## References

- Abedi, R., Costache, R., Shafizadeh-Moghadam, H., and Pham, Q. B. (2022). Flash-flood susceptibility mapping based on XGBoost, random forest and boosted regression trees. *Geocarto Int.* 37 (19), 5479–5496. doi:10.1080/10106049.2021.1920636
- Alimi, O. A., Ouahada, K., and Abu-Mahfouz, A. M. (2019). Real time security assessment of the power system using a hybrid support vector machine and multilayer perceptron neural network algorithms. *Sustainability* 11 (13), 3586. doi:10.3390/su11133586
- Amol, S., Chander, P., and Manivasagam, S. (2021). Entropy-based hybrid integration of random forest and support vector machine for landslide susceptibility analysis. *Geomatics* 1 (4), 399–416. doi:10.3390/geomatics1040023
- Bobrowsky, P. T. (2013). *Encyclopedia of natural hazards*, Dordrecht: Springer.
- Cao, Y., Jia, H., Xiong, J., Cheng, W., Li, K., Pang, Q., et al. (2020). Flash flood susceptibility assessment based on geodetector, certainty factor, and logistic regression analyses in Fujian province, China. *ISPRS Int. J. Geo-Information* 9 (12), 748. doi:10.3390/ijgi9120748
- Chang, Z., Catani, F., Huang, F., Liu, G., Meena, S. R., Huang, J., et al. (2022). Landslide susceptibility prediction using slope unit-based machine learning models considering the heterogeneity of conditioning factors. *J. Rock Mech. Geotechnical Eng.* doi:10.1016/j.jrmge.2022.07.009
- Chang, Z., Du, Z., Zhang, F., Huang, F., Chen, J., Li, W., et al. (2020). Landslide susceptibility prediction based on remote sensing images and GIS: Comparisons of supervised and unsupervised machine learning models. *Remote Sens.* 12 (3), 502. doi:10.3390/rs12030502
- Chapi, K., Singh, V. P., Shirzadi, A., Shahabi, H., Bui, D. T., Pham, B. T., et al. (2017). A novel hybrid artificial intelligence approach for flood susceptibility assessment. *Environ. Model. Softw.* 95, 229–245. doi:10.1016/j.envsoft.2017.06.012
- Chen, L., Lin, W., Chen, P., Jiang, S., Liu, L., and Hu, H. (2021). Porosity prediction from well logs using back propagation neural network optimized by genetic algorithm in one heterogeneous oil reservoirs of Ordos Basin, China. *J. Earth Sci.* 32 (4), 828–838. doi:10.1007/s12583-020-1396-5
- Cortes, C., and Vapnik, V. (1995). Support-vector networks. *Mach. Learn.* 20 (3), 273–297. doi:10.1007/bf00994018
- Criss, R. E. (2022). Hydrologic time scale: A fundamental stream characteristic. *J. Earth Sci.* 33 (5), 1291–1297. doi:10.1007/s12583-022-1655-8
- Cui, L. F., Liu, C. Q., Xu, S., Zhao, Z. Q., Liu, T. Z., Liu, W. J., et al. (2016). Subtropical denudation rates of granitic regolith along a hill ridge in Longnan, SE China derived from cosmogenic nuclide depth-profiles. *J. Asian Earth Sci.* 117, 146–152. doi:10.1016/j.jseas.2015.12.006
- Dahri, N., Yousfi, R., Bouamrane, A., Abida, H., Pham, Q. B., and Derdous, O. (2022). Comparison of analytic network process and artificial neural network models for flash flood susceptibility assessment. *J. Afr. Earth Sci.* 193, 104576. doi:10.1016/j.jafrearsci.2022.104576
- Dai, C., Li, W., Wang, D., Lu, H., Xu, Q., and Jian, J. (2021). Active landslide detection based on Sentinel-1 data and InSAR technology in Zhouqu county, Gansu province, Northwest China. *J. Earth Sci.* 32 (5), 1092–1103. doi:10.1007/s12583-020-1380-0
- Das, G., and Lepcha, K. (2019). Application of logistic regression (LR) and frequency ratio (FR) models for landslide susceptibility mapping in Relli Khola river basin of Darjeeling Himalaya, India. *SN Appl. Sci.* 1 (11), 1453–1522. doi:10.1007/s42452-019-1499-8
- Demir, G., Aytekin, M., Akgün, A., İkizler, S. B., and Tatar, O. (2013). A comparison of landslide susceptibility mapping of the eastern part of the North Anatolian Fault Zone (Turkey) by likelihood-frequency ratio and analytic hierarchy process methods. *Nat. Hazards* 65 (3), 1481–1506. doi:10.1007/s11069-012-0418-8
- Deng, H., Wu, X., Zhang, W., Liu, Y., Li, W., Li, X., et al. (2022). Slope-unit scale landslide susceptibility mapping based on the random forest model in deep valley areas. *Remote Sens.* 14 (17), 4245. doi:10.3390/rs14174245
- Do, H. M., Yin, K. L., and Guo, Z. Z. (2020). A comparative study on the integrative ability of the analytical hierarchy process, weights of evidence and logistic regression methods with the Flow-R model for landslide susceptibility assessment. *Geomatics, Nat. Hazards Risk* 11 (1), 2449–2485. doi:10.1080/19475705.2020.1846086
- Elkhrachy, I. (2022). Flash flood water depth estimation using SAR images, digital elevation models, and machine learning algorithms. *Remote Sens.* 14 (3), 440. doi:10.3390/rs14030440
- Erener, A. (2009). An approach for landslide risk assesment by using geographic information systems (gis) and remote sensing. Ph.D. Thesis, Turkey: Middle East Technical University.
- Guo, C., Xu, Q., Dong, X., Li, W., Zhao, K., Lu, H., et al. (2021). Geohazard recognition and inventory mapping using airborne lidar data in complex mountainous areas. *J. Earth Sci.* 32 (5), 1079–1091. doi:10.1007/s12583-021-1467-2
- Guzzetti, F., Carrara, A., Cardinali, M., and Reichenbach, P. (1999). Landslide hazard evaluation: A review of current techniques and their application in a multi-scale study, central Italy. *Geomorphology* 31 (1–4), 181–216. doi:10.1016/s0169-555x(99)00078-1
- Ha, H., Luu, C., Bui, Q. D., Pham, D. H., Hoang, T., Nguyen, V. P., et al. (2021). Flash flood susceptibility prediction mapping for a road network using hybrid machine learning models. *Nat. Hazards* 109 (1), 1247–1270. doi:10.1007/s11069-021-04877-5
- Haoran, Z., Guifang, Z., and Qiwen, J. (2019). Integration of analytical hierarchy process and landslide susceptibility index based landslide susceptibility assessment of the pearl river delta area, China. *IEEE J. Sel. Top. Appl. Earth Observations Remote Sens.* 12 (11), 4239–4251. doi:10.1109/jstars.2019.2938554
- Haribabu, S., Gupta, G. S., Kumar, P. N., and Rajendran, P. S. (2021). “Prediction of flood by rainfall all using MLP classifier of neural network model,” in 6th International Conference on Communication and Electronics Systems (ICCES), Coimbatre, India, 08–10 July 2021 (IEEE).
- He, Q., Wang, M., and Liu, K. (2021). Rapidly assessing earthquake-induced landslide susceptibility on a global scale using random forest. *Geomorphology* 391, 107889. doi:10.1016/j.geomorph.2021.107889
- Huang, F., Cao, Z., Guo, J., Jiang, S. H., Li, S., and Guo, Z. (2020a). Comparisons of heuristic, general statistical and machine learning models for landslide susceptibility prediction and mapping. *Catena* 191 (C), 104580. doi:10.1016/j.catena.2020.104580

## Funding

This research is funded by the National Natural Science Foundation of China (No. 52109089).

## Conflict of interest

The authors declare that the research was conducted in the absence of any commercial or financial relationships that could be construed as a potential conflict of interest.

## Publisher's note

All claims expressed in this article are solely those of the authors and do not necessarily represent those of their affiliated organizations, or those of the publisher, the editors and the reviewers. Any product that may be evaluated in this article, or claim that may be made by its manufacturer, is not guaranteed or endorsed by the publisher.

- Huang, F., Cao, Z., Jiang, S. H., Zhou, C., Huang, J., and Guo, Z. (2020b). Landslide susceptibility prediction based on a semi-supervised multiple-layer perceptron model. *Landslides* 17 (12), 2919–2930. doi:10.1007/s10346-020-01473-9
- Huang, F., Chen, J., Liu, W., Huang, J., Hong, H., and Chen, W. (2022a). Regional rainfall-induced landslide hazard warning based on landslide susceptibility mapping and a critical rainfall threshold. *Geomorphology* 408, 108236. doi:10.1016/j.geomorph.2022.108236
- Huang, F., Pan, L., Fan, X., Jiang, S. H., Huang, J., and Zhou, C. (2022b). The uncertainty of landslide susceptibility prediction modeling: Suitability of linear conditioning factors. *Bull. Eng. Geol. Environ.* 81 (5), 182. doi:10.1007/s10064-022-02672-5
- Huang, F., Tao, S., Chang, Z., Huang, J., Fan, X., Jiang, S. H., et al. (2021a). Efficient and automatic extraction of slope units based on multi-scale segmentation method for landslide assessments. *Landslides* 18 (11), 3715–3731. doi:10.1007/s10346-021-01756-9
- Huang, F., Tao, S., Li, D., Lian, Z., Catani, F., Huang, J., et al. (2022c). Landslide susceptibility prediction considering neighborhood characteristics of landslide spatial datasets and hydrological slope units using remote sensing and GIS technologies. *Remote Sens.* 14 (18), 4436. doi:10.3390/rs14184436
- Huang, F., Yan, J., Fan, X., Yao, C., Huang, J., Chen, W., et al. (2022d). Uncertainty pattern in landslide susceptibility prediction modelling: Effects of different landslide boundaries and spatial shape expressions. *Geosci. Front.* 13 (2), 101317. doi:10.1016/j.gsf.2021.101317
- Huang, F., Ye, Z., Jiang, S. H., Huang, J., Chang, Z., and Chen, J. (2021b). Uncertainty study of landslide susceptibility prediction considering the different attribute interval numbers of environmental factors and different data-based models. *Catena* 202, 105250. doi:10.1016/j.catena.2021.105250
- Huang, F., Zhang, J., Zhou, C., Wang, Y., Huang, J., and Zhu, L. (2020c). A deep learning algorithm using a fully connected sparse autoencoder neural network for landslide susceptibility prediction. *Landslides* 17 (1), 217–229. doi:10.1007/s10346-019-01274-9
- István, K., Ștefan, B., IoanAurel, I., Vasile, D., Raularian, R., and Sanda, R. (2022). Flash flood vulnerability mapping based on FFPI using GIS spatial analysis case study: Valea reia catchment area, Romania. *Sensors* 22 (9), 3573. doi:10.3390/s22093573
- Janizadeh, S., Avand, M., Jaafari, A., Phong, T. V., Bayat, M., Ahmadisharaf, E., et al. (2019). Prediction success of machine learning methods for flash flood susceptibility mapping in the Tafresh watershed, Iran. *Sustainability* 11 (19), 5426. doi:10.3390/su11195426
- Jiang, S. H., Huang, J., Huang, F., Yang, J., Yao, C., and Zhou, C. B. (2018). Modelling of spatial variability of soil undrained shear strength by conditional random fields for slope reliability analysis. *Appl. Math. Model.* 63, 374–389. doi:10.1016/j.apm.2018.06.030
- Khosravi, K., Pham, B. T., Chapi, K., Shirzadi, A., Shahabi, H., Revhaug, I., et al. (2018). A comparative assessment of decision trees algorithms for flash flood susceptibility modeling at Haraz watershed, northern Iran. *Sci. Total Environ.* 627, 744–755. doi:10.1016/j.scitotenv.2018.01.266
- Lee, D. H., Kim, Y. T., and Lee, S. R. (2020). Shallow landslide susceptibility models based on artificial neural networks considering the factor selection method and various non-linear activation functions. *Remote Sens.* 12 (7), 1194. doi:10.3390/rs12071194
- Li, D., Huang, F., Yan, L., Cao, Z., Chen, J., and Ye, Z. (2019). Landslide susceptibility prediction using particle-swarm-optimized multilayer perceptron: Comparisons with multilayer-perceptron-only, bp neural network, and information value models. *Appl. Sci.* 9 (18), 3664. doi:10.3390/app9183664
- Li, J., Zhang, H., Zhao, J., Guo, X., Rihan, W., and Deng, G. (2022a). Embedded feature selection and machine learning methods for flash flood susceptibility-mapping in the mainstream Songhua River basin, China. *Remote Sens.* 14 (21), 5523. doi:10.3390/rs14215523
- Li, Q., Huang, D., Pei, S., Qiao, J., and Wang, M. (2021a). Using physical model experiments for hazards assessment of rainfall-induced debris landslides. *J. Earth Sci.* 32 (5), 1113–1128. doi:10.1007/s12583-020-1398-3
- Li, T., Hu, D., Wang, Y., Di, Y., and Liu, M. (2022b). Correcting remote-sensed shaded image with urban surface radiative transfer model. *Int. J. Appl. Earth Observation Geoinformation* 106, 102654. doi:10.1016/j.jag.2021.102654
- Li, W., Fan, X., Huang, F., Chen, W., Hong, H., Huang, J., et al. (2020). Uncertainties analysis of collapse susceptibility prediction based on remote sensing and GIS: Influences of different data-based models and connections between collapses and environmental factors. *Remote Sens.* 12 (24), 4134. doi:10.3390/rs12244134
- Li, W., Shi, Y., Huang, F., Hong, H., and Song, G. (2021b). Uncertainties of collapse susceptibility prediction based on remote sensing and GIS: Effects of different machine learning models. *Front. Earth Sci.* 9, 731058. doi:10.3389/feart.2021.731058
- Li, Y., Deng, X., Ji, P., Yang, Y., Jiang, W., and Zhao, Z. (2022c). Evaluation of landslide susceptibility based on CF-SVM in nujiang prefecture. *Int. J. Environ. Res. Public Health* 19 (21), 14248. doi:10.3390/ijerph192114248
- Liu, J., Wang, J., Xiong, J., Cheng, W., Sun, H., Yong, Z., et al. (2021). Hybrid models incorporating bivariate Statistics and machine learning methods for flash flood susceptibility assessment based on remote sensing datasets. *Remote Sens.* 13 (23), 4945. doi:10.3390/rs13234945
- Liu, W., Luo, X., Huang, F., and Fu, M. (2019a). Prediction of soil water retention curve using Bayesian updating from limited measurement data. *Appl. Math. Model.* 76, 380–395. doi:10.1016/j.apm.2019.06.028
- Liu, W., Song, X., Huang, F., and Hu, L. (2019b). Experimental study on the disintegration of granite residual soil under the combined influence of wetting-drying cycles and acid rain. *Geomatics, Nat. Hazards Risk* 10 (1), 1912–1927. doi:10.1080/19475705.2019.1651407
- Liu, Y., Zhao, L., Bao, A., Li, J., and Yan, X. (2022). Chinese high resolution satellite data and GIS-based assessment of landslide susceptibility along highway G30 in guozigou valley using logistic regression and MaxEnt model. *Remote Sens.* 14 (15), 3620. doi:10.3390/rs14153620
- Mahmoud, S. H., and Gan, T. Y. (2018). Multi-criteria approach to develop flood susceptibility maps in arid regions of Middle East. *J. Clean. Prod.* 196, 216–229. doi:10.1016/j.jclepro.2018.06.047
- Marchi, L., Borga, M., Preciso, E., and Gaume, E. (2010). Characterisation of selected extreme flash floods in Europe and implications for flood risk management. *J. Hydrology* 394 (1–2), 118–133. doi:10.1016/j.jhydrol.2010.07.017
- Marjanović, M., Kovačević, M., Bajat, B., and Voženilek, V. (2011). Landslide susceptibility assessment using SVM machine learning algorithm. *Eng. Geol.* 123 (3), 225–234. doi:10.1016/j.enggeo.2011.09.006
- Mohammady, M., Pourghasemi, H. R., and Amiri, M. (2019). Land subsidence susceptibility assessment using random forest machine learning algorithm. *Environ. Earth Sci.* 78 (16), 503–512. doi:10.1007/s12665-019-8518-3
- Ngo, P. T. T., Pham, T. D., Nhu, V. H., Le, T. T., Tran, D. A., Phan, D. C., et al. (2021). A novel hybrid quantum-PSO and credal decision tree ensemble for tropical cyclone induced flash flood susceptibility mapping with geospatial data. *J. Hydrology* 596, 125682. doi:10.1016/j.jhydrol.2020.125682
- Nguyen, S., and Bouvier, C. (2019). Flood modelling using the distributed event-based SCS-LR model in the Mediterranean Real Collobrier catchment. *Hydrological Sci. J.* 64 (11), 1351–1369. doi:10.1080/02626667.2019.1639715
- Panahi, M., Dodangeh, E., Rezaie, F., Khosravi, K., Van Le, H., Lee, M. J., et al. (2021a). Flood spatial prediction modeling using a hybrid of meta-optimization and support vector regression modeling. *Catena* 199, 105114. doi:10.1016/j.catena.2020.105114
- Panahi, M., Jaafari, A., Shirzadi, A., Shahabi, H., Rahmati, O., Omidvar, E., et al. (2021b). Deep learning neural networks for spatially explicit prediction of flash flood probability. *Geosci. Front.* 12 (3), 101076. doi:10.1016/j.gsf.2020.09.007
- Pham, B. T., Avand, M., Janizadeh, S., Phong, T. V., Al-Ansari, N., Ho, L. S., et al. (2020). GIS based hybrid computational approaches for flash flood susceptibility assessment. *Water* 12 (3), 683. doi:10.3390/w12030683
- Pradhan, B., and Lee, S. (2010). Regional landslide susceptibility analysis using back-propagation neural network model at Cameron Highland, Malaysia. *Landslides* 7 (1), 13–30. doi:10.1007/s10346-009-0183-2
- Rahmati, O., Pourghasemi, H. R., and Zeinivand, H. (2016). Flood susceptibility mapping using frequency ratio and weights-of-evidence models in the Golastan Province, Iran. *Geocarto Int.* 31 (1), 42–70. doi:10.1080/10106049.2015.1041559
- Roy, P., Pal, S. C., Chakraborty, R., Chowdhuri, I., Malik, S., and Das, B. (2020). Threats of climate and land use change on future flood susceptibility. *J. Clean. Prod.* 272, 122757. doi:10.1016/j.jclepro.2020.122757
- Sellami, E., Maanan, M., and Rhinane, H. (2022). Performance of machine learning algorithms for mapping and forecasting of flash flood susceptibility in Tetouan, Morocco. *Int. Archives Photogrammetry, Remote Sens. Spatial Inf. Sci.* 46, 305–313. doi:10.5194/isprs-archives-xxlvi-4-w3-2021-305-2022
- Sheng, M., Zhou, J., Chen, X., Teng, Y., Hong, A., and Liu, G. (2022). Landslide susceptibility prediction based on frequency ratio method and C5.0 decision tree model. *Front. Earth Sci.* 889, 918386. doi:10.3389/FEART.2022.918386
- Shu, Y., Zheng, G., and Yan, X. (2022). Application of Multiple Geographical Units Convolutional Neural Network based on neighborhood effects in urban waterlogging risk assessment in the city of Guangzhou, China. *Phys. Chem. Earth, Parts A/B/C* 126, 103054. doi:10.1016/j.pce.2021.103054
- Sun, D., Xu, J., Wen, H., and Wang, Y. (2020). An optimized random forest model and its generalization ability in landslide susceptibility mapping: Application in two areas of three gorges reservoir, China. *J. Earth Sci.* 31 (6), 1068–1086. doi:10.1007/s12583-020-1072-9
- Tehrany, M. S., Jones, S., and Shabani, F. (2019). Identifying the essential flood conditioning factors for flood prone area mapping using machine learning techniques. *Catena* 175, 174–192. doi:10.1016/j.catena.2018.12.011
- Tien Bui, D., Ho, T. C., Pradhan, B., Pham, B. T., Nhu, V. H., and Revhaug, I. (2016). GIS-based modeling of rainfall-induced landslides using data mining-based functional trees classifier with AdaBoost, Bagging, and MultiBoost ensemble frameworks. *Environ. Earth Sci.* 75 (14), 1101–1122. doi:10.1007/s12665-016-5919-4
- Varnes, D. J. (1984). *Landslide hazard zonation: A review of principles and practice*. Paris: UNESCO Press.
- Wang, Y., Duan, H., and Hong, H. (2019). A comparative study of composite kernels for landslide susceptibility mapping: A case study in yongxin county, China. *Catena* 183, 104217. doi:10.1016/j.catena.2019.104217
- Wang, Y., Fang, Z., Hong, H., Costache, R., and Tang, X. (2021). Flood susceptibility mapping by integrating frequency ratio and index of entropy with multilayer perceptron and classification and regression tree. *J. Environ. Manag.* 289, 112449. doi:10.1016/j.jenvman.2021.112449

- Xiao, B., Zhao, J., Li, D., Zhao, Z., Zhou, D., Xi, W., et al. (2022). Combined SBAS-InSAR and PSO-RF algorithm for evaluating the susceptibility prediction of landslide in complex mountainous area: A case study of ludian county, China. *Sensors* 22 (20), 8041. doi:10.3390/s22208041
- Xiong, J., Li, J., Cheng, W., Wang, N., and Guo, L. (2019). A GIS-based support vector machine model for flash flood vulnerability assessment and mapping in China. *ISPRS Int. J. Geo-Information* 8 (7), 297. doi:10.3390/ijgi8070297
- Yao, J., Zhang, X., Luo, W., Liu, C., and Ren, L. (2022). Applications of Stacking/Blending ensemble learning approaches for evaluating flash flood susceptibility. *Int. J. Appl. Earth Observation Geoinformation* 112, 102932. doi:10.1016/j.jag.2022.102932
- Youssef, A. M., Pradhan, B., and Sefry, S. A. (2016). Flash flood susceptibility assessment in Jeddah city (Kingdom of Saudi Arabia) using bivariate and multivariate statistical models. *Environ. Earth Sci.* 75 (1), 12–16. doi:10.1007/s12665-015-4830-8
- Zhang, H., Song, Y., Xu, S., He, Y., Li, Z., Yu, X., et al. (2022). Combining a class-weighted algorithm and machine learning models in landslide susceptibility mapping: A case study of wanzhou section of the three gorges reservoir, China. *Comput. Geosciences* 158, 104966. doi:10.1016/j.cageo.2021.104966
- Zhang, Z. J., Liu, C. Q., Zhao, Z. Q., Cui, L. F., Liu, W. J., Liu, T. Z., et al. (2015). Behavior of redox-sensitive elements during weathering of granite in subtropical area using X-ray absorption fine structure spectroscopy. *J. Asian Earth Sci.* 105, 418–429. doi:10.1016/j.jseas.2015.02.015
- Zhao, G., Pang, B., Xu, Z., Yue, J., and Tu, T. (2018). Mapping flood susceptibility in mountainous areas on a national scale in China. *Sci. Total Environ.* 615, 1133–1142. doi:10.1016/j.scitotenv.2017.10.037





## OPEN ACCESS

## EDITED BY

Lijie Guo,  
Beijing Mining and Metallurgy Technology  
Group Co., Ltd., China

## REVIEWED BY

Qinzhao Liao,  
China University of Petroleum, China  
Ying Xu,  
Tianjin University, China

## \*CORRESPONDENCE

Peng Xiang,  
✉ xiangpeng811@126.com

## SPECIALTY SECTION

This article was submitted  
to Geohazards and Georisks,  
a section of the journal  
Frontiers in Earth Science

RECEIVED 18 December 2022

ACCEPTED 09 January 2023

PUBLISHED 24 January 2023

## CITATION

Xiang P, Ji HG, Zhang GQ and Li WG  
(2023), Theoretical analysis of grouting  
reinforcement for surrounding rock of  
deep shaft based on stability and water  
inflow control.  
*Front. Earth Sci.* 11:1126764.  
doi: 10.3389/feart.2023.1126764

## COPYRIGHT

© 2023 Xiang, Ji, Zhang and Li. This is an  
open-access article distributed under the  
terms of the [Creative Commons  
Attribution License \(CC BY\)](https://creativecommons.org/licenses/by/4.0/). The use,  
distribution or reproduction in other  
forums is permitted, provided the original  
author(s) and the copyright owner(s) are  
credited and that the original publication in  
this journal is cited, in accordance with  
accepted academic practice. No use,  
distribution or reproduction is permitted  
which does not comply with these terms.

# Theoretical analysis of grouting reinforcement for surrounding rock of deep shaft based on stability and water inflow control

Peng Xiang<sup>1\*</sup>, Hong Guang Ji<sup>1</sup>, Guang Quan Zhang<sup>2</sup> and  
Wen Guang Li<sup>3</sup>

<sup>1</sup>Beijing Key Laboratory of Urban Underground Space Engineering, University of Science and Technology Beijing, Beijing, China, <sup>2</sup>Hubei Provincial Engineering Technology Research Center of High Efficient Clean Utilization Shale Vanadium Resource, Wuhan University of Science and Technology, Wuhan, Hubei, China, <sup>3</sup>Sanshandao Gold Mine of Shandong Gold Group Co., Ltd., Shandong, China

To address the challenge of designing grouting reinforcement in a deep shaft to control water, this study established an elastic-plastic analytical formula for the grouted rock surrounding a shaft under the combined action of thermal, hydraulic, and mechanical fields based on the Mohr–Coulomb yield criterion. The various rules and influencing factors of stability and impermeability of the grouted rock surrounding the shaft are calculated and analyzed. The analysis shows that damage to the surrounding rock is aggravated by the action of high ground temperature and high water pressure in deep shafts, and the influence of water pressure is particularly significant. The larger the radius and cohesion of the grouted surrounding rock, the smaller the radius of its plastic zone. With an increase in the elastic modulus ratio between the grouted surrounding rock and the original rock, the radius of its plastic zone increases, so the elastic modulus of the grouted surrounding rock design should consider the original surrounding rock. With a decrease in the permeability coefficient of the grouted surrounding rock, the radial stress decreases, the tangential stress increases, and the radius of the plastic zone increases. The development of plastic zone not only affects the stability but also causes an increase in the permeability coefficient. There is mutual restriction and influence between the shaft water inflow, the permeability coefficient, the radius of the grouted surrounding rock, and the radius of its plastic zone. In the design of grouting reinforcement, the stability of surrounding rock and the control requirements of shaft water inflow should be comprehensively considered and the optimal parameters should be selected based on theoretical calculation. This study provides a theoretical basis for the optimization of grouting reinforcement parameters in a deep shaft.

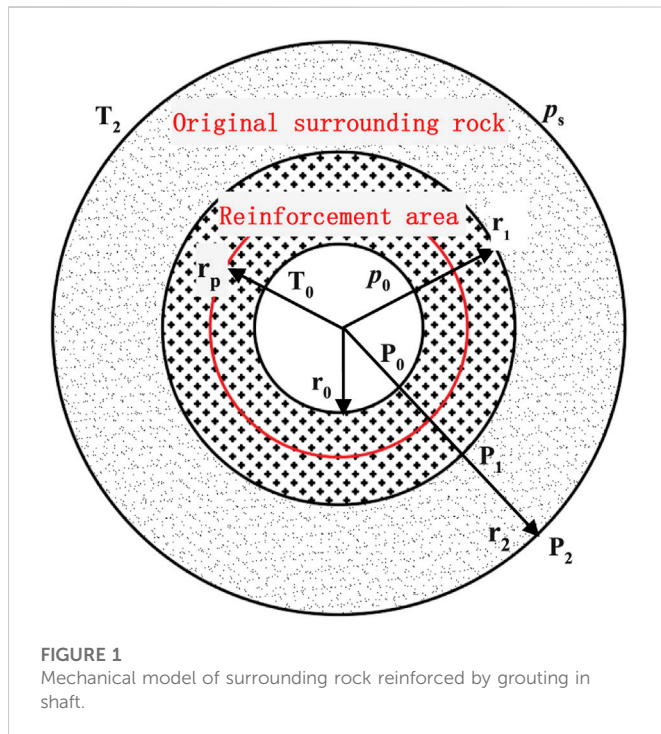
## KEYWORDS

deep shaft, grouting reinforcement, elastoplastic solution, stability, water inflow

## 1 Introduction

With the continuous promotion of the strategy of seeking mineral resources and energy in deep mines, the construction depth of mine shafts has exceeded 1500 m in China and will soon exceed 2000 m. For example, the design depth of the main shaft in the Sanshandao Gold Mine under construction in the Xiling mining area is more than 2000 m. Existing research results (Xiang et al., 2022a; Xiang et al., 2022b) show that the *in situ* stress at a depth of 2000 m is as high as 70 Mpa, the water head pressure is close to 20 Mpa, and the temperature exceeds 60 °C.





Disasters caused by high stress, high water pressure, and high temperature environments are the biggest challenges faced by the deep shaft project, of which the water hazard is the most prominent, and the pregrouting reinforcement of the surrounding rock in the working face is the main means of controlling water hazards at present. After grouting, the surrounding rock must meet impermeability requirements, and the surrounding rock's stability should not be ignored during shaft excavation.

In terms of theoretical research on the grouting reinforcement of the rock surrounding shafts, Zhang Dingli et al. put forward a new design concept of active waterproofing and drainage control and established an overall seepage mechanical model including the reinforcement area and the primary support. They clearly show that the reinforcement area and the primary support are locations where water inflow is controlled (Li et al., 2012; Zhang and Sun, 2019). Song Zhiheng et al. studied the influence of the grouted reinforcement area of a tunnel on the water inflow velocity and optimized the grouting parameters according to the numerical simulation results. Yang et al. (2017) carried out an experimental study on the influence of a grouted reinforcement area on the seepage field, and the results show that the grouted reinforcement area can bear part of the underground load and effectively reduce tunnel drainage. Li et al. (2013) established a simplified seepage model of a shaft in an infinite aquifer and analyzed and verified the influence of grouting reinforcement parameters on the external water pressure of the lining. Li et al. (2020) studied the influence of grouting reinforcement parameters on the seepage field of the surrounding rock under different waterproof and drainage types of tunnels using theoretical analysis and numerical simulation methods. Zhou et al. (2020) deduced the analytical solutions of the Darcy seepage field, the non-Darcy seepage field, and the effective stress field of the rock surrounding the tunnel and analyzed the influence of the grouting effect on the seepage and stress fields of the surrounding rock (He et al., 2020).

There have been many theoretical achievements in analytical solutions research on the stability of a circular chamber. One achievement is the elastoplastic analytical theory based on the mechanics of a circular hole in an infinite plane without considering the effects of water and temperature (Ren and Qiu, 2005; Xiao et al., 2013; Chen et al., 2017; Ma et al., 2021). Another achievement is the elastoplastic analytical theory considering the “fluid solid” coupling of groundwater or the “thermal” coupling of ground temperature (Rong and Cheng, 2004; Li et al., 2004; Shi et al., 2008; Carranza-Torres and Zhao, 2009; Lü and Xu, 2009; Xu et al., 2015; Xu et al., 2020; Jin et al., 2022). In addition, an analytical theory considers the interaction of thermal, hydraulic, and mechanical fields (Kong et al., 2005; Bai, 2011; Pandey et al., 2017; Liu et al., 2019), but most of them only involve elastic problems and cannot be directly used in the stability analysis of underground caverns. Zhang Yujun et al. established an elastic-plastic analytical solution for a circular cavern under the combined action of thermal, hydraulic, and mechanical fields but did not consider the effect of grouting (Zhang and Zhang, 2013).

To sum up, most existing research focuses on tunnel engineering, but there is little discussion of the grouting reinforcement and seepage resistance of a 2000-m deep shaft under the combined action of high stress, high water pressure, and high temperature. Therefore, in this article, an elastic-plastic analytical solution of the surrounding rock reinforced by grouting under the combined action of high stress, high water pressure, and high temperature is established, and the variation law and influencing factors of the stability and impermeability of reinforced rock in a deep shaft are analyzed, providing a theoretical basis for the design and optimization of parameters of deep grouting reinforcement.

## 2 Solution of stress and displacement of surrounding rock reinforced by grouting in shafts

Due to the high water pressure in the deep stratum, it is very difficult to control water once the water-bearing fractured stratum is exposed during shaft excavation. Therefore, the rock surrounding the working face is usually pregrouted to prevent seepage and block water; that is, the water-bearing fractured stratum is first grouted and consolidated, and then, blasting excavation is carried out.

First, the mechanical model of grouting the rock surrounding a deep shaft under the combined action of thermal, hydraulic, and mechanical forces is simplified into a stable plane model, as shown in Figure 1. The model can be regarded as the problem of steady heat conduction and steady seepage of a double-layered ring composed of the grouted reinforcement area and the original surrounding rock, which is a plane strain problem. In this model,  $r_0$  is the distance between the inner edge of the reinforced grouted rock surrounding the shaft and the shaft center,  $r_1$  is the distance from the outer edge of the grouted reinforcement to the shaft center, and  $r_2$  is the original surrounding rock. Assuming  $r_2$  is large enough, the water pressure outside the area is constant at  $P_s$ , the temperature is constant at  $T_2$ , and the stress is constant at  $P_2$ . At the inner edge of the grouted reinforcement  $r_0$ , the support pressure is  $P_0$ , the temperature is  $T_0$ , and the water pressure is 0.

## 2.1 Calculation of seepage field

It is assumed that the permeability coefficient of the material in the aforementioned model is the same in all directions, the seepage direction is mainly radial, and the buoyancy in the seepage volume force has little influence and can be ignored. Therefore, this problem can be simplified as an axisymmetric stable seepage problem. The second-order ordinary differential equation of the stable seepage field formed after grouting reinforcement is as follows:

$$\frac{d^2 p_w}{dr^2} + \frac{1}{r} \cdot \frac{dp_w}{dr} = 0. \quad (1)$$

The distribution law of water pressure in the seepage field of surrounding rock reinforced by grouting is as follows (He et al., 2020):

$$p_w = \begin{cases} \frac{p_s k_2 \ln \frac{r}{r_0}}{k_1 \ln \frac{r_2}{r_1} + k_2 \ln \frac{r_1}{r_0}}, & r_0 \leq r \leq r_1, \\ \frac{p_s \left( k_1 \ln \frac{r}{r_1} + k_2 \ln \frac{r_1}{r_0} \right)}{k_1 \ln \frac{r_2}{r_1} + k_2 \ln \frac{r_1}{r_0}}, & r_1 \leq r \leq r_2, \end{cases} \quad (2)$$

where  $k_1$  and  $k_2$  are the permeability coefficients of the reinforcement area and the original surrounding rock, respectively.

## 2.2 Calculation of temperature field

Assuming that the thermal conductivity of the material in the above model is the same in all directions and the thermal conductivity direction is mainly radial, the problem is simplified as an axisymmetric steady-state heat conduction problem. The second-order ordinary differential equation of the steady-state temperature field is as follows (Xu, 2006):

$$\frac{d^2 T}{dr^2} + \frac{1}{r} \cdot \frac{dT}{dr} = 0. \quad (3)$$

The distribution law of the temperature field of surrounding rock reinforced by grouting can be obtained as follows:

$$T = \begin{cases} T_0 + \frac{(T_s - T_0) \lambda_2 \ln \frac{r}{r_0}}{\lambda_1 \ln \frac{r_2}{r_1} + \lambda_2 \ln \frac{r_1}{r_0}}, & r_0 \leq r \leq r_1, \\ T_0 + \frac{(T_s - T_0) \left( \lambda_1 \ln \frac{r}{r_1} + \lambda_2 \ln \frac{r_1}{r_0} \right)}{\lambda_1 \ln \frac{r_2}{r_1} + \lambda_2 \ln \frac{r_1}{r_0}}, & r_1 \leq r \leq r_2, \end{cases} \quad (4)$$

where  $\lambda_1$  and  $\lambda_2$  are the thermal conductivities of the reinforcement area and the original surrounding rock, respectively.

Research shows that under the action of higher temperature, 0.4–0.45 MPa thermal stress can be generated in the rock mass when the temperature changes by 1 °C (He, 2004). The thermal stress can be approximately calculated according to the following expression (Yue et al., 2017):

$$\Delta \sigma = E \alpha \Delta T. \quad (5)$$

Then, the distribution law of thermal stress expression of shaft-surrounding rock is obtained as follows:

$$p_T = \begin{cases} E_1 \alpha_1 (T_s - T_0) \frac{\lambda_2 \ln \frac{r}{r_0}}{\lambda_1 \ln \frac{r_2}{r_1} + \lambda_2 \ln \frac{r_1}{r_0}}, & r_0 \leq r \leq r_1, \\ E_2 \alpha_2 (T_s - T_0) \frac{\left( \lambda_1 \ln \frac{r}{r_1} + \lambda_2 \ln \frac{r_1}{r_0} \right)}{\lambda_1 \ln \frac{r_2}{r_1} + \lambda_2 \ln \frac{r_1}{r_0}}, & r_1 \leq r \leq r_2, \end{cases} \quad (6)$$

where  $E_1$  and  $\alpha_1$  are the elastic modulus and linear expansion coefficient of surrounding rock in the reinforcement area, respectively;  $E_2$  and  $\alpha_2$  are the elastic modulus and linear expansion coefficient of the original surrounding rock, respectively.

## 2.3 Elastic-plastic analytical solution under the combined action of thermo-hydro-mechanical forces

### 2.3.1 Equilibrium differential equation

Assuming that the rock surrounding the grouting and surrounding rock mass are homogeneous, ignoring the dead weight of the element, and only considering the unidirectional coupling of thermal stress and seepage stress to the stress field, this study is conducted according to the axisymmetric plane strain problem, and the equilibrium differential equation is as follows (ZHANG and ZHANG, 2013):

$$\frac{d\sigma_r}{dr} + \frac{\sigma_r - \sigma_\theta}{r} + \beta \frac{dp_w}{dr} + \frac{dp_T}{dr} = 0, \quad (7)$$

where  $\beta$  is the generalized effective stress coefficient, and  $\sigma_r$  and  $\sigma_\theta$  are radial and tangential effective stresses, respectively. The compressive stress is positive, and the tensile stress is negative.

To achieve the effect of water blocking, the range of grouting reinforcement must be larger than the damage and failure area of the surrounding rock during actual excavation, so only the plastic failure area in the reinforcement body must be analyzed.

### 2.3.2 Plastic zone of the reinforcement area

In order to achieve the effect of water plugging, the range of the grouted reinforcement area must be larger than the damage zone of the surrounding rock during the actual excavation, so it is only necessary to analyze the case that the plastic zone is within the scope of reinforcement. As shown in Figure 1,  $r_p$  is the radius of the plastic zone. The equilibrium differential equation of the microelement in the plastic zone of the grouted reinforcement area can be obtained by substituting Eq. 4 and Eq. 6 into Eq. 7:

$$\frac{d\sigma_r}{dr} + \frac{\sigma_r - \sigma_\theta}{r} + (K_1 + J_1) \frac{1}{r} = 0, \quad (8)$$

where  $K_1 = \frac{\beta_1 k_2 p_s}{k_1 \ln \frac{r_2}{r_1} + k_2 \ln \frac{r_1}{r_0}}$   $J_1 = \frac{E_1 \alpha_1 \lambda_2 (T_s - T_0)}{\lambda_1 \ln \frac{r_2}{r_1} + \lambda_2 \ln \frac{r_1}{r_0}}$

It is assumed that the grouted surrounding rock meets the Mohr–Coulomb criterion after entering the plastic state, and the tangential stress is the first principal stress during excavation; that is,  $\sigma_\theta = \sigma_1$ ,  $\sigma_r = \sigma_3$ . Because the specified compressive stress is positive, the yield condition is

$$\sigma_r - \sigma_\theta = -\frac{2c_1 \cos \varphi_1}{1 - \sin \varphi_1} - \frac{2 \sin \varphi_1}{1 - \sin \varphi_1} \sigma_r, \quad (9)$$

where  $c_1$  and  $\varphi_1$  are the cohesion and the internal friction angle of the grouted surrounding rock, respectively (note: the formula in Lü and Xu (2009) is written incorrectly).

Substitute Eq. 9 into Eq. 8 to get

$$\frac{d\sigma_r}{dr} - \frac{\sigma_r}{r} - \frac{2 \sin \varphi_1}{1 - \sin \varphi_1} - \frac{2c_1 \cos \varphi_1}{r(1 - \sin \varphi_1)} + \frac{K_1 + J_1}{r} = 0. \quad (10)$$

The stress in the yield zone can be solved using Eq. 10 as follows:

$$\sigma_r = A + Br^{\frac{2 \sin \varphi_1}{1 - \sin \varphi_1}}, \quad (11)$$

where B is the integral constant, and the expression of A is as follows:

$$A = \frac{1 - \sin \varphi_1}{2 \sin \varphi_1} \cdot (K_1 + J_1) - c_1 \cot \varphi_1. \quad (12)$$

By substituting the boundary condition  $(\sigma_r)_{r=r_0} = P_0$  into Eq. 11, the radial stress  $\sigma_{r1}$  and tangential stress  $\sigma_{\theta 1}$  in the plastic zone can be obtained:

$$\sigma_{r1} = A - (A - P_0) \left( \frac{r}{r_0} \right)^{\frac{2 \sin \varphi_1}{1 - \sin \varphi_1}}, \quad (13)$$

$$\sigma_{\theta 1} = \frac{1 + \sin \varphi_1}{1 - \sin \varphi_1} (A - (A - P_0) \left( \frac{r}{r_0} \right)^{\frac{2 \sin \varphi_1}{1 - \sin \varphi_1}}) + \frac{2c_1 \cos \varphi_1}{1 - \sin \varphi_1}. \quad (14)$$

### 2.3.3 Elastic zone of the reinforcement area

The equilibrium differential equation of the microelement in the elastic zone of the grouted reinforcement area is the same as Eq. 8, and the boundary condition is  $(\sigma_r)_{r=r_p} = P_{rp}$ ,  $(\sigma_r)_{r=r_1} = P_1$ ,  $P_{rp}$  is the normal force at the elastic-plastic interface, and  $P_1$  is the normal force on the contact interface between the grouted surrounding rock and the original surrounding rock. The formula for calculating the displacement, radial stress, and tangential stress of the elastic zone is as follows:

$$\mu_{r2} = C_1 r + C_2 \frac{1}{r} + \frac{1}{2} M_1 (K_1 + J_1) r \ln r, \quad (15)$$

$$\sigma_{r2} = \frac{1}{(1 - \mu_1) M_1} \left[ C_1 + (2\mu_1 - 1) C_2 \frac{1}{r^2} + \frac{M_1 (K_1 + J_1)}{2} \ln r + (1 - \mu_1) \frac{M_1 (K_1 + J_1)}{2} \right], \quad (16)$$

$$\sigma_{\theta 2} = \frac{1}{(1 - \mu_1) M_1} \left[ C_1 + (1 - 2\mu_1) C_2 \frac{1}{r^2} + \frac{M_1 (K_1 + J_1)}{2} \ln r + \mu_1 \frac{M_1 (K_1 + J_1)}{2} \right], \quad (17)$$

$$C_1 = \frac{1}{r_p^2 - r_1^2} \left[ M_1 (1 - \mu_1) (P_{rp} r_p^2 - P_1 r_1^2) - \frac{M_1 (K_1 + J_1)}{2} (r_p^2 \ln r_p - r_1^2 \ln r_1) - (1 - \mu_1) \frac{M_1 (K_1 + J_1)}{2} (r_p^2 - r_1^2) \right], \quad (18)$$

$$C_2 = \frac{M_1 (1 - \mu_1) (P_{rp} - P_1) - \frac{M_1 (K_1 + J_1)}{2} \ln \left( \frac{r_p}{r_1} \right)}{(2\mu_1 - 1) \left( \frac{1}{r_p^2} - \frac{1}{r_1^2} \right)}, \quad (19)$$

$$M_1 = \frac{(1 + \mu_1) (1 - 2\mu_1)}{E_1 (1 - \mu_1)}. \quad (20)$$

### 2.3.4 Elastic zone of original surrounding rock

The differential equation of stress balance in the elastic zone of the original surrounding rock is consistent with Eq. 8, and only the parameter  $K_1$  and  $J_1$  is replaced by  $K_2$  and  $J_2$ , where

$$K_2 = \frac{\beta_2 k_1 p_s}{k_1 \ln \frac{r_2}{r_1} + k_2 \ln \frac{r_1}{r_0}}, \quad J_2 = \frac{E_2 \alpha_2 \lambda_1 (T_2 - T_0)}{\lambda_1 \ln \frac{r_2}{r_1} + \lambda_2 \ln \frac{r_1}{r_0}}.$$

The boundary condition is  $(\sigma_r)_{r=r_1} = P_1$  and  $(\sigma_r)_{r=r_2} = P_2$ . The calculation formula of the displacement and stress of the original surrounding rock can be obtained as follows:

$$\mu_{rs} = D_1 r + D_2 \frac{1}{r} + \frac{1}{2} M_2 (K_2 + J_2) r \ln r, \quad (21)$$

$$\sigma_{rs} = \frac{1}{(1 - \mu_2) M_2} \left[ D_1 + (2\mu_2 - 1) D_2 \frac{1}{r^2} + \frac{M_2 (K_2 + J_2)}{2} \ln r + (1 - \mu_2) \frac{M_2 (K_2 + J_2)}{2} \right], \quad (22)$$

$$\sigma_{\theta s} = \frac{1}{(1 - \mu_2) M_2} \left[ D_1 + (1 - 2\mu_2) D_2 \frac{1}{r^2} + \frac{M_2 (K_2 + J_2)}{2} \ln r + \mu_1 \frac{M_2 (K_2 + J_2)}{2} \right], \quad (23)$$

$$D_1 = \frac{1}{r_1^2 - r_2^2} \left[ M_2 (1 - \mu_2) (P_1 r_1^2 - P_2 r_2^2) - \frac{M_2 (K_2 + J_2)}{2} (r_1^2 \ln r_1 - r_2^2 \ln r_2) - (1 - \mu_2) \frac{M_2 (K_2 + J_2)}{2} (r_1^2 - r_2^2) \right], \quad (24)$$

$$D_2 = \frac{M_2 (1 - \mu_2) (P_1 - P_2) - \frac{M_2 (K_2 + J_2)}{2} \ln \left( \frac{r_1}{r_2} \right)}{(2\mu_2 - 1) \left( \frac{1}{r_1^2} - \frac{1}{r_2^2} \right)}, \quad (25)$$

$$M_2 = \frac{(1 + \mu_2) (1 - 2\mu_2)}{E_2 (1 - \mu_2)}. \quad (26)$$

### 2.3.5 Equation solving

According to the stress and displacement expressions derived previously, the elastoplastic solution can be obtained by introducing the initial values and boundary conditions. At the elastic-plastic interface of the reinforced surrounding rock,  $\sigma_{r2}$ ,  $\sigma_{\theta 2}$  meet the Mohr-Coulomb yield condition, and the following results are obtained by combining Eqs 9, 16, 17:

$$\begin{aligned} (\sigma_{r2})_{r=r_p} &= P_{rp} \\ &= \frac{1 - \sin \varphi_1}{2} \frac{2C_1 + M_1 (K_1 + J_1) \ln r_p + 0.5M_1 (K_1 + J_1)}{M_1 (1 - \mu_1)} \\ &\quad - c_1 \cos \varphi_1. \end{aligned} \quad (27)$$

At the elastic-plastic interface of the reinforced surrounding rock, the radial stress shall also meet the following requirements:

$$(\sigma_{r1})_{r=r_p} = P_{rp} = A - (A - P_0) \left( \frac{r_p}{r_0} \right)^{\frac{2 \sin \varphi_1}{1 - \sin \varphi_1}}. \quad (28)$$

In addition, the displacement continuity condition of the contact surface between the original surrounding rock and the reinforced surrounding rock can be obtained as follows:

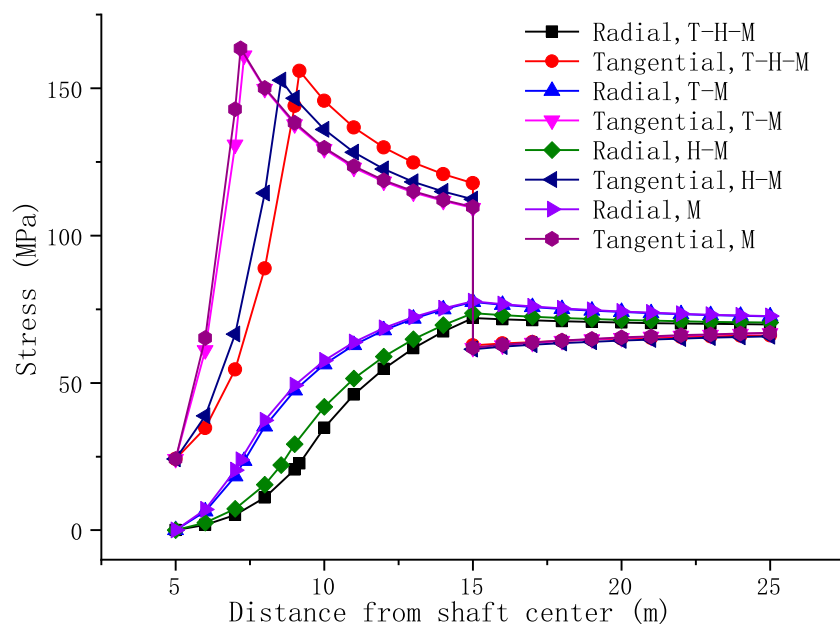


FIGURE 2

Stress distribution of surrounding rock under the combination of thermo-hydro-mechanical forces.

$$C_1 r_1 + C_2 \frac{1}{r_1} + \frac{1}{2} M_1 (K_1 + J_1) r_1 \ln r_1 = D_1 r_1 + D_2 \frac{1}{r_1} + \frac{1}{2} M_2 (K_2 + J_2) r_1 \ln r_1. \quad (29)$$

Combining the aforementioned three groups of equations, a transcendental equation about  $r_p$  can be obtained, and  $r_p$  can be determined using an iterative method. Then the area is obtained using the elastoplastic interface radial stress  $P_{rp}$  and the radial stress  $P_1$  at the interface between the original surrounding rock and the reinforcement.

### 3 Stability and impermeability analysis of surrounding rock reinforced by grouting in a deep shaft

In order to further analyze the influencing factors of stability and impermeability of surrounding rock reinforced by grouting, the following is illustrated by the specific calculation of an example. Taking a metal mine shaft of 2000 m depth in the Laizhou area of Shandong Province in China as an example, according to the mine survey and design data, the basic parameters of the shaft model at 2000m depth are as follows:

The grouted surrounding rock:  $E_1 = 30 \text{ GPa}$ ,  $\mu_1 = 0.22$ ,  $k_1 = 0.0015 \text{ m} \cdot \text{d}^{-1}$ ,  $\lambda_1 = \frac{2.46 \text{ W}}{\text{m}} \cdot \text{C}^\circ$ ,  $\alpha_1 = 1 \times 10^{-5} \text{ C}^\circ^{-1}$ ,  $c_1 = 5 \text{ MPa}$ ,  $\varphi_1 = 45^\circ$ .

The original surrounding rock:  $E_2 = 10 \text{ GPa}$ ,  $\mu_2 = 0.3$ ,  $k_2 = 0.015 \text{ m} \cdot \text{d}^{-1}$ ,  $\lambda_2 = \frac{1.51 \text{ W}}{\text{m}} \cdot \text{C}^\circ$ ,  $c_2 = 1 \text{ MPa}$ ,  $\varphi_1 = 45^\circ$ .

The shaft diameter and initial boundary conditions are as follows:  $r_0 = 5 \text{ m}$ ,  $P_2 = 60 \text{ MPa}$ ,  $T_2 = 60 \text{ C}^\circ$ ,  $p_2 = 20 \text{ MPa}$ ,  $P_0 = 0$ ,  $T_0 = 28 \text{ C}^\circ$ .

Based on the aforementioned parameters and through variable analysis, the influence law of each parameter on the performance of the grouting reinforcement area can be obtained.

### 3.1 Analysis of factors influencing the stability of grouted surrounding rock

Figure 2 shows the distribution of the radial stress and tangential stress of the surrounding rock under four conditions. It can be seen from the analysis that the radius of the plastic zone is the largest under the combined action of thermo-hydro-mechanical forces, the second largest is under the action of hydro-mechanical forces, the third largest is under the action of thermo-mechanical forces, and the smallest is under the action of mechanical forces alone. It can be seen that the surrounding rock damage is significantly exacerbated by the high temperature and high water pressure of the deep stratum, and the effect of water is significantly greater than that of temperature. Tangential stress jumps at the contact surface between the grouted rock surrounding the shaft and the original rock.

In the legend, T represents temperature, H represents hydraulic, and M represents mechanical.

Figure 3 shows that the radius of the plastic zone of the grouted surrounding rock decreases with the increase of the radius of the grouted area and surrounding rock. When the radius of grouted area exceeds a certain limit (about twice the radius of the plastic zone), the plastic zone does not change. When the radius of the grouted surrounding rock is equal to the radius of the plastic zone, the critical radius of the grouted surrounding rock can be obtained. When the radius of the grouted surrounding rock is greater than the critical value, the radius of the plastic zone decreases with an increase in the grouted reinforcement radius. When the radius of the grouted reinforcement is less than the critical value, the plastic damage range will exceed the reinforcement area. Therefore, the critical value can be used as a reference standard for the stability design of grouted surrounding rock. In addition, the higher the *in situ* stress, the larger the radius of the plastic zone of the corresponding reinforcement.

Figure 4 shows that the radius of the plastic zone increases with the increase of initial water pressure. The larger the water pressure, the

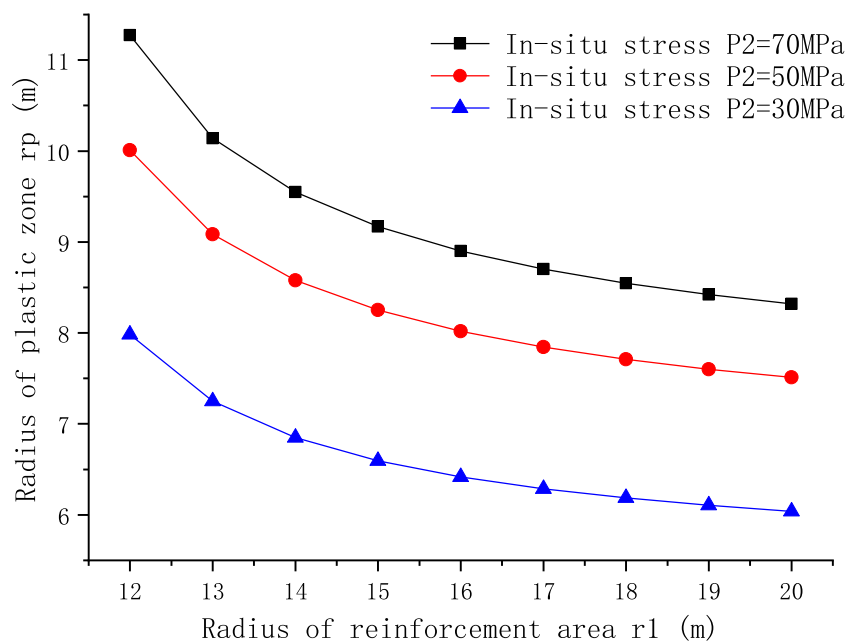


FIGURE 3

Effect of reinforcement area radius on plastic zone radius.

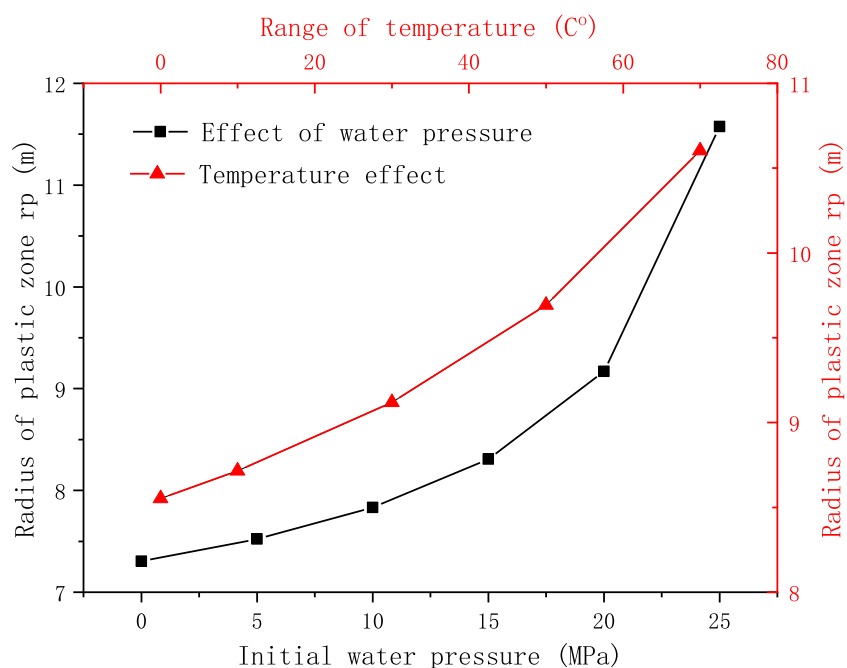


FIGURE 4

Effect of initial water pressure and temperature on plastic zone radius.

greater the rate of plastic zone increase. With an increase in the temperature difference between the wellbore and the original formation, the radius of the plastic zone in the reinforcement area increases. Due to the limited change of temperature, its impact on the plastic zone is much weaker than the water pressure.

Figure 5 shows that the radius of the plastic zone decreases with the increase of the cohesive force of the grouted surrounding rock. Increasing the cohesive force of the grouted surrounding rock has an obvious effect on improving its failure. In addition, the radius of the plastic zone increases with the increase of the elastic modulus of the surrounding



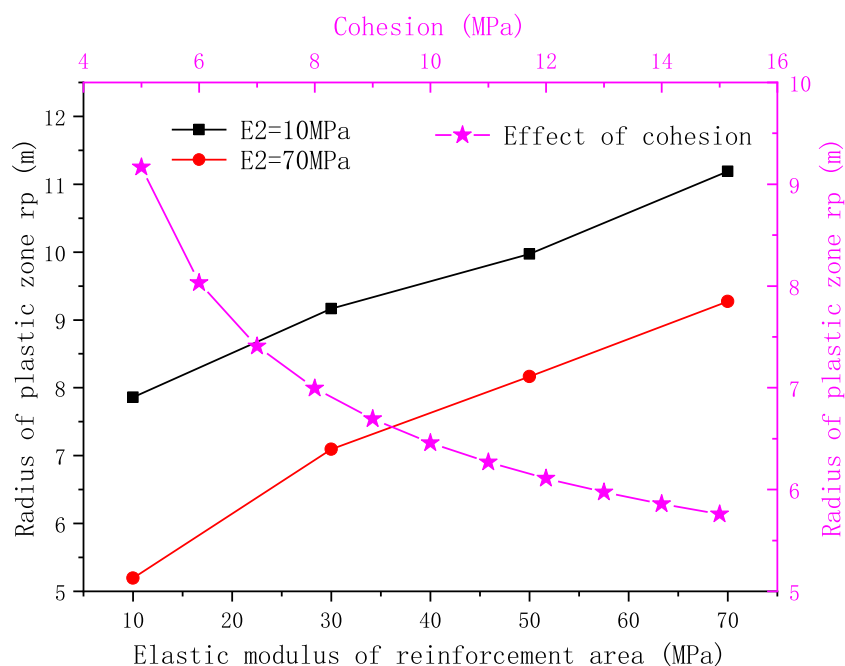


FIGURE 5

Effect of elastic modulus and cohesion on plastic zone radius.

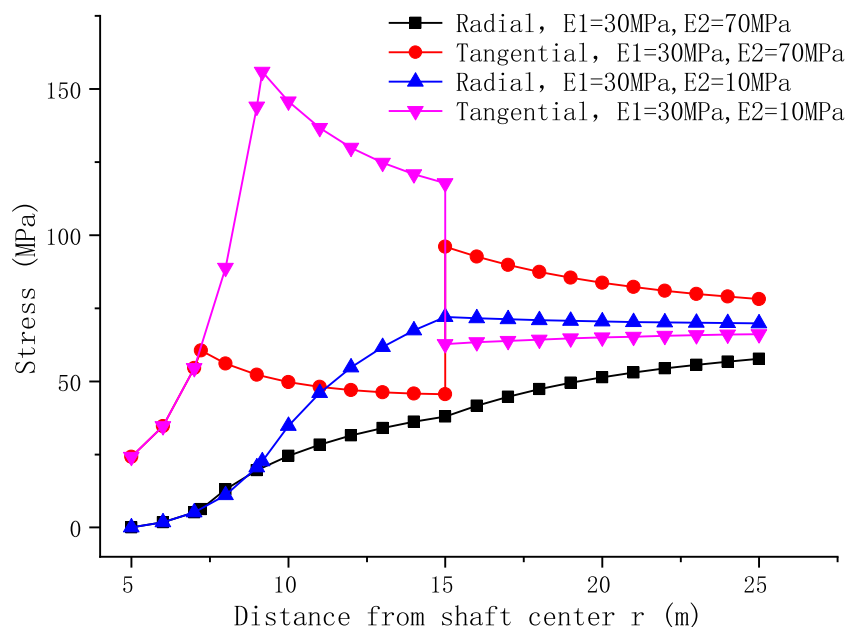


FIGURE 6

Effect of elastic modulus of original surrounding rock on stress field.

rock. The higher the elastic modulus of the original surrounding rock, the smaller the radius of the plastic zone is. It can be seen that the elastic modulus of the original surrounding rock has a great influence on the plastic zone of the grouted surrounding rock. In a word, the radius of the plastic zone increases with the increase of the elastic modulus ratio of the grouted surrounding rock and the original rock.

From the aforementioned analysis, it can be seen that too large an elastic modulus of surrounding rock reinforcement is not necessarily beneficial. To analyze the causes, Figure 6 shows the distribution of the surrounding rock stress field under two conditions. The first condition is that the elastic modulus of the grouted surrounding rock is greater than that of the original surrounding rock, which usually corresponds

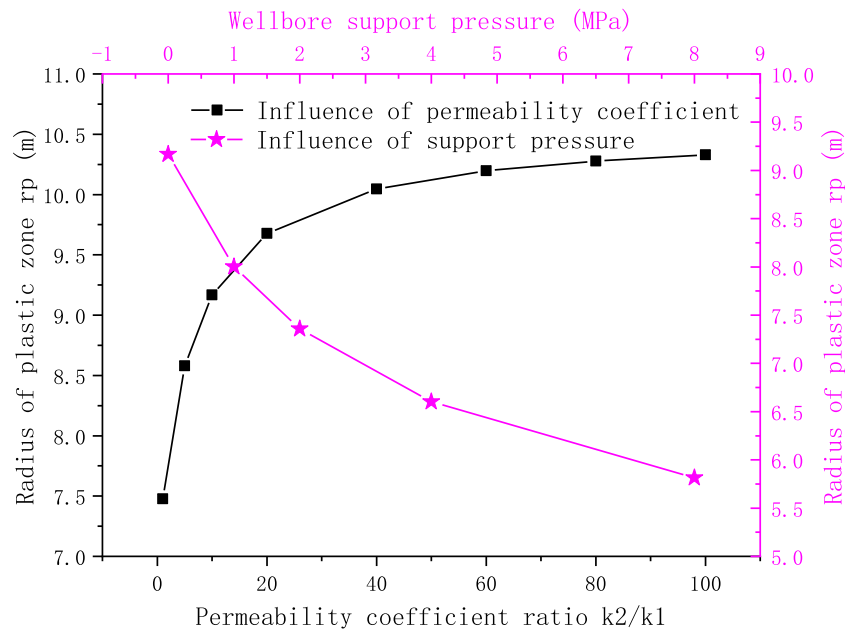


FIGURE 7

Variation of plastic zone radius with support pressure and the permeability coefficient ratio.

to the condition that the thickness of the surrounding rock fracture zone is large. After the rock surrounding the shaft is grouted, the surrounding rock in the distance is still a broken area, and the elastic modulus is relatively low. At this time, the stress after shaft excavation is mainly concentrated in the grouted surrounding rock. The stress in the grouted surrounding rock is much higher than that in the original surrounding rock, and its plastic damage range is also large. The second condition is that the elastic modulus of the grouted surrounding rock is smaller than that of the original surrounding rock, which usually corresponds to a small thickness of the fracture zone. At this time, the grouting reinforcement covers the entire fracture zone, and the surrounding rock in the distance is a relatively complete original stratum with a relatively large elastic modulus. In this case, the stress after shaft excavation is mainly concentrated in the original surrounding rock, and the stress concentration in the grouted surrounding rock is relatively small, which greatly reduces the plastic damage range. It can be seen that the jumping direction of the maximum tangential stress is related to the elastic modulus ratio of the grouted surrounding rock and the original surrounding rock. When the elastic modulus of the grouted surrounding rock is greater than the original surrounding rock, the maximum tangential stress appears at the elastoplastic interface; otherwise, it appears at the contact surface between the grouted surrounding rock and the original rock. The distribution of the plastic zone of the grouted surrounding rock is closely related to the surrounding rock characteristics. The elastic modulus design of the grouted surrounding rock should consider the original surrounding rock conditions, especially the bearing role of the original surrounding rock.

Figure 7 shows that with an increase in shaft support pressure, the plastic zone decreases significantly. It can be seen that timely support during excavation has a good effect on reducing the damage to the grouted surrounding rock. The larger the permeability coefficient ratio of the original surrounding rock and the grouted

surrounding rock, the larger the plastic zone radius is. When the coefficient ratio exceeds 40, the change in the plastic zone tends to ease. Figure 8 shows that when the permeability coefficient of the original rock is unchanged, the radial stress of the surrounding rock decreases with the reduction of the permeability coefficient of the grouted surrounding rock, and the tangential stress increases, leading to more plastic failure of the rock. Therefore, increasing the permeability coefficient of the grouted surrounding rock can reduce the radius of the plastic zone, which is beneficial to the stability of the surrounding rock. However, the increase in the permeability coefficient will also lead to an increase in the water inflow of the shaft. Therefore, the design of the permeability coefficient must comprehensively consider the surrounding rock stability and water inflow control requirements.

### 3.2 Impact analysis of water inflow

When the shaft is excavated, due to the plastic failure of some grouted surrounding rock near the shaft center, its permeability characteristics will also change. Assuming that the permeability coefficient of the plastic zone is infinite, that is, the water pressure at the elastic-plastic interface of the reinforcement surrounding rock is zero and the force of the blocked water is mainly borne by the elastic zone of the grouted surrounding rock, the expression of water pressure in the elastic zone of the grouted surrounding rock can be obtained according to Formula (2):

$$p_r = \frac{p_s k_2 \ln \frac{r}{r_p}}{k_1 \ln \frac{r_2}{r_1} + k_2 \ln \frac{r_1}{r_p}}, \quad r_p \leq r \leq r_1. \quad (30)$$

The expression of wellbore water inflow can be obtained using Darcy's law (Zhou et al., 2020):

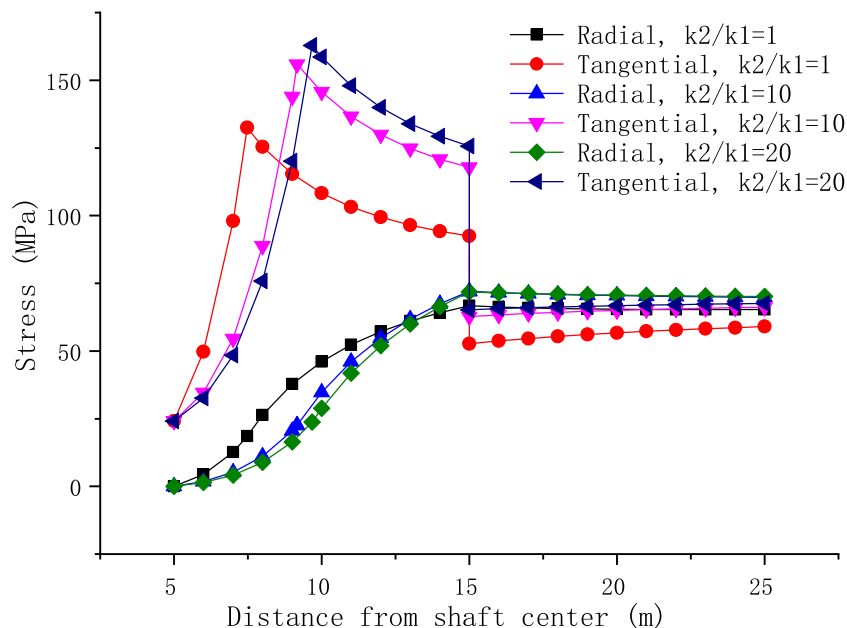


**FIGURE 8**  
Stress distribution under different permeability coefficient ratios.

**TABLE 1** Relationship between water inflow, radius, and plastic zone of grouted surrounding rock.

Radius of grouted surrounding rock/m	$r_1$			
Radius of the plastic zone/m	$q = 200 \text{ m}^3/\text{d}$	$q = 300 \text{ m}^3/\text{d}$	$q = 400 \text{ m}^3/\text{d}$	$q = 400 \text{ m}^3/\text{d}$
$r_p \neq 0$	19.6	15.0	13.5	12.6
$r_p = 0$	10.2	7.2	6.1	5.5

$$q = \frac{2\pi}{\gamma} \frac{p_s k_1 k_2 \ln \frac{r_1}{r_p}}{k_1 \ln \frac{r_2}{r_1} + k_2 \ln \frac{r_1}{r_p}}, \quad (31)$$

where  $q$ -flow is the rate per unit length of the wellbore in  $\text{m}^3 \cdot \text{d}^{-1} \cdot \text{m}^{-1}$ , and  $\gamma$  is the weight of water, measured in  $\text{N} \cdot \text{m}^{-3}$ .

It can be seen that the water inflow of the shaft is related to the permeability coefficient of the rock mass, the radius of the grouted surrounding rock, and the radius of the plastic zone. The radius of the grouted surrounding rock is  $r_1$ . The value should consider both the thickness of the plastic zone and the control requirements of the water inflow of the shaft. The grouting reinforcement radius considering the influence of the plastic zone can be obtained by combining Eqs 27–29, 31. Taking the water inflow control at a depth of 2000 m of the metal mine shaft as an example, the thickness of the aquifer is 10 m. The calculation results are shown in Table 1. With the increase of the standard value  $q$  of water inflow control, the requirements for the grouting reinforcement radius decrease accordingly. When the influence of the plastic zone is not considered ( $r_p = 0$ ), the radius of surrounding rock reinforcement is reduced by approximately half. Therefore, the radius of the surrounding rock reinforced by deep grouting should be determined comprehensively according to stability and water inflow requirements. The permeability coefficient of the plastic zone is limited, and it still has a certain ability to resist seepage and block water. Therefore, the radius of surrounding rock

reinforcement can theoretically be between the aforementioned two calculation results.

## 4 Discussion and conclusion

- (1) Compared with considering the effect of *in situ* stress only, the damage to the surrounding rock is significantly exacerbated by the high temperature and high water pressure of the deep stratum, and the effect of water is significantly greater than that of temperature. Tangential stress jumps at the contact surface between the grouted surrounding rock and the original rock, and the direction of the stress jump is related to the ratio of elastic modulus of the two. When the elastic modulus of the grouted surrounding rock is greater than the original surrounding rock, the maximum tangential stress appears at the elastoplastic interface; otherwise, it appears at the contact surface between the grouted surrounding rock and the original rock.
- (2) The radius of the plastic zone of the grouted surrounding rock decreases with the increase of the radius of the grouted surrounding rock. When the radius of the grouted surrounding rock exceeds roughly twice that of the plastic zone, the plastic zone does not change. With the increase of the *in situ* stress, water pressure, and temperature difference, the

corresponding radius of the plastic zone of the grouted surrounding rock increases.

- (3) The radius of the plastic zone decreases with an increase in the cohesion in the surrounding rock. With an increase in the elastic modulus ratio between the grouted surrounding rock and the original rock, the radius of the plastic zone increases. When designing the elastic modulus of the grouted surrounding rock, the original surrounding rock should be considered to give full play to the stress-bearing role of the original surrounding rock.
- (4) Increasing the permeability coefficient of the grouted surrounding rock can reduce the radius of the plastic zone, which is beneficial to the stability of the surrounding rock, but it will also lead to an increase in water inflow. The water inflow of the shaft, the permeability coefficient of the grouted surrounding rock, the radius of the grouted surrounding rock, and the radius of the plastic zone are all interrelated. Therefore, the grouting reinforcement parameters should be designed based on the stability of the surrounding rock and water inflow control requirements, and the optimal solution should be selected through theoretical calculation.

Due to the author's mathematical and mechanical level, this article does not consider the complete coupling effect of thermal, hydraulic, and mechanical fields. Whether the Mohr–Coulomb criterion can truly reflect the failure characteristics of surrounding rock in deep strata remains to be discussed. In addition, the interaction between the surrounding rock reinforced by grouting and the shaft wall structure needs further study.

## Data availability statement

The raw data supporting the conclusion of this article will be made available by the authors without undue reservation.

## References

- Bai, B. (2011). Analytical solutions of thermal consolidation for a hollow cylinder saturated porous medium. *Rock Soil Mech.* 32 (10), 2901–2916. doi:10.16285/j.rsm.2011.10.005
- Carranza-Torres, C., and Zhao, J. (2009). Analytical and numerical study of the effect of water pressure on the mechanical response of cylindrical lined tunnels in elastic and elasto-plastic porous media. *Int. J. Rock Mech. Min. Sci.* 46 (3), 531–547. doi:10.1016/j.ijrmms.2008.09.009
- Chen, L., Mao, X. B., Li, M., and Chen, Y. L. (2017). Elastic-plastic analysis of deep roadway fracture surrounding rock based on drucker-prager criterion. *Chin. J. Coal* 42 (2), 484–491. doi:10.13225/j.cnki.jccs.2016.6029
- He, M. C. (2004). Present state and perspective of rock mechanics in deep mining engineering. *Proceeding of the 8th Rock Mechanics and Engineering Conference*, Beijing (Beijing: Science Press), 88–94. doi:10.19721/j.cnki.1001-7372.2020.12.016
- He, X., Zhou, X. M., Guo, X. H., Xu, Y., and Ma, W. Z. (2020). Analysis of non-Darcy seepage field and stress field of surrounding rock strengthened by grouting in deep buried tunnel. *China J. Highw. Transp.* 33 (12), 200–211. doi:10.19721/j.cnki.1001-7372.2020.12.016
- Jin, B., Hu, M., and Fang, Q. H. (2022). Research on stress field of surrounding rock and lining structure of deep-buried subsea tunnel considering seepage effect. *Chin. J. Theor. Appl. Mech.* 54 (5), 1322–1330. doi:10.6052/0459-1879-21-670
- Kong, X. Y., Li, D. L., Xu, X. Z., and L. D. T. (2005). Study on the mathematical models of coupled thermal-hydrological mechanical (THM) processes. *Chin. J. Hydrodynamics* 20 (2), 269–275. doi:10.16076/j.cnki.cjhd.2005.02.02
- Li, P. F., Zhang, D. L., Zhao, Y., and Zhang, C. P. (2012). Study on water pressure distribution of composite lining of submarine tunnel and parameters of grouting reinforcement ring. *Chin. J. Rock Mech. Eng.* 31 (2), 280–288. doi:10.3969/j.issn.1000-6915.2012.02.007
- Li, Z. L., Ren, Q. W., and Wang, Y. H. (2004). Elastic-plastic analytical solution of deep-buried circle tunnel considering fluid flow field. *Chin. J. Rock Mech. Eng.* 23 (8), 1291–1295. doi:10.3321/j.issn:1000-6915.2004.08.011
- Li, W., Yang, D., and Qing, L. I. (2013). Study on the characteristic of water pressure upon lining in subject to high hydraulic pressure mountain tunnel. *J. Railw. Eng. Soc.* (11), 57–62. doi:10.3969/j.issn.1006-2106.2013.11.011
- Li, L. Y., Yang, J. S., Gao, C., Xia, W. Y., and Ma, Y. N. (2020). Analytical study on seepage field of tunnels with external drainage considering effect of grouting rings. *Chin. J. Geotechnical Eng.* 42 (1), 133–141. doi:10.11779/CJGE202001015
- Liu, G. H., Pu, H., Zhao, Z. Z., and Liu, Y. (2019). Coupled thermo-hydro-mechanical modeling on well pairs in heterogeneous porous geothermal reservoirs. *Energy* 171, 631–653. doi:10.1016/j.energy.2019.01.022
- Lü, X., and Xu, J. (2009). Elastic-plastic solution for subsea circular tunnel under the influence of seepage field. *Eng. Mech.* 26 (2), 216–221.
- Ma, Y., Lu, A., Cai, H., and Zeng, X. (2021). Analytical solution for determining the plastic zones around two unequal circular tunnels. *Tunn. Undergr. Space Technol.* 120, 104267. doi:10.1016/j.tust.2021.104267
- Pandey, S. N., Chaudhuri, A., and Kelkar, S. (2017). A coupled thermo-hydro-mechanical modeling of fracture aperture alteration and reservoir deformation during heat extraction from a geothermal reservoir. *Geothermics* 65 (1), 17–31. doi:10.1016/j.geothermics.2016.08.006
- Ren, Q. W., and Qiu, Y. (2005). Elastic-plastic solution of circular tunnel with liner. *Eng. Mech.* 22 (2), 212–217.

## Author contributions

PX and HJ contributed to the conception and design of the study. PX wrote the first draft of the manuscript. HJ, GZ, and WL wrote sections of the manuscript. All authors contributed to the manuscript revision, and read and approved the submitted version.

## Funding

This paper was supported by the Major Scientific and Technological Innovation Project of Shandong Province (No. 2019SDZY05) and the Open Fund of the Hubei Provincial Engineering Technology Research Center of High Efficient Clean Utilization Shale Vanadium Resource (No. 2021zy003).

## Conflict of interest

Author WL was employed by the Sanshandao Gold Mine of Shandong Gold Group Co., Ltd., China.

The remaining authors declare that the research was conducted in the absence of any commercial or financial relationships that could be construed as a potential conflict of interest.

## Publisher's note

All claims expressed in this article are solely those of the authors and do not necessarily represent those of their affiliated organizations, or those of the publisher, the editors and the reviewers. Any product that may be evaluated in this article, or claim that may be made by its manufacturer, is not guaranteed or endorsed by the publisher.

- Rong, C. X., and Cheng, H. (2004). Stability analysis of rocks around tunnel with ground water permeation. *Chin. J. Rock Mech. Eng.* 23 (5), 741–744. doi:10.3321/j.issn:1000-6915.2004.05.007
- Shi, Y., Zhu, Z. D., and Li, Z. J. (2008). Deformation characteristics of deep-buried caverns considering thermal effect. *Adv. Sci. Technol. Water Resour.* 28 (3), 33–36.
- Xiang, P., Ji, H. G., Geng, J. M., and Zhao, Y. W. (2022). Characteristics and mechanical mechanism of *in situ* unloading damage and core discing in deep rock mass of metal mine. *Shock Vib.* 2022, 1–13. doi:10.1155/2022/5147868
- Xiang, P., Xu, H. C., Ji, H. G., Li, Q., and Wang, H. (2022). Thermal property of granite in deep strata and its effect on thermal zone of surrounding rock. *Shock Vib.* 2022, 1–9. doi:10.1155/2022/2461684
- Xiao, J. Q., Feng, X. T., Zhang, L. C., Qiu, S. L., et al. (2013). Static elastoplastic analytical method of circular tunnel under uniform geostress field. *Chin. J. Rock Mech. Eng.* 32 (S2), 3466–3477. doi:10.3969/j.issn.1000-6915.2013.z2.061
- Xu, Z. L. (2006). *Elasticity*. Beijing, China: Higher Education Press.
- Xu, Y., Zou, J. F., Xu, Y., and Yuan, Z. (2015). Generalized Hoek-Brown solution for circular tunnel with axial and osmotic forces considered. *Rock Soil Mech.* 36 (10), 2837–2846+2854. doi:10.16285/j.rsm.2015.10.013
- Xu, Y., Zhou, X. M., He, X. N., Wu, T., Zhang, J. L., and Li, S. (2020). Thermal-solid coupling analysis of shaft wall and surrounding rocks in a mine shaft. *Rock Soil Mech.* 41 (S1), 217–226+245. doi:10.16285/j.rsm.2019.0744
- Yang, S. Z., He, C., Li, Z., Yang, W. B., and Luo, Y. W. (2017). Inner water pressure distribution law of the tunnel grouting circle in water-rich area. *J. China Univ. Min. & Technology* (3), 546–553. doi:10.13247/j.cnki.jcmt.000684
- Yue, H., Su, Y., and Fang, Y. (2017). An analysis of the temperature effect of irregular failure in deep rock mass. *Hydrogeology Eng. Geol.* 44 (01), 48–56. doi:10.16030/j.cnki.issn.1000-3665.2017.01.08
- Zhang, D., and Sun, Z. (2019). An active control waterproof and drainage system of subsea tunnels and its design method. *Chin. J. Rock Mech. Eng.* 38 (1), 1–17. doi:10.13722/j.cnki.jrme.2018.0955
- Zhang, Y. J., and Zhang, W. Q. (2013). An elastoplastic analytical solution for circular cavern considering combined thermos-hydro-mechanical action. *Rock Soil Mech.* 34 (S2), 41–44.
- Zhou, X., Xu, Y., Liu, S. J., He, X. N., et al. (2020). Research on stress and seepage fields of surrounding rock grouting of ultra-deep shafts of gold mine. *Chin. J. Rock Mech. Eng.* 39 (8), 1611–1621. doi:10.13722/j.cnki.jrme.2020.0271





## OPEN ACCESS

## EDITED BY

Guang-Liang Feng,  
Institute of Rock and Soil Mechanics  
(CAS), China

## REVIEWED BY

Bing Bai,  
Beijing Jiaotong University, China  
Jianping Sun,  
Nanyang Technological University,  
Singapore

## \*CORRESPONDENCE

Dayong Chen,  
✉ cdychendayong@163.com  
Youjun Ning,  
✉ cnningyj@foxmail.com

## SPECIALTY SECTION

This article was submitted to  
Geohazards and Georisks,  
a section of the journal  
Frontiers in Earth Science

RECEIVED 21 October 2022

ACCEPTED 09 December 2022

PUBLISHED 25 January 2023

## CITATION

Chen D, Yang Z, Wang M, Jiang X and  
Ning Y (2023), DDA simulation study on  
fracturing failure reproducibility of  
heterogeneous rock.  
*Front. Earth Sci.* 10:1076023.  
doi: 10.3389/feart.2022.1076023

## COPYRIGHT

© 2023 Chen, Yang, Wang, Jiang and  
Ning. This is an open-access article  
distributed under the terms of the  
[Creative Commons Attribution License  
\(CC BY\)](https://creativecommons.org/licenses/by/4.0/). The use, distribution or  
reproduction in other forums is  
permitted, provided the original  
author(s) and the copyright owner(s) are  
credited and that the original  
publication in this journal is cited, in  
accordance with accepted academic  
practice. No use, distribution or  
reproduction is permitted which does  
not comply with these terms.

# DDA simulation study on fracturing failure reproducibility of heterogeneous rock

Dayong Chen<sup>1\*</sup>, Zheng Yang<sup>2</sup>, Mingke Wang<sup>1</sup>, Xufei Jiang<sup>1</sup> and  
Youjun Ning<sup>3\*</sup>

<sup>1</sup>State Key Laboratory of Coal Resources and Safe Mining, China University of Mining and Technology, Xuzhou, China, <sup>2</sup>State Key Laboratory of Explosion Science and Technology, Beijing Institute of Technology, Beijing, China, <sup>3</sup>School of Mechatronic Engineering, Southwest Petroleum University, Chengdu, Sichuan, China

The mesoscale heterogeneity of rock determines its macroscale mechanical performance to a large extent. In this paper, a sub-block element discontinuous deformation analysis (DDA) method coupled with a statistic heterogeneity model was used to simulate the fracturing failure of pre-notched rock specimens. The simulation recreated the macroscale whole-process nonlinear deformation and fracturing failure of pre-notched disc and rectangular specimens with some important features explored in experiments or other numerical simulations. Combining intact heterogeneous rock specimen simulations in previous work, the effect of the heterogeneity on the reproducibility of macroscale strength and failure patterns of the specimens were investigated. Results indicate that the influence degree of the heterogeneity on the macroscale equivalent strength and fracturing failure pattern reproducibility varies with the specimen particularities (disc or rectangular, pre-notched or intact, and inclination of the pre-existing flaw), and the reason behind was discussed from the point view of stress concentration. This work is meaningful for the understanding of the result discreteness of rock specimen experiments, and assures the importance to consider the rock heterogeneity in practical rock engineering.

## KEYWORDS

rock fracturing failure, heterogeneity, reproducibility, pre-existing flaw, discontinuous deformation analysis (DDA)

## Introduction

Rock masses are composed of rock bulks and discontinuities such as joints and faults, while the rock bulk is a typical heterogeneous material consists of mineral grains, grain boundaries and defects like voids and microcracks, etc., at the mesoscale. The mesoscale mechanical heterogeneity of rock is characterized by the variation of the deformation and strength properties with the mesoscopic spatial locations, which consequently leads to the uncertain and statistic characters of the macroscale deformation and fracturing failure of rock (Tang et al., 1998; Li et al., 2022; Yang et al., 2022). An acknowledged phenomenon that could largely attributed to the heterogeneity of rock is that rock experiments of

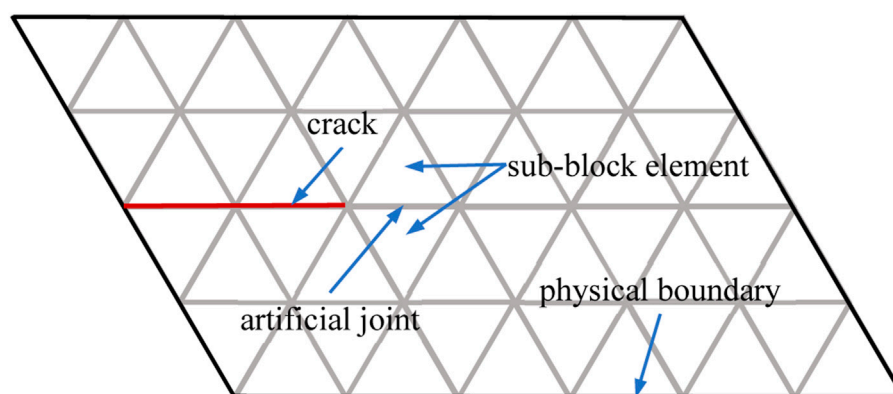


**FIGURE 1**  
Illustration of the sub-block element DDA fracturing simulation method.

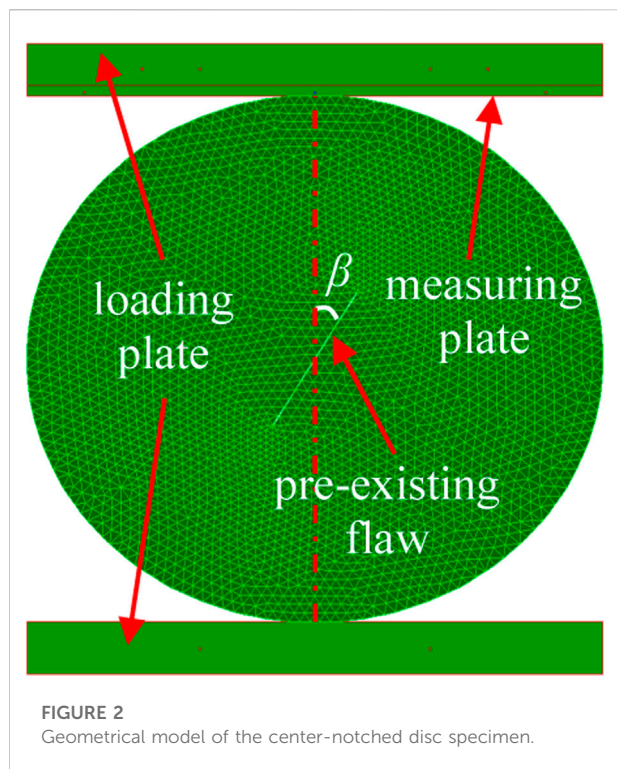
specimens generally show poor reproducibility of the macroscale strength and fracturing failure patterns (Alzaki et al., 2020; Shirole et al., 2020; Sun et al., 2022). For engineering practices, e.g., in the prediction of geological disasters and the design of rock engineering structures, the heterogeneity of rock is an important issue that should be carefully considered (Manouchehrian and Cai, 2016; He et al., 2019).

The mesoscale material components and distributions of rock could be well captured by high precision instruments and handled by the measure of image processing *etc.*, which then could be correlated to the rock mechanical properties (Zheng et al., 2020; Wang and Sun, 2021). From the theoretical aspect, Bai et al. (2019) and Bai et al. (2021) developed thermo-hydro-mechanical models for geomaterials based on the tenet of particle rearrangement in porous granular materials. Regarding the study of the mesoscale mechanical behaviors of rock, therefore the macroscale equivalent mechanical performances could also be investigated, numerical simulation is an effective and favorable approach. For example, Gui et al. (2016) conducted a comprehensive investigation of grain effect (size and distribution) in discrete element modelling of intact rock through Brazilian disc and uniaxial compressive tests using Universal Distinct Element Code. Gao et al. (2016) developed a distinct element grain-based method to simulate the microstructure of rock-like materials, which allows the assignment of specific properties to both the grains and grain boundaries. Peng et al. (2021) investigated the effect of grain size on the strength of polymineralic crystalline rock using the grain-based modeling approach in discrete element method by interpreting micro-cracking process in response to loading. Rasmussen (2022) proposed a breakable grain scheme and a method to achieve bi-modular elastic material behavior in grain-based models of rocks using the hybrid lattice/discrete element method. Wu et al. (2017) and Zhou et al. (2022) developed

Voronoi grain-based numerical manifold methods to investigate deformation and damage of intact rock at the mesoscale.

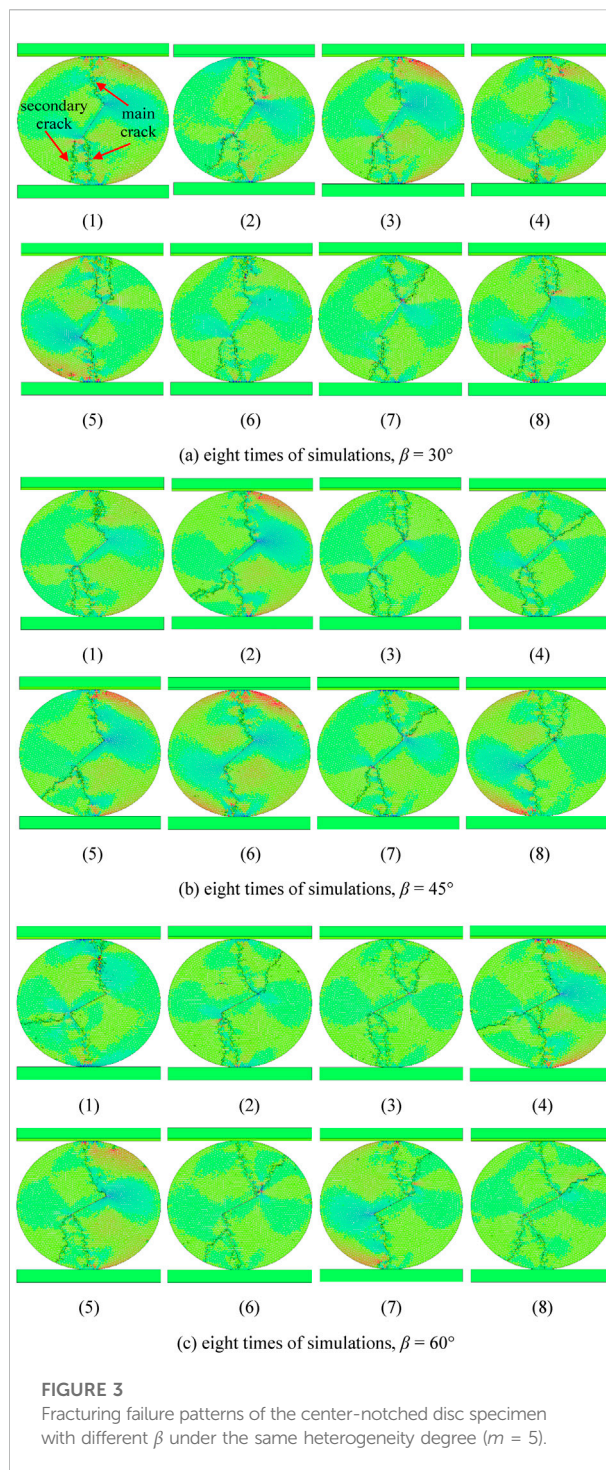
The above works simulated rock mechanical behaviors by explicitly representing the mesoscale structure of rock on the grain level, which may suffer high computational cost for large scale simulations. Alternatively, the mesoscale heterogeneity could be equivalently described by heterogeneity index of statistic models. For example, Liu et al. (2018) presented a heterogeneity index to describe mesoscale heterogeneity induced by grain size variation in intact rock. Li et al. (2022) used a random discrete element method to model rock heterogeneity. Yang et al. (2022) simulated the effect of heterogeneity on the characteristics of ubiquitous cracks in the Brazilian splitting test of rock by ABAQUS, in which the material heterogeneity is characterized by the Weibull distribution. In fact, the Weibull distribution has been widely applied to describe the mesoscale heterogeneity of materials, e.g., in the widely used rock mechanics software Rock/Realistic Failure Process Analysis (RFPA) (Tang et al., 1998; Tang et al., 2000; Tang et al., 2000). To understand the physical mechanism for the discrepancy of rock tension, Xu et al. (2020) carried out RFPA simulations of direct tension and semi-circular bending tests of intact heterogeneous rock. Tang and Zhang (2009) also presented a spatial correlation length factor into the traditional Weibull distribution to investigate the heterogeneity character of concrete failure. Combining linear elastic material constitutive relations and statistic heterogeneous models at the mesoscale, the macroscale nonlinear deformation and failure behaviors of rock could be well predicted (Tang et al., 1998).

Regarding the numerical methods to simulate the mesoscale deformation and fracturing failure of rock, discontinuous deformation analysis (DDA) (Shi and Goodman, 1985; Shi, 1992) could be a good choice among those widely used discontinuum-based methods like distinct element method (DEM) (Cundall and Hart, 1992). DDA has been widely used



in various static and dynamic rock mechanics and engineering problems (Ning et al., 2017; Ning and Lv, 2022), in which rock fracturing could be successfully simulated by the sub-block element approach (Ning et al., 2011; Jiao et al., 2012; Ni et al., 2020). Ning et al. (2021) also have introduced a mesoscale statistic heterogeneity model for rock based on the Weibull distribution introduced into DDA. In that work, the fracturing failure of intact heterogeneous disc and rectangular specimens under compression were comprehensively simulated to investigate the influence of heterogeneity on the fracturing failure pattern and macroscale equivalent response of intact rock.

In the present work, the DDA method enhanced with the sub-block fracturing modeling algorithm and the Weibull distribution heterogeneity model is applied to simulate pre-notched rock specimens, and combining intact heterogeneous rock specimen simulations in previous work, the effect of the heterogeneity on the reproducibility of macroscale strength and failure patterns of the specimens are investigated. The arrangement of the rest sections of the paper is as follows. In Section 2, the applied sub-block element DDA method for fracturing simulation and the mesoscale statistic heterogeneity model for rock are briefly introduced. In Section 3, the radial compression of center-notched disc rock specimens and uniaxial compression of center-notched rectangular rock specimens are simulated with an emphasis to investigate the fracturing failure reproducibility, along with the comparison with intact heterogeneous disc and rectangular specimens. Finally, conclusion are drawn in Section 4.



## Numerical methods

### The applied sub-block element DDA method for fracturing simulation

DDA (Shi, 1992) is a block-based discontinuous numerical method that takes six variables as  $(u_0 \ \nu_0 \ r_0 \ \varepsilon_x \ \varepsilon_y \ \gamma_{xy})$  with clear

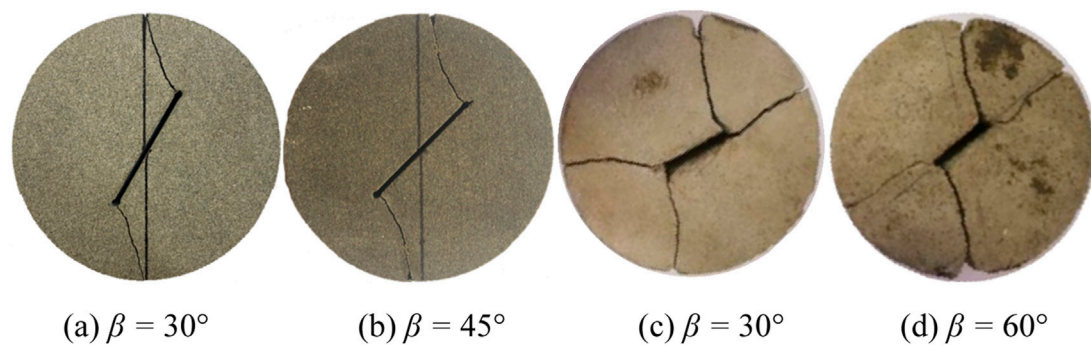


FIGURE 4

Typical experimental results of center-notched rock disc without (A) and (B), Huang et al., 2022) and with secondary cracks (C) and (D), Ou, 2020).

physical meanings for each block in two-dimension, where the first three are the translatory and rotary motions at the block center, and the last three are the normal and shear strains of the block, respectively. These variables represent a full first order approximation of the block deformation and lead to very simple form of energy formulas of elasticity, loading, constraint, inertia and contact penalty, etc. By the minimization of these energies, the corresponding sub-matrices are added to construct the global equilibrium equations of a block system through a time-marching schedule, and then the system equations are implicitly solved. Combining a strict open-close iteration to achieve the contact status convergence between blocks, DDA could be well used to solve the deformation and displacement problems of rock.

The sub-block approach is usually adopted to simulate material fracturing by DDA. As shown in Figure 1, sub-block elements are glued by artificial joints to represent continuum, and the fracturing is allowed to take place along artificial joint surfaces. In the present work, the sub-block element DDA fracturing simulation method which judges the tensile/shear fracturing along artificial joints based on the adjacent sub-block stress levels is adopted. The tensile and shear fracturing follows the maximum tensile strength criterion and the Mohr-Coulomb criterion, respectively. Compared with judging the fracturing based on the contact stresses on the artificial joint surface (Ning et al., 2011; Jiao et al., 2012), the adopted method greatly reduces the influence of sub-block divisions and especially

the artificial joint orientations on the simulation results of fracturing path and failure strength, and it was also proved that triangular elements are effective for fracturing simulation with the sub-block element DDA (Ni et al., 2020).

## Heterogeneity model

An element-level mesoscale heterogeneity model is applied in DDA based on the Weibull distribution function. By introducing the mesoscale heterogeneity, the macroscale nonlinear behaviors of rock could be well represented based on the linear-elastic constitutive relation of DDA (Ning et al., 2021). From the Weibull distribution formula,

$$p(x) = \begin{cases} \frac{mx^{m-1}}{x_0^m} \exp\left[-\left(\frac{x}{x_0}\right)^m\right], & x \geq 0 \\ 0, & x < 0 \end{cases} \quad (1)$$

the cumulative distribution function can be obtained by integration as

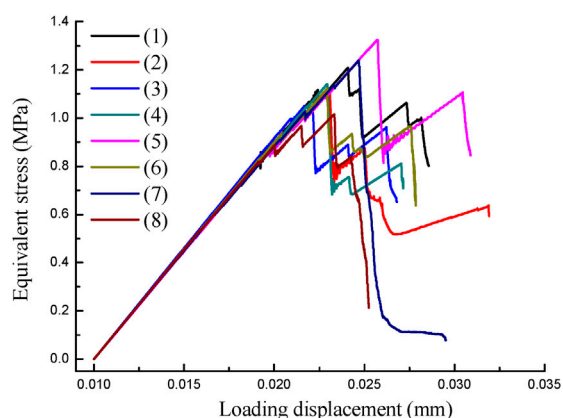
$$Q(x) = \int_0^x p(x)dx = 1 - \exp\left[-\left(\frac{x}{x_0}\right)^m\right] \quad (2)$$

Let  $Q(x) = y$  and simplify, it is derived that

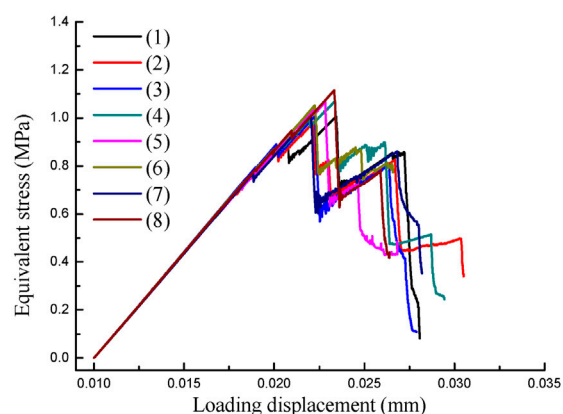
TABLE 1 Peak strength discreteness of disc specimens ( $m = 5$ ).

Peak strength (MPa)	Center-notched specimen			Intact specimen (Ning et al., 2021)
	$\beta = 30^\circ$	$\beta = 45^\circ$	$\beta = 60^\circ$	
maximum, $\sigma_{\max}^p$	1.33	1.12	1.25	4.26
minimum, $\sigma_{\min}^p$	0.97	0.91	0.96	3.65
discreteness, $\frac{\sigma_{\max}^p - \sigma_{\min}^p}{(\sigma_{\max}^p + \sigma_{\min}^p)/2} \times 100\%$	31.3%	20.7%	26.2%	15.4%

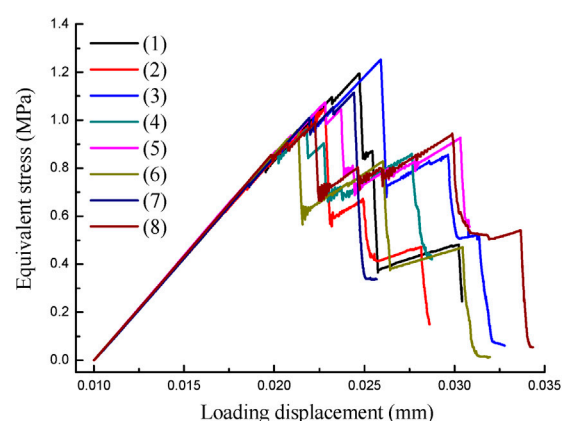




(a) eight times of simulations,  $\beta = 30^\circ$



(b) eight times of simulations,  $\beta = 45^\circ$



(c) eight times of simulations,  $\beta = 60^\circ$

**FIGURE 5**  
Diametral equivalent response curves of the center-notched disc specimen with different  $\beta$  under the same heterogeneity degree ( $m = 5$ ).

$$x = x_0 [-\ln(1 - \gamma)]^{\frac{1}{m}} \quad (3)$$

where  $\gamma$  is a random number between 0 and 1  $m$  is the heterogeneous index that controls the heterodonty degree,  $x_0$  is the homogeneous material property, and  $x$  is the heterogeneous material property corresponding to the random number  $\gamma$ . By replacing  $x_0$  with the homogeneous elastic modulus  $E$ , Poisson's ratio  $\mu$ , friction angle  $\theta$ , cohesion  $c$ , and tensile strength  $\sigma_t$ , respectively, the corresponding heterogeneous rock properties related to the random number  $\gamma$  and the heterogeneous index  $m$  can be obtained. For each DDA sub-block element, the random heterogeneous material properties are generated by a random number created by the computer, thus a heterogeneous DDA model for a problem to be simulated is constructed. Compared with the widely used finite element code RFPA for heterogeneous rock simulation, DDA gets the advantage to simulate the contacts and possible large displacements of rock.

It is worthy to be noted that most previous studies generally only considered the heterogeneity of the elasticity (modulus and Poisson's ratio) and ignored the strength (tensile strength, cohesion, and friction angle) heterogeneity. However, it is a fact that the strength varies with locations like that of the elasticity in real rock at the mesoscale, which means that the heterogeneity of strength should be considered as well. It was proved that rock is more prone to be destructed accompanied by more dispersing cracks when considering the heterogeneity of elasticity and strength simultaneously (Ning et al., 2021). Therefore, in the present study the elasticity and strength heterogeneities are both considered.

## Reproducibility investigation

Radial compression of disc specimens and uniaxial compression of rectangular specimens are widely applied experiments to test the deformation and fracturing failure behaviors of rock materials. Here, the fracturing failures of center-notched disc specimens and center-notched rectangular specimens are simulated to investigate the reproducibility of the radial compression test and the uniaxial compression test of rock, respectively, under the same heterogeneity degree. For the disc specimen, three different inclination angles of the pre-existing flaw are considered, and for each condition of the pre-existing flaw inclination, eight times of simulations are carried out under the same heterogeneity degree. Comparatively, to control the computational cost, for the rectangular specimen, two different inclination angles of the pre-existing flaw are considered, and for each condition of the pre-existing flaw inclination, five times of simulations are carried out under the same heterogeneity degree.



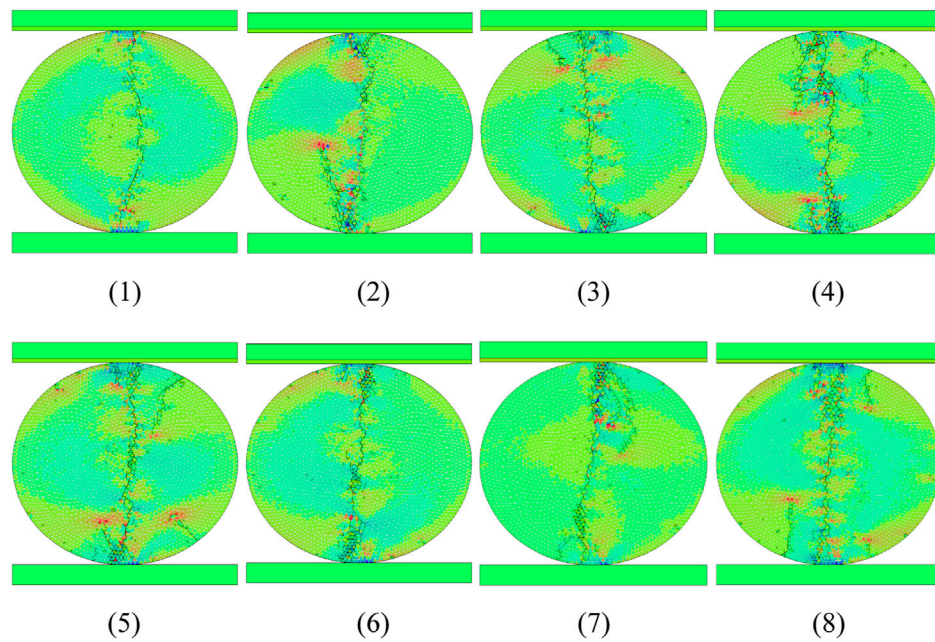


**FIGURE 6**  
Fracturing failure patterns of the intact disc specimen with  $m = 5$  (Ning et al., 2021).

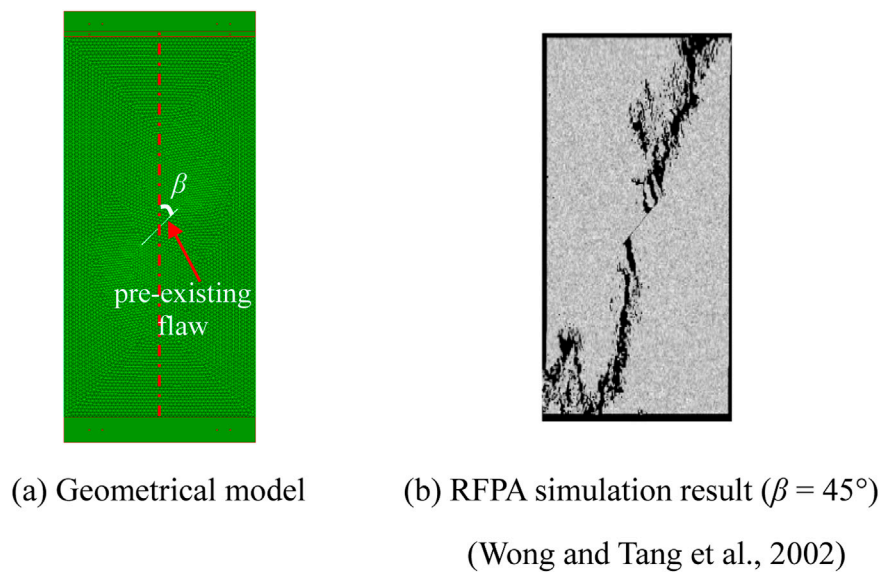


**FIGURE 7**  
Geometrical model and RFP simulation of a center-notched rectangular specimen.

In the previous work (Ning et al., 2021), the influence of the heterogeneity degree on the fracturing failure of intact disc and rectangular specimens was investigated by considering five different values of the heterogeneity index  $m$ , namely, 1.5, 2.5,

5, 20, and 200. In the present work, a middle level heterogeneity, namely,  $m = 5$ , is considered for all the simulations. Moreover, the maximum displacement ratio, step time and the contact penalty spring stiffness in the DDA simulation are  $5 \times 10^{-4}$ ,  $1 \times 10^{-6}$

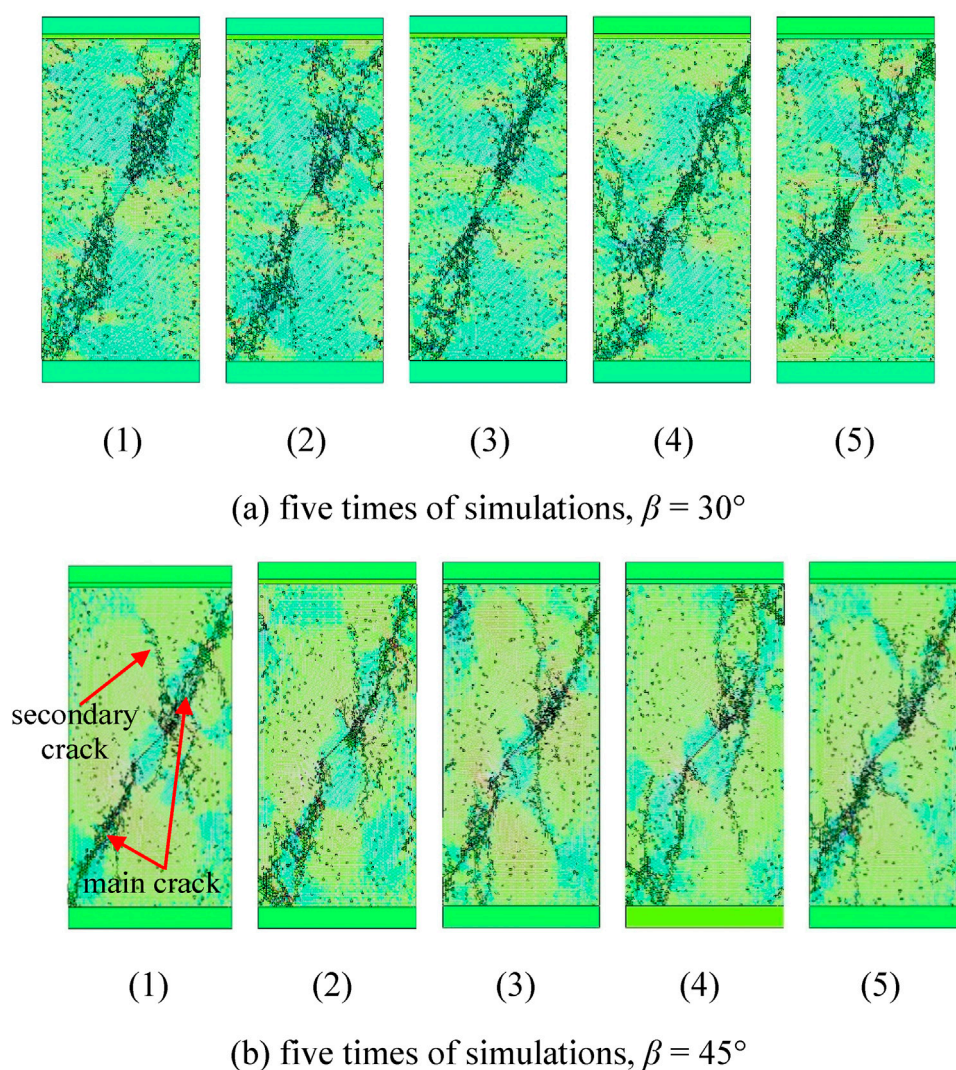


FIGURE 8

Fracturing failure patterns of the center-notched rectangular specimen with different  $\beta$  under the same heterogeneity degree ( $m = 5$ ).

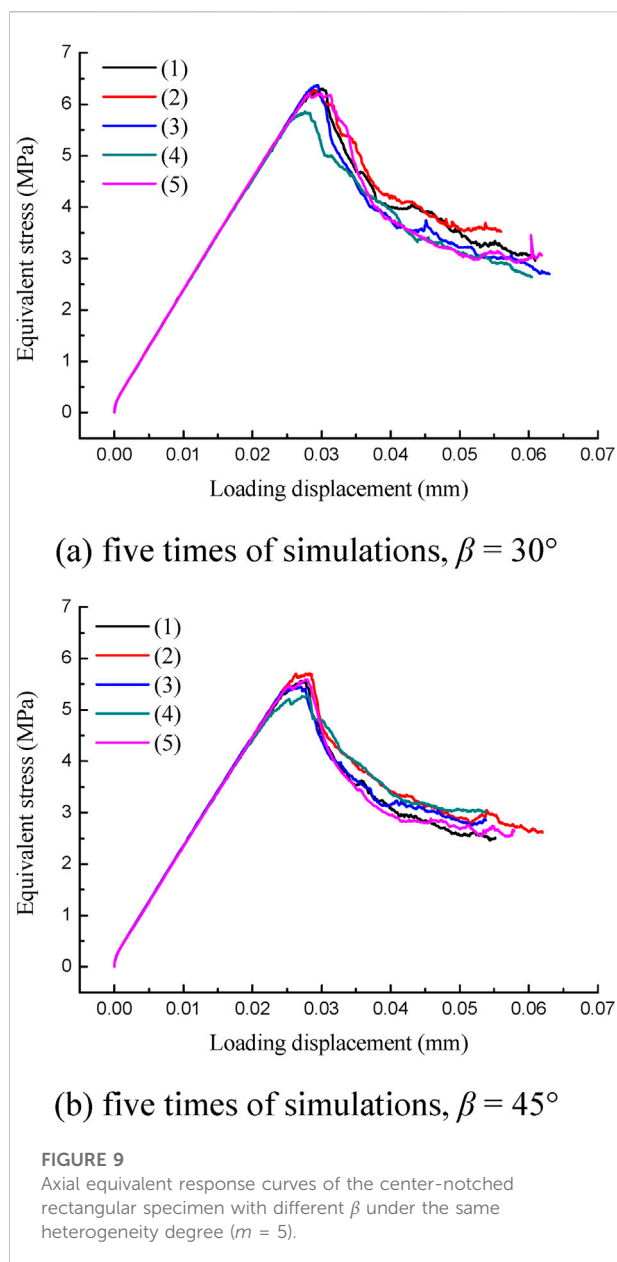
s, and 100 GPa, respectively, the same as those used in the previous work (Ning et al., 2021).

## Radial compression of center-notched disc specimen

The geometrical model of the disc is shown in Figure 2. The radius of the disc is 50 mm, and there are two platforms with a central angle of  $10^\circ$  at the upper and lower ends. The radial compression is applied by two rigid loading plates at a velocity of 2 mm/s. A measuring plate is placed between the upper loading plate and the disc to capture the diametral macroscale equivalent mechanical response of the disc under the compression (note that each DDA block is in a constant

stress state in each time step because of the first order assumption). The pre-existing flaw has dimensions of  $29 \times 0.25$  mm (Al-Shayea, 2005) and an inclination angle  $\beta$ . The two ends of the flaw are arced like, that is, normally conducted in physical experiments.

Three different  $\beta$  values, namely,  $30^\circ$ ,  $45^\circ$  and  $60^\circ$ , are considered and the corresponding sub-block element number of the model is 5511, 5469 and 5607, respectively. The mesh size is determined based on trial calculations considering the result convergency and the computational cost simultaneously. The homogeneous material properties of the disc are elastic modulus  $E = 20$  GPa, Poisson's ratio  $\mu = 0.2$ , friction angle  $\theta = 30^\circ$ , cohesion  $c = 20$  MPa and tensile strength  $\sigma_t = 5$  MPa, respectively. The upper and lower platforms of the disc are set frictionless like that in the physical experiment to avoid the lateral



constraint of the disc. For each disc model of the same inclination of the pre-existing flaw, eight times of simulations are carried out.

Figure 3 shows the fracturing failure pattern of the center-notched disc with three different inclination angles of the pre-

existing flaw, respectively. Under each inclination of the pre-existing flaw, it can be found that the main crack paths are nearly the same in the eight simulations, which start from the two ends of the pre-existing flaw and grow to the two loading ends of the disc, similar to that in the typical experimental results in Figure 4. However, the secondary cracks differ obviously in the eight simulations under each inclination of the pre-existing flaw. When there are secondary cracks, they generally start from the disc edge and propagate to the end of the pre-existing flaw. This phenomenon also agrees with the experimental results. Therefore, for the center-notched discs, the discreteness of the fracturing failure pattern due to the heterogeneity is mainly reflected by the secondary cracks.

Figure 5 shows diametral equivalent stress-loading displacement curves of the disc simulations. These curves reflect the energy accumulation and dissipation characteristics of the specimens during the deformation and fracturing process under the diametral compression. It can be found that the curves are nearly linear at the initial stage and almost duplicate for the eight simulations under each inclination of the pre-existing flaw, which indicates that the heterogeneity does not influence the reproducibility of the macroscale equivalent modulus of rock evidently. The curves quickly drop after reaching the peak, and show occasional obvious rise thereafter during the falling stage. These phenomena are in good agreement with the reported experimental results (e.g., Zhang and Wang, 2009) of radial compression of center-notched rock discs. Each rising and falling of the curves represent the rest of the old cracks and the initiation and growth of new cracks.

Table 1 lists the maximum and minimum peak values of the curves. It can be found that, in general, the disc gets relatively lower peak strength when  $\beta = 45^\circ$ , and the corresponding discreteness of the peak strength (20.7%) is the smallest among the three different conditions of the pre-existing flaw inclination. The three discreteness values for the center-notched specimens are all obvious larger than that of the intact rock disc (15.4%) with the same disc size, loading condition, material properties and heterogeneity degree ( $m = 5$ ), indicating poorer strength reproducibility of the center-notched rock discs under heterogeneity, which could be attributed to the local stress concentration because of the pre-existing flaw. Figure 6 shows the fracturing failure results of the intact disc specimen for eight times of simulations. Compared with that in Figure 3, it can be

**TABLE 2** Peak strength discreteness of rectangular specimens ( $m = 5$ ).

Peak strength (MPa)	Center-notched specimen		Intact specimen (Ning et al., 2021)
	$\beta = 30^\circ$	$\beta = 45^\circ$	
maximum, $\sigma_{\max}^p$	6.38	5.70	7.11
minimum, $\sigma_{\min}^p$	5.84	5.20	6.76
discreteness, $\frac{\sigma_{\max}^p - \sigma_{\min}^p}{(\sigma_{\max}^p + \sigma_{\min}^p)/2} \times 100\%$	8.8%	9.2%	5.0%



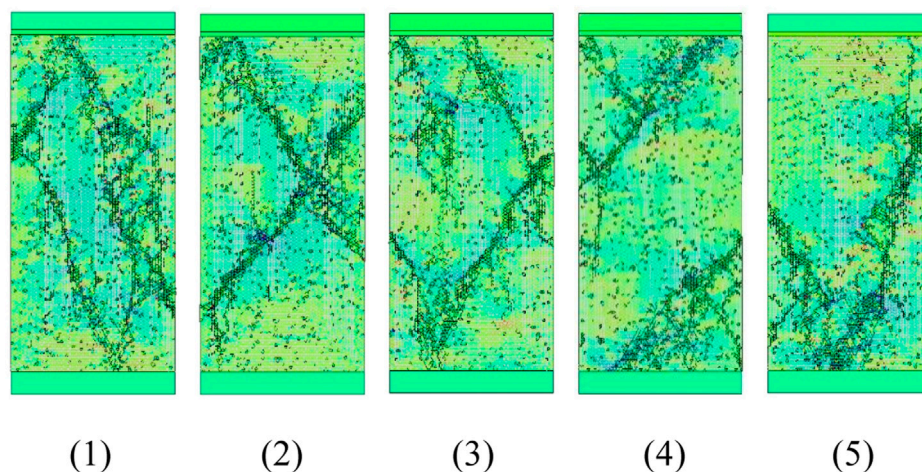


FIGURE 10

Fracturing failure patterns of the intact rectangular specimen with  $m = 5$  (Ning et al., 2021).

found that the intact specimen gets relatively better reproducibility of the fracturing failure pattern. This could be attributed to that the intact disc gets ideal tensile stress concentration along the loading diameter.

### Uniaxial compression of center-notched rectangular specimen

The geometrical model of the rectangular specimen is shown in Figure 7A. The specimen has dimensions of  $150 \times 75$  mm. The uniaxial compression is applied by two rigid loading plates at a velocity of 2 mm/s. A measuring plate is placed between the upper loading plate and the specimen to capture the axial macroscale equivalent mechanical response of the specimen under the compression. The pre-existing flaw has dimensions of  $20 \times 0.4$  mm (Wong et al., 2002) and an inclination angle  $\beta$ . The two ends of the flaw are arced like, that is, normally conducted in physical experiments. Two different  $\beta$  values, namely,  $30^\circ$  and  $45^\circ$ , are considered and the corresponding sub-block element number of the model is 13515 and 14415, respectively. The homogeneous material properties of the specimen are elastic modulus  $E = 20$  GPa, Poisson's ratio  $\mu = 0.2$ , friction angle  $\theta = 30^\circ$ , cohesion  $c = 5$  MPa and tensile strength  $\sigma_t = 2.5$  MPa, respectively. The upper and lower ends of the specimen are set frictionless like that in the physical experiment to avoid the lateral constraint of the specimen. For each rectangular specimen model of the same inclination of the pre-existing flaw, five times of simulations are carried out.

Figure 8 shows the fracturing failure pattern of the center-notched rectangular specimen with two different inclination angles of the pre-existing flaw, respectively. Under each

inclination of the pre-existing flaw, it can be found that the main crack paths are nearly the same in the five simulations, which start from the two ends of the pre-existing flaw and grow to the two opposite corners of the specimen. However, similar to that in the above disc specimen simulations, the secondary cracks differ obviously. The secondary cracks, especially when  $\beta = 45^\circ$ , generally start from the pre-existing flaw ends and propagate nearly parallel to the uniaxial loading direction. Figure 7B is the RFPA simulation result of a center-notched rectangular rock specimen that has close geometry with the specimen in Figure 8B. It can be found that the fracturing patterns obtained by DDA and RFPA agree well. Generally, for the center-notched rectangular specimens, the discreteness of the fracturing failure pattern due to the heterogeneity is also mainly reflected by the secondary cracks.

Figure 9 shows the axial equivalent stress-loading displacement curves of the rectangular specimen simulations. These curves reflect the energy accumulation and dissipation characteristics of the specimens during the deformation and fracturing process under the uniaxial compression. It can be found that the curves are nearly linear at the initial stage and almost duplicate for the five simulations under each inclination of the pre-existing flaw. Similar to that in the above disc simulations, it indicates that the heterogeneity does not influence the reproducibility of the macroscale equivalent modulus evidently. However, different from that of the disc specimens, the curves do not show the obvious occasional rise phenomenon during the falling stage after the peak for the rectangular specimens, which are also in good agreement with that of wide experiments.

Table 2 lists the maximum and minimum peak values of the curves. It can be found that, in general, the specimen gets larger

peak strength when  $\beta = 30^\circ$ , and the corresponding discreteness of the peak strength (8.8%) is relatively smaller than that when  $\beta = 45^\circ$  (9.2%). The two discreteness values for the center-notched specimens both are obvious larger than that of the intact rectangular specimen (5.0%) (Ning et al., 2021) with the same specimen size, loading condition, material properties and heterogeneity degree ( $m = 5$ ), indicating poorer strength reproducibility of the center-notched specimens under heterogeneity again. Figure 10 shows the fracturing failure results of the intact rectangular specimen for five times of simulations. Compared with that in Figure 8, it can be found that the center-notched specimen gets much better reproducibility of the fracturing failure pattern. The poorer strength reproducibility and better fracturing pattern reproducibility of the pre-notched rectangular specimen relative to the intact rectangular specimen both could be attributed to the local stress concentration because of the pre-existing flaw. Moreover, compared with that in Table 1, it also can be concluded that the rectangular specimens, center-notched or intact, have better strength reproducibility than the disc specimens under the same heterogeneity degree.

## Conclusion

In this work, by employing the sub-block element DDA method coupled with a statistic heterogeneity model based on the Weibull distribution, the fracturing failure of center-notched disc and rectangular rock specimens under the same heterogeneity degree is simulated. The simulations successfully recreate some important features of the macroscale whole-process nonlinear deformation and fracturing failure of pre-notched rock specimens that are explored in experiments or other numerical simulations. Regarding the reproducibility under the same heterogeneity degree, by combining previous work on intact heterogeneous specimen simulations, it is mainly concluded that:

- 1) The influence of the heterogeneity on the fracturing failure pattern reproducibility is mainly reflected by the secondary cracks for the pre-notched specimens and the intact disc specimen. The pre-notched disc specimen has poorer fracturing failure pattern reproducibility than the intact disc specimen because of the ideal tensile stress concentration along the loading diameter in the intact disc. Comparatively, the pre-notched rectangular specimen has much better fracturing failure pattern reproducibility than the intact rectangular specimen because of the stress concentration induced by the pre-existing flaw.
- 2) The heterogeneity does not influence the reproducibility of the macroscale equivalent modulus of the specimens evidently, but its influence on the reproducibility of the macroscale equivalent strength is obvious. Generally, the pre-notched specimens have

poorer macroscale strength reproducibility than the intact specimens, and the rectangular specimens have better macroscale strength reproducibility than the disc specimens. Moreover, for the pre-notched specimens, the macroscale strength reproducibility also varies with the inclination of the pre-existing flaw remarkably.

The exact microstructures of rock including the mineral grain shapes and microcracks *etc.*, will be considered in the future work on DDA simulations of rock heterogeneities.

## Data availability statement

The raw data supporting the conclusion of this article will be made available by the authors, without undue reservation.

## Author contributions

DC: Methodology, Validation, Funding acquisition; ZY: Formal analysis, Writing—Original Draft; MW: Formal analysis; XJ: Formal analysis; YN: Conceptualization, Software, Writing—Review and Editing, Funding acquisition.

## Funding

This research was financially supported by the open project of the State Key Laboratory of Coal Resources and Safe Mining, CUMT, China (Grant SKLCRSM16KF08), the National Key Research and Development Program of China (grant No. 2021YFC2902105), the National Natural Science Foundation of China (grant No. 51604261), and the Sichuan Province Science and Technology Support Program, China (grant No. 2020YJ0416).

## Conflict of interest

The authors declare that the research was conducted in the absence of any commercial or financial relationships that could be construed as a potential conflict of interest.

## Publisher's note

All claims expressed in this article are solely those of the authors and do not necessarily represent those of their affiliated organizations, or those of the publisher, the editors and the reviewers. Any product that may be evaluated in this article, or claim that may be made by its manufacturer, is not guaranteed or endorsed by the publisher.



## References

- Al-Shayea, N. A. (2005). Crack propagation trajectories for rocks under mixed mode I-II fracture. *Eng. Geol.* 81, 84–97. doi:10.1016/j.enggeo.2005.07.013
- Alzaki, T., Al-Dughaimi, S., Muqtadir, A., Kandil, M. E., and Dvorkin, J. (2020). Effect of heterogeneity on failure of natural rock samples. *Sci. Rep.-UK.* 10, 14723–14726. doi:10.1038/s41598-020-71780-7
- Bai, B., Yang, G., Li, T., and Yang, G. (2019). A thermodynamic constitutive model with temperature effect based on particle rearrangement for geomaterials. *Mech. Mat.* 139, 103180. doi:10.1016/j.mechmat.2019.103180
- Bai, B., Zhou, R., Cai, G., Hu, W., and Yang, G. (2021). Coupled thermo-hydro-mechanical mechanism in view of the soil particle rearrangement of granular thermodynamics. *Comput. Geotech.* 137, 104272. doi:10.1016/j.compgeo.2021.104272
- Cundall, P. A., and Hart, R. D. (1992). Numerical modelling of discontinua. *Eng. Comput.* 9, 101–113. doi:10.1108/eb023851
- Gao, F., Stead, D., and Elmo, D. (2016). Numerical simulation of microstructure of brittle rock using a grain-breakable distinct element grain-based model. *Comput. Geotech.* 78, 203–217. doi:10.1016/j.compgeo.2016.05.019
- Gui, Y., Zhao, Z., Ji, J., Wang, X., Zhou, K., and Ma, S. (2016). The grain effect of intact rock modelling using discrete element method with Voronoi grains. *Geotech. Lett.* 6, 136–143. doi:10.1680/jgele.16.00005
- He, W., Hayatdavoudi, A., Shi, H., Sawant, K., and Huang, P. (2019). A preliminary fractal interpretation of effects of grain size and grain shape on rock strength. *Rock Mech. Rock Eng.* 52, 1745–1765. doi:10.1007/s00603-018-1645-4
- Huang, J., Tang, H., Pan, X., Gan, Z., Hua, W., and Dong, S. (2022). Investigation of the compression-shear fracture propagation for rocks accounting for confining pressure and crack surface friction. *Theor. Appl. Fract. Mec.* 119, 103346. doi:10.1016/J.TAFMEC.2022.103346
- Jiao, Y., Zhang, X., and Zhao, J. (2012). Two-dimensional DDA contact constitutive model for simulating rock fragmentation. *J. Eng. Mech.* 138, 199–209. doi:10.1061/(ASCE)EM.1943-7889.0000319
- Li, L., Guan, J., and Liu, Z. (2022). A random discrete element method for modeling rock heterogeneity. *Geomech. Geophys. Geo.* 8, 12–13. doi:10.1007/S40948-021-00320-Y
- Liu, G., Cai, M., and Huang, M. (2018). Mechanical properties of brittle rock governed by micro-geometric heterogeneity. *Comput. Geotech.* 104, 358–372. doi:10.1016/j.compgeo.2017.11.013
- Manouchehrian, A., and Cai, M. (2016). Influence of material heterogeneity on failure intensity in unstable rock failure. *Comput. Geotech.* 71, 237–246. doi:10.1016/j.compgeo.2015.10.004
- Ni, K., Yang, J., Ning, Y., and Kang, G. (2020). A modified sub-block DDA fracturing modelling method for rock. *Eng. Anal. Bound. Elem.* 111, 154–166. doi:10.1016/j.enganabound.2019.11.008
- Ning, Y., and Lv, X. (2022). Research progress in DDA and NMM simulations of rock mechanics and engineering problems. *Chin. J. Appl. Mech.* 39, 657–672. doi:10.11776/j.issn.1000-4939.2022.04.007
- Ning, Y., Yang, J., An, X., and Ma, G. (2011). Modelling rock fracturing and blast-induced rock mass failure via advanced discretisation within the discontinuous deformation analysis framework. *Comput. Geotech.* 38, 40–49. doi:10.1016/j.compgeo.2010.09.003
- Ning, Y., Yang, Z., Wei, B., and Gu, B. (2017). Advances in two-dimensional discontinuous deformation analysis for rock-mass dynamics. *Int. J. Geomech.* 17, E6016001. doi:10.1061/(ASCE)GM.1943-5622.0000654
- Ning, Y., Lv, X., and Yang, Z. (2021). DDA simulation study on mechanical failure of heterogeneous rock. *Geofluids* 2021, 1416560. doi:10.1155/2021/1416560
- Ou, C. (2020). Experimental and numerical study on dynamic splitting of Brazilian flattened disc with prefabricated cracks. *Guangzhou Univ.* 912. doi:10.27040/d.cnki.ggzdu.2020.000912
- Peng, J., Wong, L. N. Y., and Teh, C. I. (2021). Influence of grain size on strength of polyminerall crystalline rock: New insights from DEM grain-based modeling. *J. Rock Mech. Geotech.* 13, 755–766. doi:10.1016/J.JRMGE.2021.01.011
- Rasmussen, L. L. (2022). A breakable grain-based model for bi-modular rocks. *Int. J. Rock Mech. Min.* 151, 105028. doi:10.1016/J.IJRMMS.2021.105028
- Shi, G. (1992). Discontinuous deformation analysis: A new numerical model for the statics and dynamics of deformable block structures. *Eng. Comput.* 9, 157–168. doi:10.1108/eb023855
- Shi, G., and Goodman, R. E. (1985). Two dimensional discontinuous deformation analysis. *Int. J. Numer. Anal. Mater.* 9, 541–556. doi:10.1002/nag.1610090604
- Shirole, D., Walton, G., and Hedayat, A. (2020). Experimental investigation of multi-scale strain-field heterogeneity in rocks. *Int. J. Rock. Mech. Min.* 127, 104212. doi:10.1016/j.ijrmms.2020.104212
- Sun, S., Wang, J., Le, H., Fan, H., and Wang, W. (2022). Experimental and numerical investigation on compressive strength and crack behavior of rock-like specimens with open flaws under confining loads. *Front. Earth. Sc-switz.* 10, 972194. doi:10.3389/FEART.2022.972194
- Tang, C., Yang, W., Fu, Y., and Xu, X. (1998). A new approach to numerical method of modelling geological processes and rock engineering problems—Continuum to discontinuum and linearity to nonlinearity. *Eng. Geo.* 49, 207–214. doi:10.1016/S0013-7952(97)00051-3
- Tang, C., Tham, L. G., Lee, P. K. K., Tsui, Y., and Liu, H. (2000). Numerical studies of the influence of microstructure on rock failure in uniaxial compression—part II: Constraint, slenderness and size effect. *Int. J. Rock Mech. Min.* 37, 571–583. doi:10.1016/S1365-1609(99)00122-7
- Tang, X., and Zhang, C. (2009). Meso-scale modeling of concrete: Effects of heterogeneity. *J. Hydroelectr. Eng.* 28, 56–62.
- Wang, Y., and Sun, S. (2021). Image-based rock typing using grain geometry features. *Comput. Geosci-UK.* 149, 104703. doi:10.1016/J.CAGEO.2021.104703
- Wong, R. H. C., Tang, C., Chau, K. T., and Lin, P. (2002). Splitting failure in brittle rocks containing pre-existing flaws under uniaxial compression. *Eng. Fract. Mech.* 69, 1853–1871. doi:10.1016/S0013-7944(02)00065-6
- Wu, Z., Fan, L., Liu, Q., and Ma, G. (2017). Micro-mechanical modeling of the macro-mechanical response and fracture behavior of rock using the numerical manifold method. *Eng. Geol.* 225, 49–60. doi:10.1016/j.enggeo.2016.08.018
- Xu, Y., Yao, W., and Xia, K. (2020). Numerical study on tensile failures of heterogeneous rocks. *J. Rock Mech. Geotech.* 12, 50–58. doi:10.1016/j.jrmge.2019.10.002
- Yang, B., Cao, X., Han, T., Li, P., and Shi, J. (2022). Effect of heterogeneity on the extension of ubiquitous cracks in rock materials. *Fractal. Fract.* 6, 317. doi:10.3390/FRACTALFRACT6060317
- Zhang, S., and Wang, Q. (2009). Determination of rock fracture toughness by split test using five types of disc specimens. *Rock Soil Mech.* 30, 12–18. doi:10.16285/j.rsm.2009.01.019
- Zheng, K., Qiu, B., Wang, Z., Li, X., Li, J., and Gao, K. (2020). Image-based numerical study of three-dimensional meso-structure effects on damage and failure of heterogeneous coal-rock under dynamic impact loads. *Particuology* 51, 132–141. doi:10.1016/j.partic.2019.09.008
- Zhou, G., Xu, T., Konietzky, H., Zhu, W., Heng, Z., Yu, X., et al. (2022). An improved grain-based numerical manifold method to simulate deformation, damage and fracturing of rocks at the grain size level. *Eng. Anal. Bound. Elem.* 134, 107–116. doi:10.1016/J.ENGANABOUND.2021.10.005



## OPEN ACCESS

## EDITED BY

Jun Zhao,  
Anhui University of Science and  
Technology, China

## REVIEWED BY

Wei Yuan,  
Southeast University, China  
Qingwen Shi,  
North China Institute of Science and  
Technology, China

## \*CORRESPONDENCE

Zhaofeng Chen,  
✉ 38057@qzc.edu.cn

## SPECIALTY SECTION

This article was submitted  
to Geohazards and Georisks,  
a section of the journal  
Frontiers in Earth Science

RECEIVED 30 December 2022

ACCEPTED 14 March 2023

PUBLISHED 28 March 2023

## CITATION

Chen Z, Xu L, Huang C, Wu L and Shang Y  
(2023), Study on the time-varying fatigue  
reliability of the invert structure of subway  
tunnel under the action of train loads.  
*Front. Earth Sci.* 11:1134219.  
doi: 10.3389/feart.2023.1134219

## COPYRIGHT

© 2023 Chen, Xu, Huang, Wu and Shang.  
This is an open-access article distributed  
under the terms of the [Creative  
Commons Attribution License \(CC BY\)](#).  
The use, distribution or reproduction in  
other forums is permitted, provided the  
original author(s) and the copyright  
owner(s) are credited and that the original  
publication in this journal is cited, in  
accordance with accepted academic  
practice. No use, distribution or  
reproduction is permitted which does not  
comply with these terms.

# Study on the time-varying fatigue reliability of the invert structure of subway tunnel under the action of train loads

Zhaofeng Chen<sup>1,2\*</sup>, Linrong Xu<sup>2</sup>, Changxi Huang<sup>3</sup>, Lei Wu<sup>2</sup> and Yonghui Shang<sup>2</sup>

<sup>1</sup>College of Civil Engineering and Architecture, Quzhou University, Quzhou, Zhejiang, China, <sup>2</sup>School of Civil Engineering, Central South University, Changsha, Hunan, China, <sup>3</sup>Dongguan Comprehensive Traffic Operation Command Center, Dongguan, Guangdong, China

**Introduction:** The present study examines the fatigue reliability of subway tunnel invert structures subjected to train-induced loads, a critical factor in ensuring the safety and longevity of these vital infrastructures.

**Methods:** By integrating higher-order moment theory, fatigue equations, and cumulative damage theory, this research analyzes the impact of train loads on invert structures, taking into account factors such as tension stress, compression stress, train axle weight, speed, and lining thickness.

**Results:** The findings indicate that the reinforcement of the invert structure is required under tension stress, while it is not necessary for compression stress. Notably, the train's axle weight and speed exert a significant influence on the fatigue reliability index, with speed displaying a marginally greater effect than axle weight. Conversely, the lining thickness demonstrates a negligible impact on the reliability index. As time progresses, the fatigue reliability index diminishes, resulting in an elevated probability of failure.

**Discussion:** In light of these findings, it is imperative to conduct regular inspections and maintain the tensile state of the invert structure, which warrants the most attention. To safeguard the safety and longevity of subway tunnel invert structures, it is essential to concentrate on the aspects related to tensile stress and closely monitor train loads, specifically axle weight and speed.

## KEYWORDS

time-varying fatigue reliability, higher order moment, performance function, invert structure, subway tunnel, train loads

## 1 Introduction

The tunnel is an integral component of highway and railroad engineering construction projects (Zhou et al., 2020). Scholars have made significant progress in tunnel engineering theory over the past few decades. This research topic has shifted from deterministic research (Shi et al., 2021; Wang et al., 2022; Zhou et al., 2023) to randomness and uncertainty (Chen et al., 2014), which better reflect the realistic issues of underground engineering. As a result, most tunnel engineering research has become closely associated with reliability theory, which has become a significant subject of research, spanning the construction and operation periods. During the operation period, the tunnel is primarily subjected to dynamic cyclic

train loads over an extended period, leading to deterioration of the structure beneath the rails.

In the field of engineering, various factors such as soil parameters, train loads, lining structure, and surrounding rock pressure can impact the fatigue of structures, and these effects are often unpredictable and unknown. In order to ensure the safety and reliability of subway tunnel components during operation, it is crucial to consider the randomness and uncertainty of these factors and conduct a reliability study based on the establishment of fatigue performance functions. Reliability methods are founded on the principles of probability theory. These methods involve randomly selecting parameters in a model and using these parameters to calculate the established reliability model, thus determining the reliability index and the likelihood of failure. When dealing with practical engineering problems, it is necessary to consider multiple random factors and utilize appropriate reliability methods, such as the first-order reliability method (FORM), the second-order reliability method (SORM) (Fattahi and Jiryaee, 2022), the Monte Carlo method (Xie et al., 2022), and the response surface method (Li and Yang, 2019), to calculate the reliability indices for different research objects. Examples have shown that the reliability technique is more aligned with real-world conditions as it takes into account the force situation in a complex geological environment.

The application of reliability theory to engineering problems dates back to early times, but its use in tunnel engineering was first proposed by Rosenblueth and Esteva (1972). They used reliability methods based on performance functions and determined the probability of failure in tunnel structures by assuming the type of distribution of random variables. In 1985, Ellingwood and Hwang conducted research on the reliability method and applied it in the safety analysis of geotechnical engineering (Ellingwood and Hwang, 1985). Laso et al. (1995) used the method to perform a reliability analysis of the tunnel support system and evaluated its safety based on the obtained failure probability. Lü and Low (2011) utilized the reliability method in the stability analysis of tunnel structural systems and established a stochastic polynomial model for the safety analysis of tunnel structures. Mollon et al. (2009) and Mollon et al. (2011) improved the traditional reliability method by using a quadratic polynomial model to calculate the failure probability of tunnel structures (Mollon et al., 2009; Mollon et al., 2011). Chen et al. (2014) improved the response surface method and the first-second-order moment method to calculate the safety of tunnels during construction. They confirmed the superiority of the improved method over traditional methods.

The reliability analysis methods mentioned above mainly focus on the stability of the surrounding rock, support systems, and settlement changes during the construction period of tunnels. However, during the tunnel operation period, the degradation of the structural components under train loads must also be considered. This idea is known as time-varying reliability. There are few studies that address this aspect. For example, Mori and Ellingwood (1993) examined the time-varying characteristics of external loads and simplified them to a stochastic process. The results of their predictions provided a theoretical foundation for the life prediction of similar bridge structures in service. Qing Li (2004) reviewed the current time-varying reliability methods and proposed several improved methods for the reliability index of time-varying degradation of bridge junction performance under chloride salt

attack in coastal areas. Frangopol et al. (1997) conducted a study on the time-varying reliability of concrete girder bridges in service in the United States, proposing a time-varying resistance decay model. This model was integrated into the flexural and shear load capacity model of reinforced concrete bridges, resulting in accurate predictions. Val and Melchers (1996) used a similar reliability method to determine the time-varying laws of reinforced concrete slab bridges under the influence of specific parameters.

The reliability of tunnels has been studied by several researchers using various approaches. However, each method has its own strengths and limitations when applied to engineering problems. It is crucial to consider the actual engineering background while selecting the reliability method. The primary stress pattern during the tunnel's operational phase is the cyclic train loads over a long period of time. Hence, the analysis of the tunnel structure's reliability should consider not only the structural time-variability but also the randomness and uncertainty of the factors that influence it. Despite numerous studies on bridge structures, there are relatively fewer studies on tunnel structures. This highlights the need for research on subway tunnels. The present study aims to investigate the time-dependent reliability analysis of the structure under subway train loads. The goal is to determine the limit state function of fatigue failure of the invert structure, which is subjected to the combined action of train loads and surrounding rock pressure. The study also proposes a new time-varying reliability calculation method based on high-order moment theory.

## 2 Performance function of structures

The commonly used reliability methods for structural analysis include the First-Order Reliability Method (FORM), the Second-Order Reliability Method (SORM), the Monte Carlo Method, the Response Surface Method, and the higher-order Moment Theory. A review of existing literature shows that the higher-order Moment Theory is characterized by its high computational efficiency, accuracy, and wide application in engineering structural reliability analysis. In this paper, we adopt the Moment Method to analyze the time-varying reliability of the invert structure of subway tunnels under long-term dynamic fatigue loads. The study obtains the time-varying fatigue reliability index and failure probability of the invert structure under compression and tension and identifies the relationship between the fatigue reliability index and the service deterioration index of the invert structure. This research provides a new idea for the reliability calculation of the invert structure of subway tunnels and provides theoretical support for the evaluation of the service state of subway tunnel structures.

It is relatively convenient to obtain parameters for reliability analysis of the structure using the first-order second-moment theory. However, the method requires repeated iterative verification, which has minor computational efficiency and accuracy. Theoretically, the higher order, the higher the calculation accuracy. Structure engineering problems are much more complex, and various factors should be considered. Hence, establishing the performance functions is more complicated, and the computational difficulty and computation time will sharply increase. Currently, some scholars have proposed a higher-order moment theory that can better solve more complex issues with high computational efficiency and

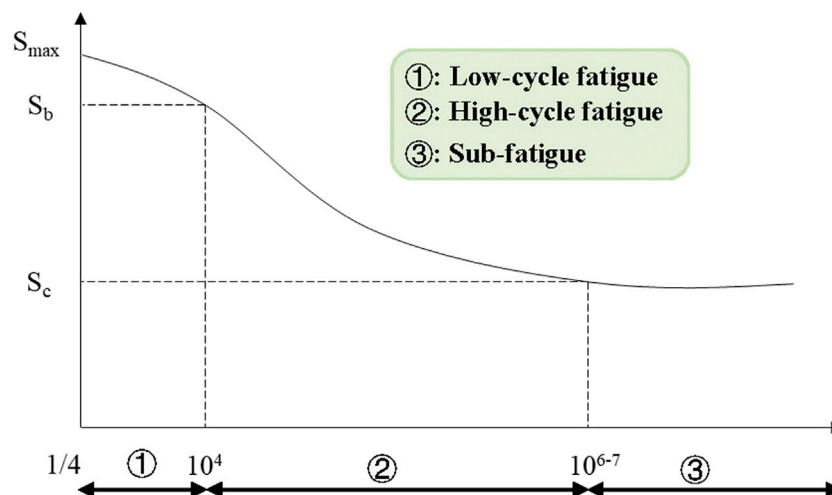


**FIGURE 1**  
Typical fatigue life curve ( $S$ - $N$  curve) (Shiozawa et al., 2001).

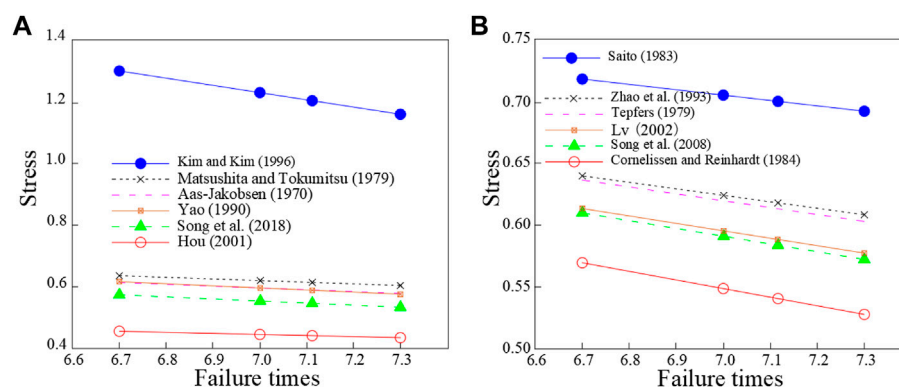


**FIGURE 2**  
Comparative analysis of fatigue equation results for concrete under (A) compression conditions (Aas-Jakobsen, 1970; Matsushita and Tokumitsu, 1979; Yao, 1990; Kim and Kim, 1996; Hou, 2001; Song et al., 2008); and (B) tension conditions (Song et al., 2008; Tepfers, 1979; Saito, 1983; (Zhao et al., 1993) (Cornelissen and Reinhardt, 1984) (Lü, 2002).

accuracy (Rosenblueth, 1975; Zhao and Ono, 2000; Zhao and Ono, 2001; Zhao et al., 2006). Therefore, this paper will use a higher-order moment method to analyze the time-varying fatigue reliability of the invert structure of subway tunnels.

The typical fatigue life curve ( $S$ - $N$  curve) is shown in Figure 1. It can be separated into three fatigue areas with various tendencies of variation, i.e., low-cycle fatigue, high-cycle fatigue, and sub-fatigue. Different parts of the  $S$ - $N$  curve can be fitted using various fitting functions, which include the exponential function equation, power function equation, three-parameter equation, four-parameter equations, etc. The subway tunnel is an important transportation facility with a high frequency of use, and the stress state of its invert structure is much lower than the strength limit of the concrete material. Hence, it is in line with the high-cycle fatigue, which will be the focus of this paper.

Figure 2 compares the results of the fatigue equation for concrete under different compression and tension conditions (as listed in Tables 1, 2) where the stress level is dimensionless. As shown in Figure 2A, with the increase in fatigue cycles, the stress level calculated by the concrete fatigue equation for each stress condition slowly and linearly decreases. However, the stress level calculated by Kim and Kim (1996) is greater than 1, while the other equations result in stress levels less than 1, indicating that concrete stress levels generally decrease with fatigue cycles. Considering the fatigue characteristics of subway tunnel structures, the results obtained from Song et al. (2008) are more consistent with the research object, have a clearer formula, and are more convenient for engineering applications. The predicted results are also conservative and in line with the fatigue stress state of subway tunnel structures, ensuring service safety. Although the stress level

obtained by Hou (2001) fatigue equation is lower, it underestimates the fatigue stress level of subway tunnel structures. The formula proposed by Song et al. (2008) can be used to study the time-varying fatigue reliability of the subway tunnel under-track structure.

By analyzing the above results, the fatigue equation for concrete under pressure state proposed by Song et al. (2008) is used for the establishment of the fatigue function of the structure under the rail of the subway tunnel, and the expression of the equation is as follows:

$$S_{\text{cmax}} = 0.9885 - 0.0618 \lg N \quad (1)$$

Where  $S_{\text{cmax}}$  is the maximum compressive stress of concrete;  $N$  is the number of fatigue cycles.

In Figure 2B, the stress level calculated by the concrete fatigue equation in each tensile state decreases linearly as the number of fatigue cycles increases. Similar to the results obtained in the compressed state, the stress level in the tensile state is generally less than 1, consistent with the actual engineering situation. It is found that the stress level obtained from the concrete fatigue equation calculation by Cornelissen is too conservative, which may cause misjudgment of the fatigue calculation results of subway tunnel structures. The fatigue equation proposed by Song et al. (2008), as expressed in Eq. 2, is more consistent with the research object and has relatively conservative prediction results that are safe for actual engineering use and in line with the concept of safe operation of the subway tunnel.

$$\lg N = 16.67 - 16.76 S_{\text{tmax}} + 5.17 S_{\text{tmin}} \quad (2)$$

Where  $S_{\text{tmax}}$  is the maximum tensile stress of concrete,  $S_{\text{tmin}}$  is the minimum tensile stress of concrete;  $N$  is the number of fatigue cycles.

### 3 Performance function of the invert structure of the subway tunnel

Long-term exposure of the subway tunnel structure to the cyclic stress imparted by the upper train loads will produce fatigue damage to the tunnel structure, particularly the tunnel invert structure. From the standpoint of fatigue stress damage to concrete, there is frequently both compressive and tensile damage. Thus, fatigue analysis will also be conducted from these two perspectives. Miner fatigue cumulative damage theory (Miner, 1945) is widely used in analyzing the fatigue failure probability of the invert concrete structure of the tunnel:

$$P_f = P[D(t) > 1] \quad (3)$$

Where  $D(t)$  is the loss factor.

The total damage to the tunnel invert structure in the tension or compression state within 1 year is:

$$D(1) = \sum_{i=1}^{\infty} \frac{n_i}{N_i} \quad (4)$$

Assume that the concrete material is repeated  $n_i$  times under the action of the stress value of  $\sigma_i$ , which can be expressed by:

$$C = N_i (\sigma_i - \sigma_{\text{min}})^m \quad (5)$$

Where  $m$  is the concrete material constant,  $\sigma_{\text{min}}$  is the minimum stress level.

Hence, Eq. 4 can be expressed by:

$$D(1) = \sum_{i=1}^{\infty} \frac{n_i (\sigma_i - \sigma_{\text{min}})^m}{C} \quad (6)$$

Therefore, the fatigue strength of the invert structure of the subway tunnel under  $N_e$  times equal amplitude repetitive stress after  $t$  years is obtained as  $\sigma_r(N_0)$ , which can be obtained from the S-N curve of the concrete material, then the cumulative loss value after  $t$  years is:

$$D(t) = \sum_{i=1}^{\infty} \frac{n_i (\sigma_i - \sigma_{\text{min}})^m}{N_e t [\sigma_r(N_0 - \sigma_{\text{min}})]^m} \quad (7)$$

Here, set  $\Delta\sigma_i = \sigma_i - \sigma_{\text{min}}$ , assuming the probability density function of repeated random stress variation is  $f_{\Delta\sigma_i}(\Delta\sigma_i)$ . For high circumferential cyclic fatigue structures, when the total number of cycles is large enough ( $>10^5$ ),  $N_0 = \sum_{i=0}^{\infty} n_i$ . Then the number of cycles  $n_i = N f_{\Delta\sigma_i}(\Delta\sigma_i) = N_e t f_{\Delta\sigma_i}(\Delta\sigma_i)$  and the cumulative loss value is:

$$D(t) = \sum_{i=0}^{\infty} \frac{f_{\Delta\sigma_i}(\Delta\sigma_i) (\Delta\sigma_i)^m}{[\sigma_r N_0 - \sigma_{\text{min}}]^m} = \frac{E(\Delta\sigma_i)^m}{[\sigma_r N_0 - \sigma_{\text{min}}]^m} \quad (8)$$

Where  $E(\Delta\sigma_i)^m$  is the m-order origin moment of  $\Delta\sigma_i$ ;  $\sigma_r(N_0)$  is the concrete tensile or compressive fatigue strength under equal amplitude repetitive stress;  $m$  is the concrete material constant, and the value of  $m$  is determined according to the relevant literature and is taken as 19.38 in bending and tension and 16.90 in compression (Ou, 2016), hence:

$$P_f = P \left\{ \frac{E(\Delta\sigma_i)^m}{[\sigma_r N_0 - \sigma_{\text{min}}]^m} > 1 \right\} \quad (9)$$

Accounting for computational model uncertainty variables  $\gamma$  in the equation:

$$P_f = P \left\{ \sigma_r(N_0) < \sigma_{\text{min}} + \gamma [E(\Delta\sigma_i)^m]^{\frac{1}{m}} \right\} = P \{ \sigma_r(N_0) < \sigma_e \} \quad (10)$$

The limiting state equation is obtained as follows:

$$g(X, Y, t) = \sigma_r(N_0) - \sigma_e \quad (11)$$

Substituting Eqs 1, 2 into Eq. 11, respectively, we obtain the limit state equation for the compressive fatigue of concrete in the invert structure of the subway tunnel as

$$g(X, Y, t) = 0.9885 f_{cu} - 0.0618 f_{cu} \lg(N_e t) - \sigma_{ec} \quad (12)$$

Where  $\sigma_{ec}$  is the equal amplitude equivalent repetitive compressive stress of the invert structure of the subway tunnel.

The tensile fatigue limit state equation is:

$$g(X, Y, t) = 0.994 f_{tu} + 0.3084 \sigma_{tmin} - 0.0602 f_{tu} \lg(N_e t) - \sigma_{et} \quad (13)$$

Where  $\sigma_{et}$  is the equal amplitude equivalent repetitive tensile stress of the invert structure of the subway tunnel.

According to the Chinese code for the design of concrete structures GB 50010-2015 (Zhou et al., 2021), under fatigue



loading, the tensile and compressive stress amplitudes of concrete can be calculated according to the following formula respectively:

$$\sigma_{t\max} = \frac{M_{\max}(h - x_0)}{I_0} \quad (14)$$

$$\sigma_{c\max} = \frac{M_{\max}x_0}{I_0} \quad (15)$$

Where  $M_{\max}$  is the maximum moment caused by the combined effect of train loads and rock surrounding pressure;  $h$  is the height of the cross-section;  $x_0$  is the center of gravity position;  $I_0$  is the cross-sectional moment of inertia.

Therefore, the standard stress spectrums of concrete at the fatigue analysis location are:

$$\Delta\sigma_{et} = \sigma_{et} - \sigma_{t\min} = \gamma \left[ \frac{1}{N_0} \sum_{i=0}^{\infty} n_i (\Delta\sigma_{ti})^{19.38} \right]^{1/19.38} \\ = \gamma [E(\Delta\sigma_{ti})^{19.38}]^{1/19.38} \quad (16)$$

$$\Delta\sigma_{ec} = \sigma_{ec} - \sigma_{c\min} = \gamma \left[ \frac{1}{N_0} \sum_{i=0}^{\infty} n_i (\Delta\sigma_{ci})^{16.9} \right]^{1/16.9} = \gamma [E(\Delta\sigma_{ci})^{16.9}]^{1/16.9} \quad (17)$$

The subway tunnel structure experiences the continuous cyclic impact of dynamic train load when in service. As a result, the invert structure may experience fatigue damage over time, which could affect train operation safety and passenger safety. When the subway tunnel operates for a long time in a complex underground environment, the material properties of both the tunnel structure and the surrounding rock structure may deteriorate. Hence, the reliability of the tunnel structure must be calculated, taking into account not only fatigue damage but also the time-varying decay of resistance (Stewart and Val, 1999).

$$R_1(t) = R_0 \gamma(t) \quad (18)$$

Where  $R_0$  is the original resistance without considering the effect of time,  $\gamma(t)$  is a reasonable resistance decay function.

This paper uses a polynomial decay function to better express the correlation between parameters and the design life of the subway tunnel, considering the environment it will be used in. The expression for the polynomial decay function is as follows:

$$\gamma(t) = 1 - k_1 t + k_1 t^2 \quad (19)$$

Where  $k_1$  and  $k_2$  are the attenuation coefficient related to the type of structure, generally divided into high, medium, and low three different attenuation rates, combined with the subway tunnel structure used in this paper to study the environment, determine the parameters  $k_1$  and  $k_2$  in the function to take the value of 0.005 and 0, respectively (Vu and Stewart, 2000).

The invert structure of the subway tunnel may experience two different stress states depending on the action form of the train and the bottom surrounding rock pressure state. These stress states can be categorized into two types: compressive strength state and tensile strength state. The exact stress state experienced by the invert structure will depend on the specific environmental conditions.

When the invert structure of the subway tunnel is in the compressive state, the limit state equation is obtained as follows:

$$g_1(t) = K_p \beta a b h \min f_{c0} (1 - 0.005t) - \sigma_1 \quad (20)$$

$K_p$  is the uncertainty factor,  $\beta$  is the Longitudinal bending coefficient of the component, and  $\beta = 1$  for tunnel linings,  $a$  is the eccentricity influence factor,  $b$  is Lining section width,  $h$  is Lining section height,  $f_{c0}$  is the ultimate compressive strength of concrete,  $t$  is time,  $\sigma_1$  is axial structural force.

When the invert structure of the subway tunnel is in the tensile state, the limit state equation is obtained as follows:

$$g_1(t) = K_p \beta \frac{1.75bh}{\frac{6e_0}{h} - 1} \min f_{t0} (1 - 0.005t) - \sigma_1 \quad (21)$$

$f_{t0}$  is the ultimate tensile strength of concrete;  $e_0$  is the axial force eccentricity distance.

To summarize, the subway tunnel operates under dynamic train loads and complex environmental conditions. The analysis conducted reveals that the final limit state equation for the tensile fatigue of the concrete structure of the invert structure of the subway tunnel can be expressed as follows:

$$G(X, Y, t) = (0.994 f_{tu} - 0.0602 f_{tu} \lg(N_e t)) (1 - 0.005t) + 0.3084 \sigma_{t\min} - \sigma_{et} \quad (22)$$

Similarly, the final limit state equation for the compressive fatigue of the invert structure of the subway tunnel can be obtained as follows:

$$G(X, Y, t) = (0.9885 f_{cu} - 0.0618 f_{cu} \lg(N_e t)) (1 - 0.005t) - \sigma_{ec} \quad (23)$$

## 4 Time-varying fatigue reliability analysis of invert structure of subway tunnel

In this section, a subway tunnel (liner thickness is 300 mm) with a daily operating time of 15 h is investigated. The subway train has a load vibration frequency of 1.0 Hz, a standard operating speed of 80 km/h, a total length of 80 m, and an axle weight of 14t. The cyclic train loads acting on the invert structure are considered as an equal amplitude fatigue load, and the number of repetitions is 4.

Combined with the research background of the subway tunnel provided in this paper, the time-varying fatigue limit state functional of the invert structure of the subway tunnel under longitudinal compression can be obtained by using the equation as follows:

$$G(X, Y, t) = (0.9885 f_{cu} - 0.0618 f_{cu} \lg(1.7345 \times 10^6 t)) (1 - 0.005t) - \sigma_{ec} \quad (24)$$

$f_{cu}$  is a variable that varies with time, and other variables neglect the effect of time. In this paper, six influencing factors that do not vary with time are considered, and their random variables are described in detail, as shown in Table 3.

The general description of the random variables given in Table 3 is in the original spatial state, while the failure probability of the fatigue state of the tunnel invert is solved by the higher-order moment method. After Rosenblatt's inverse normal transformation, the seven-point estimates corresponding to each

TABLE 1 Arrangement of fatigue equations of concrete under compression condition.

References	Sample	Expression
Aas-Jakobsen (1970)	Cubic	$S_{c\max} = 1 - \beta(1 - R)\lg N$
Matsushita and Tokumitsu (1979)	Cylinder	$S_{c\max} = 1 - \frac{(\lg N - 0.23)(1 - S_{c\min})}{17}$
Yao (1990)	—	$S_{c\max} = S_{c\min} + \frac{(1 - S_{c\min})}{(1.09 - 0.074\lg N)}$
Kim and Kim (1996)	Cylinder	$S_{c\max} = -7.6\left(\frac{f_c}{f_1}\right)^{2/30} \lg N + 126\left(\frac{f_c}{f_1}\right)^{-1/40}$
Hou (2001)	—	$S_{c\max} = 1.16 - 0.153 \frac{\lg N}{[1 + (0.34\lg N)^5]^{1/5}} - 0.038\lg N$
Song et al. (2008)	—	$S_{c\max} = 0.9885 - 0.0618\lg N$

Note:  $S_{c\max} = f_{c\max}/f_c$ ;  $R$  is the stress ratio, and  $R = f_{c\min}/f_{c\max}$ ;  $N$  is fatigue cycle;  $f_{c\min}$  and  $f_{c\max}$  are the minimum and maximum values of fatigue load respectively;  $\beta$  is the correction factor, generally taking a value of 0.064;  $f_1$  is 1 Mpa.

TABLE 2 Arrangement of fatigue equation of concrete under tensile condition.

References	Sample	Expressions
Tepfers, (1979)	Cubic	$S_{t\max} = 1 - \beta(1 - R)\lg N$
Saito (1983)	—	$S_{t\max} = 0.9873 - 0.0413\lg N$
Zhao et al. (1993)	—	$S_{t\max} = A - B\lg N$
Cornelissen and Reinhardt (1984)	Cylinder	Dry sample: $\lg N = 14.81 - 14.52S_{t\max} + 2.79S_{t\min}$ Sealed maintenance specimens: $\lg N = 13.92 - 14.52S_{t\max} + 2.79S_{t\min}$
Lü (2002)	Prism	$\lg N = 16.67 - 16.76S_{t\max} + 5.17S_{t\min}$
Song et al. (2008)	—	$\lg N = 16.67 - 16.76S_{t\max} + 5.17S_{t\min}$

Note:  $\beta$  is the correction factor, generally taking a value of 0.0685; The axial, split, and bending tensions correspond to A and B of 0.970 and 0.05, 0.965 and 0.054, 0.942 and 0.045, respectively;  $S_{t\max}$  is the maximum stress level;  $S_{t\min}$  is the minimum stress level.

TABLE 3 General description of random variables.

Variables	Number	Unit	Mean value	Coefficient of variation	Distribution type
$f_{cu}$	$\gamma$	MPa	32.5	0.098	Log-normal distribution
$P$	$x_1$	kN	280	0.15	Normal distribution
$E_\gamma$	$x_2$	MPa	$3.5 \times 10^4$	0.08	Log-normal distribution
$E_k$	$x_3$	N/m	$4 \times 10^7$	0.1	Normal distribution
$K_f$	$x_4$	—	1.35	0.035	Normal distribution
$E_t$	$x_5$	MPa	$1.5 \times 10^4$	0.1	Weibull distribution
$\gamma$	$x_6$	—	1	0.05	Log-normal distribution

Note:  $f_{cu}$  is the concrete compressive strength,  $P$  is the train load,  $E_\gamma$  is the modulus of elasticity of the invert structure,  $E_k$  is the fastener stiffness,  $K_f$  is the lateral force adjustment factor,  $E_t$  is the liner elasticity model,  $\gamma$  is uncertainty variable factor.

random variable are determined, and the values obtained are shown in Table 4.

The above calculation steps have been conducted to obtain the origin moment of concrete under longitudinal compression. The calculation results are then substituted into Eq. 24, resulting in the following expression:

$$G(X, Y, t) = \frac{(0.9885\gamma - 0.0618\gamma \lg(1.7345 \times 10^6 t))(1 - 0.005t)}{-(\sigma_{c\min} + 5.124x_6)} \quad (25)$$

In order to study the effect of time on reliability and failure probability, it is essential to consider the continuity of time  $T$ . A time period of 70 years was selected, with a time interval of 1 year. When

TABLE 4 Random variable seven-point inverse normal transition value.

Variables	Point 1	Point 2	Point 3	Point 4	Point 5	Point 6	Point 7
$y$	18.8834	22.4782	27.6532	32.3452	37.1567	42.0678	47.7832
$x_1$	144.542	193.421	234.331	280	331.321	382.412	439.438
$x_2$	27137.6	29906.6	32795.3	35053.3	39126.4	44217.6	49541.8
$x_3$	$2.45 \times 10^7$	$3.04 \times 10^7$	$4 \times 10^7$	$4 \times 10^7$	$4.43 \times 10^7$	$4.94 \times 10^7$	$5.46 \times 10^7$
$x_4$	1.0532	1.1437	1.2567	1.35	1.474	1.562	1.6834
$x_5$	$0.42 \times 10^4$	$0.82 \times 10^4$	$1.12 \times 10^4$	$1.5 \times 10^4$	$1.94 \times 10^4$	$2.46 \times 10^4$	$2.86 \times 10^4$
$x_6$	0.8263	0.8875	0.9433	0.9978	1.0522	1.1327	1.2143

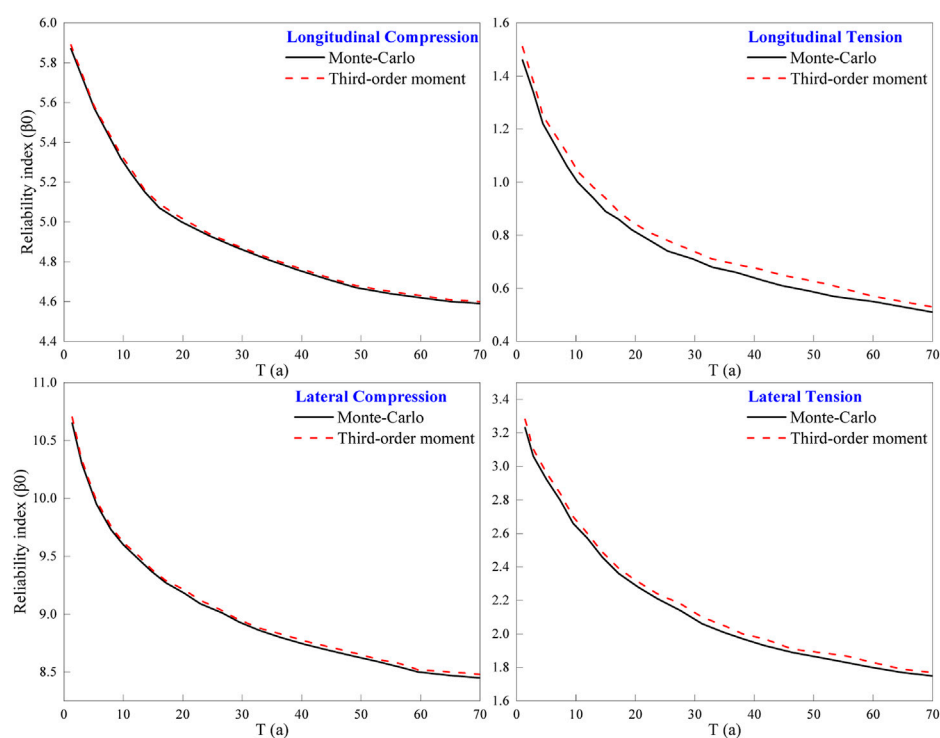
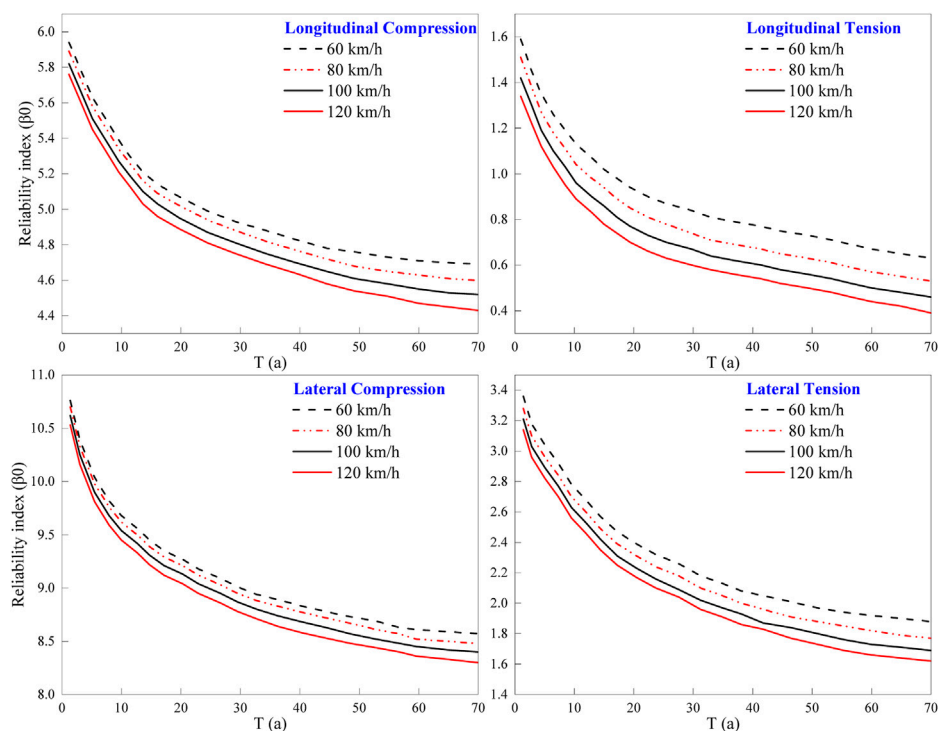


FIGURE 3  
Variation of time-varying fatigue reliability of invert structures of subway tunnels.

the selected time is 1 year, the expression with only two variables can be obtained. Then, the first third-order moments of this expression are estimated using the seven-point estimation method. Similarly, the first third-order moments of this expression can be obtained for each time period. Finally, the reliability indexes and corresponding failure probabilities of the concrete structure of the invert structure of the subway tunnel under fatigue stress in each time period are calculated using the third-order moment method. Additionally, the Monte Carlo method (4 million times) was used for comparative analysis to verify the feasibility and rapidity of the third-order moment method. The trend of the reliability indexes with time was obtained by collating and analyzing the calculation results shown in Figure 3.

The fatigue reliability of the concrete structure of the invert structure of the subway tunnel was calculated, and the results indicate that there is no significant fatigue problem for this part of

the structure under the action of dynamic train load. The calculated fatigue reliability indexes are above 4.5 in both lateral and longitudinal compression cases, with a corresponding failure probability of less than  $0.86 \times 10^{-7}$ . The lateral fatigue results are even better, with all indexes above 8.0, and it can be considered that the failure probability under this force condition is close to zero. However, in the lateral bending-tension edge of the invert structure, the fatigue reliability indexes of concrete bending-tension fatigue cracking range from 1.774 to 3.235, with corresponding failure probabilities between  $2.436 \times 10^{-6}$  and  $3.356 \times 10^{-4}$ . On the other hand, the fatigue reliability indexes of bending and tensile fatigue cracking of concrete in the longitudinal tension edge are only between 0.473 and 1.421, with corresponding failure probabilities between 0.104 and 0.293. These results indicate that bending and tensile fatigue cracking is more likely to occur in the longitudinal tension edge of the invert structure under train load and complex environmental



**FIGURE 4**  
Effects of different train speeds on the fatigue reliability of the invert structure.

conditions, especially in long-term service conditions. Moreover, the probability of failure increases significantly over time.

The results obtained from the two methods (the third-order moment method and the Monte Carlo method) overlap, indicating that the third-order moment method is both accurate and efficient in evaluating the fatigue reliability of concrete structures in subway tunnel invert structures. The Monte Carlo method, while commonly used for reliability verification, requires a high number of calculation runs, making it less efficient. Thus, the third-order moment method is a suitable choice for the analysis of fatigue reliability in invert structure of subway tunnels.

## 5 Parametric analysis

In the previous section, we examined the time-varying fatigue reliability of the invert structure of the subway tunnel under train load stress. However, during actual subway operation, there are variations in operating speed, train type, and lining thickness in different sections. These variations can impact the fatigue life of the subway tunnel structure, necessitating detailed research and comparative analysis. In this section, we will further discuss the influences of subway train speed, axle weight, and tunnel lining thickness.

### 5.1 Effects of the train speed

The train speeds are set to 60, 80, 100, and 120 km/h, and the fatigue reliability indices of the invert structure of the subway

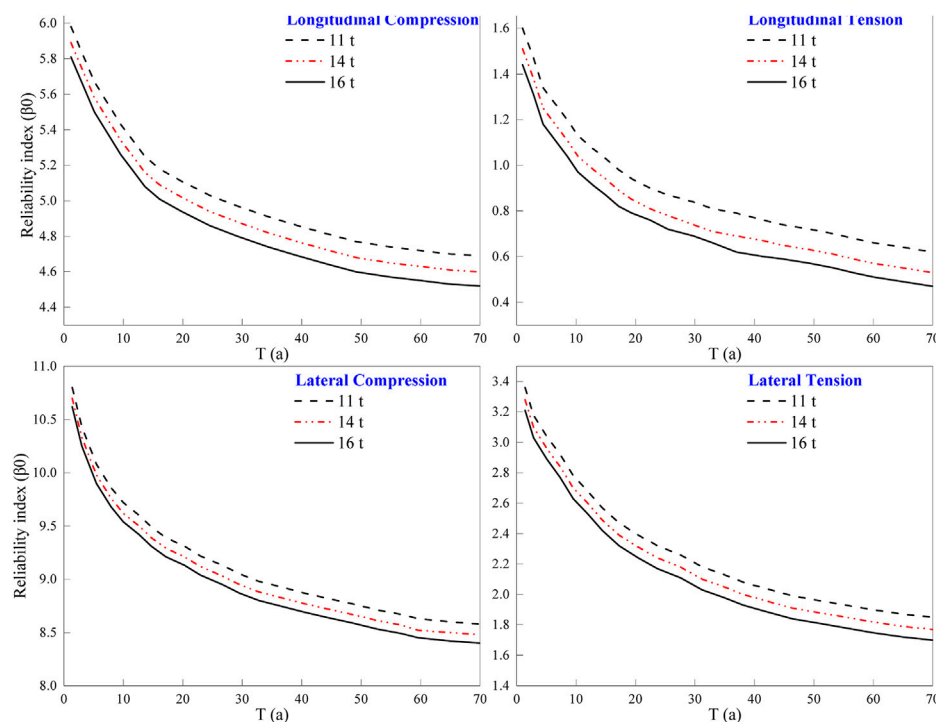
tunnel under different operating speeds are calculated using the third-order moment method. The calculated results are depicted in Figure 4.

Figure 4 illustrates how the time-varying fatigue reliability of the invert structure of the subway tunnel changes at four different speeds for longitudinal and lateral compression and tension. All four cases show a decrease in the fatigue reliability index and an increase in failure probability as the number of fatigue cycles increases. When the train speed increases, the fatigue reliability index decreases, and the failure probability increases, but the rate of change slows down. The worst damage occurs in the longitudinal tension position, followed by the lateral tension position. This suggests that the invert structure will experience significant concrete tension damage due to cyclic train loads, which are also affected by factors such as surrounding rock pressure, groundwater conditions, and structural form. Train speed has a significant impact on the fatigue reliability index of the invert structure, so a comprehensive analysis is necessary to determine the fatigue life in different regions and interval sections.

### 5.2 Effects of axle weight

This study will evaluate the effects of axle weight on the fatigue reliability of the invert structure of the subway tunnel. The train axle weights are set to 11, 14, and 16 t based on the actual service conditions of the subway tunnel.

Figure 5 shows the fatigue time variation reliability indexes of the invert structure of a subway tunnel under three different train axle



**FIGURE 5**  
Effect of different axle weights on the fatigue reliability of the invert structure.

weights in both longitudinal and lateral compression and tension. As fatigue cycles increase, the reliability index decreases, and the probability of failure increases, indicating degradation of the concrete material during service. Increasing train axle weights results in a continuous decrease in the fatigue reliability index and an increase in the probability of failure, with the most severe damage occurring at the location of longitudinal tension and then transverse tension. This effect is consistent with the influence of train speed and reduces the service life of the invert structure of the subway tunnel. The effect of different train axle weights on the fatigue life is slightly greater than that of train speed and should be evaluated for tunnel sections with high pedestrian flow. While heavier trains may be needed for transporting large numbers of people, such sections require special attention to avoid unpredictable dangers. Therefore, it is important to evaluate the impact of different axle weights on the fatigue life of the invert structure in high-pedestrian-flow interval sections. While it may be necessary to use trains with heavier axle weights in these sections to meet capacity demands and prevent overcrowding, the increased weight will also accelerate the degradation of the concrete structure, potentially posing a safety risk.

### 5.3 Effects of lining thickness of the subway tunnel

The lining thicknesses of the subway tunnel are set to 300, 350, 400, and 450 mm. The fatigue reliability indices are calculated using the third-order moment method; the obtained fatigue reliability index calculation results are shown in Figure 6.

Figure 6 shows the fatigue time variation reliability index of the concrete structure of the invert structure at four different lining thicknesses in longitudinal compression, tension, and lateral compression and tension, and they all exhibit similar trends. As the fatigue time increases, the fatigue reliability index decreases, and the failure probability increases. When the lining thickness increases under longitudinal tension, the fatigue reliability index decreases slowly, and the failure probability increases slowly. However, under longitudinal compression, lateral compression, and lateral tension, the fatigue reliability index does not change significantly. The most severe fatigue failure occurs under transverse tension, regardless of the lining thickness, and the most severe fatigue failure occurs under longitudinal tension. These findings suggest that the concrete structure of the invert structure of subway tunnel will experience severe concrete strain degradation from long-term cyclic train loads. This is also influenced by the surrounding rock pressure and tunnel structure type within the subway tunnel. Although the lining thickness has a certain influence on the fatigue reliability index of the concrete structure of the invert structure at the local position, this influence is less than that of the previous two influencing parameters. Therefore, when designing the tunnel lining thickness, it is necessary to meet only the minimum requirements of the design and save construction costs to realize the concept of green environment protection.

According to the analysis above, different factors such as train speeds, axle weights, and lining thicknesses have impacts on the fatigue reliability index and failure risk of the concrete



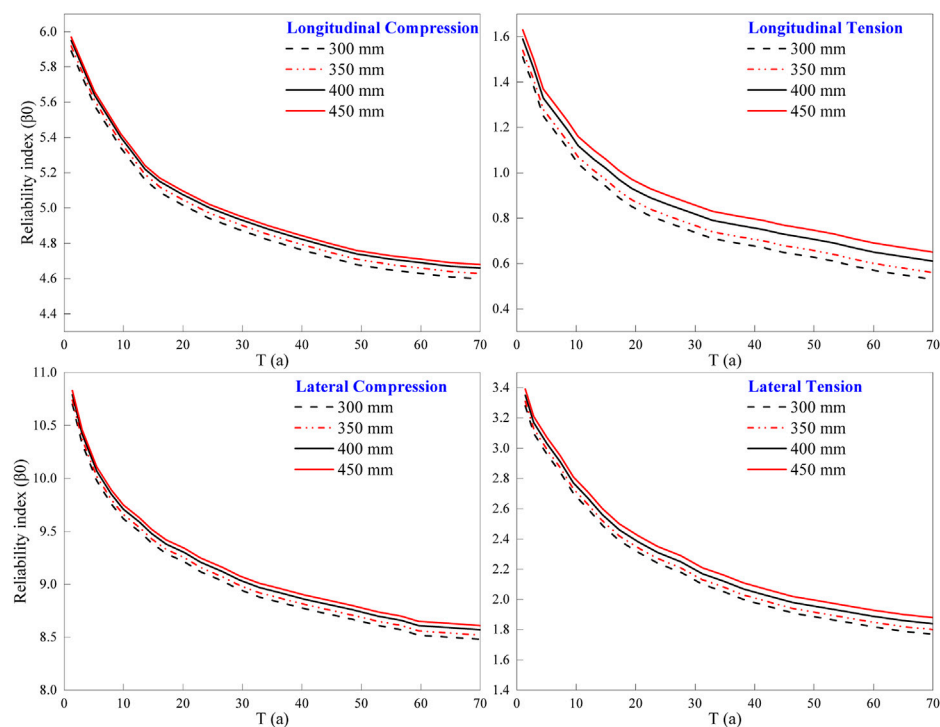


**FIGURE 6**  
Effect of different lining thicknesses on the fatigue reliability of the invert structure.

construction of the subway tunnel. The influence pattern of these factors on the fatigue reliability index of the invert structure is similar, showing a gradual decrease of the fatigue reliability index and a corresponding increase in failure probability with increasing fatigue time, but none of these factors change the location of the most severe damage, which occurs mainly along the longitudinal axis. This is related to the uniform distribution of the surrounding rock pressure and the continuous force produced by the train's dynamic load combined with the direction of the tunnel. The results of the fatigue reliability analysis of the concrete structure of the invert structure indicate that on-site inspections of the subway tunnel should focus on the areas most susceptible to damage. The time-varying fatigue reliability analysis of the invert structure of the subway tunnel is more consistent with the actual service period, and the computed results provide a scientific and theoretical basis and technical indicators for the subsequent evaluation of the subway tunnel's health status.

## 6 Conclusion

A study was conducted to assess the reliability of the concrete structure of the invert structure in subway tunnels over time, considering the repeated loads from trains. Higher-order moment theory, fatigue equation, and cumulative damage theory

were used for this purpose. The results of this study will provide insight into the health and reliability of subway tunnels and facilitate their condition monitoring. Key findings include the following:

- (1) The extent of fatigue damage in the invert structure of subway tunnels is largely determined by the stress it is under. Stress levels were measured and used to predict the concrete's stress tolerance, which was then used to determine the stress limit for the invert structure before fatigue damage occurs.
- (2) The results of the time-varying fatigue performance function of the invert structure of the subway tunnel are essentially consistent with those obtained from the Monte Carlo method, indicating the method's suitability for fatigue reliability analysis of the invert structure. The probability of failure in the case of compression is low, while the concrete is more susceptible to bending and tension fatigue cracking in the case of tension, necessitating reinforcement of the invert structure for longitudinal and lateral tension concrete detection and maintenance.
- (3) Train axle weight and speed have a relatively large impact on the fatigue reliability index, with speed having a slightly greater effect than axle weight, and lining thickness having a negligible effect. As the number of fatigue cycles increases over time, the fatigue reliability index decreases continuously, and the corresponding probability of failure increases continuously. The area requiring the most

inspection and maintenance is determined to be the tensile state of the invert structure.

## Data availability statement

The original contributions presented in the study are included in the article/Supplementary Material, further inquiries can be directed to the corresponding author.

## Author contributions

All authors listed have made a substantial, direct, and intellectual contribution to the work and approved it for publication.

## References

- Aas-Jakobsen, K. T. (1970). *Fatigue of concrete beam and s. Pichanur*, Pichanur, Tamil Nadu; NTH Institute of Betongkonstruksjoner.
- Chen, L. H., Chai, X. B., and Fan, H. Z. (2014). "Tunnel reliability analysis based on the combination of modified FOSM and numerical calculation program," in *Applied mechanics and materials* Switzerland; (Zürich, Switzerland: Trans Tech Publ), 1174–1181.
- Cornelissen, H. A. W., and Reinhardt, H. W. (1984). Uniaxial tensile fatigue failure of concrete under constant-amplitude and programme loading. *Mag. Concr. Res.* 36, 216–226. doi:10.1680/mac.1984.36.129.216
- Ellingwood, B., and Hwang, H. (1985). Probabilistic descriptions of resistance of safety-related structures in nuclear plants. *Nucl. Eng. Des.* 88, 169–178. doi:10.1016/0029-5493(85)90059-7
- Fattahi, H., and Jiryaee, F. (2022). Reliability analysis of surface settlement caused by mechanized tunneling—a case study. *J. Min. Environ.* 13, 201–216. doi:10.22044/jme.2022.11570.2143
- Frangopol, D. M., Lin, K.-Y., and Estes, A. C. (1997). Reliability of reinforced concrete girders under corrosion attack. *J. Struct. Eng.* 123, 286–297. doi:10.1061/(asce)0733-9445(1997)123:3(286)
- Hou, J. P. (2001). *Study of fatigue damage criterion for concrete materials* (PhD Thesis). Dalian, China, Dalian University of Technology.
- Kim, J.-K., and Kim, Y.-Y. (1996). Experimental study of the fatigue behavior of high strength concrete. *Cem. Concr. Res.* 26, 1513–1523. doi:10.1016/0008-8846(96)00151-2
- Laso, E., Lera, M. S. G., and Alarcón, E. (1995). A level II reliability approach to tunnel support design. *Appl. Math. Model.* 19, 371–382. doi:10.1016/0307-904x(95)00019-g
- Li, T. Z., and Yang, X. L. (2019). An efficient uniform design for Kriging-based response surface method and its application. *Comput. Geotech.* 109, 12–22. doi:10.1016/j.compgeo.2019.01.009
- Lü, P. Y. (2002). *Uniaxial and biaxial dynamic strength and deformation test study of concrete*. PhD Thesis Dalian, China; (Dalian University of Technology).
- Lü, Q., and Low, B. K. (2011). Probabilistic analysis of underground rock excavations using response surface method and SORM. *Comput. Geotech.* 38, 1008–1021. doi:10.1016/j.compgeo.2011.07.003
- Matsushita, H., and Tokumitsu, Y. (1979). "A study on compressive fatigue strength of concrete considered survival probability," in *Proceedings of the Japan society of civil engineers* Tokyo, Japan; (Japan Society of Civil Engineers), 127–138.
- Miner, M. A. (1945). Cumulative damage in fatigue. *J. Appl. Mech.* 12 (3). doi:10.1115/1.4009458
- Mollon, G., Daniel, D., and Abdul-Hamid, S. (2009). Probabilistic analysis and design of circular tunnels against face stability. *Int. J. Geomech.* 9, 237–249. doi:10.1061/(asce)1532-3641(2009)9:6(237)
- Mollon, G., Dias, D., and Soubra, A.-H. (2011). Probabilistic analysis of pressurized tunnels against face stability using collocation-based stochastic response surface method. *J. Geotech. Geoenvironmental Eng.* 137, 385–397. doi:10.1061/(asce)gt.1943-5606.0000443
- Mori, Y., and Ellingwood, B. R. (1993). Reliability-based service-life assessment of aging concrete structures. *J. Struct. Eng.* 119, 1600–1621. doi:10.1061/(asce)0733-9445(1993)119:5(1600)
- Ou, Z. M. (2016). *Fatigue reliability analysis methods and application for slab track structure*. Nanjing, China: Southeast Univ.
- Qing Li, C. (2004). Reliability based service life prediction of corrosion affected concrete structures. *J. Struct. Eng.* 130, 1570–1577. doi:10.1061/(asce)0733-9445(2004)130:10(1570)
- Rosenblueth, E., and Esteva, L. (1972). Reliability basis for some Mexican codes. *Spec. Publ.* 31, 1–42. doi:10.14359/17921
- Rosenblueth, E. (1975). Point estimates for probability moments. *Proc. Natl. Acad. Sci.* 72, 3812–3814. doi:10.1073/pnas.72.10.3812
- Saito, M. (1983). Direct tensile fatigue of concrete by the use of friction grips. *J. Proc.* 80, 431–438. doi:10.14359/10867
- Shi, Q., Pan, J., Wang, S., Liu, S., Mishra, B., and Seitz, S. (2021). Field monitoring of delayed coal burst in an advancing entry of a deep coal mine. *Min. Metall. Explor.* 38, 2417–2431. doi:10.1007/s42461-021-00508-6
- Shiozawa, K., Lu, L., and Ishihara, S. (2001). S-N curve characteristics and subsurface crack initiation behaviour in ultra-long life fatigue of a high carbon-chromium bearing steel. *Fatigue Fract. Eng. Mat. Struct.* 24, 781–790. doi:10.1046/j.1460-2695.2001.00459.x
- Song, Y. P., Wang, H. L., and Jia, J. Q. (2008). Behavior of concrete under multi-axial fatigue loading. *J. Build. Struct.* 29, 260–265.
- Stewart, M. G., and Val, D. V. (1999). Role of load history in reliability-based decision analysis of aging bridges. *J. Struct. Eng.* 125, 776–783. doi:10.1061/(asce)0733-9445(1999)125:7(776)
- Tepfers, R. (1979). Tensile fatigue strength of plain concrete. *J. Proc.* 76, 919–934. doi:10.14359/6969
- Val, D. V., and Melchers, R. E. (1996). "Reliability assessment of existing concrete bridges," in *Structural reliability in bridge engineering: Design, inspection, assessment, rehabilitation and management. Proceedings of the WorkshopNational science foundation*. Lakewood, Colorado; (Federal Highway Administration, Colorado Department of Transportation). 356,
- Vu, K. A. T., and Stewart, M. G. (2000). Structural reliability of concrete bridges including improved chloride-induced corrosion models. *Struct. Saf.* 22, 313–333. doi:10.1016/s0167-4730(00)00018-7
- Wang, X., Li, J., Zhao, X., and Liang, Y. (2022). Propagation characteristics and prediction of blast-induced vibration on closely spaced rock tunnels. *Tunn. Undergr. Space Technol.* 123, 104416. doi:10.1016/j.tust.2022.104416
- Xie, P., Zhang, R., Zheng, J., and Li, Z. (2022). Probabilistic analysis of subway station excavation based on BIM-RF integrated technology. *Autom. Constr.* 135, 104114. doi:10.1016/j.autcon.2021.104114
- Yao, M. C. (1990). *Study of fatigue properties of concrete under equal and variable amplitude repetitive stresses*. Beijing, China: Research report of the Ministry of Railways Scientific Research Institute.

## Conflict of interest

The authors declare that the research was conducted in the absence of any commercial or financial relationships that could be construed as a potential conflict of interest.

## Publisher's note

All claims expressed in this article are solely those of the authors and do not necessarily represent those of their affiliated organizations, or those of the publisher, the editors and the reviewers. Any product that may be evaluated in this article, or claim that may be made by its manufacturer, is not guaranteed or endorsed by the publisher.

- Zhao, G. Y., Wu, P. G., and Zhan, W. W. (1993). Tensile fatigue performance of high-strength concrete. *J. Civ. Eng.* 26, 13–19.
- Zhao, Y.-G., Lu, Z.-H., and Ono, T. (2006). A simple third-moment method for structural reliability. *J. Asian Archit. Build. Eng.* 5, 129–136. doi:10.3130/jaabe.5.129
- Zhao, Y.-G., and Ono, T. (2001). Moment methods for structural reliability. *Struct. Saf.* 23, 47–75. doi:10.1016/s0167-4730(00)00027-8
- Zhao, Y.-G., and Ono, T. (2000). New point estimates for probability moments. *J. Eng. Mech.* 126, 433–436. doi:10.1061/(asce)0733-9399(2000)126:4(433)
- Zhou, H., He, C., Wang, S., Peng, F., Zhu, S., and Yuan, D. (2020). Dynamic stress concentration factors and damage mode of horseshoe tunnels crossing fault fracture zone. *Geotech. Geol. Eng.* 38, 5127–5141. doi:10.1007/s10706-020-01352-z
- Zhou, H., He, C., Wang, X., Chen, Y., and Li, J. (2023). Assessment of the seismic response of shallow buried elliptical tunnels. *J. Earthq. Eng.* 27, 465–487. doi:10.1080/13632469.2021.2009057
- Zhou, Y., Zheng, S., Chen, L., Long, L., and Wang, B. (2021). Experimental investigation into the seismic behavior of squat reinforced concrete walls subjected to acid rain erosion. *J. Build. Eng.* 44, 102899. doi:10.1016/j.jobe.2021.102899

# Frontiers in Earth Science

Investigates the processes operating within the major spheres of our planet

Advances our understanding across the earth sciences, providing a theoretical background for better use of our planet's resources and equipping us to face major environmental challenges.

## Discover the latest Research Topics

[See more →](#)

### Frontiers

Avenue du Tribunal-Fédéral 34  
1005 Lausanne, Switzerland  
[frontiersin.org](https://frontiersin.org)

### Contact us

+41 (0)21 510 17 00  
[frontiersin.org/about/contact](https://frontiersin.org/about/contact)

